

Structural Insights into the

Conformations of

Biomolecules

Henry P. Wood

Supervisors:

Professor Jonathan P. Waltho

Professor David P. Hornby

Dept. of Molecular Biology and Biotechnology

Thesis submitted to the University of Sheffield

for the degree of Doctor of Philosophy

Jan, 2021

To Charlotte.

Table of Contents

1. Introduction.....	16
1.1 Enzymes.....	17
1.1.1 Background.....	17
1.1.2 Enzyme Catalysis.....	17
1.1.3 Enzyme Regulation.....	22
1.2 Phosphoryl Transfer Enzymes	24
1.2.1 Background.....	24
1.2.2 Metal Fluorides	24
1.2.3 β PGM.....	26
1.3 Alginate.....	30
1.3.1 Background.....	30
1.3.2 Polysaccharide Lyases	34
1.3.3 Dp0100.....	34
2. NMR Theory and Methods	38
2.1 Theory	38
2.1.1 Background	38
2.1.2 Spin	38
2.1.3 Longitudinal Magnetization.....	39
2.1.4 The NMR Signal.....	40
2.1.5 Chemical shift	40
2.1.6 J-Coupling.....	41
2.1.7 Relaxation	42
2.1.8 The Nuclear Overhauser Effect	44
2.2 Experiments	45
2.2.1 Correlation Spectroscopy.....	45
2.2.2 Total Correlation Spectroscopy	46

2.2.3 NOE Spectroscopy.....	47
2.2.4 Rotating Frame NOE Spectroscopy.....	48
2.2.5 The Heteronuclear Single Quantum Correlation Experiment.....	49
3. Allomorphy	51
3.1 Abstract	53
3.2 Introduction.....	54
3.3 Results.....	57
3.3.1 β PGM _{WT} exchanges slowly between two stable conformations	57
3.3.2 Influence of physiological factors on the conformational exchange	58
3.3.3 The conformational exchange involves <i>cis-trans</i> proline isomerisation	59
3.3.4 β PGM _{WT} lag phase depends on the phosphorylating agent	61
3.3.5 β PGM catalysis utilises a <i>cis</i> K145-X146 peptide bond.....	62
3.3.6 β PGM forms two different transient phospho-enzyme species	64
3.4 Discussion	67
3.5 Methods.....	70
3.5.1 β -Phosphoglucomutase (β PGM) expression and purification.....	70
3.5.2 NMR spectroscopy.....	70
3.5.3 Kinetic experiments using coupled assays.....	73
3.5.4 X-ray crystallography	74
3.6 Acknowledgements.....	76
3.7 Author Contributions	76
3.8 Competing Financial Interest.....	76
3.9 Data Deposition	76
3.10 Figures.....	78
4. Enzymatic Production of β -glucose 1,6-bisphosphate.....	85
4.1 Abstract	87

4.2 Main	88
4.3 Conclusions.....	96
4.4 Conflicts of interest.....	96
4.5 Acknowledgements.....	97
4.6 Materials and Methods.....	98
4.6.1 Reagents:.....	98
4.6.2 Gene sequence for β PGM _{D170N} :	98
4.6.3 β PGM expression and purification:	98
4.6.4 NMR Spectroscopy:.....	99
4.6.5 Kinetic Assays:	101
4.6.6 β G1P preparation:	102
4.6.7 β G16BP production and purification:.....	103
4.7 Figures.....	104
5. Novel alginate conformation.....	110
5.1 Abstract.....	112
5.2 Introduction.....	112
5.3 Results.....	114
5.3.1 Atypical conformation of polyG exists in TM5 biding site.....	114
5.3.2 Atypical coordination of polyG repeats in active site of TM5	115
5.3.3 PolyG residue environment is not uniform.....	116
5.3.4 Dominant solution conformation of triG is not 4C_1 chair conformation.....	118
5.3.5 Dominant solution structure of polyG contains no residues in the 4C_1 chair conformation	119
5.4 Discussion	120
5.5 Materials and Methods.....	123
5.5.1 Preparation of polyG.....	123

5.5.2 X-ray crystallography, data collection, structure determination and refinement..	123
5.5.3 NMR spectroscopy.....	124
5.5.4 Data availability.....	125
5.6 Tables and Figures	126
6. Conclusions and Future Directions	135
7. References.....	138
8. Appendix A – Supplementary Information.....	157
9. Appendix B – Supplementary Information.....	173
10. Appendix C – Supplementary Information.....	181

List of Tables

Table 5.1. X-ray crystallographic data.....	126
Table 5.2. Chemical shifts in ppm for polyG oligomers.....	127
Table 5.3. Peak integrals for anomeric proton resonances in quantitative 1-D ¹ H spectra of polyG oligomers.....	128
Table 5.4. Correlations in ROESY spectrum involving anomeric protons of polyG oligomers.	129

List of Figures

Figure 1.1. Energy levels diagram	18
Figure 1.2. Energy levels diagram for a hypothetical enzyme reaction.....	19
Figure 1.3. The GS and TS for a concerted phosphoryl transfer reaction	26
Figure 1.4. The open and closed forms of β PGM.....	27
Figure 1.5. The active site of β PGM highlighting the two sites that coordinate phosphate.	28
Figure 1.6. Substrate positioning in TSA complexes representing Step 1 and Step 2 of the catalytic cycle of β PGM.	29
Figure 1.7. The catalytic cycle of β PGM.....	30
Figure 1.8. Fischer projections for the two uronic acids which comprise alginate.	31
Figure 1.9. Structure of the junction zone.....	32
Figure 1.10. Conformations of α -L-guluronic acid and β -D-mannuronic acid.	33
Figure 1.11. Crystal structure of the catalytic domain of Dp0100 in substrate-free form.	35
Figure 1.12. Proposed reaction mechanism of alginate lyase Dp0100.	36
Figure 1.13. The structure of the active site of the catalytic domain in Dp0100 bound to a polyM pentasaccharide.	36
Figure 2.1. Spectral density functions for two different fluctuating transverse magnetic fields.	43
Figure 2.2. The basic pulse sequence for a 2D COSY experiment.....	46
Figure 2.3. The basic pulse sequence for a 2D TOCSY experiment.	47
Figure 2.4. The basic pulse sequence for a 2D NOESY experiment.	48
Figure 2.5. The basic pulse sequence for a 2D ROESY experiment.	49
Figure 3.1. β PGM catalytic cycle.	78
Figure 3.2. Effect of different phosphorylating agents on β PGM.	79
Figure 3.3. Exchange behaviour in β PGM _{WT}	80
Figure 3.4. Conformational plasticity of the active site of β PGM.....	81
Figure 3.5. Kinetic profiles of β PGM activity.	82
Figure 3.6. Kinetic model of β PGM activity.	83
Figure 3.7. Mechanisms of regulation and activity profiles in monomeric enzymes.	84
Figure 4.1. <i>In vitro</i> phosphorylation and catalytic cycle of β PGM.	104
Figure 4.2. Comparison of octahedral Mg _{cat} coordination in β PGM _{WT} ^P (Step 1) and β PGM _{WT} (Step 2).....	105

Figure 4.3. Kinetic experiments involving β PGM _{WT} and β PGM _{D170N}	106
Figure 4.4. ^{31}P and ^{19}F NMR experiments involving β PGM _{WT} and β PGM _{D170N}	107
Figure 4.5. NMR experiments recorded on a sample of the final β G16BP product, purified following its production by β PGM _{D170N} and prepared in 100% $^2\text{H}_2\text{O}$	108
Figure 5.1. Proposed mechanism of Dp0100-catalysed depolymerisation of polyG alginates.....	130
Figure 5.2. X-ray crystal structure of TM5 in complex with polyG oligomers.....	131
Figure 5.3. 1-D ^1H NMR spectra of L-guluronic acid oligomers.....	132
Figure 5.4. ROESY spectrum of triG.....	133
Figure 5.5. $^1\text{H}^{13}\text{C}$ -HSQC spectrum of triG.	134

List of Abbreviations

NMR	Nuclear magnetic resonance
TS	Transition state
GS	Ground state
TSA	Transition state analogue
k_{cat}	Turnover number
K_m	Michaelis constant
K_i	Inhibitor constant
NAC	Near attack conformer
PTM	Post translational modification
GCK	Human glucokinase
NAD/H	Nicotinamide adenine dinucleotide
NADP/H	Nicotinamide adenine dinucleotide phosphate
cAMP	Cyclic adenosine monophosphate
β G1P	β -Glucose 1-phosphate
β G16BP	β -Glucose 1,6-bisphosphate
G6P	Glucose 6-phosphate
α G16BP	α -Glucose 1,6-bisphosphate
F16BP	Fructose 1,6-bisphosphate
AcP	Acetyl phosphate
β PGM	β -Phosphoglucomutase
β PGM ^P	Phosphorylated β -phosphoglucomutase
A	β -phosphoglucomutase conformer A
B	β -phosphoglucomutase conformer B
A ^P	Phosphorylated β -phosphoglucomutase conformer A
B ^P	Phosphorylated β -phosphoglucomutase conformer B
HAD	Haloacid dehalogenase
Mg _{cat}	Catalytic magnesium
G6PDH	Glucose 6-phosphate dehydrogenase
G	α -L-guluronic acid
M	β -D-mannuronic acid
polyG	poly α (1–4)-L-guluronic acid
polyM	poly β (1–4)-D-mannuronic acid
TM5	Truncation mutant of Dp0100
HSQC	Heteronuclear single quantum correlation
TROSY	Transverse relaxation optimised spectroscopy
COSY	Correlation spectroscopy
TOCSY	Total correlation spectroscopy
NOE	Nuclear Overhauser effect
NOESY	Nuclear Overhauser effect spectroscopy
ROESY	Rotating frame Overhauser spectroscopy
HEPES	4-(2-hydroxyethyl)-1-piperazineethanesulfonic acid
TSP	Trimethylsilylpropanoic acid
EDTA	Ethylenediaminetetraacetic acid

Acknowledgements

The person who coined the phrase ‘The Hard Problem of Consciousness’ evidently never worked on β PGM. Despite several decades-worth of discoveries regarding the inner workings of this little enzyme, it continues to fascinate us with new levels of complexity. β PGM has been a wonderful enzyme to work with and it has sat patiently whilst I have crystallised it, exposed it to high-field magnets and force-fed it colossal quantities of substrate.

After β PGM, thank you to Jon. Whilst doing this PhD I have had an enormous amount of freedom to pursue the things that I’m interested in. I’ve always thought that it must be quite difficult not to poke and prod a student to get them to do the work that you want doing. Jon has never told me to do anything and I am grateful of his commitment to this hands-off approach. He is a tremendous supervisor with great patience and kindness. I am also grateful for his mentorship regarding NMR, kinetics and, importantly, paper writing, as well as the useful insight into academic life (basically lots of marking I think...).

Thank you also to Dave Hornby. I have immensely enjoyed discussions with you about science and always left your office with a renewed enthusiasm. Thanks for all the advice.

Thanks to Jeremy for all the help and encouragement when I was learning to program and to everyone else whose scripts I’ve scraped ideas and tips from. Thanks also to Mike for taking a keen interest in whatever lab talk I gave (and everyone else’s as well for that matter). And to Rosie for being Rosie!

Thanks to Angus for all your help during my time here, especially at the start when I didn’t know “naff all” as you’d say. And to Dr. Dix for teaching me the art of crystallography and for letting us off when it’s a 3am shoot.

Aaron, although I trained you and taught you everything you know, you have still managed to teach me a few things as well. Your thoroughness and breadth of knowledge (in everything except barbershop locations) has made a significant impression on me. Yash, your cheerful demeanour has brought a lot of positivity to the lab. Good luck with your future ventures. Alex, thanks for all the help with ethics! What a shame we couldn’t share a fed reather or ten this year.

Thanks to Pete and Clare for keeping the lab going, and for sharing your knowledge of proteins, columns, NMR and good cake recipes. Nicky, thanks for all your help with everything technical, be it NMR, figure-making or some useful feature of Linux that I wasn't aware of and for the daily chit-chats during the dark days of lockdown. Andrea, thanks for all your help with NMR and for always letting me slot in another experiment. I've always enjoyed your company even when it was just over zoom. Hope you can get back to doing what you love (He fills) very soon.

Thanks Marym and Mahreen for all the cakes. Marym: I will send you my address once you've started your bakery...

Thank you to Nanette, Stewart, Grace and Steve for being a second family to me and looking after me during most of my time here, in particular, selflessly developing a nutrition plan for me to ensure I didn't drop below 15 stone.

Mum and Dad, I owe you an enormous debt of gratitude for setting me off in life. I don't think I've ever made a decision without first thinking what you would do and I am incredibly lucky to have parents like you.

Finally, thank you to Charlotte, for always putting up with me and being there for me. Especially during these last weeks, I have relied on your support more than I'd ever like to admit.

Author Contributions

Paper 1 –Allomorphy as a post-translational control of enzyme activity

Published in Nature Communications, 11, Article number: 5538 (2020)

H.P.W., F.A.C.N., N.J.B., C.R.T., A.J.R., J.P.W. designed research; H.P.W., F.A.C.N., C.R.T., A.J.R. produced isotopically enriched protein; H.P.W. performed coupled assay kinetic experiments; H.P.W., C.R.T. produced and purified β G1P and β G16BP; H.P.W., F.A.C.N., C.R.T., A.M.H., M.J.C. acquired NMR experiments; H.P.W., F.A.C.N., N.J.B., C.R.T. analysed NMR data; F.A.C.N., N.J.B., C.R.T. performed backbone resonance assignments; H.P.W., A.J.R., S.R.D. performed and analysed X-ray crystallography experiments; F.A.C.N. conceived and developed the allomorphy mechanism; H.P.W., F.A.C.N., N.J.B., C.R.T., J.P.W. wrote the paper with help from all authors.

Paper 2 – Enzymatic Production of β -glucose 1,6-bisphosphate through manipulation of catalytic magnesium coordination

Published in Green Chemistry, 23, 752-762 (2021)

H.P.W., F.A.C.N., N.J.B., C.R.T., J.P.W. designed research; H.P.W., F.A.C.N. produced isotopically enriched protein; H.P.W. performed coupled assay kinetic experiments; H.P.W., C.R.T. produced and purified β G1P and β G16BP; H.P.W., F.A.C.N., A.M.H., M.J.C. acquired NMR experiments; H.P.W., N.J.B. analysed NMR data; H.P.W., F.A.C.N., N.J.B., J.P.W. wrote the paper with help from all authors.

Paper 3 – Novel alginate conformation facilitates dual specificity of alginate lyase, dp0100

H.P.W., S.J., J.P.W., D.W.R. designed research; S.E.S produced protein; H.P.W. performed NMR experiments; H.P.W., A.M.H. acquired NMR experiments; H.P.W., J.P.W. analysed NMR data; S.J., S.R.D. performed and analysed X-ray crystallography experiments; H.P.W. wrote the paper with help from all authors.

Abstract

This thesis describes how conformational changes play a role in the function of two enzymes. For the phosphoryl transfer enzyme, β -phosphoglucomutase (β PGM), a novel post-translational regulatory mechanism is reported, underpinned by a *cis-trans* proline isomerism of the K145-P146 peptide bond in the substrate-free enzyme that repositions the K145 sidechain. The reaction intermediate, β -glucose 1,6-bisphosphate (β G16BP), phosphorylates both species into the active *cis* conformer, whereas alternative activators react with both conformers without altering the isomerisation state. This creates a population of phosphorylated species that possesses reduced activity. This behaviour of the substrate-free enzyme, termed allomorphy, manifests as a kinetic lag phase and enables β PGM to lay latent in the cell with low phosphatase activity towards valuable glycolytic metabolites such as fructose 1,6-bisphosphate. Allomorphy alleviates the requirement for a delay in metabolism following upregulation of β PGM expression. In another system, the dual-specific alginate lyase, Dp0100, is observed bound to a novel conformation of poly α (1–4)-L-guluronic acid (polyG). It is shown using NMR that this conformation is not dominant in solution and is likely to be stabilised only within the Dp0100 active site. The bound polyG conformation is strikingly different to the dominant kinked chain solution conformation and mirrors that of poly β (1–4)-D-mannuronic acid (polyM). Dp0100 can therefore use the same active site to catalyse cleavage of both substrates. These results highlight the functional importance of conformational changes in two specific biological systems and offer detailed mechanistic insights that may inform developments of enzyme targeting drugs and improvements to commercial alginate technologies.

1. Introduction

The structure of a biomolecule governs its function. It is testament to the truth of this statement that the field of structural biology occupies such a prominent position in the domain of the life sciences. The tertiary or quaternary structure of an enzyme dictates the structure of the biomolecules that it can interact with. For many enzymes, detailed descriptions of the active site have been reported, and the structure-function relationship is again apparent at this lower level, with the precise arrangement of amino acids at this focal point facilitating catalysis of a particular chemical reaction. For other enzymes, even more structural information has been gathered, providing insight into the changes in structure that take place during a progression through the catalytic cycle. Other structural changes have regulatory significance, with post-transitional modifications such as phosphorylation and glycosylation often having dramatic effects on enzyme activity. Because many structural biology techniques provide a static picture of a biomolecule, or report only indirectly on changes in conformation, there is a considerable gap between our current understanding of events that happen at the atomic scale and being able to directly observe enzyme structures moving and interacting with biomolecules over the course of a catalytic cycle. Computer simulations have gone some way to filling in this gap, but their reliability is still questionable.

The importance of understanding how enzymes and proteins function is evident from their impact on modern medicine. Currently, eight of the top ten best selling drugs in the world are derived from protein structures.¹ The ability to design enzymes to perform specific functions is a long-held goal of chemical biologists.² There are many obstacles to achieving this goal, one of which is an incomplete understanding of structure-function relationships, and in particular, how appropriate conformational changes are programmed. Understanding how conformational changes in proteins occur and what their consequences are is therefore an important step in the mission to design enzymes and proteins from scratch.

This thesis investigates two enzymes where conformational changes result in different functions. In one case, the enzyme β -phosphoglucomutase (β PGM) exchanges between two conformations in its substrate-free state. One of these conformations confers full activity, the other has a structural impairment in the active site that leads to a reduced level of activation. The factor controlling the exchange is the substrate with which the enzyme is phosphorylated, which results in a novel mechanism of enzyme regulation. The second case involves a

conformational change in the substrate of the alginate lyase, Dp0100. Dp0100 exhibits specificity for two substrates that differ substantially in their proposed conformation. To do this, it stabilises a contorted form of one substrate in order to roughly mimic the structure of the other, and has an active site that is set up to handle the small differences that remain.

1.1 Enzymes

1.1.1 Background

The chemical reactions of molecules are governed by enthalpy and entropy. The Gibbs free energy (G) is a thermodynamic potential, just like enthalpy (H) and entropy (S), and it is derived from the first law of thermodynamics (Equation 1.1).

$$\Delta G = \Delta H - T\Delta S \quad (1.1)$$

Gibbs free energy is useful in determining whether a chemical reaction will proceed spontaneously at a particular temperature ($\Delta G < 0$). Reactions that are accompanied by an increase in entropy and a decrease in enthalpy will proceed spontaneously. The spontaneity of reactions for which only one of these thermodynamic factors is favourable will depend on the magnitude of the changes involved. The spontaneity of a reaction says nothing about the rate at which the reaction proceeds. Reactions that are spontaneous can also be slow; for example the oxidation of iron in water. In any reaction the reactant transitions between relatively stable configurations. To do this the reactant must temporarily take on less-stable configurations. The least stable of these configurations is called the transition state (TS) and this transformation presents a barrier of energy, with the free energy of the transition state being the top of this barrier. The size of the barrier between the reactant state and the transition state (ΔG^\ddagger) determines the rate of the reaction at a given temperature (Figure 1.1). In this way, ΔG^\ddagger is analogous to the activation energy (E_a) term in the Arrhenius equation in that its magnitude is inversely proportional to the rate of reaction.

1.1.2 Enzyme Catalysis

A catalyst is a substance that, for a given reaction, reduces the energy of the TS, and therefore increases the number of molecules with enough energy to overcome the energy barrier of the reaction without ever being used up (Figure 1.2). Enzymes are proteins that catalyse reactions and are the most prominent biological catalysts. Non-enzymatic catalysts are used at an

industrial scale and can be expensive, environmentally unfriendly, or require high temperatures to work. Enzymes, on the other hand, usually exhibit optimal activity at temperatures below 40 °C and are cheap to produce. The mechanism by which enzymes reduce the energy barrier of a reaction is therefore of great interest and is an active area of research. Several theories have been presented to explain how enzymes work; some of these are discussed below.

Transition state theory states that the reactants are in a quasi-equilibrium with the activated complex that represents the transition state (TS)³. This treatment leads to the conclusion that a greater concentration of the activated complex leads to a faster reaction. Later it was hypothesised that enzymes catalyse chemical reactions by binding to the TS of the reaction in an active site of complementary shape⁴ and stabilising the TS more than it is stabilised by the solvent. This hypothesis has been borne out by myriad crystal structures and binding studies describing in great detail the interactions between the active site of enzymes and analogues of the TS for the reaction which they catalyse.⁵ In actual fact, stabilisation of the TS must be greater than the stabilisation of the reactant state or ground state (GS) to lead to a reduced

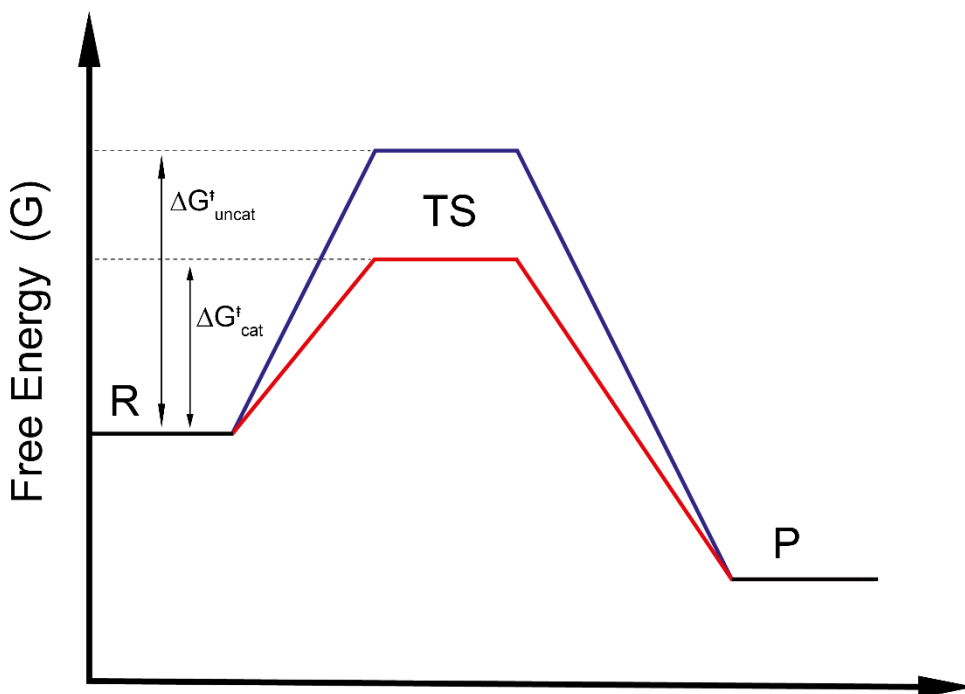


Figure 1.1. Energy levels diagram showing the differences in energy between the reactant (R), the transition state (TS) and the product (P) of a hypothetical spontaneous reaction. The blue line represents the energy barrier for the uncatalysed reaction and the red line represents the energy barrier for the same reaction in the presence of a catalyst. $\Delta G^{\ddagger}_{\text{uncat}}$ and $\Delta G^{\ddagger}_{\text{cat}}$ represent the differences in energy between the reactants and the transition state in the uncatalysed reaction and the catalysed reaction, respectively.

activation barrier. This specificity for the TS over the GS is one of the main questions regarding the origin of the catalytic power of enzymes. Catalytic antibodies provide a good measure of how difficult this problem is to overcome. Catalytic antibodies are antibodies that are raised to be complementary to transition state analogues (TSAs)⁶. Because of this they are capable of binding to, and stabilising, the corresponding TS and catalysing the reaction. Catalytic antibodies have largely been a disappointment however, and the rate enhancements that they achieve have been meagre compared to those measured for natural enzymes.⁷ This is possibly due to the fact that catalytic antibodies are not well equipped to selectively bind the TS over the GS, and that other factors have evolved to enable this in natural enzymes.

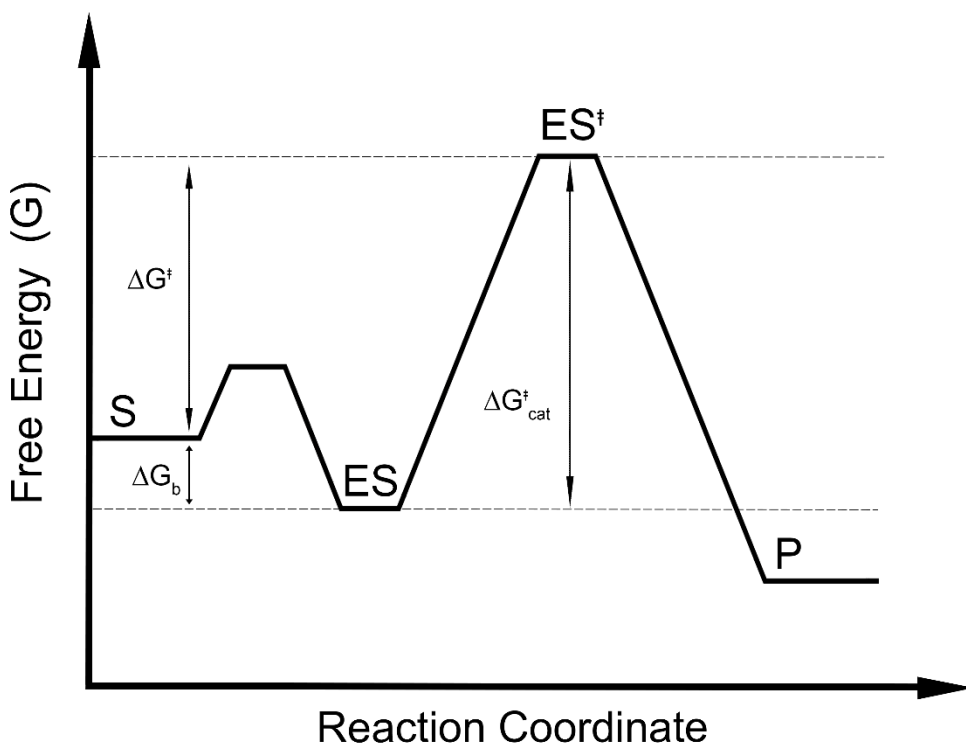


Figure 1.2. Energy levels diagram for a hypothetical enzyme reaction showing the differences in energy between the substrate (S), the enzyme-substrate complex (ES), the enzyme-bound transition state (ES^{\ddagger}) and the product (P). ΔG_b represents the binding energy, ΔG^{\ddagger} represents the energy barrier for the reaction and $\Delta G_{\text{cat}}^{\ddagger}$ represents the energy barrier for the chemical step of the reaction.

1.1.2.1 Electrostatics

One proposal that has received considerable support is that of the catalytic proficiency of enzymes being largely an electrostatic effect.^{8–11} In this hypothesis, the transition state is

stabilised by electrostatic interactions between the TS and residues in the active site of the enzyme. Solvent molecules are capable of stabilising the charges that can accumulate on a TS; however, the organisation of hydrogen bonded water molecules around a charged TS is accompanied by a considerable decrease in entropy, thus negating the stabilisation achieved. Conversely, in an enzyme active site, polar groups are prearranged, and the entropic cost of organising these groups is paid only once when the protein folds. The TS is therefore stabilised by the enzyme more than it is in the solvent. Additionally, enzyme active sites often exclude solvent^{12–15}, which is thought to dramatically reduce the dielectric constant of the environment, although this is difficult to measure. The strength of the interaction between two charges is inversely proportional to the dielectric constant, as described by Equation 1.2, where F_e is the electric force between two charged objects; q_1 and q_2 are the electric charges of the two objects; ϵ_0 represents the dielectric constant of the medium; and r is the distance between the two objects.

$$F_e = \frac{q_1 q_2}{4\pi\epsilon_0 r^2} \quad (1.2)$$

In water the dielectric constant is 80.2 at 20 °C¹⁶, but in enzyme active sites this can be reduced considerably¹⁷ and therefore positively contributes to the stabilisation of charged transition states bound to the enzyme. The dielectric constant can be reduced by exclusion of water from the active site once the substrate is bound, which often occurs when an enzyme closes.

1.1.2.2 Dynamics

The observation of solvent exclusion following enzyme lid closure demonstrates that protein motions or dynamics evidently have a limited role in catalysis. The extent of the contribution of dynamical effects to catalysis in other ways is debated.^{18–22} Enzymes exhibit motions on many different timescales, from bond vibrations that occur on the femtosecond timescale, to domain motions and folding events that may take seconds.²³ How these motions relate to the catalytic effect is debated. For example, it has been proposed by some researchers that the energy from water molecules colliding with the surface of the enzyme can be transmitted through the enzyme structure to the active site where the energy is harnessed to reduce the activation barrier and therefore directly contributes to reducing the barrier for the chemical step.²⁴ Other work has suggested that at each stage of the catalytic cycle, there exists a small population of enzyme that adopts the conformation required for the next step in the cycle.²⁵ An important distinction to be made regarding enzyme dynamics is whether they play a non-

negligible role in the chemical step or instead contribute to achieving the correct positioning and alignment of the substrate for catalysis to take place. This distinction has been used to invalidate some of the reports of enzyme dynamics contributing to enzyme catalysis.²⁷

1.1.2.3 Ground State Destabilisation

Another proposal is that of ground state destabilisation, whereby the enzyme active site places conformational strain on the reactant, raising its energy and therefore decreasing the energy barrier between the enzyme bound GS and the TS complex.²⁶ One problem that has been raised with this proposal is that by increasing the energy of the GS complex, k_{cat} falls, but only at the expense of an increased K_m . The second order rate constant for the reaction (k_{cat}/K_m) remains unchanged however and the proposal does not explain how the enzyme reduces the energy of the TS relative to the same TS in solvent.²⁷ Additionally, other results have shown the theory of GS destabilisation to be unlikely. This work begins with the assumption that enzymes have evolved to reduce the energy barrier either through stabilisation of the TS or destabilisation of the GS. By de-evolving enzymes by mutating critical catalytic residues, the primary effect is destabilisation of the TS, and no mutants were found to cause stabilisation of the GS. This suggests that these key residues were originally selected for their contribution to TS stabilisation, and not their ability to destabilise the GS.

1.1.2.4 Near Attack Conformers

The final proposal discussed in this section is the concept of near attack conformers (NACS).^{28–30} In this hypothesis, the energy barrier for the attainment of the TS is partitioned into that corresponding to an invariant chemical step and a portion attributed to a conformational component. By stabilising NACs, which are arrangements of the substrate that are close to the TS architecture, the energy barrier is reduced. Crystallographic evidence for NACs has been reported^{31,32} although these studies are limited in their ability to present absolute stability measurements because they rely on analogues and non-wildtype enzyme variants.

Despite a vast amount of knowledge regarding the complexities of enzymes, our understanding of the origin of the catalytic power of enzymes remains incomplete.^{33–35}

1.1.3 Enzyme Regulation

Living organisms are heavily reliant on enzymes to drive their metabolism and bring chemical reactions onto a similar timescale to each other. Because of their power and importance, enzymes are subject to heavy regulation. In this way, enzyme activity can be controlled according to the needs of the organism, conferring the ability to respond to environmental stimuli such as a sudden abundance of food. Enzyme regulatory mechanisms operate on different levels and the activity of a single enzyme can be sensitive to several different regulatory processes. Regulatory mechanisms that control the concentration of an enzyme can be considered coarse control mechanisms, whereas mechanisms that result in a change of enzyme activity are fine controls. These categories and some examples of each are discussed briefly below.

1.1.3.1 Coarse Control Mechanisms

Coarse control mechanisms modulate the concentration of an enzyme. This occurs at different stages between gene transcription and protein translation, but also includes protein degradation and enzyme clustering. The regulation of the *lac* operon is a well-known example of a transcriptional control system.^{36,37} In this case, transcription of the *lac* operon, which encodes the proteins for metabolising lactose, is stimulated by the presence of allactose. Once transcribed and translated, the enzymes encoded by the *lac* operon enable the organism to make use of the lactose as a food source. With this system in place, the enzymes are not required to be continually synthesised and can be produced in response to an influx of lactose. Coarse control systems also include enzyme degradation.³⁸ Enzymes are regularly targeted for degradation, and therefore the lifetime of an enzyme is short.³⁹ This ensures that an activity does not continue for longer than it is required, and enables the repurposing of useful amino acids. Another lesser understood aspect of coarse control is enzyme co-clustering. By sequestering a population of enzyme in a particular compartment or region in the cell, the activity of the enzyme can be localized. It also confers a higher effective concentration of the enzyme.⁴⁰⁻⁴¹ The coarse control mechanisms described operate on a timescale of hours to days.

1.1.3.2 Fine Control Mechanisms

Fine control mechanisms alter enzyme activity post-translationally and usually operate on a faster timescale than coarse control systems (sub-second to minutes). This cohort of

mechanisms include post-translational modifications (PTMs)^{42,43} and regulatory molecules, which are often found to work via allostery, whereby a change at one site of an enzyme is propagated to another site where it causes an effect. Other less well-known mechanisms such as allokairy, which is described below, also belong to the category of fine control mechanisms. Allostery is widespread in the biological world, and is used by organisms in signalling, cooperative binding and feedback.⁴⁴⁻⁴⁵ It is facilitated through the covalent or non-covalent binding of an effector. This binding event is transmitted through a conformational change, which results in effects that occur at sites distal to the site of binding. The mechanism for this transmission has been the subject of considerable interest. There is certainly no predictive understanding of the phenomenon; however, considerable progress has been made in elucidating structural aspects of allostery. It has become clear that a spectrum of protein motions, from domain motion to local unfolding events, can contribute to the allosteric effect.⁴⁶ Allostery has been exploited in the design of drugs that target proteins, and a large number of proteins have been successfully targeted by allosteric inhibitors, regulators and activators.⁴⁷ Allokairy is another fine control mechanism and shares similarities with allostery.^{48,49} In both cases there is an exchange between at least two forms of the enzyme, which exhibit different activities. In allostery, this exchange is influenced by an effector molecule that binds outside the active site, whereas in allokairy, the substrate itself serves as the effector, and the effect is entirely kinetic. Human glucokinase (GCK), for example, has been shown to exhibit a sigmoidal kinetic response to an increasing concentration of its substrate – glucose.^{48,49} This is attributed to the enzyme exchanging between a state with high affinity for glucose and a state with low affinity. In the presence of substrate, the high-affinity state is stabilised, but after product release, GCK relaxes back to the low-affinity state. As the concentration of substrate increases, the likelihood of the high-affinity state reacting with a second molecule of substrate increases. With increasing substrate concentration, the balance of populations shifts in favour of the high-affinity state and the overall activity of the sample increases. The extent to which allokairy occurs in other enzymes is still unclear, but it nonetheless creates opportunities for developing new kinds of drugs, in the same way that allostery has been exploited.

1.2 Phosphoryl Transfer Enzymes

1.2.1 Background

Phosphoryl transfer is a process of critical importance in biology. Many of the most important biomolecules contain phosphate esters,⁵⁰ of which the most prominent examples are DNA and RNA, which constitute the genetic material for all living organisms. Both of these nucleic acids contain phosphate esters. So too do molecules such as adenosine phosphates, nicotinamide adenine dinucleotide phosphate (NADP) and glucose 6-phosphate, which are vital components of metabolism. Additionally, it is estimated that approximately one third of the human proteome is phosphorylated at any point in time.⁵³ Phosphate esters are intrinsically highly stable; for example, the hydrolysis of alkyl phosphate dianions proceeds at an estimated rate of $2 \times 10^{-20} \text{ s}^{-1}$,⁵¹ giving them a half-life of 1.1×10^{12} years. Likewise, double-stranded DNA is estimated to have a half-life for hydrolysis of over 100,000 years.⁵² In order to bring the rate of reactions involving phosphate onto a biologically relevant timescale, a multitude of enzymes have evolved to catalyse phosphoryl transfer: DNA and RNA polymerases; kinases and phosphatases; and GTPases and ATPases. Together these illustrate the diversity among phosphoryl transfer enzymes. The enhanced rates that these enzymes achieve above the non-enzymatic reactions in water are among the highest observed in the natural world.⁵⁴ For this reason, phosphoryl transfer enzymes and their mechanisms have garnered considerable interest.

1.2.2 Metal Fluorides

The use of metal fluorides in the study of phosphoryl transfer enzymes has proved a successful endeavour and the mechanism of enzymatic phosphoryl transfer is now widely agreed to consist of a concerted mechanism involving in-line nucleophilic attack on the phosphate.⁵⁵ The application of metal fluorides originates in the finding, following the discovery of cyclic adenosine monophosphate (cAMP), that inclusion of NaF in the reaction mixture resulted in an increase in cAMP production by liver homogenates.⁵⁶ It was later discovered that this increase was owed to the constitutive activation of the guanine-nucleotide-binding regulatory component of adenylyl cyclase, which occurred in an Al³⁺-ion-dependent manner.⁵⁷ It was then reported that AlF₄⁻ binds in the nucleotide binding site of this subunit, alongside GDP, in a way that mimics the γ -phosphate of GTP^{58,59}, and the first crystal structures of an AlF₄⁻-bound GTPase were solved.^{60,61} From these crystal structures, it was apparent that the AlF₄⁻

moiety was behaving as a mimic, not of the ground-state of GTP hydrolysis, but of the transition state. Following this development, crystal structures of other phosphoryl transfer enzymes in complex with AlF_4^- were solved,⁶² and other metal fluorides, such as MgF_3^- and BeF_3^- , began to be adopted as analogues for the transition state and ground state of phosphoryl transfer.^{63,64} MgF_3^- behaves differently to AlF_4^- , in that in the active site of an enzyme, it adopts trigonal bipyramidal geometry, and is therefore isosteric as well as isoelectric with the phosphoryl moiety, PO_3^- . Conversely, beryllium possesses a simpler electronic configuration to aluminium and magnesium, and is therefore incapable of using empty d-orbitals to expand its coordination number and accept more than four bonds. Enzyme bound BeF_3^- therefore adopts tetrahedral geometry and is a good mimic of the ground state of phosphoryl transfer (Figure 1.3). There have since been many successful applications of metal fluorides to the study of a variety of phosphoryl transfer enzymes.^{65–75} Of note is the misidentification of a high energy phosphorane intermediate of enzymatic phosphoryl transfer in βPGM ⁷⁶, which was later unequivocally identified as a $\beta\text{PGM}:\text{MgF}_3:\text{G6P}$ complex.⁷⁷ This led to a significant and ongoing application of metal fluorides to the study of βPGM .

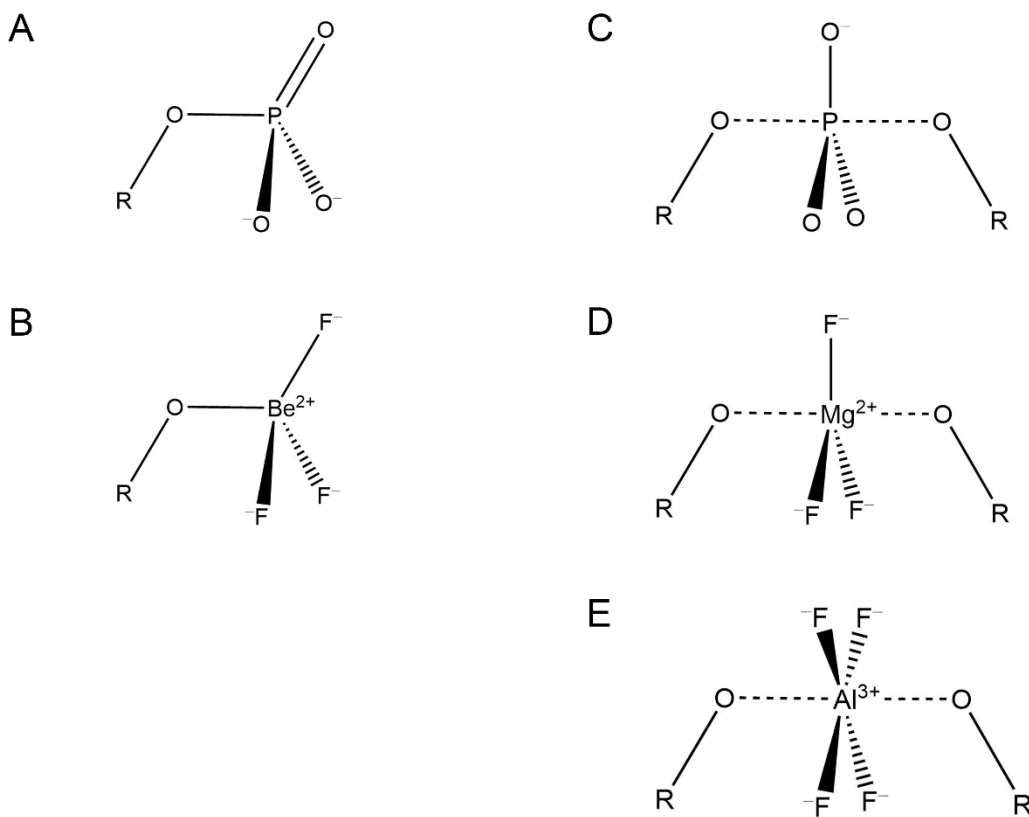


Figure 1.3. The GS and TS for a concerted phosphoryl transfer reaction alongside metal fluoride analogues that are used to probe each state. (a) Phosphate monoester. (b) BeF_3^- moiety. (c) Proposed TS of a concerted phosphoryl transfer reaction. (d) MgF_3^- moiety. (e) AlF_4^- moiety.

1.2.3 β PGM

β PGM (E.C. 5.4.2.6) from *Lactococcus lactis* (*L. lactis*) is a member of the haloalkanoic acid dehalogenase (HAD) superfamily of enzymes.^{81,129} The 25 kDa enzyme is magnesium dependent and catalyses the isomerisation reaction between β -glucose 1-phosphate (β G1P) and glucose 6-phosphate (G6P) via a β -glucose 1,6-bisphosphate (β G16BP) intermediate⁷⁹, which is released before rebinding in the opposite orientation.⁸⁰ β PGM consists of two domains, termed the core domain and the cap domain, connected by a hinge region^{81,82}, about which the cap domain rotates 33–36° relative to the core domain on transitioning from the open, substrate-free form to the closed and inhibited, transition state analogue (TSA) bound form⁸² (Figure 1.4). β PGM has been studied extensively using metal fluoride analogues in conjunction with NMR and X-ray crystallography, and much is known about the workings of the active site of the enzyme.^{31,32,65,82,83} There are two phosphate binding sites in β PGM, the first of which is the site at which the enzyme becomes phosphorylated, termed the proximal site. This site contains

the nucleophilic residue, D8, as well as its close neighbour, residue D10, which acts as the general base during the catalytic cycle.³²

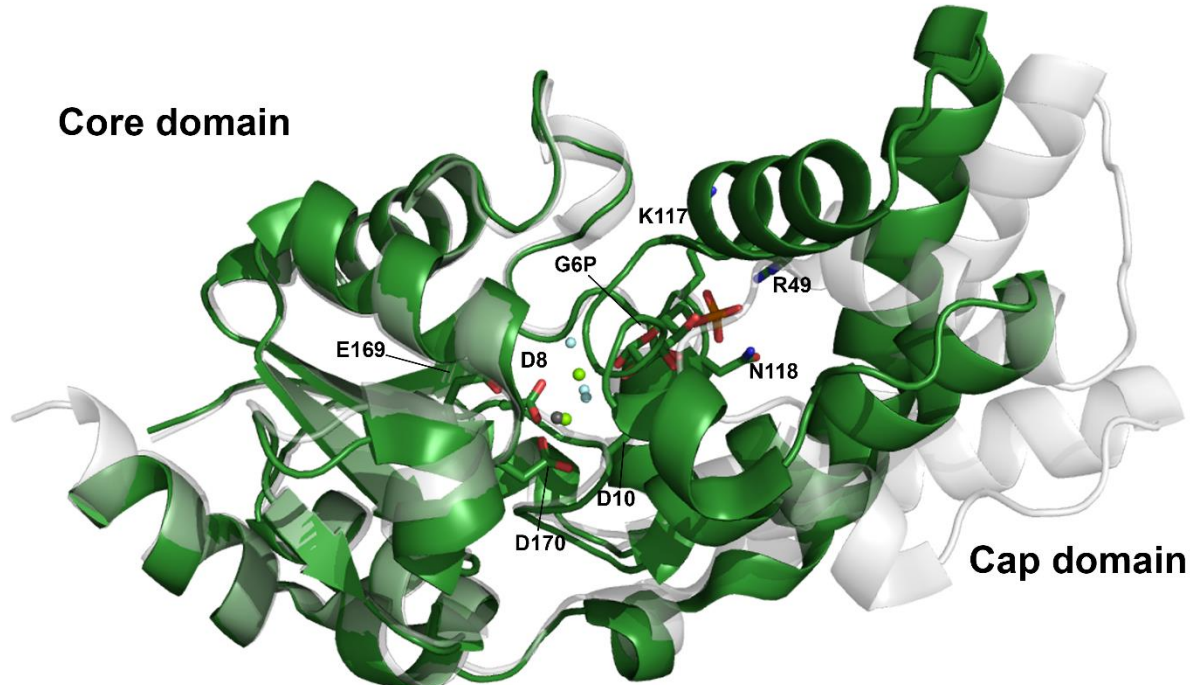


Figure 1.4. The open and closed forms of βPGM. Substrate-free βPGM (PDB 2WHE) is shown in transparent grey cartoon representation with a grey Mg^{2+} ion. A βPGM: MgF_3 :G6P complex (PDB 2WF5) is shown in green cartoon representation. G6P is shown as sticks (green carbon atoms), Mg^{2+} ions and F^- ions are shown as green and cyan spheres respectively. The core domain roughly corresponds to residues 1–16 and 84–221 (84–218 in 2WF5) and the cap domain to residues 17–83. Selected residue side chains of the βPGM: MgF_3 :G6P complex are shown in stick representation.

Residues D8 and D10, alongside residues E169 and D170, coordinate the catalytic Mg^{2+} ion, Mg_{cat} . The second phosphate binding site, termed the distal site, is a positively charged pocket formed between the cap and core domains during closure of the enzyme. In this site, which is non-reactive, the phosphate is coordinated by the guanidinium group of residue R49, along with the backbone amide of residue K117, and the sidechains of residues S116 and N118. Despite the structural differences between the βG1P and G6P substrates, crystal structures evidence that the coordination of the phosphate bound to the distal site is the same, irrespective of which substrate is bound (Figure 1.5). The structural differences are instead accommodated by a rearrangement of structural water molecules, which satisfy the hydrogen bonding of the substrate where the enzyme does not⁸³ (Figure 1.6).

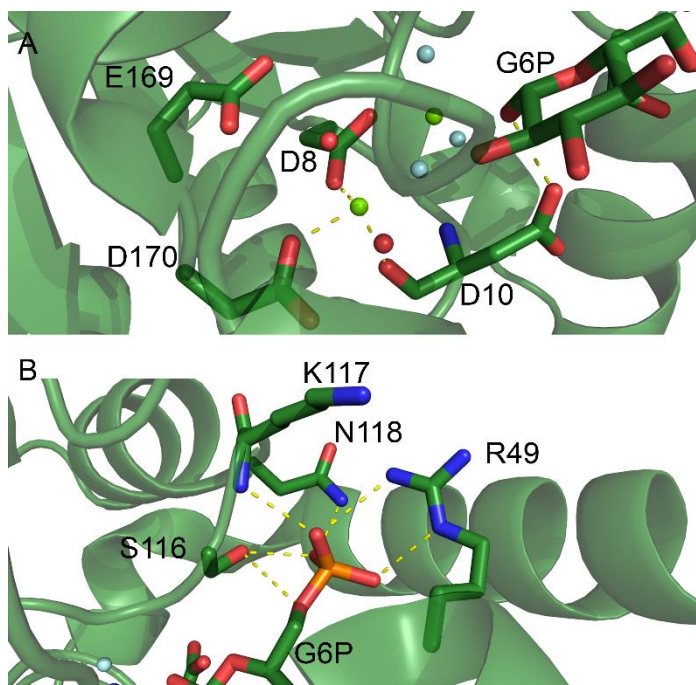


Figure 1.5. The active site of β PGM highlighting the two sites that coordinate phosphate. (a) The proximal phosphate site in which phosphate is transferred between the substrate and residue D8 of the enzyme. **(b)** The distal phosphate binding site in which the non-reacting phosphate of the substrate is coordinated. Key residues and G6P are shown as sticks (green carbon atoms) and the rest of the protein is shown in transparent green cartoon representation. Mg²⁺ ions, F⁻ ions and water molecules are represented by green, cyan and red spheres, respectively.

The kinetics of β PGM have been studied using two techniques. One technique is a coupled assay in which the reaction product, G6P, is converted to 6-phosphogluconolactone by glucose 6-phosphate dehydrogenase (G6PDH), and the concomitant reduction of NAD⁺ to NADH is monitored by a change in absorbance at 340 nm (NADH molar extinction coefficient = 6220 M⁻¹ cm⁻¹). The other method uses ³¹P NMR time course experiments to measure the increase in the peak integral, and thus the concentration of G6P over time. G6P is distinguished from β G1P by its chemical shift.

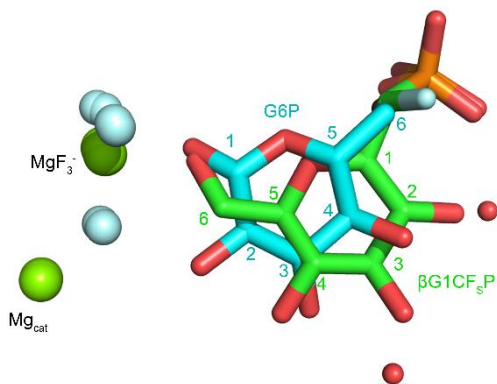


Figure 1.6. Substrate positioning in TSA complexes representing Step 1 and Step 2 of the catalytic cycle of β PGM. The TSA complex for Step 1 (green carbon atoms) is composed of an MgF_3^- moiety and (S)-1- β -phosphonofluoromethylene-1-deoxy-D-glucopyranose (β G1CFsP), which is an analogue of β G1P. The TSA complex for Step 2 (cyan carbon atoms) consists of an MgF_3^- moiety and G6P. Mg^{2+} ions, F^- ions and water molecules are represented as green, cyan and red spheres, respectively. Carbon numbers for each of the pyranose rings are coloured the same as the carbon atoms that they describe.

The catalytic cycle of β PGM is described by a ping pong mechanism. In the first step of the reaction (Step 1), β G1P is phosphorylated by β PGM^P generating β G16BP, which is then released from the active site. In Step 2, β G16BP rebinds and its 1-phosphate is transferred to the enzyme generating G6P and regenerating β PGM^P. β PGM^P can be generated *in vitro* with phosphorylating agents other than β G16BP, with acetyl phosphate (AcP) and α -glucose 1,6 bisphosphate (α G16BP) being commonly used^{79,84} (Figure 1.7). Kinetic parameters reported in the literature for β PGM vary, with reported values for k_{cat} between 17 s⁻¹⁷⁹ and 177 s⁻¹⁸⁰. This appears to depend on the handling of the kinetic curves as well as the type of phosphorylating agent used.

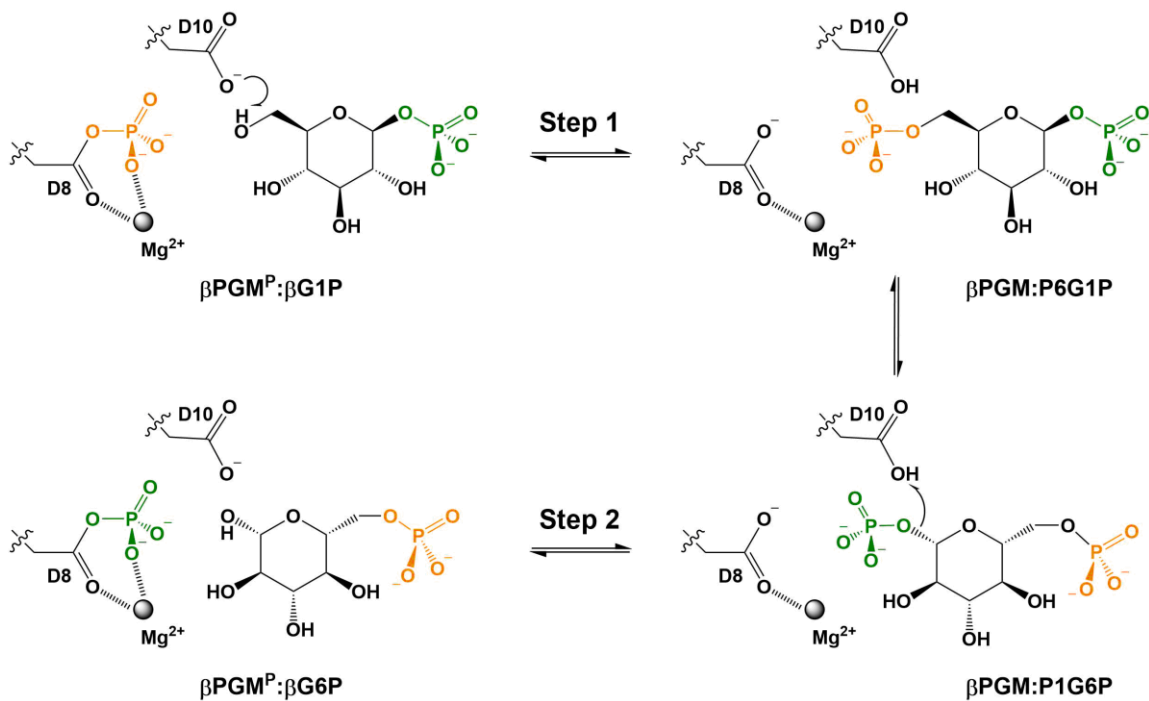


Figure 1.7. The catalytic cycle of β PGM. In Step 1, β G1P binds to phosphorylated β PGM (β PGM^P) and phosphoryl transfer takes place to produce β G16BP. The β G16BP is released from the active site but then rebinds in the opposite orientation. In Step 2, β G16BP phosphorylates β PGM using its 1-phosphate to produce β G6P and regenerate β PGM^P. β G6P quickly equilibrates with its α -anomer, and is usually represented without an anomeric configuration G6P label. Residue D8 acts as a nucleophile and attacks the phosphate, whilst D10 plays the role of general acid/base in the reaction.

1.3 Alginate

1.3.1 Background

Alginate is a linear, co-polysaccharide consisting of two types of uronic acid: α -L-guluronic acid (G) and β -D-mannuronic acid (M).^{85,86} These two saccharides are epimers at C5 (Figure 1.8) and in alginate are linked by 1–4 bonds. Alginate can be found naturally in brown algae and various species of bacteria but serving different purposes in each class. In brown algae, alginate is localised to cell walls where its role is structural.^{87,88} The purpose of alginate in bacteria is less well understood. Bacteria of the genera *Azotobacter* and *Pseudomonas* are known to contain alginate, and various roles have been proposed for the polysaccharide, including its importance during part of the bacterial lifecycle during which the cell becomes enclosed within a cyst formed from extracellular polysaccharides.⁸⁹

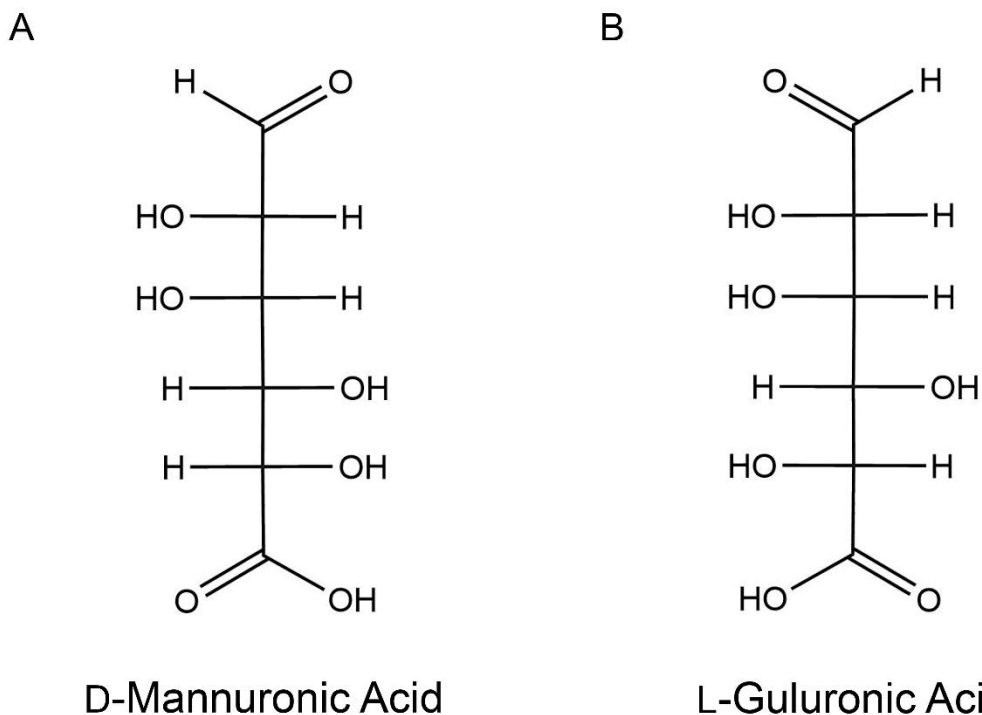


Figure 1.8. Fischer projections for the two uronic acids which comprise alginate. (a) D-mannuronic acid. (b) L-guluronic acid.

Alginates from different species differ considerably in their composition^{90,91}. Broadly, three chain compositions are common: G-rich regions, containing stretches of polyG; M-rich regions, and regions where G and M residues alternate. This diversity is generated post-polymerisation, and alginate is synthesised as a homopolymer of M residues. The biosynthetic process is better understood in bacteria than in brown algae. In bacteria, alginate synthesis begins with sugars such as glucose and fructose, which are processed by proteins encoded in the *alg* biosynthetic gene cluster, into GDP-mannuronic acid. Polymerisation of GDP-mannuronic acid occurs at the cytoplasmic membrane, and polyM chains are then exported into the periplasm where they are processed by epimerases and lyases, before being secreted through the outer membrane⁸⁹. Alginates are capable of forming gels when in the presence of Ca^{2+} ions. Gelation is known to arise because of specific interactions between polyG regions and Ca^{2+} ions, which brings alginate chains together to form junction zones. At these junction zones, the ratio of G to Ca^{2+} is 4:1⁹² and various models have been proposed for the structure at these inter-chain regions. One model that has gained widespread recognition is termed the Egg-Box Model, after the similarity in appearance between the Ca^{2+} ion nested amongst four G residues and an egg in an egg-box⁹³ (Figure 1.9). In this model, 10 oxygen atoms belonging to two chains of polyG,

coordinate a single Ca^{2+} ion. There is, however, no consensus on the structure of alginate junction zones.^{94,95}

Commercially, alginate has found many uses⁹⁶, primarily in the food and biotechnology industries. In food technology, alginate is used as a gelling agent and a thickener. Biomedically, the most common use for alginate is a thickener or stabiliser of oral forms of medications. There are more specialised uses however, and these include using alginate gels to deliver drugs, dress wounds, culture cells and alleviate heartburn.^{97,98} Controlling the properties and the gelation process of alginate is therefore of considerable interest.

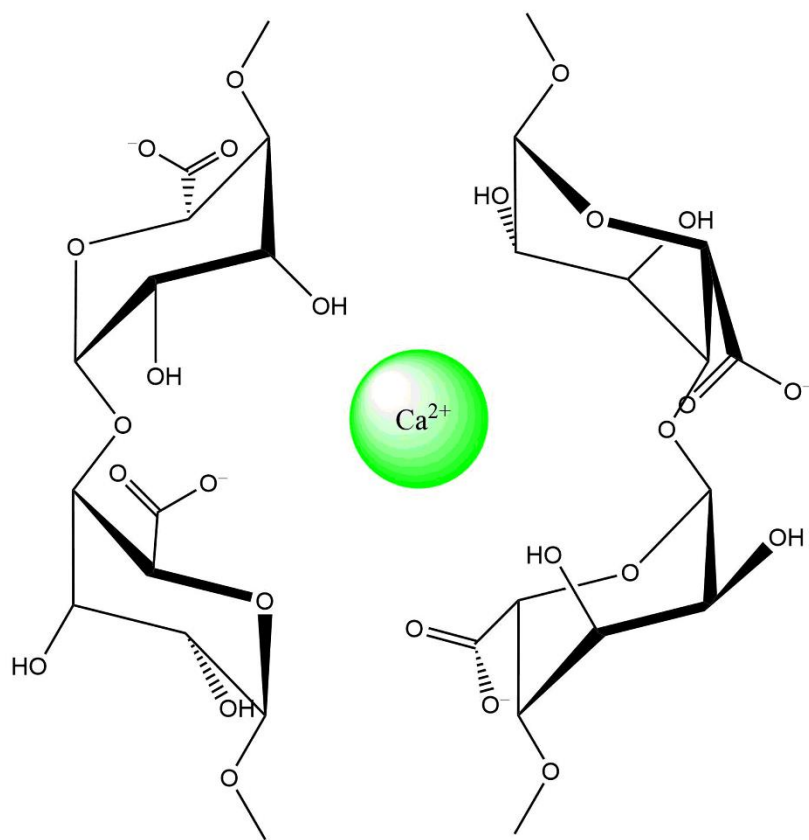


Figure 1.9. Structure of the junction zone between two chains of G-rich alginate proposed in ref. 93.

At the residue level, alginate conformation is an important determinant of function, and considering the shape of alginate residues is important in understanding gelation and reactions involving alginate. Ignoring D- and L-enantiomers, pyranose sugars have 38 distinct conformations, which can be classified into five categories: chair, boat, skew boat, half-chair and envelope⁹⁹. The residue conformation of alginate has been studied using a diverse experimental toolset including X-ray crystallography, NMR spectroscopy and fibre diffraction. These works have unanimously concluded that the dominant conformation adopted by G and

M residues, in both monomeric and polymeric form, is the chair conformation. G residues are known to adopt the $^1\text{C}_4$ chair conformation and M residues adopt the $^4\text{C}_1$ conformation (Figure 1.10).^{90,91,100–105} In this conformation, the bulky carboxylate group has an equatorial configuration, which is to be expected. These residue shapes inevitably dictate the conformation of alginate chains. PolyM is proposed to adopt a ribbon-like structure whereas polyG forms a kinked chain. How these arrangements affect the ability of alginate to interact with Ca^{2+} ions is not completely clear, with the fibre diffraction patterns produced using Ca^{2+} alginate being of poor quality.^{95,107} Most conclusions about Ca^{2+} coordination to date are therefore drawn from computational models of alginate.

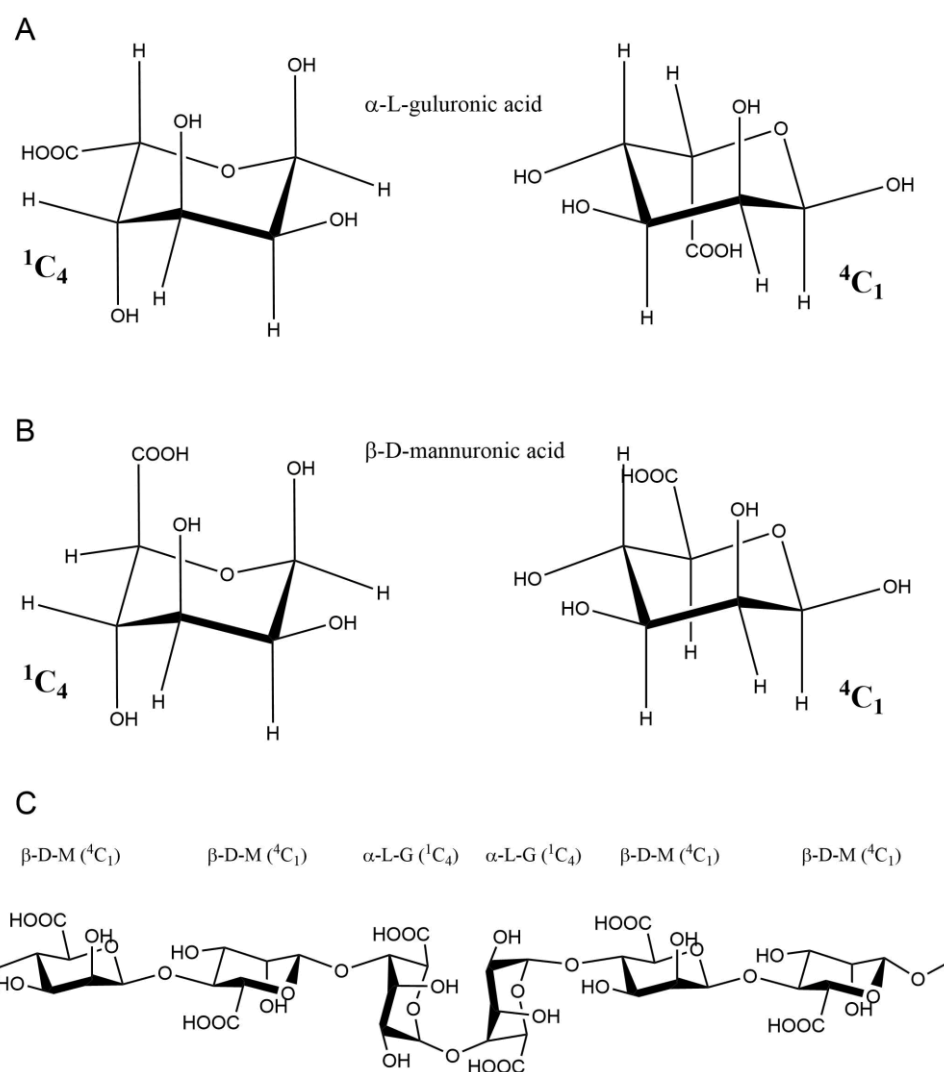


Figure 1.10. Conformations of α -L-guluronic acid and β -D-mannuronic acid. (a) Chair conformations of α -L-guluronic acid. (b) Chair conformations of β -D-mannuronic acid. (c) Proposed chain structure of alginate illustrating the difference in the chain conformation between stretches of multiple α -L-guluronic acid residues (kinked chain) and multiple β -D-mannuronic acid residues. Adapted from reference 104.

1.3.2 Polysaccharide Lyases

Two types of enzyme exist to modify alginate chains: epimerases, which catalyse the interconversion of G and M residues, and lyases, which depolymerise alginate. The enzymatic mechanism for epimerisation is thought to involve abstraction of the C5 proton to create a carbanion. A proton is then reintroduced with a different configuration resulting in the alternative C5 epimer. Alginate lyases are part of a broader family of polysaccharide lyases (PL; E.C. 4.2.2.-). They exhibit diversity in both the substrates that they react with – either polyG regions [E.C. 4.2.2.11], polyM regions [E.C. 4.2.2.3] or both [E.C. 4.2.2.-] – although this definition misses polyMG specific alginate lyases, which have been reported¹⁰⁷), in their manner of cleavage (exolytic or endolytic), and in the minimal size of their cleavage products. There are 37 PL families in the Carbohydrate-Active enZYmes (CAZy) database, of which 9 are alginate lyases.^{108,109} The consensus mechanism for these enzymes is a β -elimination reaction, which results in an unsaturated sugar at one side of the cleavage site and a new reducing sugar at the other side.^{110,111} This mechanism differs from the other mechanism utilised for polysaccharide depolymerisation, which is a hydrolysis reaction, and is made possible because of the acidity of the carboxylate at C5.¹¹² The first step in the β -elimination reaction involves neutralisation of the negative charge of the carboxylate by formation of a salt bridge (Figure 1.12). This is followed by abstraction of the proton at C5. Up to this point, the lysis reaction mirrors the epimerisation reaction. Finally, β -elimination of the glycosidic bond leaves an unsaturated monosaccharide.¹¹⁰ Alginate lyases have been found in a range of organisms including marine algae, marine molluscs, bacteria, fungi and viruses.¹¹³

1.3.3 Dp0100

Dp0100 is an alginate lyase belonging to a recently discovered PL family. The enzyme originates from the thermophilic bacterium, *Defluviitalea phaphyphila* (*D. phaphyphila*). *D. phaphyphila* is an obligate anaerobic and Gram-negative bacterium, which has an optimal growth temperature of 55–60 °C.¹¹⁴ The organism is of considerable interest owing to its ability to utilise brown algae as a carbon source under thermophilic conditions, converting biomolecules such as alginate and mannitol into ethanol and acetic acid. One of the key enzymes used by *D. phaphyphila* to depolymerise alginate is Dp0100, a 201 kDa protein with endolytic activity towards both polyG and polyM regions of alginate. The gene sequence encoding Dp0100 (*dp0100*) contains an N-terminal secretion signal, and Dp0100 is therefore

believed to act extracellularly.¹¹⁴ Structurally, Dp0100 consists of eight conserved domains, of which the minimal catalytic unit has been shown to contain a heparinase II/III-like domain and a DUF4962 domain.¹⁰⁸ The catalytic subunit of Dp0100 has a three-domain architecture, with a largely helical N-terminal domain, a central domain formed from two β -sheets and a distorted α -helix, and a C-terminal domain comprising a β -sandwich of 16 β -strands (Figure 1.11).

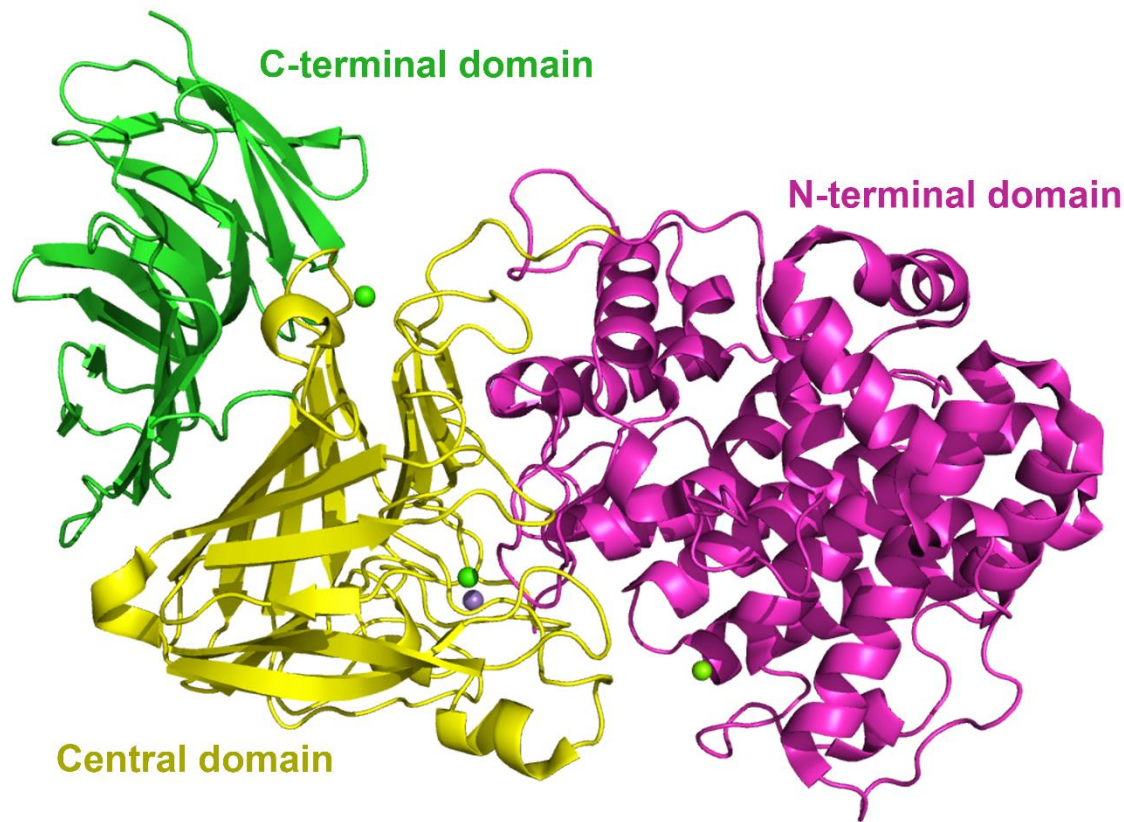


Figure 1.11. Crystal structure of the catalytic domain of Dp0100 in substrate-free form. Ca^{2+} ions and Mn^{2+} ions are represented as green and purple spheres, respectively. Residues 1–361 make up the N-terminal domain (pink cartoon), residues 362–616 form the central domain (yellow cartoon), and residues 617–770 the C-terminal domain (green cartoon). The structure is PDB 6JP4.

The substrate binding site is a cleft formed between the N-terminal domain and the central domain, and it is open at both ends. The active site cleft is lined with positively charged residues to facilitate interaction with the negatively charged C5 carboxylate group of alginate residues. Complexes of a Dp0100 truncation mutant with polyM oligosaccharides, suggest that the mechanism of alginate depolymerisation by Dp0100 does conform to the consensus β -elimination reaction described for other PL enzymes, as depicted in Figure 1.12.¹⁰⁸

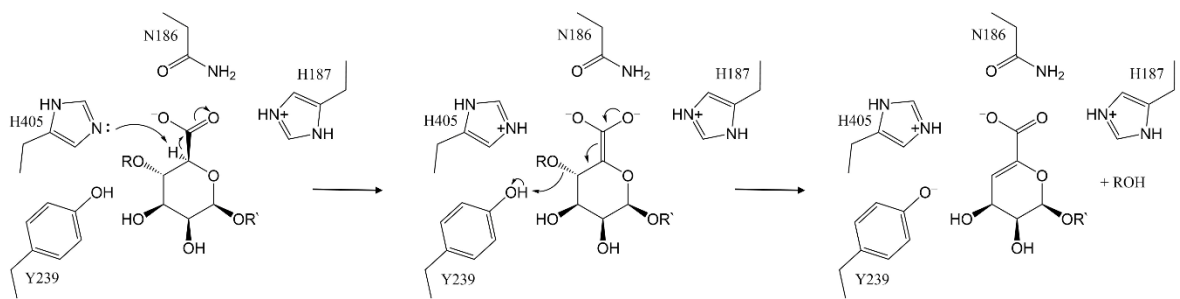


Figure 1.12. Proposed reaction mechanism of alginate lyase Dp0100. Abstraction of the H5 proton of β -D-mannuronic acid by H405 results in a negatively charged carbanion intermediate, which then collapses via β -elimination to leave an unsaturated sugar.

Histidine residue, H405, is positioned to act as the general base and abstract the H5 proton as well as to stabilise the C5 carbanion that results, in conjunction with residues N186 and H187 (Figure 1.13). Furthermore, the sidechain of residue Y239 is in close proximity to the oxygen atom leaving group attached to C4, and may act as a general acid during the final step of the reaction (Figure 1.12). Alanine mutants of each of these residues (N186, H187, Y239 and H405) exhibited severely impaired activity, with H187A and H405A variants being completely inactive.¹⁰⁸

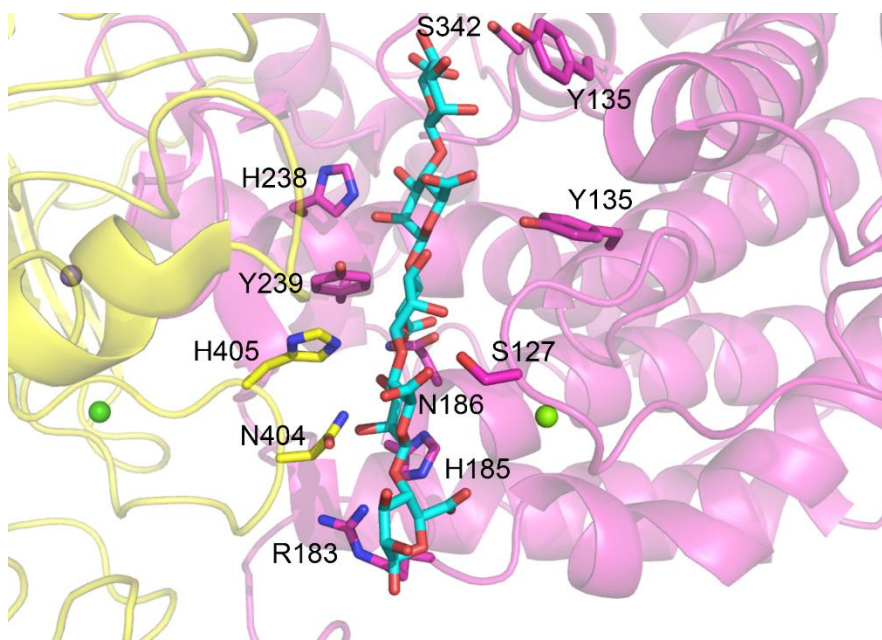


Figure 1.13. The structure of the active site of the catalytic domain in Dp0100 bound to a polyM pentasaccharide. The central domain (yellow) and the N-terminal domain (pink) are shown in transparent cartoon representation, with key residues in the enzyme-substrate interaction shown as sticks and the polyM pentasaccharide shown as sticks (cyan carbon atoms). Ca^{2+} ions and Mn^{2+} ions are represented as green and purple spheres, respectively. The residues in the polyM pentasaccharide uniformly adopt the $^4\text{C}_1$ chair conformation. The structure is PDB 6JPN.

This thesis contains a structural exploration of the two enzymes (β PGM and Dp0100) introduced above. The aim of the work is to investigate the importance of conformational change in the catalysis of two different chemical reactions by these enzymes. The contribution of enzyme dynamics to the chemical step of enzyme-catalysed reactions is widely debated. What is definite is that, for at least some enzymes, conformational changes are vital in certain stages of the catalytic cycle and in regulation of enzyme activity. Herein, NMR and X-ray crystallography are applied to these enzyme systems with the aim of answering two important questions. Firstly, what is the significance of the, to-date unexplained, slow-exchange process that occurs in the substrate-free form of β PGM? The dynamic is revealed to be caused by a *cis-trans* proline isomerism, and is shown to lead to different levels of enzyme activity depending on the phosphorylating agent used to activate the enzyme. This exchange phenomenon is likely to have regulatory significance in the host species, *L. lactis*. Secondly, how is the alginate lyase, Dp0100, able to catalyse the cleavage of both polyM and polyG alginate, when the two polymers have such different chain structures? An X-ray crystal structure of Dp0100 is presented containing a novel conformation of polyG alginate bound in its active site. The existence of this unusual polyG chain conformation in solution is investigated by NMR, but no evidence is found to suggest that the novel conformation is dominant. It is therefore probable that Dp0100 is able to stabilise this alternative chain conformation within the enzyme active site. Remarkably, this results in the oligosaccharide chain of polyG taking on a structure akin to that of the alternative substrate of Dp0100, polyM. The conformational change enforced on the substrate is therefore likely to play a role in enabling the dual specificity of Dp0100. Hence, the results presented in this thesis reveal, in structural and mechanistic detail, the importance of conformational change in enzyme catalysis for two specific enzyme systems.

2. NMR Theory and Methods

2.1 Theory

2.1.1 Background

Nuclear magnetic resonance (NMR) spectroscopy is a powerful technique that enables conclusions to be drawn about atoms and their environments. The field of NMR spectroscopy is relatively mature, with modern spectrometers many times more powerful and automated than in the mid-20th Century. Though it is a well-developed field, it remains an area of active study. There are various ways to conceptualise the process by which an NMR signal is generated and some are more useful than others. Fundamentally, NMR is a quantum mechanical phenomenon, but simplifications and classical conceptualisations can be carried quite far and prove useful in understanding many aspects of NMR spectroscopy. The following section consists of a brief summary of some NMR concepts and experiments that are applicable to the research included in this thesis. This draws on some very good books on the subject by Derome, Neuhaus, Keeler, Levitt, Pascal and Williamson.^{115–119}

2.1.2 Spin

NMR spectroscopy is possible because of the intrinsic property of spin that subatomic particles possess. The spin of a subatomic particle is a non-classical physical property that can be thought of as a kind of intrinsic angular momentum that arises without the particle actually rotating. Just like any spinning particle with charge, atomic nuclei possess an intrinsic magnetic moment, with the properties of intrinsic spin and intrinsic magnetism being proportional to one another. The proportionality constant between these two properties is called the gyromagnetic ratio (or magnetogyric ratio), which is expressed in the units of rad s⁻¹ T⁻¹. NMR spectroscopy deals with the magnetism possessed by nuclei, and gyromagnetic ratios are specific to a particular nuclear isotope. Both the spin angular momentum (or the spin polarization) and the magnetic moment of a nucleus are vectors, and can point in any direction. In a sample of water, for example, the distribution of magnetic moments of hydrogen nuclei in the sample is isotropic, and does not have a particular direction that is represented more than any other. The nuclei that hold particular importance in NMR are the ones with a ground state nuclear spin of $\frac{1}{2}$. These

are not the only nuclei that are used in NMR spectroscopy, but all of the nuclei mentioned in this thesis have ground state nuclear spin $\frac{1}{2}$.

2.1.3 Longitudinal Magnetization

When a magnetic field is applied to a sample of nuclei, the magnetic moments of these nuclei begin to rotate about the axis of the field; this is called precession, and the rate of precession is the Larmour frequency. In an applied magnetic field with a strength of 18.8 Tesla for example, the Larmour frequency of ^1H nuclei is 800 MHz, and a magnetic moment from a ^1H nucleus in this field will precess 800 million times each second. The angle of precession relative to the vector of the external magnetic field depends on the direction that the magnetic moment was pointing when the magnetic field was applied. In the absence of any fluctuating magnetic fields, the overall magnetic moment of the sample is zero because of the isotropic distribution of individual magnetic moments. However, the rapid thermal motion of molecules in the sample, each of which possesses other magnetic moments due to the orbit of electrons around the nucleus, means that at any time, a nucleus will experience both the large applied field and a much smaller local field from nearby molecules. The fluctuation of the total field experienced by a nucleus leads to a wandering motion for the magnetic moment of the nucleus. This wandering behaviour enables magnetic moments of nuclei to change, and over the course of several seconds, leads to the generation of a total sample magnetic moment that is parallel to the applied magnetic field; termed longitudinal magnetization. This is because a magnetic moment, given the opportunity, is slightly more likely to align with the applied magnetic field than to oppose it. The population difference between the more aligned spins and less aligned spins can be calculated using the Boltzmann distribution in Equation 2.1, where N_{upper} and N_{lower} represent the populations of spins in the higher energy state and lower energy state, respectively; ΔE is the difference in energy between the two states; k is Boltzmann's constant; T is the temperature in Kelvin; h is Plank's constant and ν is the Larmour frequency.

$$\frac{N_{\text{upper}}}{N_{\text{lower}}} = e^{\frac{-\Delta E}{kT}} = e^{\frac{-hv}{kT}} \quad (2.1)$$

The population difference between the high and low energy states is very slight, but does increase with the strength of the applied field. In an 18.8 Tesla NMR spectrometer at a temperature of 298 K, for example, there are 64 more particles in the lower energy state than in the higher energy state for every million particles. This small difference in populations

means that the magnetic moment is also small. It is measurement of this total magnetic moment that NMR spectroscopy is concerned with. In the discussion of J-coupling and the nuclear Overhauser effect (NOE) later in this text, this scenario is simplified to two populations of spins: one population aligned with the applied magnetic field (spin up), and the other aligned against it (spin down). There is a slight population difference in favour of the spins aligned with the applied field.

2.1.4 The NMR Signal

Rather than measure the longitudinal magnetization of a sample, which is tiny in comparison to the applied field and impractical to study (it is much like trying to measure the luminous flux of a battery powered torch held in the beam of a powerful searchlight), the magnetization is instead rotated into the transverse plane where it can be more easily measured. To do this, NMR spectrometers use an oscillating magnetic field provided by a radiofrequency (RF) pulse at the Larmour frequency, which utilises the power of resonance to create a magnetic field that is perpendicular to the applied field and causes the magnetization to rotate. This occurs in a matter of microseconds. Once the RF pulse is switched off, the sample magnetic moment begins to rotate around the applied magnetic field once more at the Larmour frequency. The rotation of this bulk magnetization can now be measured with a detector placed in the transverse plane. A coil of wire placed next to the sample will produce an oscillating current as the magnetization rotates past it, generating the NMR signal. The wandering behaviour of individual magnetic moments once again leads to the return of the bulk magnetization to align with the applied field. The detector therefore experiences a gradual decay of the oscillating transverse magnetization, which is known as a free-induction decay (FID). The FID information can be processed using a Fourier transform to extract the frequency of precession. This sequence of events underpins the modern NMR experiment, and by building on this foundation, much that occurs on the atomic scale can be observed on the macroscopic level. Spectrometers are now able to derive enough information from NMR experiments to determine protein structures, as well as other impressive feats.

2.1.5 Chemical shift

In a typical molecule, the Larmour frequency for the nuclei is not necessarily uniform. Since electrons are charged particles in orbit around the nucleus, they too are magnetic. This creates local electronic environments in a molecule and means that the Larmour frequencies can be

subtly different between nuclei. This phenomenon is called chemical shift and is fundamental to NMR spectroscopy. In a typical NMR spectrum containing nuclei in different electronic environments, several NMR signals will be observed, each at a different frequency. As Larmour frequencies are dependent on the strength of the applied field, chemical shifts are usually measured in a field-independent manner by comparing to a reference chemical shift, and are so small that the chemical shift is usually reported in parts per million (ppm). This field-independent chemical shift (δ) is described by Equation 2.2, where ω^0 is the chemical shift of the nucleus of interest, and ω_{ref}^0 is the chemical shift of the reference nucleus.

$$\delta = \frac{\omega^0 - \omega_{ref}^0}{\omega_{ref}^0} \quad (2.2)$$

For example, if a nucleus has a Larmour frequency of 800,001,600 Hz, and the Larmour frequency of a reference nucleus is 800,000,000 Hz, then the chemical shift in ppm is 1,600 Hz divided by 800,000,000 Hz, which is 2×10^{-6} , i.e. 2 parts in one million (2 ppm). Certain chemical groups have distinctive chemical shifts, which sometimes makes it possible to assign the signals in an NMR spectrum to particular nuclei in a molecule.

2.1.6 J-Coupling

Another fundamental phenomenon in NMR spectroscopy is J-coupling. The magnetic field belonging to one nucleus can add or detract from nearby the total field experienced by neighbouring nuclei. This effect is a through-bond effect, and occurs by transmission of magnetization through the bonding electrons that connect the two nuclei. In a system where two spins are J-coupled, each spin can exist in either the spin up or spin down state. The magnetic field experienced by the measured nucleus is affected by the spin state of the coupled nucleus. When the coupled nucleus is in the spin up state, the magnetic field experienced by the measured nucleus increases slightly. When the coupled nucleus is in the spin down state, the measured nucleus experiences a slightly decreased magnetic field. These changes in field impact the Larmour frequency, and the measured nucleus therefore exhibits two different NMR signals, which appear either side of the signal that would be observed in the absence of J-coupling. J-coupling is an important effect in NMR spectroscopy and it is exploited in the heteronuclear single quantum correlation (HSQC) experiment to transfer magnetization between ^1H nuclei and another nucleus (commonly ^{15}N).

2.1.7 Relaxation

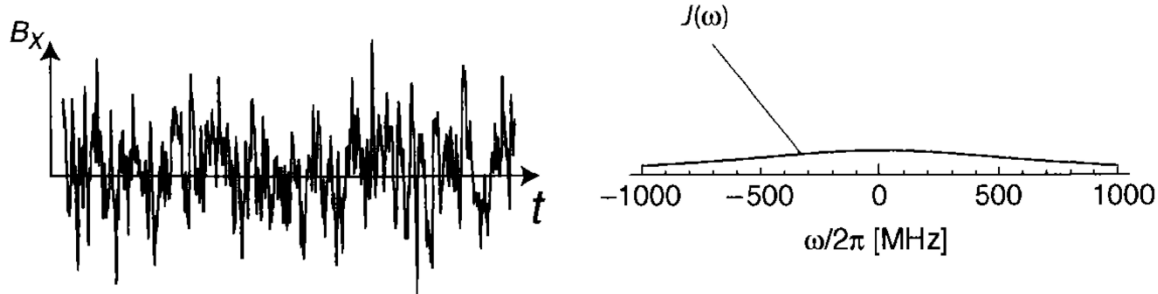
2.1.7.1 T₁ Relaxation

Once the RF pulse used to generate the NMR signal has been switched off, the magnetic moments in the sample are no longer at thermal equilibrium. In order for the system to return to its thermal equilibrium state (that of longitudinal magnetization aligned with the magnetic field), the spins must interact with the environment (also known as the lattice). This process is called relaxation, and can occur because of changing local magnetic fields in the sample which cause the total magnetic field to fluctuate slightly over time and space, as mentioned earlier. The rapidity of the fluctuating magnetic field can be conveyed by the autocorrelation function of the field, which is an expression of the correlation between the magnitude of the field at a given time point and the magnitude of the same field after a delay has elapsed. In a rapidly fluctuating field, the correlation between the magnitude of the field measured before and after a given delay, τ , is small. In field that fluctuates slowly, however, the magnitude of the field is less likely to have changed considerably after the same time interval (Figure 2.1).

The autocorrelation function roughly approximates to a simple exponential decay. The steepness of this decay is governed by the correlation time, τ_c , which is a property of a molecule describing the average time it takes for the molecule to rotate by one radian. Correlation times are also influenced by solution viscosity and temperature. Taking the Fourier transform of the autocorrelation function gives the spectral density function. This can be viewed as the probability of an event occurring at a particular frequency. For molecules with a small value of τ_c (~ 0.1 ns), there are fluctuations that occur at a wide range of frequencies, leading to a broad spectral density function. For molecules with longer correlation times (1–10 ns), the spectral density function is narrower, and fewer high frequency fluctuations occur (Figure 2.1). For a spin to relax from the high energy spin up state to the low energy spin down state through spin-lattice relaxation an event at the Larmour frequency is required to induce it. The spectral density function describes how often events at the Larmour frequency occur. With very broad and very narrow spectral density functions (small and large molecules, respectively), events at the Larmour frequency (~800 MHz at a field strength of 18.8 T, for example) occur infrequently. The maximum number of events at the Larmour frequency occurs for medium sized molecules,

and the spin-lattice relaxation time constant, known as T_1 , passes a minimum for molecules with correlation times somewhere in between those of small and large molecules.

A



B

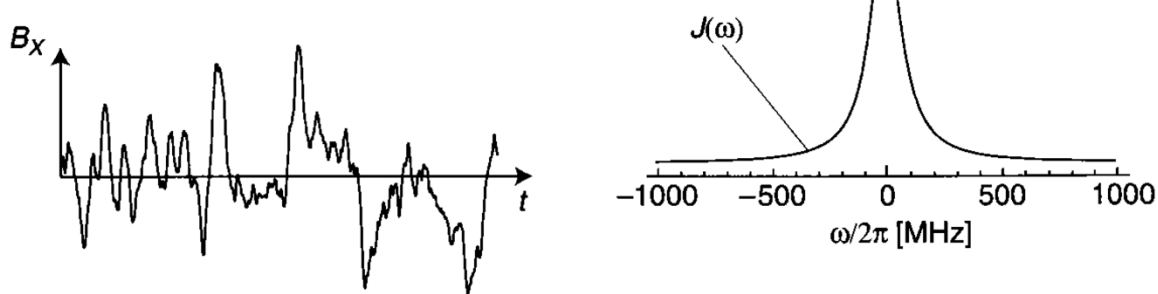


Figure 2.1. Spectral density functions for two different fluctuating transverse magnetic fields. (a) A rapidly fluctuating transverse magnetic field corresponds to a broad spectral density function, with events happening at lots of different frequencies. (b) A transverse field that fluctuates less rapidly corresponds to a broader spectral density function, with fewer events occurring with high frequency. Adapted from ref. 117.

2.1.7.2 T_2 Relaxation

T_1 relaxation corresponds to the restoration of longitudinal magnetization aligned with the applied magnetic field. This occurs because the bulk magnetization is rotated away from its thermal equilibrium position by a temporary oscillating magnetic field. Another effect that this RF pulse has is the creation of coherences, that is, spins that are in sync with each other, rotating at the same frequency. Because of slight fluctuations in the local magnetic field experienced by each nucleus, the population of spins will precess at slightly different Larmour frequencies. Gradually therefore, the coherences fall out of sync and the original coherence of spins is lost. This causes the magnitude of the transverse magnetization to decrease to zero. This can be visualised by imagining two clocks, one of which runs very slightly fast. If at first they are set to the same time, the clocks will remain in sync for a number of full rotations,

representing a state of coherence. As time passes however, the two clocks diverge more and more until they read completely different times. Because T_1 relaxation also manifests as a loss of transverse magnetization, the time constant for transverse relaxation, T_2 , must be at least as short as T_1 . In the case of larger molecules, T_2 is much shorter than T_1 , because transverse relaxation partly depends on the spectral density at zero frequency. With larger molecules, the spectral density function narrows, and unlike T_1 relaxation which relies on events with the Larmour frequency, the frequency of events with a frequency of 0 Hz only continues to increase.

2.1.8 The Nuclear Overhauser Effect

The NOE is a phenomenon whereby magnetization is transferred between spins in an unusual way that depends upon relaxation. NOEs are useful in NMR spectroscopy because the magnitude of an NOE is inversely proportional to the distance over which it occurs. For this reason NOEs can be used as a measure of inter-nuclear distance, which proves very useful for exploring the three-dimensional structures of biomolecules. As described earlier, the tiny fluctuations in the magnetic field experienced by spins facilitates transitions from higher to lower energy levels in the process called relaxation. T_1 relaxation depends on events occurring at the Larmour frequency and involves single-quantum transitions. In the case of two spin $\frac{1}{2}$ nuclei, typically labelled I and S, each of the spins, once excited, can return to a lower energy state via single-quantum transitions, represented by the probabilities W_{II} and W_{1s} . Spins can also lose energy by transfer to other spins in a process called cross-relaxation. This occurs between nuclei that are in close proximity and is stimulated by low frequency energy. These transitions are known as forbidden transitions, of which there are two types: the double-quantum transition, with probability W_2 , and the zero-quantum transition, with probability W_0 . Double- and zero-quantum transitions cannot be stimulated by RF pulses, but when they occur, they lead to a population difference between the two nuclei and can therefore be detected as a negative intensity change of the signal for the distal spin. NOESY experiments enable detection of this useful signal. Each of these relaxation transitions depends upon fluctuations in the magnetic field, which means that each transition probability is dependent in some way on the molecular tumbling rate. The relationship between each of the four transition probabilities and the correlation time in this simple two-spin system is shown in Equations 2.3–2.6, where $K = \mu_0/4\pi\hbar\gamma_I\gamma_Sr_{IS}^{-3}$ and ω_I and ω_S are the Larmour frequencies of spins I and S, respectively. The consequence of these relationships is that the magnitude and size of the signal enhancement caused by an NOE changes with the correlation time of the molecule in the sample.

$$W_{0IS} = \frac{1}{20} K^2 \frac{\tau_c}{1 + (\omega_I - \omega_s)^2 \tau_c^2} \quad (2.3)$$

$$W_{1I} = \frac{3}{20} K^2 \frac{\tau_c}{1 + \omega_I^2 \tau_c^2} \quad (2.4)$$

$$W_{1S} = \frac{3}{20} K^2 \frac{\tau_c}{1 + \omega_s^2 \tau_c^2} \quad (2.5)$$

$$W_{2IS} = \frac{3}{5} K^2 \frac{\tau_c}{1 + (\omega_I + \omega_s)^2 \tau_c^2} \quad (2.6)$$

2.2 Experiments

The below text details some of the NMR experiments that were used to generate the results presented in this thesis. Correlation spectroscopy (COSY) and total correlation spectroscopy (TOCSY) were used in the assignment of the spectra of various oligosaccharides. NOE spectroscopy (NOESY) and rotating frame NOE spectroscopy (ROESY) were used to make deductions about the structure and conformation of oligosaccharides. The heteronuclear single quantum correlation (HSQC) experiment was used extensively in structural studies of β PGM and in validating the identity of β G16BP.

2.2.1 Correlation Spectroscopy

The 2D COSY experiment relies on the transfer of magnetization between nuclei via J-coupling, and is therefore useful for tracing which protons in a spectrum are closely connected by covalent bonds. The basic pulse sequence for the homonuclear COSY experiment is relatively simple and consists of a $\pi/2$ pulse, followed by an incremented delay and then a final $\pi/2$ pulse before acquisition of the signal is started (Figure 2.2). The second pulse rotates all y-magnetization (assuming an x-phase pulse) onto the $-z$ -axis, rendering it undetectable. The x-magnetization that is left generates a signal, but its intensity depends on how much chemical shift evolution has evolved during the delay. As this delay is incremented, the intensity of the signal oscillates at a frequency that corresponds to the chemical shift. The result is a dataset that has chemical shift encoded twice, once in the acquired FID, and once indirectly in the oscillating intensity of the transverse magnetization that remains after the second pulse. When the resulting array of FIDs is Fourier transformed twice, a 2D spectrum is produced, which can

be represented as a contour plot. In the absence of any magnetization transfer effects, peaks would appear in this spectrum for each spin with a distinct chemical shift (ω_i) at position (ω_i , ω_i), creating a line of peaks along the diagonal of the spectrum (diagonal peaks). In a COSY experiment however, magnetization is transferred between J-coupled spins with the second pulse. This means that the chemical shift evolution of a J-coupled spin (here termed spin S) proceeds at the frequency of the original spin (ω_s) and is therefore indirectly encoded due to the incremented delay. After transfer of magnetization to the second spin (spin I), the magnetization precesses at the frequency of this spin (ω_i), and this is the frequency that is recorded in the FID. After the double Fourier transform therefore, peaks appear in the spectrum with a position of (ω_s , ω_i) and (ω_i , ω_s). These peaks sit away from the diagonal and are called cross peaks. COSY cross peaks are highly useful because not only do they clarify a 1D spectrum by spreading signals out into a second dimension, but they also highlight J-coupled spins. This information enables assignments of the corresponding 1D spectrum to be made. By following the coupling of spins, it is possible to walk through the covalent bonds and determine connectivities in the sample molecule.

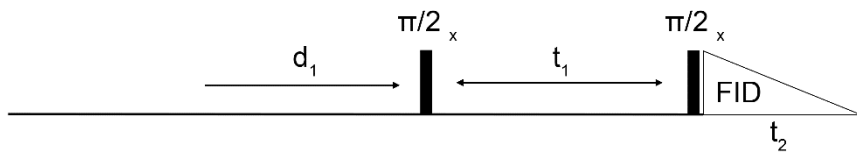


Figure 2.2. The basic pulse sequence for a 2D COSY experiment.

2.2.2 Total Correlation Spectroscopy

The TOCSY experiment (Figure 2.3) works on the same principle as the COSY experiment, and exploits J-coupling between spins to transfer magnetization between spins that are part of a contiguous coupled spin system. Instead of the second $\pi/2$ pulse in the COSY experiment, TOCSY experiments employ a spin lock after the delay period to allow magnetization to propagate from one spin to all the spins that it is connected to via a contiguous J-coupled network. A spin lock is a long pulse that is applied with the same phase as the transverse magnetization. The magnetization precesses around the oscillating magnetic field, and is therefore effectively locked in the same position on the transverse plane. The resulting

spectrum has cross peaks not only between spins that are connected by J-coupling, but also between spins that are not directly J-coupled, but that are part of the same contiguous system of J-coupling.

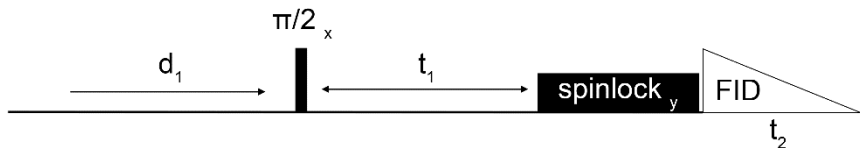


Figure 2.3. The basic pulse sequence for a 2D TOCSY experiment.

2.2.3 NOE Spectroscopy

The 2D NOESY experiment (Figure 2.4) bears the same hallmarks as the simplest homonuclear 2D experiment, the COSY. The pulse sequence also has two pulses separated by an incremented delay. In the NOESY however, the second pulse is followed by a mixing period of a fixed length after which a third $\pi/2$ pulse returns the magnetization on the $-z$ -axis to the transverse plane for acquisition. During the mixing period, cross-relaxation occurs between spins that are close together in space ($<5 \text{ \AA}$ apart), which leads to cross peaks between these spins in the resultant 2D spectrum. Magnetization that remains in the transverse plane after the second $\pi/2$ pulse is discarded through phase cycling. The process of cross-relaxation is described by the Solomon equations, and these show that the cross-relaxation rate constant is dependent on the spectral density function at twice the Larmour frequency and at zero frequency. A consequence of this is that the rate constant for cross-correlation between two spins (σ_{12}) is dependent on the correlation time of the molecule in the sample as described in Equation 2.7, where b is the dipole-dipole coupling constant (which describes the magnitude of the local fields); $j(\omega)$ is the spectral density at frequency ω ; and $\omega_{0,1}$ and $\omega_{0,2}$ are the Larmour frequencies of spins 1 and 2, respectively.

$$\sigma_{12} = b^2 \left[\frac{3}{10} j(\omega_{0,1} + \omega_{0,2}) - \frac{1}{20} j(\omega_{0,1} - \omega_{0,2}) \right] \quad (2.7)$$

For small molecules, the cross-relaxation rate constant bears a positive charge and leads to positive peaks in the 2D NOESY spectrum. As the correlation time of the molecule increases, the spectral density function narrows and the contribution to the cross-relaxation rate constant

from the spectral density function at twice the Larmour frequency (which is the minuend in the equation for the cross-relaxation rate constant) becomes increasingly negligible. This leaves only the term that depends on the spectral density function at zero frequency (the subtrahend) and the cross-relaxation constant crosses the x-axis to become negative, leading to cross peaks with negative intensity in the 2D NOESY spectrum. At correlation time at which the cross-relaxation rate constant crosses the x-axis, the NOESY experiment becomes ineffective, because little to no cross-relaxation occurs.

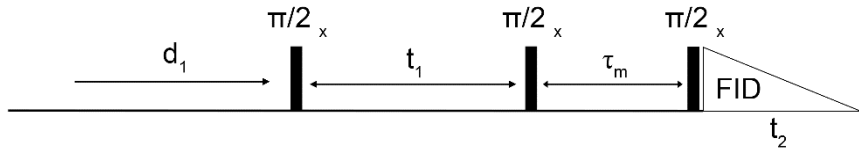
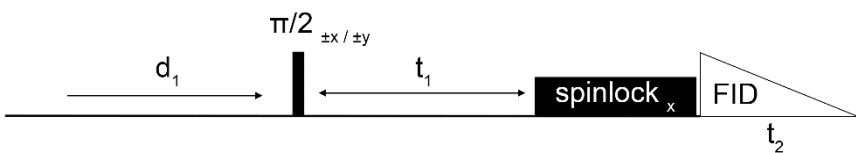


Figure 2.4. The basic pulse sequence for a 2D NOESY experiment.

2.2.4 Rotating Frame NOE Spectroscopy

The 2D ROESY experiment is closely related to the 2D NOESY experiment and again exploits cross-relaxation between spins to facilitate magnetization transfer and extract information about the proximity of spins in the sample. In the first part of the pulse sequence, the 2D ROESY experiment mirrors the 2D NOESY experiment. Instead of the last two pulses in the 2D NOESY experiment however, which rotate magnetization out of, and then back into, the transverse plane for the mixing period, the 2D ROESY experiment utilises a spin lock. The spin lock holds the magnetization in the transverse plane, whilst preventing chemical shift evolution from taking place (Figure 2.5). During this spin lock pulse, magnetization transfer via cross-relaxation can occur, just as it does in the NOESY experiment. The advantage that the 2D ROESY confers is that the resulting cross peaks in the processed spectrum are positive regardless of the correlation time of the molecule in the sample, and there is no cross over point where the cross-relaxation rate approaches zero. This is a consequence of the mixing period taking place whilst spins are in the transverse plane rather than the longitudinal plane. With the RF field (B_1) switched on, the Larmour frequency of the spins in the sample is dependent on B_1 rather than the applied field, B_0 . B_1 is much smaller than B_0 and the Larmour frequency is therefore in the range of kilohertz rather than megahertz. The spectral density at twice this (much smaller) Larmour frequency, which is the minuend in the equation for cross-relaxation

rate constant (Equation 2.7), is therefore not negligible as it usually is with large molecules. The cross-relaxation rate constant is therefore invariably positive, resulting in positive NOE crosspeaks in the ROESY spectrum. For this reason, the ROESY experiment is particularly useful for molecules of ~1000 Da, such as oligosaccharides, whose size (and therefore rate of molecular tumbling) results in NOE enhancements of close to 0 in NOESY experiments. Another advantage the 2D ROESY experiment has over the 2D NOESY is that peaks arising because of spin diffusion (where magnetization transfer occurs sequentially over two or more



spins) can bear an opposite sign to peaks arising from a single transfer event. In the NOESY experiment, these spin diffusion peaks can be easily misinterpreted, whereas in the ROESY experiment they are easier to identify and disregard.

Figure 2.5. The basic pulse sequence for a 2D ROESY experiment.

2.2.5 The Heteronuclear Single Quantum Correlation Experiment

The HSQC experiment is of great utility in the study of proteins by NMR spectroscopy. In the HSQC experiment, magnetization is transferred between ^1H nuclei and another type of nucleus (commonly ^{15}N) using J-coupling. The experiment can be divided into three sections which are followed by an acquisition period. In the first section, a pulse sequence called INEPT transfers magnetization from the ^1H nuclei to ^{15}N with which they are J-coupled. In a sequence of amino acids, this occurs only between the hydrogen and nitrogen atoms of the backbone amide, as well as between bonded hydrogen and nitrogen atoms in amino acid side chains. The INEPT sequence is followed by an incremented delay where the chemical shift of the ^{15}N spins is allowed to evolve. Finally a second INEPT sequence transfers magnetization back to ^1H and the signal is recorded. The resulting data therefore contains both proton and nitrogen chemical shift information and following a double Fourier transform, the spectrum contains cross peaks at $(\omega_{\text{H}}, \omega_{\text{N}})$. By measuring the ^{15}N chemical shift indirectly and acquiring the signal from ^1H spins, the problem of low signal intensity due to the small gyromagnetic ratio of ^{15}N nuclei is bypassed. The HSQC experiment has many variations, and is a vital tool for protein NMR spectroscopists. The INEPT sequence that it is built from can be adapted and added to enable

magnetization transfer between additional J-coupled nuclei, and as such, multi-dimensional experiments can be constructed that enable assignment of the cross peaks in the HSQC spectrum to particular residues in a protein.

3. Allomorphy as a Mechanism of Post-Translational Control of Enzyme Activity

Allomorphy as a mechanism of post-translational control of enzyme activity

Henry P. Wood^{a,1}, F. Aaron Cruz-Navarrete^{a,1,*}, Nicola J. Baxter^{a,b,1}, Clare R. Trevitt^a, Angus J. Robertson^{a,c}, Samuel R. Dix^a, Andrea M. Hounslow^a, Matthew J. Cliff^b, and Jonathan P. Waltho^{a,b,*}

^aKrebs Institute for Biomolecular Research, Department of Molecular Biology and Biotechnology, The University of Sheffield, Sheffield, S10 2TN, United Kingdom;

^bManchester Institute of Biotechnology and School of Chemistry, The University of Manchester, Manchester, M1 7DN, United Kingdom; ^cPresent address: Laboratory of Chemical Physics, National Institute of Diabetes and Digestive and Kidney Diseases, National Institutes of Health, Bethesda, Maryland 20892, United States

¹H.P.W., F.A.C.N. and N.J.B contributed equally to this work

*To whom correspondence may be addressed: Prof. Jonathan Waltho and F. Aaron Cruz-Navarrete, Krebs Institute for Biomolecular Research, Department of Molecular Biology and Biotechnology, University of Sheffield, Sheffield, S10 2TN, United Kingdom, +44 114 22717, j.waltho@sheffield.ac.uk, ORCID 0000-0002-7402-5492, facruznavarrete1@sheffield.ac.uk, ORCID 0000-0002-5233-581X

Keywords: allomorphy | *cis-trans* proline isomerisation | enzyme regulation | phosphoryl transfer enzyme | NMR spectroscopy | X-ray crystallography

3.1 Abstract

Enzyme regulation is vital for metabolic adaptability in living systems. Fine control of enzyme activity is often delivered through post-translational mechanisms, involving for example allosteric or allokinetic regulation. β -phosphoglucomutase (β PGM) from *Lactococcus lactis* is a phosphoryl transfer enzyme that is required for complete catabolism of trehalose and maltose, through the isomerisation of β -glucose 1-phosphate to glucose 6-phosphate via β -glucose 1,6-bisphosphate. Surprisingly for such a gatekeeper of glycolysis, no fine control mechanism of β PGM has yet been reported. Herein, we describe allomorphy, a hitherto unidentified post-translational control mechanism of enzyme activity. In β PGM, isomerisation of the K145-P146 peptide bond results in the near-equal population of two conformers that have different activities owing to repositioning of the K145 sidechain. *In vivo* phosphorylating agents, such as fructose 1,6-bisphosphate, generate phosphorylated forms of both conformers, leading to a lag phase in activity until the more active phosphorylated conformer dominates. In contrast, the reaction intermediate β -glucose 1,6-bisphosphate, which is at a very low concentration in the absence of β -glucose 1-phosphate, is able to couple the conformational switch and the phosphorylation step, resulting in the rapid generation of the more active phosphorylated conformer. In enabling different responses to several allomorphic activators, allomorphy allows an organism to maximise its responsiveness to environmental changes while minimising the diversion of valuable metabolites.

3.2 Introduction

Enzyme regulation is vital in maintaining the balance of catabolism and anabolism in living systems.^{36,44,120} Enzyme activity is subject to precise control, sometimes involving manifold layers of regulation, and failure often results in metabolic disorders and disease.^{121,122} Regulatory mechanisms are divided into two broad categories: those relating to the control of enzyme concentration (coarse control) and those that modulate enzyme activity (fine control). In coarse control, concentration is determined by transcriptional modulation of gene expression and the balance between the rates of translation and degradation, with additional contributions from maturation, cellular compartmentalisation and local co-clustering.^{40,41,123,124} Coarse control occurs on relatively long timescales (hours to days). In fine control, a diverse group of regulatory mechanisms act to modulate enzyme activity over much shorter timescales (< second to minutes). This group includes the binding of regulatory molecules and reversible covalent modification^{42,43}, and often involves allosteric modulation, where an effector, acting somewhere other than the active site, stabilises forms of the enzyme with a reduced or enhanced activity.^{44,125–127} Alternatively, allokairy is a fine control mechanism, where the activity of a monomeric enzyme is modulated by the near-equivalence of the conformational exchange rate and the catalytic rate in a substrate concentration-dependent manner.^{49,50}

Precise enzyme regulation allows organisms to be responsive to environmental changes and to exploit multiple energy sources. *Lactococcus lactis* (*L. lactis*) is a Gram-positive bacterium that has worldwide usage in the manufacture of fermented dairy products and in the commercial production of lactic acid.¹²⁸ It can grow on a variety of carbohydrate media including trehalose and maltose.^{129–131} Trehalose is transported into *L. lactis* by the phosphoenolpyruvate-dependent phosphotransferase system, yielding trehalose 6-phosphate (T6P), which is phosphorolysed by P_i-dependent trehalose 6-phosphate phosphorylase to β-glucose 1-phosphate (βG1P) and glucose 6-phosphate (G6P)¹³² (Supplementary Fig. 3.1). In contrast, maltose enters cells by the ATP-dependent permease system and is phosphorolysed by the action of P_i-dependent maltose phosphorylase to βG1P and glucose.¹³³ Glucose is subsequently phosphorylated to G6P by glucokinase and enters glycolysis via fructose 1,6-bisphosphate (F16BP). For complete catabolism of both trehalose and maltose, the isomerisation of βG1P to G6P is catalysed by β-phosphoglucomutase (βPGM, EC 5.4.2.6, 25 kDa). βPGM deficient *L. lactis* is unable to grow or has impaired growth, when the sole carbon source is trehalose or

maltose, respectively.¹³⁴ With maltose, β G1P accumulates intracellularly and is excreted into the growth medium. Correspondingly, both P_i -dependent trehalose 6-phosphate phosphorylase and P_i -dependent maltose phosphorylase (Supplementary Fig. 3.1) operate in the reverse sense to their physiological roles in wild-type *L. lactis*, resulting in β G1P being combined with G6P to form T6P or polymerised to form amylose ($\alpha(1\rightarrow4)$ -linked glucose units). In trehalose and maltose metabolism, therefore, β PGM acts as the gatekeeper to and from glycolysis, and is expected to be subject to tight regulation. In terms of coarse control, transcription of the β PGM gene (*pgmB*), which is located in the *tre* operon, is subject to negative transcriptional control by glucose and lactose.¹³⁰ When *L. lactis* switches from metabolising glucose to metabolising maltose (or by implication, trehalose), there is a significant rise in the specific activity of β PGM over a period of several hours. However, no fine control mechanism has yet been identified at basal levels of β PGM, which would allow the cell to compete more successfully during a transition between carbohydrate sources.

β PGM is a monomeric magnesium-dependent phosphoryl transfer enzyme of the haloacid dehalogenase (HAD) superfamily.^{32,77–79,82–84,135} The active site is located in the cleft between the α/β core domain (M1–D15, S88–K216) and the α -helical cap domain (T16–V87), with closure of the cleft through domain reorientation occurring during catalysis. Two phosphate group binding sites are present, a *proximal* site adjacent to the carboxylate nucleophile and the catalytic Mg^{2+} ion, and a *distal* site located ~8 Å away in the closed enzyme.⁸² During steady-state catalysis, β G1P binds to phosphorylated β PGM (β PGM^P, phosphorylated on D8) and forms β -glucose 1,6-bisphosphate (β G16BP). Release to solution and subsequent rebinding of β G16BP in the alternate orientation⁸⁰ leads to the formation of G6P and the regeneration of β PGM^P (Fig. 3.1). *In vitro*, a phosphorylating (priming) agent is required to initiate the catalytic cycle since the half-life of β PGM^P is ~30 s.⁸⁴ *In vivo*, potential candidates for this agent include F16BP, β G1P, G6P, α -glucose 1,6-bisphosphate (α G16BP), and acetyl phosphate (AcP), as well as the reaction intermediate, β G16BP. However, only β G16BP allows β PGM to reach its maximum catalytic rate, and a significant lag phase is observed in the reaction with α G16BP as the phosphorylating agent⁸⁴, until the β G16BP concentration greatly exceeds its resting concentration in the cell. In the current kinetic model for β PGM catalysis, α G16BP is also required to act as a very strong inhibitor of β PGM. α G16BP is a close structural analogue of β G16BP⁷⁹, but very similar kinetic behaviour is observed when AcP is used as the phosphorylating agent³², suggesting that other factors are contributing to post-translational

control of β PGM. Here we show that a hitherto unidentified mechanism is operating in β PGM, which we have termed allomorphy to illustrate its relationship to and distinction from allostery and allokairy. In the substrate-free enzyme, the isomerisation of proline 146 results in the near-equal population of two conformers that have different activities. Alternative phosphorylating agents such as F16BP and AcP generate phosphorylated forms of both conformers, resulting in a lag phase in β PGM activity until the more active phosphorylated conformer dominates. In contrast, the β G16BP reaction intermediate is able to couple the conformational switch and the phosphorylation step, resulting in the rapid generation of the more active phosphorylated species. This allows the β G16BP concentration to effectively act as a surrogate of the β G1P concentration and modulate the activity of β PGM according to the carbohydrate source available to *L. lactis*.

3.3 Results

3.3.1 β PGM_{WT} exchanges slowly between two stable conformations

The observation of a lag phase when using either α G16BP or AcP^{32,84} as the phosphorylating agent implies that the target of phosphorylation, the substrate-free enzyme, has a role in post-translational control. Hence, the solution properties of substrate-free wild-type β PGM (β PGM_{WT}) were investigated using NMR spectroscopy. In the previous backbone resonance assignment of β PGM_{WT} (BMRB 7235⁷⁷ performed in standard NMR buffer (50 mM K⁺ HEPES (pH 7.2), 5 mM MgCl₂, 2 mM NaN₃, 10% (v/v) ²H₂O and 1 mM trimethylsilyl propanoic acid (TSP)) containing 10 mM NH₄F, two features were apparent during the analysis: 1) peaks of thirty active site residues were missing from the spectra owing to line-broadening resulting from conformational exchange on the millisecond timescale and 2) a large number of unassigned ¹H_N, ¹⁵N, ¹³C α , ¹³C β and ¹³C' resonances were present with a low intensity. To test whether HEPES or NH₄F were contributing to the millisecond conformational exchange, spectra were recorded in tris buffer (50 mM tris (pH 7.2), 5 mM MgCl₂, 2 mM NaN₃, 10% (v/v) ²H₂O and 1 mM TSP), and mixtures of HEPES and tris buffers in order to transfer the assignment between conditions¹³⁶. It was noticed that the inclusion of 5 mM tris in the standard NMR buffer increased the intensity of the unassigned resonances significantly and therefore all observable resonances in the spectra were re-assigned using standard triple resonance TROSY-based methodology¹³⁷. Excluding the ten proline residues and the N-terminal methionine, the backbone resonances of 193 out of a total of 210 residues (92%) were assigned. Seventeen residues located in the vicinity of the active site remained unassigned (L9, D10, G11, R38, L44, K45, G46, S48, R49, E50, D51, S52, L53, K117, N118, D170 and S171). Notably, 102 of the assigned residues displayed pairs of resonances in the ¹H¹⁵N-TROSY spectrum (Fig. 3.2a, Supplementary Fig. 3.2a), consistent with the population of two β PGM_{WT} conformers (70% *conformer A*, BMRB 28095 and 30% *conformer B*, BMRB 28096). A further five residues (K145, A147, D149, I150 and Q176) have assignments in *conformer A*, but are missing assignments in *conformer B*, owing to some differential millisecond conformational exchange occurring in the two species. The β PGM_{WT} conformers are present in the spectra as a result of slow conformational exchange rather than as chemically distinct species, since the addition of 3 mM BeCl₂ and 10 mM NH₄F to the β PGM_{WT} sample induced the population of a single β PGM_{WT}:BeF₃ complex (an analogue of phosphorylated *conformer A*; BMRB 17851³¹)

(Supplementary Fig. 3.3a). The exchange between *conformer A* and *conformer B* is on the multi-second timescale, with $k_{\text{ex}} \leq 1.0 \text{ s}^{-1}$ from ZZ-exchange measurements. Differences in chemical shift between the two conformers (Supplementary Fig. 3.4a) indicate that the regions of $\beta\text{PGM}_{\text{WT}}$ involved in the multi-second conformational exchange process are located primarily in the core domain and comprise the D137–A147 loop, the β -strands (K109–A113 and D133–A136) at the outer edge of the β -sheet and the I152–S163 and Q172–A183 α - and β_{10} -helical regions (Fig. 3.3). Predicted random coil index order parameters (RCI-S^2)¹³⁸ show a decrease in value for *conformer B* in two regions (G32–R38 in the cap domain and D133–K145 in the core domain) (Supplementary Fig. 3.5a), which indicates increased conformational flexibility compared with *conformer A*.

3.3.2 Influence of physiological factors on the conformational exchange

An investigation of factors that affect the population distribution of *conformer A* and *conformer B* was performed using $^1\text{H}^{15}\text{N}$ -TROSY spectra of $\beta\text{PGM}_{\text{WT}}$ recorded under different conditions of temperature, pH, hydrostatic pressure, MgCl_2 (0–100 mM), NaCl (0–200 mM), K^+ HEPES buffer (0–200 mM) and $\beta\text{PGM}_{\text{WT}}$ concentration (0.1–1.2 mM). All of these perturbations had little or no effect, apart from the addition of either MgCl_2 (100 mM) or NaCl (200 mM) to standard NMR buffer, which shifted the population of $\beta\text{PGM}_{\text{WT}}$ primarily to *conformer A* (Supplementary Fig. 3.6a–d). Buffer exchange into deionised water resulted in *conformer B* being the dominant population. However, both *conformer A* and *conformer B* remained populated when Mg^{2+} was removed from the NMR buffer solution, showing that the multi-second conformational exchange is not simply a result of incomplete saturation of the catalytic Mg^{2+} binding site. These observations indicate that chloride anions perturb the population distribution.

The inorganic ionic composition of *L. lactis* cytoplasm (~2 mM Mg^{2+} , ~50 mM Na^+ , ~400 mM K^+ , ~50 mM Cl^-)¹³⁹ overlaps with the concentration ranges tested, where the population distribution between *conformer A* and *conformer B* remained unaffected. Therefore, it is expected that both *conformer A* and *conformer B* are populated in cytoplasm. However, the intracellular milieu is a complex mix of metabolites that could influence this equilibrium. This environment was mimicked through the use of bovine skimmed milk, a medium in which *L. lactis* thrives within the dairy industry. It is expected that the organic components in milk will

also be present in cytoplasm. Moreover, the inorganic ionic composition (~ 5 mM Mg²⁺, ~ 24 mM Na⁺, ~ 38 mM K⁺, ~ 28 mM Cl⁻)¹⁴⁰ is similar to cytoplasm (except for K⁺, which has no effect on the equilibrium between *conformer A* and *conformer B*), so any effects will be due to the influence of metabolites. β PGM_{WT} was diluted 5-fold into fresh skimmed milk, which had been filtered to remove species with a molecular weight larger than 10 kDa. The ¹H¹⁵N-TROSY spectrum revealed that both *conformer A* and *conformer B* were populated with a similar ratio (60% *conformer A* and 40% *conformer B*) to β PGM_{WT} recorded in standard NMR buffer (Supplementary Fig. 3.2c, Supplementary Fig. 3.7a). However, minor chemical shift changes in the active site loops and the sharpening of some peaks that were line-broadened under standard conditions indicated that one of the milk components was binding in the vicinity of the active site. The two dominant organic components of the filtered milk were lactose and citrate (Supplementary Fig. 3.2d). Titration of lactose into β PGM_{WT} had no effect on the ¹H¹⁵N-TROSY spectrum, whereas titration of citrate led to equivalent chemical shift changes and sharpening of line-broadened peaks to those observed in milk. Similar effects were observed in both *conformer A* and *conformer B*. Hence, β PGM_{WT} was crystallised in the presence of citrate and the structure was determined to 2.1 Å resolution (PDB 6YDM; Supplementary Fig. 3.8a–c, Supplementary Table 1). Two chains are present in the crystallographic asymmetric unit, one of which has citrate and acetate bound, whilst the other has tris and acetate bound. Citrate is coordinated in the active site by residues T16, H20, V47–R49 and A115–K117 and mimics substrate binding to some extent. Both monomers share a similar fold and overlay closely with a previously reported substrate-free β PGM_{WT} structure (PDB 2WHE⁸²: non-H atom RMSDs of 0.56 Å and 0.95 Å). Although only one of the two conformers observed in solution is represented in the crystal, the NMR experiments show that both *conformer A* and *conformer B* remain well-populated under physiological conditions.

3.3.3 The conformational exchange involves *cis-trans* proline isomerisation

Exchange phenomena on multi-second timescales in proteins are often a consequence of *cis-trans* isomerisation of Xaa-Pro peptide bonds.^{141,142} The largest differences in chemical shift between *conformer A* and *conformer B* are observed for residues in a loop (D137–A147) containing two proline residues (P138 and P146) (Supplementary Fig. 3.4a). From the crystal structures of the substrate-free form of the enzyme (PDB 6YDL (Supplementary Table 1) determined to 1.5 Å resolution, which compares closely with PDB 2WHE⁸² (non-H atom

RMSD = 0.53 Å) and PDB 1ZOL⁷⁹ (non-H atom RMSD = 0.65 Å)), nine *trans* Xaa-Pro peptide bonds are present in β PGM_{WT}, whereas the K145-P146 peptide bond adopts a *cis* conformation. Proline residues with *cis* peptide bonds have ¹³C β atoms that resonate 2.0–2.5 ppm downfield from those with *trans* peptide bonds¹⁴³ and therefore the isomerisation state of the Xaa-Pro peptide bonds for β PGM_{WT} in solution was investigated. All but one of the assigned proline residues in *conformer A* and *conformer B* possess ¹³C β chemical shifts in the range 30.4–31.9 ppm consistent with the population of *trans* Xaa-Pro peptide bonds (Supplementary Fig. 3.5b). In contrast, the ¹³C β chemical shift for P146 (34.7 ppm) corroborates the presence of a *cis* K145-P146 peptide bond in solution for *conformer A*. However for *conformer B*, the absence of proline ¹³C β resonances for P146 and P148, owing to millisecond conformational exchange in the K145–I150 region, precluded an identification of the isomerisation state for these proline residues using NMR methods.

To explore whether proline isomerisation at the K145-P146 peptide bond is the source of the multi-second conformational exchange in β PGM_{WT}, the β PGM variant P146A (β PGM_{P146A}) was prepared and the solution properties of the substrate-free form were investigated. A ¹H¹⁵N-TROSY spectrum shows that only a single species is present (Fig. 3.2b, Supplementary Fig. 3.2b) and 194 out of a total of 211 residues (92%) were assigned using standard TROSY-based methodology (BMRB 27920¹⁴⁴). The same seventeen residues as β PGM_{WT} remain unassigned owing to millisecond conformational exchange. The chemical shifts of β PGM_{P146A} were compared with those of *conformer A* and *conformer B* of β PGM_{WT} (Supplementary Fig. 3.4b, c). While the largest perturbations relate to the mutation site (together with an associated propagation of effects through the P148–V158 and S171–G182 α -helices), additional significant and widespread chemical shift differences are present between *conformer A* and β PGM_{P146A}, especially in the D137–A147 loop. In contrast, much smaller chemical shift changes are observed between *conformer B* and β PGM_{P146A}, indicating that the solution conformations for these species are closely similar. However, although the K145-A146 peptide bond in β PGM_{P146A} is likely to adopt a *trans* conformation as the dominant population, the isomerisation state remains ambiguous using NMR methods. Therefore, β PGM_{P146A} was crystallised and the structure was determined to 2.0 Å resolution (PDB 6YDK; Supplementary Table 1). The cap and the core domains of the crystal structure superimpose closely with those of β PGM_{WT} (non-H atom RMSD = 0.33 Å, PDB 2WHE⁸²; non-H atom RMSD = 0.48 Å, PDB

6YDL; non-H atom RMSD = 0.51 Å, PDB 1ZOL⁷⁹). The D137–A147 loop exhibits elevated temperature factors, consistent with the lower predicted RCI-S² values derived from NMR chemical shifts (Supplementary Fig. 3.5c). The electron density is best fit by the *trans* conformation of the K145-A146 peptide bond (ω dihedral angle = −177°) (Fig. 3.4a, c). In comparison to β PGM_{WT}, the D137–A147 loop adopts a different conformation, although both a 3₁₀-helix (D137–V141) and a β -turn hydrogen bond (A147_{HN}–S144_{CO}) are retained. These perturbations in structure are consistent with the chemical shift changes observed between *conformer A* and β PGM_{P146A} and support the β PGM_{P146A} structure being a close model of *conformer B*.

The most pronounced consequence of the change in isomerisation state of the K145-A146 peptide bond is the failure of the K145 sidechain in β PGM_{P146A} to engage in the active site (Fig. 3.4a). Instead, this sidechain is positioned in the open cleft between the cap and core domains, and is exposed to solvent. In β PGM_{WT}, the ε -amino group of K145 is coordinated by the carbonyl oxygen atom of A113, the carboxylate sidechain of E169, and a water molecule that is replaced in the transition state analogue (TSA) complex (PDB 2WF5⁸²) by a fluoride ion that mimics an oxygen atom of the transferring phosphoryl group. An electrostatic relationship also exists between the ε -amino group and the carboxylate group of D8. In β PGM_{P146A}, the position of the missing ε -amino group of K145 and its β PGM_{WT} hydrogen bonding are satisfied by a water molecule. The predicted RCI-S² order parameters for β PGM_{P146A} and β PGM_{WT} (Supplementary Fig. 3.5a, c) share similar profiles apart from around the D137–A147 loop, where the RCI-S² values for β PGM_{P146A} indicate increased dynamic properties that broadly mirror those of *conformer B* in β PGM_{WT}. Together, these data reveal that β PGM_{P146A} reflects the properties of *conformer B*, and link the chemical shift and RCI-S² differences between conformers to the isomerisation state of the K145-X146 peptide bond. Thus, the multi-second exchange between *conformer A* and *conformer B* in solution involves *cis-trans* proline isomerisation of the K145-P146 peptide bond.

3.3.4 β PGM_{WT} lag phase depends on the phosphorylating agent

To ensure that the extent of the lag phase observed previously with AcP is not a method dependent observation³², the effect of different phosphorylating agents on the mutase activity of β PGM_{WT} was investigated by monitoring the conversion of 50 μM β G1P to G6P with either

F16BP (1 mM), AcP (8 mM) or β G16BP (10 μ M) present as phosphorylating agents, using the standard glucose 6-phosphate dehydrogenase coupled assay.⁸⁴ Despite the crucial involvement of β G16BP as the reaction intermediate in the catalytic cycle, its concentration in the cell can vary markedly and is dependent upon the concentration of β G1P. Therefore, F16BP is the most likely phosphorylating agent of β PGM *in vivo* when *L. lactis* is growing on glucose-rich media (~50 mM F16BP¹²⁸) versus $K_m \sim 100 \mu\text{M}$ ⁷⁹). AcP is also a potential activator *in vivo*, as although it is present at lower concentrations (1–3 mM in *E. coli*^{145,146}) versus $K_m \sim 800 \mu\text{M}$ ⁷⁹), it is inherently a much faster phosphorylating agent. In the coupled assay experiments with β PGM_{WT} (Fig. 3.5a), when either F16BP or AcP was used as the phosphorylating agent, their progression curves display significant lag phases. The lag is considerably more pronounced in the F16BP experiment, and consequently the maximum rate of β G1P to G6P conversion is not achieved before the substrate is exhausted. When β G16BP was used as the phosphorylating agent the kinetic profile shows a linear, fast initial rate. Consequently, initial rate measurements were made at several β G1P and β G16BP concentrations (10–700 μM and 0.4–100 μM , respectively) and were globally fitted to an equation derived for a ping-pong mechanism with β G1P inhibition.⁸⁴ Accurate fits were obtained at β G16BP concentrations up to 10 μM , since above this concentration the model no longer describes the data. At elevated β G16BP concentrations, the back reaction from β G16BP to β G1P becomes significant, and the free β G16BP concentration is attenuated owing to a multimeric interaction between β G16BP and Mg²⁺ ions³²). Accordingly, the data above 10 μM β G16BP were omitted from the fitting. This analysis yielded values for k_{cat} of $382 \pm 12 \text{ s}^{-1}$, K_m (β G1P) of $91 \pm 4 \mu\text{M}$, K_m (β G16BP) of $8.5 \pm 0.3 \mu\text{M}$ and K_i (β G1P) of $1510 \pm 100 \mu\text{M}$ (Supplementary Fig. 3.9a). These values are all higher than those previously reported for β PGM owing to the extension of the analysis to higher β G1P and Mg²⁺ concentrations.

3.3.5 β PGM catalysis utilises a *cis* K145-X146 peptide bond

To assess whether β PGM is active as *conformer B*, the effect of different phosphorylating agents on the mutase activity of β PGM_{P146A} was investigated by monitoring the conversion of 50 μM β G1P to G6P with either F16BP (1 mM), AcP (8 mM) or β G16BP (10 μM) present as phosphorylating agents using the standard glucose 6-phosphate dehydrogenase coupled assay. As for β PGM_{WT}, the kinetic profiles for β PGM_{P146A} display significant lag phases with F16BP and AcP, while the progression curves with β G16BP show a linear, fast initial rate (Fig. 3.5b).

Consequently, initial rate measurements were made at several β G1P and β G16BP concentrations (5–500 μ M and 2–100 μ M respectively) and were globally fit to the equation used for β PGM_{WT} above. For β PGM_{P146A}, the fitting yielded values for k_{cat} of $19.2 \pm 0.2 \text{ s}^{-1}$, K_m (β G1P) of $157 \pm 3 \mu\text{M}$, K_m (β G16BP) of $175 \pm 3 \mu\text{M}$ and K_i (β G1P) of $933 \pm 32 \mu\text{M}$ (Supplementary Fig. 3.9b). In addition, the equilibration of β G1P and G6P for both β PGM_{WT} and β PGM_{P146A} was monitored by ^{31}P NMR spectroscopy using AcP as a phosphorylating agent (Supplementary Fig. 3.9c, d).³² The time courses show a similar overall profile together with the presence of the lag phase and subsequent fitting of the linear segments yielded a k_{obs} of $70 \pm 30 \text{ s}^{-1}$ for β PGM_{WT} and a k_{obs} of $1.1 \pm 0.2 \text{ s}^{-1}$ for β PGM_{P146A}. The variation between the kinetic parameters derived using the two methods is caused by inhibition resulting from different levels of phosphate-containing species present in the assays. However, the data clearly demonstrate that β PGM_{P146A} is active, with a ~20-fold reduction in k_{cat} , a ~21-fold increase in K_m for β G16BP and a similar K_m and K_i for β G1P, when compared with β PGM_{WT}.

The mechanism of β PGM_{P146A} catalytic activity was explored by preparing a TSA complex containing MgF₃⁻ and G6P^{65,82} and the resulting β PGM_{P146A}:MgF₃:G6P TSA complex was investigated using NMR spectroscopy. The observed ^{19}F chemical shifts are indistinguishable from those of the β PGM_{WT}:MgF₃:G6P TSA complex (Supplementary Fig. 3.9e, f) and a $^1\text{H}^{15}\text{N}$ -TROSY spectrum peak comparison (BMRB 7234⁷⁷) indicates an almost identical correspondence between frequencies. Such close agreement allowed a backbone resonance assignment (211 residues – 100%) using 3D HNCACB and 3D HN(CA)CO spectra (BMRB 28097). Residues with the largest chemical shift differences between the β PGM_{P146A}:MgF₃:G6P and β PGM_{WT}:MgF₃:G6P TSA complexes are located within 4 Å of residue 146 (K145, A147 and A177) and within 5 Å of residue K145 (S48, V141 and A142) (Supplementary Fig. 3.4d). Taken together, these results confirm that β PGM_{P146A} can assemble a stable and wild-type like β PGM_{P146A}:MgF₃:G6P TSA complex in solution. The β PGM_{P146A}:MgF₃:G6P TSA complex was crystallised and the structure was determined to 1.0 Å resolution (PDB 6YDJ; Supplementary Table 1). This complex superimposes very closely with the β PGM_{WT}:MgF₃:G6P TSA complex (non-H atom RMSD = 0.18 Å, PDB 2WF5⁸²) and identifies both the positioning of the K145 sidechain in the active site and the *cis* K145-A146 peptide bond (ω dihedral angle = 14°; compared with ω dihedral angle = 12° for the K145-P146 peptide bond in the β PGM_{WT}:MgF₃:G6P TSA complex) (Fig. 3.4b, d). The 6-phosphate group of G6P is in the *distal* site and the trigonal MgF₃⁻ moiety mimicking the transferring

phosphoryl group is coordinated in the *proximal* site between D8 (atom Oδ1) and the 1-OH group of G6P. The donor-acceptor distance and the angle of alignment are 4.1 Å and 174°, respectively (compared with 4.3 Å and 176°, respectively for the βPGM_{WT}:MgF₃:G6P TSA complex). The catalytic Mg²⁺ ion coordination also has comparable octahedral geometry to the βPGM_{WT}:MgF₃:G6P TSA complex and to substrate-free βPGM_{P146A}. Together, these data demonstrate that βPGM_{P146A} is able to populate a *cis* K145-A146 peptide bond and achieve full domain closure with concomitant formation of transition state geometry. Additionally, assuming that βG16BP binding is diffusion controlled, the increase in K_m for βG16BP in βPGM_{P146A} reflects the energetic cost of the *trans* to *cis* isomerisation of the K145-A146 peptide bond.¹⁴⁷ As in βPGM_{WT}, these results imply that *conformer A* of βPGM_{P146A} represents the more active form.

3.3.6 βPGM forms two different transient phospho-enzyme species

The possible involvement of *conformer B* in the modulation of enzyme activity was investigated using real-time NMR methods by comparing the phosphorylation of βPGM under saturating conditions of either F16BP (50–100 mM), AcP (60–100 mM) or βG16BP (35 mM). Residue A113 is a well-resolved reporter of the relevant species – *conformer A* and *conformer B*, and their phosphorylated counterparts, A^P and B^P. The carbonyl of A113 is coordinated by the ε-amino group of K145 (in *conformer A*) or a water molecule (in *conformer B*) and its amide proton is hydrogen bonded to the carbonyl of F7 (adjacent to the D8 nucleophile) (Fig. 3.4a, b).

On addition of F16BP to βPGM_{P146A}, the two dominant species observed are *conformer B* and B^P (Fig. 3.2b). The presence of *conformer B* shows that the rate of βPGM_{P146A} phosphorylation is very similar to the dephosphorylation rate for B^P (through hydrolysis), and only an apparent rate constant can be measured. The apparent rate constant for dephosphorylation was determined to be $0.02 \pm 0.002 \text{ s}^{-1}$ from the rate of reduction of the free F16BP concentration in ¹H NMR experiments. The ¹H and ¹⁵N chemical shifts of B^P, assigned using fast acquisition 3D HNCO and 3D HNCA NMR experiments, mirror those of *conformer B*, except for the active site residues F7–D8, A113–A115 and hinge residues T16–E18, owing to their proximity to phosphorylated D8 (Supplementary Fig. 3.4e). Resonances from the D137–A147 loop show no significant differences between both forms, indicating that the K145-A146 peptide bond is

in a *trans* conformation in B^P (the *conformer B* to A^P transition results in large chemical shift changes for the D137–A147 loop; Supplementary Fig. 3.4f). *Conformer B* and B^P are also observed when AcP was used as the phosphorylating agent, and a minor population of A^P is present, correlating with a small increase in the population of B^P relative to *conformer B* (Supplementary Fig. 3.7b). Identification of A^P is based on the assignment and structure of the $\beta\text{PGM}_{\text{WT}}:\text{BeF}_3$ complex (BMRB 17851; PDB 2WFA³¹), where the K145-P146 peptide bond is in a *cis* conformation and the K145 sidechain is engaged in the active site. Notably, when βG16BP was used as the phosphorylating agent, B^P is not observed (Fig. 3.2b, Supplementary Fig. 3.7b). Instead, the $A^P:\text{G6P}$ and $B:\beta\text{G16BP}$ complexes are the primarily populated species. The $A^P:\text{G6P}$ complex has similar chemical shifts to the $\beta\text{PGM}_{\text{WT}}:\text{BeF}_3$ complex, and the slow exchange between the $A^P:\text{G6P}$ and the $B:\beta\text{G16BP}$ complexes correlates with the measured k_{cat} values for $\beta\text{PGM}_{\text{P146A}}$.

In $\beta\text{PGM}_{\text{WT}}$, A^P is the dominant species observed on addition of F16BP (Fig. 3.2a, Supplementary Fig. 3.3c). Therefore, the phosphorylation rate of $\beta\text{PGM}_{\text{WT}}$ by F16BP under these conditions must be faster than the hydrolysis rate of A^P ($k_{\text{hydrolysis}} = 0.06 \pm 0.006 \text{ s}^{-1}$). A minor population of the $A:\text{F16BP}$ complex is also present, indicating that under these conditions the phosphorylation rate is slower than the chemical shift difference between the A^P and $A:\text{F16BP}$ peaks (140 Hz). Significantly, a minor population of B^P is also observed. This species is populated transiently (~5 min) and disappears at longer timeframes, whereas A^P and the $A:\text{F16BP}$ complex populations remain dominant while the phosphorylating agent is at high concentration. Hence, the B^P population is converting to the more stable A^P species with a rate constant of $\geq 0.003 \text{ s}^{-1}$, which mirrors the *trans* to *cis* isomerisation rate constants of Xaa-Pro peptide bonds in model peptides.¹⁴¹ Equivalent behaviour is observed when AcP was used as the phosphorylating agent (Supplementary Fig. 3.3b, 3.7a), except that an $A:\text{AcP}$ complex is not detected. When βG16BP was used as a phosphorylating agent, B^P does not accumulate at any point in the 3 hour time course. The only detectable species is an $A:\beta\text{G16BP}$ complex (Fig. 2a, Supplementary Fig. 3.3d, 3.7a), which is identified by the similarity of chemical shift distribution with the $\beta\text{PGM}_{\text{D10N}}:\beta\text{G16BP}$ complex (BMRB 27174; PDB 5OK1³²). The low intensity of the A113 peak, along with peaks of other active site residues (Fig. 3.2a, Supplementary Fig. 3.3d, 3.7a), results from millisecond conformational exchange between species within the catalytic cycle, which correlates with the measured k_{cat} values for $\beta\text{PGM}_{\text{WT}}$.

Overall therefore, the consequence of phosphorylation by the reaction intermediate β G16BP is markedly different to that of other phosphorylating agents, in that it generates no detectable B^P or lag phase, even when the initial population of *conformer B* is high.

3.4 Discussion

Substrate-free β PGM_{WT} exists in solution as two distinct conformers with near-equal populations, which differ in the isomerisation state of the K145-P146 peptide bond and interconvert at a rate between 0.003 s⁻¹ and 1.0 s⁻¹. *Conformer A* contains the *cis*-isomer of this peptide bond, as observed in the crystal structures of substrate-free β PGM_{WT}, while *conformer B* contains the *trans*-isomer, as mimicked by the β PGM_{P146A} variant. In the crystal structure of β PGM_{P146A}, the *trans* K145-A146 peptide bond positions the sidechain of K145 away from the site of phosphoryl transfer, which is significantly different to its location in all other substrate-free and TSA complex structures reported for β PGM_{WT}. The removal of this positively charged amine group from the active site of *conformer B* disrupts the charge balance in the vicinity of the D8 nucleophile and therefore transition state stability will be severely impaired.^{66,70} However, kinetics data for the mutase reaction indicate that β PGM_{P146A} is only ~20-fold less active than β PGM_{WT}, and has a similar affinity for β G1P. In the crystal structure of the β PGM_{P146A}:MgF₃:G6P TSA complex, which mimics the transition state of the phosphoryl transfer step, the K145-A146 peptide bond adopts the *cis*-isomer and the sidechain of K145 is able to engage in the active site. Hence, *conformer A* remains the preferred route for phosphoryl transfer in β PGM_{P146A}, despite it being ~1000 times less stable than in β PGM_{WT} because of the *trans* to *cis* isomerisation of the K145-A146 peptide bond¹⁴⁷.

This disruption of the active site has regulatory significance, as *conformer B* of β PGM_{WT} constitutes a substantial population of the resting substrate-free enzyme. *In vitro*, linear initial kinetics and full activation of the enzyme are achieved only when β G16BP is used as the phosphorylating agent. Phosphorylation of both β PGM_{WT} and β PGM_{P146A} with either F16BP or AcP leads to a lag phase, with the lag caused by F16BP lasting ~3.5 times longer than that observed with AcP. Moreover, real-time NMR experiments establish that the phosphorylation of both β PGM_{WT} and β PGM_{P146A} with either F16BP or AcP result in the generation of B^P. In β PGM_{WT}, B^P isomerises completely into A^P in <5 min, whereas in β PGM_{P146A}, B^P is consistently more populated than A^P. In contrast, B^P is not observed for either β PGM_{WT} or β PGM_{P146A} when β G16BP is used as the phosphorylating agent. This result demonstrates that phosphorylation with β G16BP leads to the stabilisation of *conformer A*, resulting in production of A^P, regardless of the initial β PGM conformation, even for the β PGM_{P146A} variant despite the considerable energetic cost of the *conformer B* to *conformer A* transition. Thus, *conformer B*

and B^P are significantly less active forms of β PGM, and the slow transition from B^P to A^P is part of the characteristic lag phase observed in the coupled assay kinetics. The longer lag in the F16BP experiments and the observation of a β PGM_{wt}:F16BP complex are consistent with F16BP having a slower phosphorylation rate than AcP. Therefore, β PGM is able to follow alternative kinetic pathways depending on the phosphorylating agent present, with its overall catalytic rate determined by the rate limiting step in each pathway (Fig. 3.6a, b).

The response of β PGM to different phosphorylating agents also has functional significance. In *L. lactis*, the sole source of β G16BP is β PGM itself. In contrast, F16BP accumulates during glycolysis, reaching a concentration of up to ~50 mM.¹²⁸ Hence, F16BP is likely to be the primary source of β PGM activation *in vivo*, with AcP contributing to a lesser extent.^{145,146} Correspondingly, a proportion of β PGM will populate the less active B^P species. Following a switch from glucose to maltose or trehalose metabolism, which will greatly increase the β G1P concentration (Supplementary Fig. 3.1), β G16BP will begin to accumulate (Fig. 1, 3.6a, b). As a result, the *conformer B* and B^P populations will be recruited into the more active A^P species. This two-state control mechanism allows *L. lactis* to effectively catabolise maltose or trehalose, while the increase in transcription of *pgmB* is in progress.¹³¹ Furthermore, when carbohydrate levels are low, a significant proportion of the basal β PGM population will be maintained as *conformer B*, which will consequently reduce the undesirable dephosphorylation of F16BP and also hinder the conversion of G6P to β G1P.

The multi-second substrate-dependent non-allosteric conformational exchange mediated through *cis-trans* proline isomerisation seen in β PGM represents a hitherto unidentified mechanism of post-translational enzyme regulation. This regulation mechanism relies on the existence of alternative pathways with different rate limiting steps, where the catalytic rate depends on the capacity of an activator, acting as a substrate, to bias the enzyme population towards the fastest pathway, by stabilising the most active conformation (Fig. 3.7). Similar to allostery and allokairy, this mechanism depends on the ability of the enzyme to adopt at least two conformations with distinct activities, but does not require the binding of an additional effector to the protein, nor an equivalence between the conformational exchange rate and the catalytic rate. We suggest the name “allomorphy” for this mechanism, from the greek *allos* meaning “other” and *morphe* meaning “form”, in keeping with the previously described allosteric and allokairy mechanisms.⁴⁹

Allomorphy may modulate the activity of other monomeric enzymes with hysteretic behaviour, i.e. those that exhibit a burst or lag phase in their kinetic profile.¹⁴⁸ Several theoretical models have been put forward to rationalise hysteretic behaviour, such as the mnemonic¹⁴⁹ and the ligand-induced slow transition¹⁵⁰ models, but detailed structural-based molecular mechanisms have proved elusive. To our knowledge, only one such mechanism, allokairey in human glucokinase, has been described in detail.^{49,50} Allomorphy is a different fine control regulatory mechanism and is potentially widespread, at least across phosphomutases; for example, both rabbit muscle and *L. lactis* α -phosphoglucomutases appear to be hysteretic enzymes^{151,152}, but belong to very different protein superfamilies. Like β PGM, these enzymes require a phosphorylating agent to initiate the catalytic cycle and, for the latter, the use of the reaction intermediate results in linear kinetics, whereas alternative phosphorylating agents produce a lag phase in their kinetic profiles. Similarly, α -phosphomannomutase from *Galdieria sulphuraria*, which also requires the addition of a phosphorylating agent to initiate the catalytic cycle, exhibits linear kinetics when α -mannose 1-phosphate and α -mannose 1,6-bisphosphate (or α -glucose 1-phosphate and α G16BP) are included in the reaction, but has a lag phase when there is a mismatch between substrate and phosphorylating agent, or when F16BP is used as the phosphorylating agent.¹⁵³ All of these observations are consistent with the presence of allomorphic control.

In summary, allomorphy is a novel fine control mechanism by which part of an enzyme population is maintained in a more latent state, and is quickly switchable between high and low activity levels, without allosteric effectors. It delivers important control with which *L. lactis* is able to reconcile two seemingly contradictory requirements: the need to maximise its responsiveness to changes in carbohydrate source and the need to minimise unproductive diversion of valuable metabolites.

3.5 Methods

3.5.1 β -Phosphoglucomutase (β PGM) expression and purification

Wild type β PGM (β PGM_{WT}) and the P146A variant (β PGM_{P146A}) proteins were expressed using either natural abundance, ¹⁵N or ²H¹⁵N¹³C isotopic enrichment¹⁵⁴ and purified using methodology that minimised the presence of contaminating phosphoryl transfer enzymes (e.g. phosphoglucose isomerase and β PGM from *E. coli*).^{32,144} Unless otherwise stated, reagents were purchased from Sigma-Aldrich, GE Healthcare, Melford Laboratories or CortecNet. β G1P was synthesised enzymatically as described previously.³² β G16BP was produced enzymatically from β G1P and AcP using the D170N variant of β PGM and was purified further by a barium salt precipitation procedure.¹⁵⁵

3.5.2 NMR spectroscopy

3.5.2.1 ¹H¹⁵N-TROSY and ¹H¹⁵N BEST-TROSY experiments

¹H¹⁵N-TROSY spectra of β PGM_{WT} and β PGM_{P146A} were acquired at 298 K using 0.5–1 mM ¹⁵N- β PGM in standard NMR buffer (50 mM K⁺ HEPES (pH 7.2), 5 mM MgCl₂, 2 mM NaN₃ with 10% (v/v) ²H₂O and 1 mM trimethylsilyl propanoic acid (TSP)). Typically, ¹H¹⁵N-TROSY spectra were accumulations of 16 transients, with 256 increments and spectral widths of 32–36 ppm centred at 120 ppm in the indirect ¹⁵N dimension. ¹H¹⁵N-TROSY-based ZZ-exchange experiments were performed at mixing times of 100, 300, 500 and 900 ms. Rapid acquisition ¹H¹⁵N BEST-TROSY experiments to monitor the steady-state behaviour of ¹⁵N- β PGM_{WT} (0.2 mM) and ¹⁵N- β PGM_{P146A} (0.2 mM) were acquired in standard kinetic buffer (200 mM K⁺ HEPES (pH 7.2), 5 mM MgCl₂, 2 mM NaN₃ with 10% (v/v) ²H₂O and 1 mM TSP) containing either 50–100 mM F16BP, 60–100 mM AcP or 35 mM β G16BP. The ¹H¹⁵N BEST-TROSY spectra were recorded at 298 K using a Bruker 600 MHz Neo spectrometer equipped with a 5-mm TCI cryoprobe and z-axis gradients as 11 min experiments (16 transients, 128 increments and a recycle delay of 0.2 s) with selective ¹H pulses centred on the amide region (8.3 ppm). Excitation pulses (90°) were 1.7 ms (pulse shape Eburp2), whereas refocusing pulses (180°) were 1.4 ms (pulse shape Reburp). The experimental dead-time was approximately 5 min.

3.5.2.2 Rapid mixing NMR experiments

To observe the species present immediately following the addition of phosphorylating agent to β PGM_{WT}, NMR experiments were recorded with the use of a homemade rapid mixing device. The equipment comprised a 2 m length of 0.8 mm internal diameter EFTE tubing (GE Healthcare), connected at one end to a 1 mL syringe and inserted at the other end through the lid of an NMR tube. The tubing was loaded with phosphorylating agent (550 μ L 100 mM F16BP or 250 μ L 320 mM AcP, prepared in standard kinetic buffer) and a small, additional volume of air was drawn in to prevent premature mixing of the phosphorylating agent with the 550 μ L 1.2 mM ^{15}N - β PGM_{WT} sample prepared in standard kinetic buffer. The rapid mixing device was loaded into a Bruker 600 MHz Neo spectrometer and allowed to equilibrate thermally at 298 K. Following mixing by syringe action of the phosphorylating agent (final concentration: 50 mM F16BP or 100 mM AcP) with the β PGM_{WT} sample, the spectrometer was locked (with ~7% (v/v) $^2\text{H}_2\text{O}$), tuned and shimmed, and the ^1H 90° pulse length was calibrated. A series of $^1\text{H}^{15}\text{N}$ BEST-TROSY spectra were recorded as 142 s experiments (4 transients, 128 increments and a recycle delay of 0.15 s). The experimental dead-time was approximately 156 s.

3.5.2.3 Backbone resonance assignment

Multi-dimensional heteronuclear NMR spectra for ^1H , ^{15}N and ^{13}C backbone resonance assignment of $^2\text{H}^{15}\text{N}^{13}\text{C}$ - β PGM_{WT} in standard NMR buffer containing 10 mM tris were acquired at 298 K on a Bruker 800 MHz Avance III spectrometer equipped with a 5-mm TCI cryoprobe and z-axis gradients. The standard Bruker suite of $^1\text{H}^{15}\text{N}$ -TROSY and 3D TROSY-based constant time experiments were acquired (HNCO, HN(CA)CO, HNCA, HN(CO)CA, HNCACB, HN(CO)CACB) using non-uniform sampling (NUS) with a multi-dimensional Poisson Gap scheduling strategy with exponential weighting.¹⁵⁶ NUS data were reconstructed using multi-dimensional decomposition in TopSpin3.¹⁵⁷ Backbone resonance assignments for *conformer A* and *conformer B* present simultaneously in the spectra were obtained using a simulated annealing algorithm employed by the *asstools* assignment program¹⁵⁴ and assignments were confirmed using sequential backbone amide to amide correlations obtained from TROSY-based (H)N(COCA)NNH and H(NCOCA)NNH experiments.¹⁵⁸ Multi-dimensional heteronuclear NMR spectra for ^1H , ^{15}N and ^{13}C backbone resonance assignment of the $^2\text{H}^{15}\text{N}^{13}\text{C}$ - β PGM_{P146A}:MgF₃:G6P TSA complex in standard NMR buffer containing 15

mM NaF and 10 mM G6P were acquired at 298 K on a Bruker 800 MHz Avance I spectrometer equipped with a 5-mm TXI probe and z-axis gradients. $^1\text{H}^{15}\text{N}$ -TROSY and 3D TROSY-based constant time experiments were acquired (HN(CA)CO and HNCACB) and backbone resonance assignments were obtained using *asstools*.¹⁵⁴ Multi-dimensional heteronuclear NMR spectra for ^1H , ^{15}N and ^{13}C backbone resonance assignment of phosphorylated $^2\text{H}^{15}\text{N}^{13}\text{C}$ - $\beta\text{PGM}_{\text{P146A}}$ in standard kinetic buffer containing 75–100 mM F16BP were acquired at 298 K on a Bruker 800 MHz Neo spectrometer equipped with a 5-mm TXI probe and z-axis gradients. $^1\text{H}^{15}\text{N}$ -TROSY and 3D TROSY-based constant time experiments were acquired (HNCO and HNCA) using non-uniform sampling (NUS) with a multi-dimensional Poisson Gap scheduling strategy with exponential weighting.¹⁵⁶ NUS data were reconstructed using multi-dimensional decomposition in TopSpin4.¹⁵⁷ TROSY resonances were assigned by comparing the correlated ^{13}C chemical shifts with those of $\beta\text{PGM}_{\text{P146A}}$ (BMRB 27920¹⁴⁴) and the $\beta\text{PGM}_{\text{WT}}:\text{BeF}_3$ complex (BMRB 17851³¹). Experiments were processed using TopSpin (Bruker) or FELIX (Felix NMR, Inc.) and figures were prepared using FELIX. ^1H chemical shifts were referenced relative to the internal TSP signal resonating at 0.0 ppm, and ^{13}C and ^{15}N and chemical shifts were referenced indirectly using nuclei-specific gyromagnetic ratios. Differences in chemical shift were calculated as: $\Delta\delta = [(\delta_{\text{HN-X}} - \delta_{\text{HN-Y}})^2 + (0.12 \times (\delta_{\text{N-X}} - \delta_{\text{N-Y}}))^2]^{1/2}$, where X and Y are the two species being compared.

3.5.2.4 Kinetic experiments using ^{31}P NMR spectroscopy

Reaction kinetics for $\beta\text{PGM}_{\text{P146A}}$ -catalysed reactions were followed using a Bruker 500 MHz Avance DRX spectrometer (operating at 202.456 MHz for ^{31}P) equipped with a room-temperature broadband probe. The equilibration of 10 mM βG1P with G6P by 1–3 μM $\beta\text{PGM}_{\text{P146A}}$ was measured in standard kinetic buffer at 298 K. The reaction was initiated by and timed from the addition of 20 mM AcP and monitored by the acquisition of consecutive ^{31}P spectra without proton-phosphorus decoupling with 256 transients and a 1 s recycle delay. A spectral width of 50 ppm centred at –10 ppm enabled the observation of the relevant phosphorus signals. Normalised integral values of both the βG1P and G6P peaks following baseline correction and 5 Hz Lorentzian apodisation were plotted against time to give kinetic profiles. The linear steady-state portion of the G6P integral data was fitted using a linear least-squares fitting algorithm to derive the observed rate constant, k_{obs} .

3.5.2.5 ^{19}F NMR spectroscopy

One dimensional ^{19}F NMR experiments were acquired at 298 K on a Bruker 500 MHz Avance III spectrometer (operating at 470.536 MHz for ^{19}F) equipped with a 5-mm QCI-F cryoprobe and z-axis gradients. Samples were prepared using 0.5 mM natural abundance $\beta\text{PGM}_{\text{WT}}$ or $\beta\text{PGM}_{\text{P146A}}$ in standard NMR buffer (without 10% (v/v) $^2\text{H}_2\text{O}$) containing 15 mM NaF and 10 mM G6P. The spectrometer lock was provided by $^2\text{H}_2\text{O}$ sealed inside a glass capillary tube inserted into the sample tube. Typically, ~6000 transients were acquired without ^1H decoupling over a spectral width of 120 ppm and were processed with sinebell functions shifted by 60°.

3.5.2.6 $\beta\text{PGM}_{\text{WT}}$ in filtered milk

Fresh skimmed bovine milk purchased from a local supermarket was filtered using a 10 kDa MWCO Vivaspin (Sartorius) to remove fat micelles and milk proteins. A 1 mM $^{15}\text{N}-\beta\text{PGM}_{\text{WT}}$ sample prepared in standard NMR buffer was diluted 5-fold with the resulting milk flow-through and 10% (v/v) $^2\text{H}_2\text{O}$ and 1 mM TSP were added to the sample. Experiments were acquired at 298 K on a Bruker 800 MHz Avance I spectrometer equipped with a 5-mm TXI probe and z-axis gradients. The pH of the sample was estimated as pH 6.8 using the residual ^1H resonances of HEPES buffer originating from the standard NMR buffer.

3.5.2.7 $\beta\text{PGM}_{\text{WT}}$ in deionised water

A 1.4 mM $^{15}\text{N}-\beta\text{PGM}_{\text{WT}}$ sample in standard NMR buffer containing an additional 200 mM NaCl was buffer-exchanged into freshly produced deionised water (18.2 MΩ.cm, Purelab Classic, Elga-Veolia), with an equivalent dilution of the previous buffer by a factor of 18.7×10^6 . The resulting sample contained 0.9 mM $\beta\text{PGM}_{\text{WT}}$ at pH 6.3 and was supplemented with 10% (v/v) $^2\text{H}_2\text{O}$ for the deuterium lock. Experiments were acquired at 298 K on a Bruker 800 MHz Avance I spectrometer equipped with a 5-mm TXI probe and z-axis gradients.

3.5.3 Kinetic experiments using coupled assays

All kinetic assays for $\beta\text{PGM}_{\text{WT}}$ and $\beta\text{PGM}_{\text{P146A}}$ were conducted at 298 K using a FLUOstar OMEGA microplate reader (BMG Labtech) in standard kinetic buffer (200 mM K^+ HEPES (pH 7.2), 5 mM MgCl_2 , 1 mM NaN_3) in a 160 μL reaction volume. The rate of G6P production was measured indirectly using a glucose 6-phosphate dehydrogenase (G6PDH) coupled assay, in which G6P is oxidised and concomitant NAD^+ reduction is monitored by the increase in

absorbance at 340 nm (NADH extinction coefficient = 6220 M⁻¹ cm⁻¹). βPGM_{WT} and βPGM_{P146A} concentrations were determined using a NanoDrop OneC spectrophotometer (Thermo Scientific) and diluted accordingly (βPGM extinction coefficient = 19 940 M⁻¹ cm⁻¹). For the determination of *k*_{cat} and *K*_m values for βPGM_{WT}, the reaction was initiated by dilution of the enzyme prepared in standard kinetic buffer to a final concentration of 1 nM βPGM_{WT} in solutions of 1 mM NAD⁺ and 5 units mL⁻¹ G6PDH and variable concentrations of βG1P (10, 20, 30, 50, 70, 100, 150, 200, 300, 500, 700 μM) and βG16BP (0.4, 1, 2, 5, 10 μM). For the determination of *k*_{cat} and *K*_m values for βPGM_{P146A}, the reaction was initiated by dilution of the enzyme prepared in standard kinetic buffer to a final concentration of 100 nM βPGM_{P146A} in solutions of 1 mM NAD⁺ and 5 units mL⁻¹ G6PDH and variable concentrations of βG1P (5, 10, 15, 20, 30, 50, 70, 100, 200, 300, 500 μM) and βG16BP (2, 5, 10, 35, 50, 100 μM). The initial rate of G6P production was fitted using a linear least-squares fitting algorithm to determine the reaction velocity (*v*₀) at each βG1P and βG16BP concentration at a total enzyme concentration (*E*_T). Mean data from triplicate measurements were subsequently globally fitted to Equation 3.1⁸⁴, which is derived for a ping-pong mechanism and adapted to account for βG1P inhibition (*K*_i) to calculate *k*_{cat} and individual *K*_m values (*K*_{βG1P} and *K*_{βG16BP}), with their corresponding standard deviations, using an in-house python non-linear least-squares fitting algorithm.

$$v_0 = \frac{k_{cat}[E_T][\beta G1P][\beta G16BP]}{[\beta G1P][\beta G16BP] + K_{\beta G1P}[\beta G16BP] + K_{\beta G16BP}[\beta G1P]\left(\frac{K_i + [\beta G1P]}{K_i}\right)} \quad (3.1)$$

Kinetic experiments demonstrating the effect of different phosphorylating agents were conducted by the addition of either 5 nM βPGM_{WT} or 200 nM βPGM_{P146A} to solutions containing either 1 mM F16BP, 8 mM AcP or 10 μM βG16BP, together with 1 mM NAD⁺, 5 units mL⁻¹ G6PDH and 50 μM βG1P. F16BP represents an equilibrium mixture of an α-anomer (15%), a β-anomer (81%) and two open chain forms with an interconversion rate of 8 s⁻¹.¹⁵⁹

3.5.4 X-ray crystallography

3.5.4.1 Crystallisation and data collection

For the crystallisation experiments of βPGM_{WT}, βPGM_{P146A}, the βPGM_{P146A}:MgF₃:G6P TSA complex and the βPGM_{WT}:citrate complex, frozen aliquots of βPGM_{WT} or βPGM_{P146A} in

standard native buffer (50 mM K⁺ HEPES (pH 7.2), 5 mM MgCl₂, 2 mM NaN₃) were thawed on ice and centrifuged briefly to pellet insoluble material. For the βPGM_{P146A}:MgF₃:G6P TSA complex, 15 mM NaF and 10 mM G6P were added to the βPGM_{P146A} sample, whereas for the βPGM_{WT}:citrate complex, 50 mM citrate was added to the βPGM_{WT} sample. Solutions were adjusted to a final protein concentration of 0.4–0.6 mM, incubated for 1 h and mixed 1:1 with precipitant (24–34% (w/v) PEG 4000, 200 mM sodium acetate and 100 mM tris-HCl (pH 7.5)). Crystals were grown at 290 K by hanging-drop vapour diffusion using a 2 µl drop suspended on a siliconised glass cover slip above a 700 µL well. Rod-shaped or large plate crystals grew typically over several days. Crystals were harvested using a mounted LithoLoop (Molecular Dimensions Ltd) and were cryo-protected in their mother liquor containing an additional 25% (v/v) ethylene glycol (and 50 mM citrate for the βPGM_{WT}:citrate crystals) prior to plunging into liquid nitrogen. Diffraction data were collected at 100 K on the MX beamlines at the Diamond Light Source (DLS), Oxfordshire, United Kingdom.

3.5.4.2 Data processing, structural determination and refinement

Data were processed using the xia2 pipeline¹⁶⁰ and resolution cut-offs were applied using CC-half values and Aimless.¹⁶¹ The crystals diffracted in the *P2₁2₁2₁* spacegroup, with cell dimensions that varied depending on the degree of enzyme closure. Structures were determined by molecular replacement with MolRep¹⁶² using the highest resolution model with the most appropriate cap and core domain relationship as a search model. Model building was carried out in COOT¹⁶³ with ligands not included until the final rounds of refinement with REFMAC5¹⁶⁴ so that they could be built into unbiased difference Fourier maps. The βPGM_{P146A}:MgF₃:G6P TSA complex structure was refined with anisotropic B-factors, whereas both the βPGM_{WT} structures and the substrate-free βPGM_{P146A} structure were refined isotropically. Structure validation was carried out in COOT and MolProbity¹⁶⁵. Superpositions were carried out using PyMOL¹⁶⁶. To confirm the isomerisation state of the K145-A146 peptide bond in the structures of substrate-free βPGM_{P146A} and the βPGM_{P146A}:MgF₃:G6P TSA complex, difference density maps (Fo – Fc) were generated using REFMAC5 with the S144–P148 segment omitted from the final structures. Omit map figures were prepared using CCP4mg.¹⁶⁷ Additional details for X-ray crystallography data collection, data processing and refinement are provided in Supplementary Table 1.

3.6 Acknowledgements

We would like to thank Dr Claudine Bisson for helpful discussions and interpretation of X-ray crystallography data and Prof. Nicholas Williams for useful insight into β G16BP purification. We would also like to thank the beamline scientists at the Diamond Light Source (DLS) for the provision of synchrotron radiation facilities and assistance with data collection. This research was supported by the Biotechnology and Biological Sciences Research Council (BBSRC; H.P.W. – Grant Number X/009906-20-26, N.J.B. – Grant Number BB/M021637/1 and BB/S007965/1, C.R.T – Grant Number BB/P007066/1), Consejo Nacional de Ciencia y Tecnología, Mexico (CONACYT; F.A.C.N. – Grant Number 472448) and The Royal Society (S.R.D. – Grant Number R/152968).

3.7 Author Contributions

H.P.W., F.A.C.N., N.J.B., C.R.T., A.J.R., J.P.W. designed research; H.P.W., F.A.C.N., C.R.T., A.J.R. produced isotopically enriched protein; H.P.W. performed coupled assay kinetic experiments; H.P.W., C.R.T. produced and purified β G1P and β G16BP; H.P.W., F.A.C.N., C.R.T., A.M.H., M.J.C. acquired NMR experiments; H.P.W., F.A.C.N., N.J.B., C.R.T. analysed NMR data; F.A.C.N., N.J.B., C.R.T. performed backbone resonance assignments; H.P.W., A.J.R., S.R.D. performed and analysed X-ray crystallography experiments; F.A.C.N. conceived and developed the allomorphy mechanism; H.P.W., F.A.C.N., N.J.B., C.R.T., J.P.W. wrote the paper with help from all authors.

3.8 Competing Financial Interest

The authors declare no competing financial interest.

3.9 Data Deposition

The atomic coordinates and structure factors have been deposited in the Protein Data Bank (www.rcsb.org) with the following codes: β PGM:citrate complex (PDB 6YDM), substrate-free β PGM (PDB 6YDL), substrate-free β PGM_{P146A} (PDB 6YDK) and β PGM_{P146A}:MgF₃:G6P

TSA complex (PDB 6YDJ). The NMR chemical shifts have been deposited in the BioMagResBank (www.bmrb.wisc.edu) with the following accession numbers: substrate-free β PGM *conformer A* (BMRB 28095), substrate-free β PGM *conformer B* (BMRB 28096) and β PGM_{P146A}:MgF₃:G6P TSA complex (BMRB 28097).

3.10 Figures

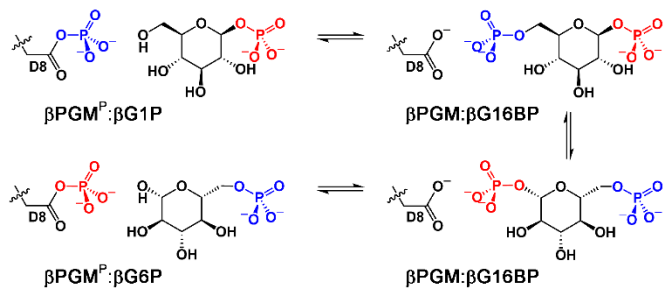


Figure 3.1. βPGM catalytic cycle. βPGM reaction scheme for the enzymatic conversion of βG1P to G6P via a βG16BP intermediate. The phosphoryl transfer reaction between phospho-enzyme ($\beta\text{PGM}^{\text{P}}$, phosphorylated at residue D8) and βG1P is illustrated with the transferring phosphate (blue) in the *proximal* site and the 1-phosphate (red) of βG1P in the *distal* site. The equivalent reaction between $\beta\text{PGM}^{\text{P}}$ and G6P is shown with the transferring phosphate (red) in the *proximal* site and the 6-phosphate (blue) of G6P in the *distal* site.

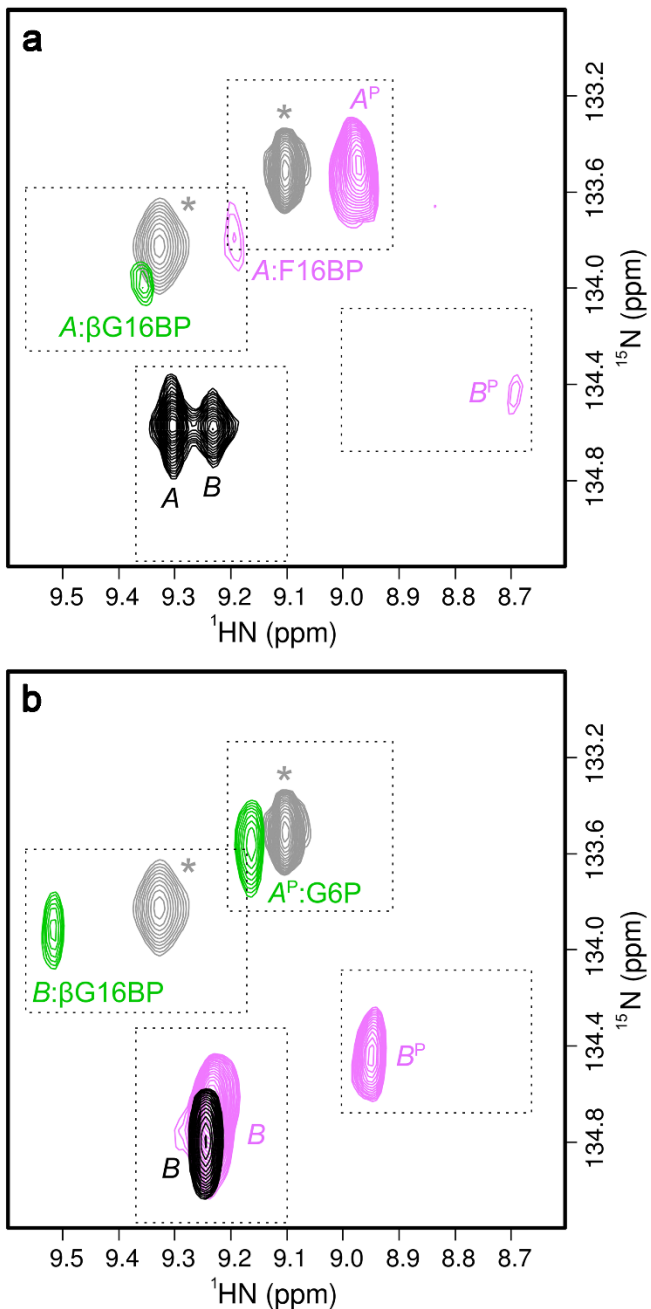


Figure 3.2. Effect of different phosphorylating agents on βPGM. **a, b,** Overlays of a section of ¹H¹⁵N-TROSY spectra highlighting the behaviour of residue A113. **(a)** βPGM_{WT} (black) populates *conformer A* and *conformer B* in slow exchange. βPGM_{WT} supplemented with F16BP (pink) populates phosphorylated *conformer A* (*A*^P) as the dominant species, phosphorylated *conformer B* (*B*^P) and a βPGM_{WT}:F16BP species (*A*:F16BP). βPGM_{WT} supplemented with βG16BP (green) populates an *A*:βG16BP complex. **(b)** βPGM_{P146A} (black) populates one conformer (*conformer B*). βPGM_{P146A} supplemented with F16BP (pink) populates *conformer B* and *B*^P. βPGM_{P146A} supplemented with βG16BP (green) populates a *A*^P:G6P complex and a *B*:βG16BP complex. (*) The βPGM_{WT}:BeF₃ complex (grey; δ_N = 133.5 ppm) (BMRB 17851³¹), an analogue of *A*^P, and the Mg²⁺-saturated βPGM_{D10N}:βG16BP complex (grey; δ_N = 133.8 ppm) (BMRB 27174³²), a mimic of the *A*:βG16BP complex, are shown for comparison.

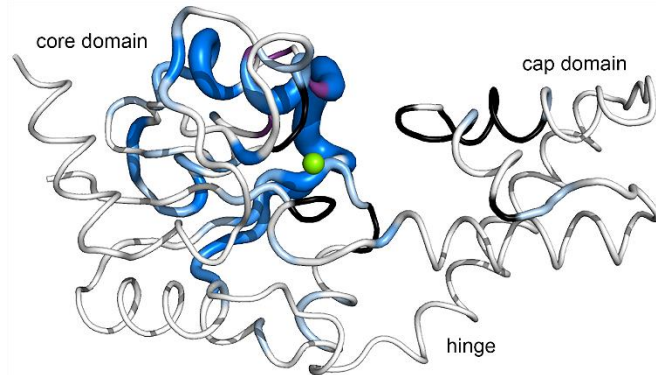


Figure 3.3. Exchange behaviour in β PGMwt. Crystal structure of β PGMwt (PDB 2WHE⁸²) showing residues of β PGMwt undergoing conformational exchange on different timescales. Residues which populate two conformations in slow exchange are coloured in shades of blue according to chemical shift differences between *conformer A* and *conformer B*, with the intensity of colour and thickness of the backbone corresponding to larger values. Residues in *conformer A* and *conformer B* with missing backbone amide peaks in the $^1\text{H}^{15}\text{N}$ -TROSY spectrum of β PGMwt are coloured black, whereas missing backbone amide peaks in *conformer B* only are coloured purple. The amide $^1\text{H}^{15}\text{N}$ coherences are likely broadened beyond detection due to intermediate exchange on the millisecond timescale. The catalytic Mg^{2+} ion is indicated as a green sphere.

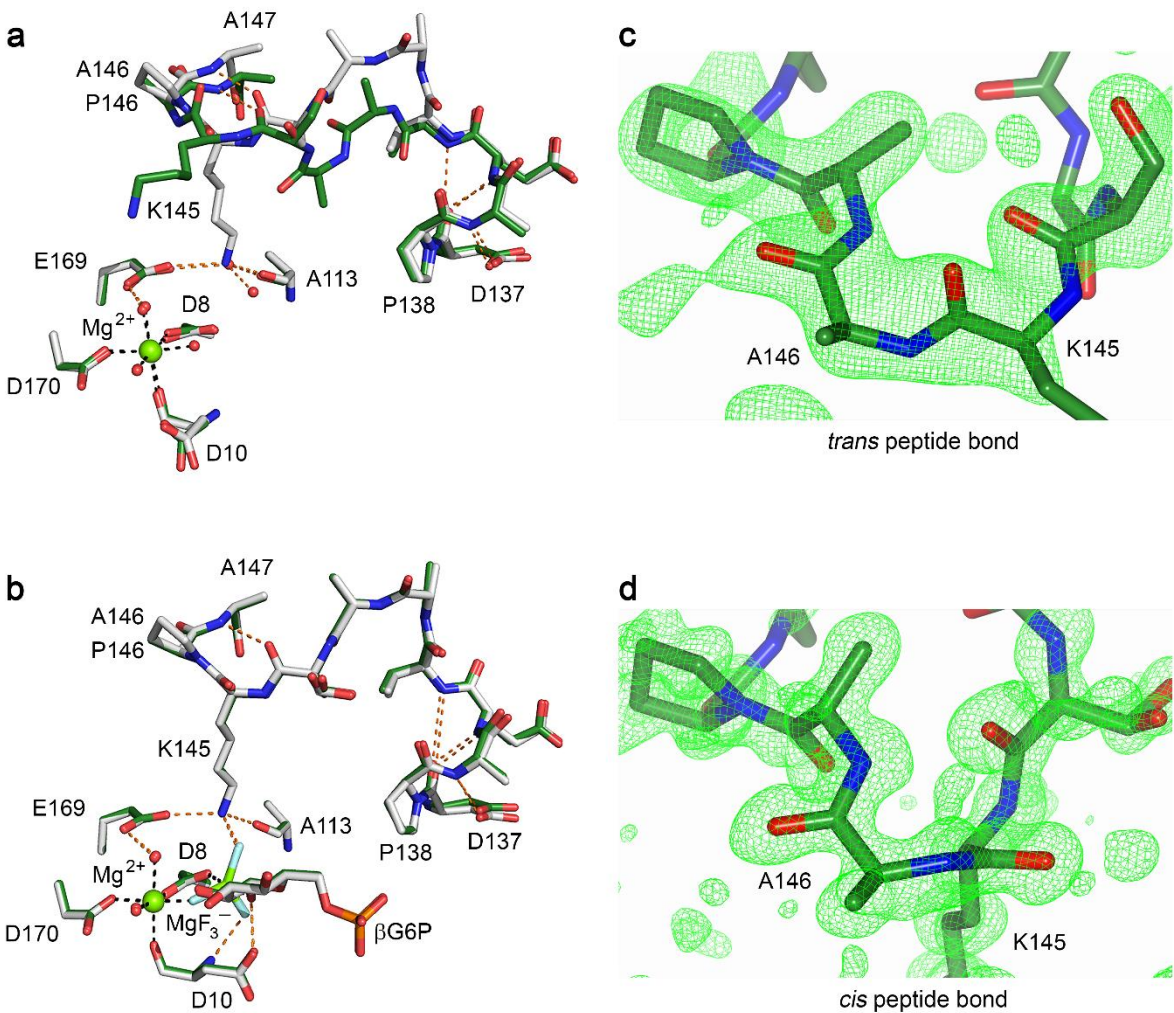


Figure 3.4. Conformational plasticity of the active site of β PGM. **a, b,** Active sites of β PGM_{WT} (as *conformer A*) and β PGM_{P146A} superposed on the core domain. **(a)** Selected residues are shown as sticks for the crystal structures of β PGM_{WT} (grey carbon atoms; PDB 6YDL) and β PGM_{P146A} (dark green carbon atoms; PDB 6YDK). In β PGM_{WT}, a *cis* K145-P146 peptide bond allows coordination of the K145 sidechain by E169 and A113, whereas in β PGM_{P146A} a *trans* K146-A146 peptide bond changes significantly the backbone conformation of the D137–A147 loop, which precludes active site engagement of the K145 sidechain. The catalytic Mg²⁺ ion is drawn as a green sphere, black dashes indicate metal ion coordination and orange dashes show probable hydrogen bonds. **(b)** Selected residues, the MgF₃⁻ moiety and G6P are shown as sticks for the crystal structures of the β PGM_{WT}:MgF₃:G6P TSA complex (grey carbon atoms; PDB 2WF5⁸²) and the β PGM_{P146A}:MgF₃:G6P TSA complex (dark green carbon atoms; PDB 6YDJ). β PGM_{WT} maintains the *cis* K145-P146 peptide bond, whereas β PGM_{P146A} changes the isomerisation state of the K145-A146 peptide bond from a *trans* conformation in the substrate-free enzyme to a *cis* conformation in the transition state. **c, d,** Omit map generated by refinement in the absence of residues S144–P148 in β PGM_{P146A}. **(c)** The S144–P148 segment, containing a *trans* K145–A146 peptide bond, with positive difference density (Fo – Fc; green mesh contoured at +2.5 σ) in substrate-free β PGM_{P146A}. **(d)** The S144–P148 segment, containing a *cis* K145–A146 peptide bond, with positive difference density (Fo – Fc; green mesh contoured at +2.5 σ) in the β PGM_{P146A}:MgF₃:G6P TSA complex.

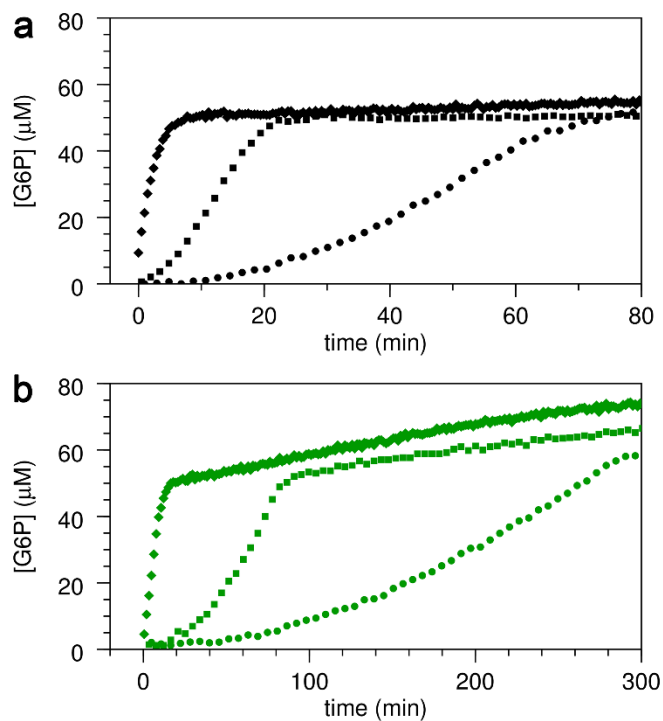


Figure 3.5. Kinetic profiles of β PGM activity. **a, b,** Reaction kinetics for the conversion of β G1P to G6P catalysed by β PGM_{WT} and β PGM_{P146A}. The rate of G6P production was measured indirectly using a glucose 6-phosphate dehydrogenase coupled assay, in which G6P is oxidised and concomitant NAD⁺ reduction is monitored by the increase in absorbance at 340 nm. Reaction catalysed by either (a) β PGM_{WT} or (b) β PGM_{P146A} in standard kinetic buffer using either F16BP (circles), AcP (squares) or β G16BP (diamonds) as a phosphorylating agent. For clarity, between 100% and 8% of the data points are included in the kinetic profiles. Following β G1P substrate depletion, the kinetic profiles show an apparent increase in G6P concentration, which results from: (1) the concentration of the reaction ingredients through evaporation from the assay plate wells and (2) for the reactions recorded using β G16BP, the enzyme-dependent conversion of remaining β G16BP to G6P via β PGM^P, occurring at a rate proportional to the amount of enzyme.

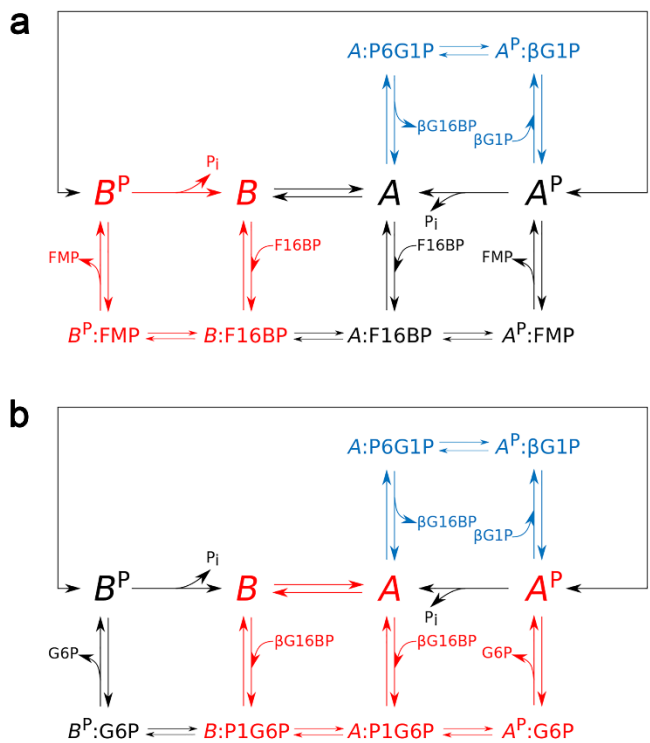


Figure 3.6. Kinetic model of β PGM activity. **a, b,** Reaction schemes for β PGM_{WT} with different phosphorylating agents. The favoured pathways are shown (red text) for β PGM_{WT} with (a) F16BP as a phosphorylating agent and (b) β G16BP as a phosphorylating agent. The β G16BP generating steps are highlighted in blue text. The double-headed arrows connecting A^P and B^P indicate that these species interconvert with a multi-second exchange rate, similar to that described for the interconversion of *conformer A* and *conformer B*.

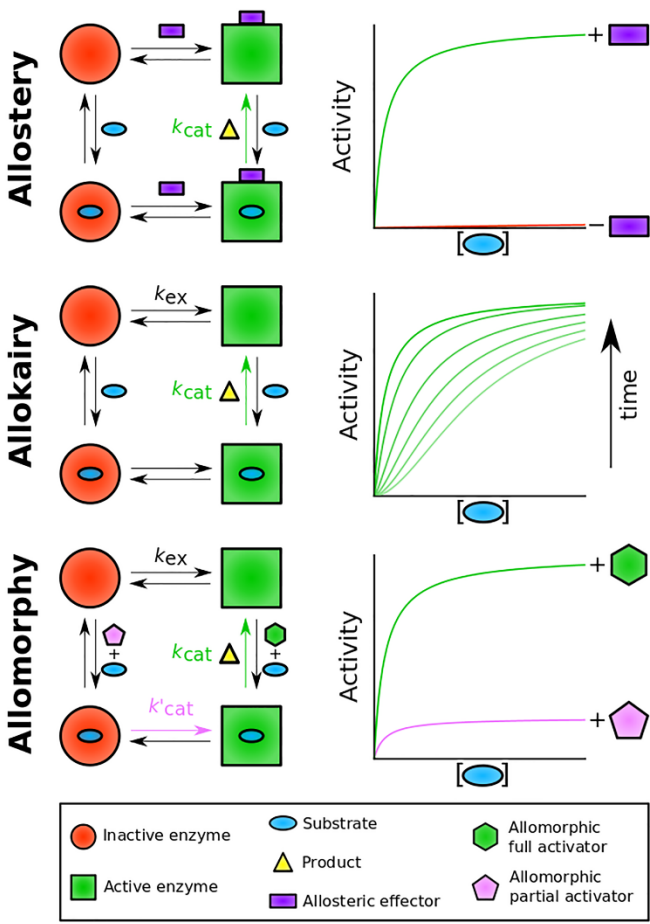


Figure 3.7. Mechanisms of regulation and activity profiles in monomeric enzymes. In allosteric, binding (or reaction) of an allosteric effector (purple rectangle) outside of the active site shifts the enzyme population from an inactive form (red circle and red profile) to an active form (green square and green profile), which stimulates the transformation of substrate (blue oval) to product (yellow triangle) at the catalytic rate (k_{cat} , green arrow). In allokairy, binding of substrate in the active site shifts the enzyme population from an inactive form to an active form, at an exchange rate (k_{ex}) that is similar to k_{cat} , resulting in time-dependent activity profiles (gradient of light green to dark green profiles). Following exhaustion of substrate, the enzyme population returns to the original equilibrium position. In allomorphy, reaction of the activating substrate, termed here allomorphic full activator (green hexagon), in the active site shifts the enzyme population from an inactive form to an active form, which stimulates the transformation of the native substrate (blue oval) to product (yellow triangle) at the maximal catalytic rate (k_{cat} , green arrow and green profile). However, reaction of alternatives substrates, termed here allomorphic partial activators (pink pentagon), in the active site are unable to shift the enzyme population from an inactive form to an active form, resulting in a slower overall catalytic rate (k'_{cat} , pink arrow and pink profile). The exchange rate (k_{ex}) between the two enzyme forms is much slower than k_{cat} . Following exhaustion of the allomorphic activator, the enzyme population returns to the original equilibrium position.

4. Enzymatic Production of β -glucose 1,6-bisphosphate through manipulation of catalytic magnesium coordination

Enzymatic production of β -glucose 1,6-bisphosphate through manipulation of catalytic magnesium coordination

Henry P. Wood,^a Nicola J. Baxter,^{a,b} F. Aaron Cruz-Navarrete,^a Clare R. Trevitt,^a Andrea M. Hounslow^a and Jonathan P. Waltho^{a,b,*}

^aKrebs Institute for Biomolecular Research, Department of Molecular Biology and Biotechnology, The University of Sheffield, Sheffield, S10 2TN, United Kingdom; ^bManchester Institute of Biotechnology and School of Chemistry, The University of Manchester, Manchester, M1 7DN, United Kingdom

* To whom correspondence may be addressed: Prof. Jonathan Waltho, Krebs Institute for Biomolecular Research, Department of Molecular Biology and Biotechnology, The University of Sheffield, Sheffield, S10 2TN, +44 114 22717, j.waltho@sheffield.ac.uk, ORCID 0000-0002-7402-5492

Keywords: glucose bisphosphate | enzymatic production | NMR spectroscopy

4.1 Abstract

Manipulation of enzyme behaviour represents a sustainable technology that can be harnessed to enhance the production of valuable metabolites and chemical precursors. β -glucose 1,6-bisphosphate (β G16BP) is a native reaction intermediate in the catalytic cycle of β -phosphoglucomutase (β PGM) that has been proposed as a treatment for human congenital disorder of glycosylation involving phosphomannomutase 2. Strategies to date for the synthesis of β G16BP suffer from low yields or use chemicals and procedures with significant environmental impacts. Herein, we report the efficient enzymatic synthesis of anomer-specific β G16BP using the D170N variant of β PGM (β PGM_{D170N}), where the aspartate to asparagine substitution at residue 170 perturbs the coordination of a catalytic magnesium ion. Through combined use of NMR spectroscopy and kinetic assays, it is shown that the weakened affinity and reactivity of β PGM_{D170N} towards β G16BP contributes to the pronounced retardation of Step 2 in the two-step catalytic cycle, which causes a marked accumulation of β G16BP, especially at elevated MgCl₂ concentrations. Purification, employing a simple environmentally considerate precipitation procedure requiring only a standard biochemical toolset, results in a β G16BP product with high purity and yield. Overall, this synthesis strategy illustrates how manipulation of the catalytic magnesium coordination of an enzyme can be utilised to generate large quantities of a valuable metabolite.

4.2 Main

Enzyme engineering represents an emerging technology with the potential to deliver solutions to many sustainable development problems.^{168,169} Biofuel production, plastic degradation and the clean generation of industrial reagents and precursors are three examples of areas where enzymes already make a significant contribution.^{170–173} Research that aims to foster a deeper understanding of enzyme catalysis is therefore of great interest. Phosphoryl transfer enzymes are at the forefront of research models for investigating the origins of enzyme catalysis because they exhibit some of the largest enzymatic rate enhancements known.^{51,54} In addition, phosphate esters are often covalently incorporated into pharmaceutical products to improve bioavailability.^{174,175} β -phosphoglucomutase (β PGM; EC 5.4.2.6) has emerged as an archetypal enzyme in the study of phosphoryl transfer, and substantial progress has been made in understanding its mechanism of catalysis.^{31,82–84,135,176} This magnesium-dependent enzyme from *Lactococcus lactis* (subspecies *lactis* IL1403) catalyses the isomerisation between β -glucose 1-phosphate (β G1P) and glucose 6-phosphate (G6P) via a β -glucose 1,6-phosphate (β G16BP) intermediate, which is released to solution before rebinding in the alternate orientation (Fig. 4.1).^{80,135} The β G1P substrate of β PGM is commercially unavailable, but appropriate quantities for research have been produced enzymatically from maltose using a simple method involving maltose phosphorylase.³² To initiate the catalytic cycle, β PGM requires priming with a phosphorylating agent to generate the active phospho-enzyme (β PGM^P, phosphorylated on residue D8) and β G16BP can perform this role *in vivo*. Since β G16BP is also commercially unavailable, alternative phosphorylating agents such as acetyl phosphate (AcP), fructose 1,6-bisphosphate (F16BP) and α -glucose 1,6-bisphosphate (α G16BP) have been used to generate β PGM^P *in vitro*, but these compounds are less effective and produce complicated kinetic behaviour.^{79,84}

β G16BP has also been identified as a potential pharmacological chaperone for the management of a human congenital disorder of glycosylation involving phosphomannomutase 2.²⁰⁹ Acting as a weakly binding competitive inhibitor, β G16BP is able to rescue the compromised activity of pathological variants of phosphomannomutase 2 by stabilising the protein fold. Therefore, further investigations of phosphomannomutase 2 and of β PGM are reliant on the availability of substantial quantities of β G16BP. Three strategies have been reported previously for the

synthesis of β G16BP; however, each of these methods either delivers low yields or uses chemicals and procedures with significant environmental impacts. Firstly, the chemical synthesis of β G16BP from α -glucose involves an eight-step protocol, requiring considerable time and technical expertise, together with the use of harmful and environmentally hazardous reagents.⁸⁴ Low yields are obtained, since the β -anomer must be selected carefully on the basis of solubility from a racemic mixture of glucosaccharide products. Secondly, an enzymatic production method utilises a non-native reaction of phosphofructokinase to generate β G16BP from β G1P using adenosine triphosphate as the phosphoryl donor.^{80,209} Purification of the product, though, cannot be achieved simply using precipitation procedures, since contaminating adenosine diphosphate co-precipitates with β G16BP,¹⁷⁷ and therefore ion-exchange HPLC purification is required. The use of HPLC columns is inherently damaging to the environment owing to the use of triethylammonium bicarbonate as a volatile buffer mobile phase, which during its production results in the release of large quantities of carbon dioxide.¹⁷⁸ Thirdly, an extraction method involves the removal of β G16BP from a variant of β PGM that co-purifies with a stoichiometric quantity of the molecule.³² This method suffers from low yields, since it relies on very high recombinant β PGM production levels, and requires a week-long protein growth and purification procedure for each new batch of β G16BP. The limited availability of β G16BP therefore represents a significant barrier to the structural, kinetic and therapeutic investigations of phosphomutase enzymes. Herein, we describe a room-temperature, enzymatic method using the D170N variant of β PGM (β PGM_{D170N}) for the production of 100% anomer-specific β G16BP, which requires only micromolar quantities of enzyme and a simple environmentally considerate purification procedure that can be performed easily by a non-chemist over the course of two days. Through combined use of NMR spectroscopy and kinetic assays, it is shown that the weakened affinity and reactivity of β PGM_{D170N} towards β G16BP contributes to the pronounced retardation of Step 2 in the two-step catalytic cycle, which causes a marked accumulation of β G16BP, especially at elevated MgCl₂ concentrations. More generally, this enzymatic synthesis strategy illustrates how manipulation of catalytic magnesium coordination can be utilised to generate large quantities of a valuable metabolite.

β PGM has two phosphoryl transfer steps in its catalytic cycle: Step 1 comprises phosphoryl transfer from β PGM^P to the β G1P substrate forming the β G16BP reaction intermediate,

whereas Step 2 involves phosphoryl transfer from β G16BP to β PGM forming the G6P product and regeneration of β PGM^P (Fig. 4.1). When wild-type β PGM (β PGM_{WT}) is incubated in the presence of Mg²⁺ ions, with 20 mM AcP as the phosphorylating agent and 10 mM β G1P as a substrate, β G16BP generated in the catalytic cycle does not accumulate to detectable levels when monitored using ³¹P NMR experiments.³² Instead, β G16BP rebinds the enzyme with micromolar affinity in the alternate orientation, for the Step 2 reaction. Thus, the tight binding and high reactivity of β G16BP maintains a low steady state concentration, which precludes the harvesting of this species in useful quantities. The crystal structures of substrate-free β PGM_{WT} (PDB: 6YDL¹⁷⁹) and of the β PGM_{WT}^P analogue complex (β PGM_{WT}:BeF₃ complex, PDB: 2WFA³¹) indicate that the catalytic magnesium ion (Mg_{cat}) is coordinated through three enzyme atoms in the former and four phospho-enzyme atoms in the latter (Fig. 4.2). Therefore, the differential coordination and affinity of Mg_{cat} provides an appropriate target with which to manipulate β PGM to shift the balance in the rate constants of Step 1 and Step 2 so that β G16BP will accumulate to a greater extent. Two potential strategies emerged where Step 2 could be retarded with respect to Step 1, which involved either performing the reactions of the catalytic cycle under Mg²⁺-free conditions or perturbing Mg_{cat} coordination through point mutation to alter its binding properties. In either scenario, it was hypothesised that β PGM with a compromised Mg_{cat} site could be phosphorylated efficiently by reactive phosphorylating agents such as AcP, thereby generating β PGM^P and subsequent reaction with β G1P to produce β G16BP in Step 1 (Fig. 4.1). In contrast, phosphorylation of β PGM by β G16BP in Step 2 is less likely under these circumstances, which would lead to an accumulation of the reaction intermediate that could be harvested.

To explore whether AcP is able to phosphorylate Mg_{cat}-free β PGM_{WT}, ³¹P NMR experiments were acquired to measure the change in AcP concentration over time in the presence and absence of 300 μ M β PGM_{WT}. The addition of β PGM_{WT} resulted in a 25% increase in the rate of AcP hydrolysis (Fig. 4.3A), implying that β PGM_{WT}^P is generated in the absence of Mg_{cat}. Consequently, the Step 1 reaction between Mg_{cat}-free β PGM_{WT} and 10 mM β G1P in the presence of 50 mM AcP, together with the Step 2 production of G6P, was monitored using ³¹P NMR time-course experiments. However, there was no detectable accumulation of β G16BP (Fig. 4.4A–C) and the appearance of G6P product proceeded with a rate constant of 6.7×10^{-3} s⁻¹, which is 4 orders of magnitude smaller than the rate constant observed in the presence of 5

mM MgCl₂.³² Hence, the observed enzymatic activity appears to arise simply due to the presence of very low levels of residual Mg²⁺ ions associated with the reagents. Taken together, these results indicate that both Mg_{cat}-bound βPGM_{WT}^P and Mg_{cat}-free βPGM_{WT}^P can be generated by AcP, but both the Step 1 and Step 2 phosphoryl transfer reactions are seriously impaired by the absence of Mg_{cat}.

Given the low rate of βG16BP production in the absence of Mg²⁺ ions in the reaction buffer, a more subtle modification of the enzyme Mg_{cat} site was engineered. In βPGM_{WT}, Mg_{cat} is coordinated octahedrally by a carboxylate oxygen atom of residue D8, a carboxylate oxygen atom of residue D170 and the carbonyl oxygen atom of residue D10, together with three water molecules. In βPGM_{WT}^P, one of the water molecules (water 3) is displaced by a phosphate oxygen atom of the D8 aspartyl phosphate moiety, creating bidentate coordination of Mg_{cat} in a six-membered ring of atoms (Fig. 4.2). Point mutations involving residue D8 have been reported to result in the complete loss of measurable catalytic activity.⁷⁹ Therefore, perturbation of Mg_{cat} was achieved through the generation of the D170N variant (βPGM_{D170N}), where the carboxamide group of residue N170 retains an oxygen atom with which to coordinate Mg_{cat}, but the sidechain is not charged. Accordingly, the reaction of βPGM_{D170N} with 10 mM βG1P and 20 mM AcP in the presence of 100 mM MgCl₂ was monitored using ³¹P NMR time-course experiments and, in contrast to βPGM_{WT}, the βG16BP intermediate was observed to accumulate to a level comparable with the initial βG1P concentration (Fig. 4.4D–E). The G6P product was only generated to a measurable extent once the AcP concentration had reduced significantly (Fig. 4.4F). Hence, perturbation of Mg_{cat} in βPGM_{D170N} (in the presence of excess AcP) results in a substantial retardation of phosphorylation of βPGM_{D170N} by βG16BP (Step 2) with respect to phosphorylation of βG1P by βPGM_{D170N}^P (Step 1), therefore allowing βG16BP to accumulate.

To investigate the source of the retardation of Step 2, glucose 6-phosphate dehydrogenase (G6PDH; EC 1.1.1.49) coupled assay experiments were conducted to assess the ability of βPGM_{D170N} to bind and convert the substrates of Step 2 (βG16BP) and Step 1 (βG1P). Initial rate measurements were recorded at increasing concentrations of βG16BP, which revealed that βPGM_{D170N} had an apparent K_m (βG16BP) = 150 ± 13 μM (Fig. S4.1A). This value is 18-fold weaker than that measured for βPGM_{WT} (K_m (βG16BP) = 8.5 ± 0.3 μM¹⁷⁹). Analogous experiments at increasing concentrations of βG1P indicated that βPGM_{D170N} had an apparent

K_m (β G1P) = 6.9 ± 1.0 μM , which is similar in magnitude to the K_m (β G1P) for β PGM_{WT} (K_m (β G1P) = 14.7 ± 0.5 μM ⁸⁴). These experiments also demonstrated that a similar level of β G1P inhibition was operating in β PGM_{D170N} (apparent K_i (β G1P) = 1540 ± 170 μM) and β PGM_{WT} (K_i (β G1P) = 1510 ± 100 μM ¹⁷⁹) (Fig. S4.1B). The K_m (Mg^{2+}) value for the overall reaction of β G1P to G6P was also measured for β PGM_{D170N} using increasing concentrations of MgCl₂ (Fig. S4.2). These experiments resulted in an apparent K_m (Mg^{2+}) = 690 ± 110 μM , which is only 4-fold weaker than that determined for β PGM_{WT} using the same method (apparent K_m (Mg^{2+}) = 180 ± 40 μM). Overall, at 1 mM β G1P, 100 μM β G16BP and 5 mM MgCl₂ the observed rate constant for the overall reaction of β G1P to G6P catalysed by β PGM_{D170N} ($k_{\text{obs}} = 3.0 \times 10^{-3}$ s^{-1}) is 79,000-fold smaller than that for β PGM_{WT} ($k_{\text{obs}} = 237$ s^{-1}).

The observable accumulation of β G16BP in the ³¹P NMR spectra of the β PGM_{D170N}-catalysed reaction (Fig. 4.4D–F) presented an opportunity to measure the effects of Mg^{2+} ion concentration on Step 1 and Step 2 independently within the same experiment (Fig. 4.1), although it should be noted that kinetic parameters obtained using ³¹P NMR methods and the G6PDH coupled assay differ significantly due to the effects of the different conditions employed.^{32,179} ³¹P NMR time-course experiments were therefore conducted at increasing concentrations of MgCl₂ to measure simultaneously the initial rates of β G16BP production in Step 1 and G6P production in Step 2 (Fig. 4.3B–C). The initial rates of β G16BP production increased linearly with MgCl₂ concentration and so could not be fitted to a Michaelis-Menten equation over the concentration range 5 – 100 mM (Fig. 4.3B), indicating that the affinity of β PGM_{D170N} for Mg_{cat} in Step 1 is low. Extraction of the initial rates of G6P production in Step 2 resulted in an apparent K_m (Mg^{2+}) = 27 ± 4 mM (Fig. 4.3C). These observations therefore reveal that β G16BP accumulation can be greatly enhanced by using elevated concentrations of Mg^{2+} ions. For β PGM_{D170N} at 5 mM MgCl₂, the initial rate of Step 1 ($k_{\text{obs}} = 9.0 \times 10^{-3}$ s^{-1}) is only 3-fold faster than that of Step 2 ($k_{\text{obs}} = 3.0 \times 10^{-3}$ s^{-1}), while at 100 mM MgCl₂ Step 1 ($k_{\text{obs}} = 0.24$ s^{-1}) exceeds Step 2 ($k_{\text{obs}} = 1.2 \times 10^{-2}$ s^{-1}) by a factor of 20 (Fig. 4.3B–C, Fig. 4.4G–H). A control experiment employing elevated NaCl concentrations demonstrated that the increased initial rate of Step 1 at higher concentrations of MgCl₂ is not caused by Cl[−] ions alone (Fig. 4.4I). Therefore, the Mg^{2+} ion concentration at which the production of β G16BP is performed has a strong bearing on its yield.

Taken together, this analysis demonstrates that the D170N point mutation causes a pronounced retardation of Step 2 together with a more modest change to Step 1. The reduced apparent K_m value of $\beta\text{PGM}_{\text{D}170\text{N}}$ for $\beta\text{G}16\text{BP}$ is in line with this behaviour. However, the substantially different apparent K_m (Mg^{2+}) values determined for Step 1 and Step 2 is not, and was surprising given the perturbation of the Mg_{cat} binding site in $\beta\text{PGM}_{\text{D}170\text{N}}$. One plausible explanation for these observations is that a Cl^- ion binds in the active site in substrate-free $\beta\text{PGM}_{\text{D}170\text{N}}$ to mitigate the loss of the negative charge resulting from the D170N point mutation. The presence of a Cl^- ion at the Mg_{cat} binding site would rescue the binding of Mg_{cat} but hamper the binding of $\beta\text{G}16\text{BP}$ and the approach of its phosphodianion to the nucleophilic D8 in Step 2. In contrast, AcP is able to generate $\beta\text{PGM}_{\text{D}170\text{N}}^{\text{P}}$ in a Mg_{cat} -independent manner (Fig. 4.1 and Fig. 4.3A) and the presence of the D8 aspartyl phosphate moiety will obviate the formation of the $\text{Mg}_{\text{cat}}-\text{Cl}$ moiety.

To obtain evidence for a putative Mg_{cat} -halide moiety binding to substrate-free $\beta\text{PGM}_{\text{D}170\text{N}}$, 10 mM NaF was added to substrate-free $\beta\text{PGM}_{\text{D}170\text{N}}$ containing 5 mM MgCl_2 and ^{19}F NMR experiments were recorded (Fig. 4.4J–K). A $\beta\text{PGM}_{\text{D}170\text{N}}$ -bound ^{19}F species was observed with a chemical shift of -171 ppm, which corresponds to an analogous peak seen for substrate-free $\beta\text{PGM}_{\text{WT}}$ acquired under similar conditions.⁷⁷ Elevation to 100 mM MgCl_2 did not result in increased saturation of Mg_{cat} , but instead reduced the ^{19}F peak integral to 80% of its size at 5 mM MgCl_2 , suggesting that at higher concentrations, Cl^- ions are displacing the F^- ion bound at the Mg_{cat} site (Fig. 4.4J–K). In the experiment containing 100 mM MgCl_2 , three free ^{19}F species are present in solution that are separated by chemical shift differences of exactly 37 ppm. Free F^- (-118 ppm) and free MgF^+ (-155 ppm) have been assigned previously,⁷⁷ whereas the peak resonating at -192 ppm is likely to be a free $\text{Mg}-\text{F}-\text{Mg}^{3+}$ species, based on the partitioning behaviour between discrete species as the MgCl_2 concentration is increased. Comparison of the chemical shifts of the $\beta\text{PGM}_{\text{D}170\text{N}}$ -bound ^{19}F species with those of the three free species suggests that it is closer in identity to MgF^+ . Therefore, the primary candidate for such an enzyme-bound species is a $\text{Mg}_{\text{cat}}-\text{F}$ moiety, which in turn provides supporting evidence for the binding of a $\text{Mg}_{\text{cat}}-\text{Cl}$ moiety to substrate-free $\beta\text{PGM}_{\text{D}170\text{N}}$ that would consequently play a role in the retardation of Step 2 relative to Step 1.

The large-scale generation of $\beta\text{G}16\text{BP}$ by the $\beta\text{PGM}_{\text{D}170\text{N}}$ -catalysed reaction at high concentrations of MgCl_2 thus presented an opportunity for harvesting significant quantities of

this valuable compound and so a robust production protocol was devised. Recombinant $\beta\text{PGM}_{\text{D}170\text{N}}$ is overexpressed in high yields from *Escherichia coli* BL21(DE3) cells (>100 mg/L) using routine culture techniques and is readily purified using a two-step protocol involving ion-exchange chromatography followed by a size-exclusion chromatography step. $\beta\text{PGM}_{\text{D}170\text{N}}$ can be stored at -20 °C for long periods and responds well to multiple freeze-thaw cycles, meaning that once purified, a batch of enzyme can be used for numerous βG16BP preparations. In order to characterise $\beta\text{PGM}_{\text{D}170\text{N}}$ further, $^1\text{H}^{15}\text{N}$ -TROSY NMR spectra were recorded using samples of ^{15}N - $\beta\text{PGM}_{\text{D}170\text{N}}$ and ^{15}N - $\beta\text{PGM}_{\text{WT}}$. Comparison of the spectra revealed that $\beta\text{PGM}_{\text{D}170\text{N}}$ has a similar solution behaviour and overall protein fold to $\beta\text{PGM}_{\text{WT}}$ (Fig. S4.3). The slow-exchange behaviour that arises in $\beta\text{PGM}_{\text{WT}}$ from *cis-trans* proline isomerisation at the K145-P146 peptide bond is also observable in $\beta\text{PGM}_{\text{D}170\text{N}}$.¹⁷⁹ Notably, around 15 peaks are present for $\beta\text{PGM}_{\text{D}170\text{N}}$ that are absent in the spectrum of $\beta\text{PGM}_{\text{WT}}$. These additional peaks indicate that a backbone conformational exchange process, occurring on the millisecond timescale in $\beta\text{PGM}_{\text{WT}}$, has been abolished in $\beta\text{PGM}_{\text{D}170\text{N}}$.¹⁷⁹

To assess the stability of $\beta\text{PGM}_{\text{D}170\text{N}}$ and to check for time-dependent reversion to $\beta\text{PGM}_{\text{WT}}$ by deamidation,¹⁸⁰ a sample of $\beta\text{PGM}_{\text{D}170\text{N}}$ was incubated at 25 °C for 48 h and both $^1\text{H}^{15}\text{N}$ -TROSY NMR spectra and ^{31}P NMR time-course experiments were acquired every 24 h. A comparison of $^1\text{H}^{15}\text{N}$ -TROSY spectra recorded for $\beta\text{PGM}_{\text{D}170\text{N}}$ preincubated at 25 °C for 0 h and 48 h shows a near-identical correspondence of peaks indicating that the incubation process has a negligible effect on the integrity of $\beta\text{PGM}_{\text{D}170\text{N}}$ (Fig. S4.4A). In comparisons of $\beta\text{PGM}_{\text{D}170\text{N}}$ and $\beta\text{PGM}_{\text{WT}}$ $^1\text{H}^{15}\text{N}$ -TROSY spectra, the absence of observable $\beta\text{PGM}_{\text{WT}}$ peaks in the $\beta\text{PGM}_{\text{D}170\text{N}}$ spectra indicates that reversion of $\beta\text{PGM}_{\text{D}170\text{N}}$ to $\beta\text{PGM}_{\text{WT}}$ through deamidation is not a process that occurs readily under these sample conditions (Fig. S4.4B–C). Analysis of the ^{31}P NMR time-course experiments for the equilibration of 10 mM βG1P with G6P catalysed by $\beta\text{PGM}_{\text{D}170\text{N}}$ (preincubated at 25 °C for 0 h, 24 h and 48 h) demonstrates a consistent behaviour of immediate βG16BP production followed by conversion to G6P as product with no change in k_{obs} , further confirming the stability of $\beta\text{PGM}_{\text{D}170\text{N}}$ (Fig. S4.5A).

To mimic the effect of $\beta\text{PGM}_{\text{D}170\text{N}}$ reversion to $\beta\text{PGM}_{\text{WT}}$ through deamidation, a control ^{31}P NMR time-course experiment was also conducted using a sample of $\beta\text{PGM}_{\text{D}170\text{N}}$ that had been spiked with 0.1 % $\beta\text{PGM}_{\text{WT}}$ (Fig. S4.5B). The kinetic profile shows an initial burst of G6P

production by β PGM_{WT} together with a decrease in the ratio of the β G16BP concentration at its maximum (β G16BP_{max}) to the concentration of G6P at its maximum (G6P_{max}). The ³¹P NMR time-course experiments testing β PGM_{D170N} stability revealed no burst of G6P production nor any change in either k_{obs} or the β G16BP_{max}:G6P_{max} ratio. Together, these results indicate that β PGM_{D170N} does not undergo detectable deamidation to β PGM_{WT} and is stable at 25 °C over a 48-hour time frame.

³¹P NMR time-course experiments were used to monitor the β PGM_{D170N}-catalysed conversion of β G1P to G6P to determine the optimal point at which to harvest β G16BP. In a representative reaction (see Materials and Methods) the β G16BP concentration reached a maximum after 265 min at 25 °C. Following quenching of the reaction at this point, and removal of β PGM_{D170N}, the solution was found to contain β G16BP alongside contaminants that included significant amounts of β G1P, G6P and inorganic phosphate (P_i), in a ratio of 1 : 0.07 : 0.2 : 3.9, respectively. As substrates of β PGM, these phosphorylated impurities are undesirable, therefore the solution was subjected to a barium salt precipitation and ion-exchange protocol to obtain the sodium salt of β G16BP with high purity. Barium salts of phosphate species are relatively insoluble,¹⁸¹ and the difference in relative solubility of the β G16BP barium salt compared with those of β G1P and G6P was exploited to enable purification.^{182–184}

To confirm the identity and assess the purity of the final β G16BP product, a sample of the fine powder was analysed using ¹H, ¹³C and ³¹P NMR experiments (Fig. 4.5A–D). The identity of the resulting compound was established to be β G16BP by comparison of ¹H and ¹³C chemical shifts with previously reported values.⁸⁴ Glucose and maltose contaminants were identified in the sample using ¹H chemical shifts and scalar coupling constants (BMRB: bmse000015, BMRB: bmse000017). Based on integral values of the anomeric proton signals and of the phosphorus signals in quantitative ¹H and ³¹P NMR spectra, the β G16BP concentration was determined to be 67 mM, which represented 98% of the total phosphorylated glucosaccharide components and 72% of the total glucosaccharide components present in the final sample. β G1P, G6P and glucose comprised <1%, 1% and 3%, respectively, of the total glucosaccharide content. Maltose was present at a greater concentration in the sample (24%), but as a bystander in the reactions of β PGM, and not known to bind to phosphomannomutase 2, this contamination is unlikely to be problematic for users. P_i was also present at a concentration

2.9-fold higher than that of β G16BP. The glucose, maltose and P_i components, which were carried through into the final β G16BP product are contaminants derived from the enzymatic synthesis of β G1P and would otherwise not be present if a purer source of β G1P were used. Residual HEPES buffer and acetate were also present as minor contaminants. The final yield for the β PGM_{D170N}-catalysed conversion of β G1P to β G16BP was 33.6% and the yield for the overall conversion of maltose to β G16BP was 7.7%. Since the equilibrium for the enzymatic conversion of maltose to β G1P lies in favour of maltose, conducting the reactions for the maltose phosphorylase synthesis of β G1P and the β PGM_{D170N} synthesis of β G16BP in a one-pot system is likely to lead to higher β G16BP yields. The removal of β G1P by β PGM_{D170N} would drive the maltose reaction to produce more β G1P, which in turn would result in a greater overall yield of β G16BP. This approach has been demonstrated previously for the protocol involving maltose phosphorylase and phosphofructokinase.⁸⁰ To demonstrate the biochemical effectiveness of the final β G16BP product at activating β PGM_{WT}, a kinetic experiment was conducted using the G6PDH coupled assay. β PGM_{WT} was mixed with the β G1P substrate and activated using either 1 μ M β G16BP or 8 mM AcP as the phosphorylating agent. The kinetic profile obtained was linear for the β G16BP-containing reaction, but exhibited a lag phase when AcP was used (Fig. 4.3D). As β G16BP is the only phosphorylating agent known to induce linear initial kinetics in β PGM,¹⁷⁹ this experiment provided a clear demonstration of the activity of the final β G16BP product.

4.3 Conclusions

The successful manipulation of β PGM behaviour to facilitate β G16BP production is a demonstration of how detailed structural and mechanistic knowledge of an enzyme can lead to novel engineering strategies. Specifically, the modification of the metal binding site of the enzyme dramatically increases the steady state concentration of its reactive metabolite. This highlights the transformative potential that enzymes have within chemical industries and vindicates the intensive study of these useful biomolecules.

4.4 Conflicts of interest

There are no conflicts to declare.

4.5 Acknowledgements

We would like to thank Prof. Nicholas Williams for useful insight into β G16BP purification. This research was supported by the Biotechnology and Biological Sciences Research Council (BBSRC; H.P.W. – Grant Number X/009906-20-26, N.J.B. – Grant Number BB/M021637/1 and BB/S007965/1, C.R.T – Grant Number BB/P007066/1) and Consejo Nacional de Ciencia y Tecnología, Mexico (CONACYT; F.A.C.N. – Grant Number 472448).

4.6 Materials and Methods

4.6.1 Reagents:

Unless stated otherwise, reagents were purchased from Sigma-Aldrich, Fischer Scientific, Alfa Aesar and VWR. Isotopically enriched $^{15}\text{NH}_4\text{Cl}$ was purchased from CortecNet.

4.6.2 Gene sequence for $\beta\text{PGM}_{\text{D170N}}$:

```
1-CATATGTTAAAGCAGTATTGTTGATTTAGATGGTGTATTACAGATAACCGCAGAGTATCATTAGAGCTTGG-75
76-AAAGCTTGGCTGAAGAAATTGGCATTAATGGTGTGACCGCCAATTAAATGAGCAATTAAAGGGTCTCACGA-150
151-GAAGACTCGCTTCAGAAAATTCTAGATTTAGCTGATAAAAAAGTATCAGCTGAGGAATTAAAGAACTTGCTAAG-225
226-AGAAAAAAATGATAACTATGTGAAATGATTCACTGGATGTGTCGCCAGCCGATGTCATCCTGGAATTACAATTA-300
301-CTCAAAGATTACGTTCAAATAAAATCAAATTGCTTAGCGTCGGCTTCTAAGAATGGCCATTATTAGAG-375
376-AGAATGAATTAACTGGATATTTGATGCAATTGCTGATCCGGCTGAAGTTGCAGCATAAAACCAGCACCAGAT-450
451-ATTTTATTGCAGCAGCACATGCAGTGGGTGTTGCCCTCTGAATCAATTGGTTAGAGAATTCTCAAGCTGGA-525
526-ATTCAAGCCATCAAAGATTCAAGGGCTTACCAATTGGTAGGGCGCCAGAAGATTGGGAGATGATATGTC-600
601-ATTGTGCCTGATACTTCACACTATACATTAGAATTGGAAAGTTGGCTCAAAAGCAAAATAACTCGAG-675
```

4.6.3 βPGM expression and purification:

The $\beta\text{PGM}_{\text{D170N}}$ gene sequence was created by modifying the *pgmB* gene (encoding the $\beta\text{PGM}_{\text{WT}}$ enzyme) from *Lactococcus lactis* (subspecies *lactis* IL1403) (NCBI: 1114041). The $\beta\text{PGM}_{\text{D170N}}$ gene was generated and cloned by GenScript into a pET22b(+) vector. The $\beta\text{PGM}_{\text{WT}}$ and $\beta\text{PGM}_{\text{D170N}}$ plasmids were transformed into *Escherichia coli* BL21(DE3) cells and grown using ^{15}N isotopically enriched M9 minimal media.¹⁵⁴ Cells were grown to an OD₆₀₀ of 0.6 at 37 °C and overexpression was induced with 0.5 mM (final concentration) isopropyl β-D-1-thiogalactopyranoside (IPTG) before a 16-hour incubation at 25 °C and centrifugation (Sigma Model 3-15; 9,000 rpm for 10 min) to harvest the cells. The $\beta\text{PGM}_{\text{WT}}$ and $\beta\text{PGM}_{\text{D170N}}$ proteins were purified using the following protocol. The cell pellet was resuspended in ice-cold standard buffer (50 mM K⁺ HEPES buffer (pH 7.2), 5 mM MgCl₂, 2 mM NaN₃, 1 mM EDTA) containing a cOmplete protease inhibitor cocktail. The cell suspension was sonicated on ice for 6 × 20 s pulses separated by 60 s intervals. The cell lysate was separated from the insoluble cell debris using centrifugation (Beckman Coulter Avanti centrifuge, Rotor: JA-25-50) at 20,000 rpm for 30 min at 4 °C. The soluble fraction was loaded onto a DEAE-Sepharose anion-

exchange column connected to an ÄKTA Prime purification system, which had been washed previously with 1 M NaOH and 6 M guanidinium chloride and equilibrated with 5 column volumes of standard buffer. Bound proteins were eluted using a gradient of 0 to 50% standard buffer supplemented with 1 M NaCl over 300 mL. Fractions containing β PGM were identified using SDS-PAGE and were concentrated to a 5–10 mL volume using centrifugation in a Vivaspin (10 kDa molecular weight cut off; Sartorius) at 4,500 rpm and 4 °C (Thermo Scientific Heraeus Labofuge 400 R). The concentrated protein sample was loaded onto a pre-packed Hiload 26/600 Superdex 75 size-exclusion column connected to an ÄKTA Prime purification system, which had been washed previously with degassed 1 M NaOH and equilibrated with 3 column volumes of degassed standard buffer supplemented with 1 M NaCl. Following elution, the fractions containing β PGM were checked for purity and were pooled and buffer-exchanged into standard buffer for β PGM_{WT} and standard buffer containing 50 mM MgCl₂ for β PGM_{D170N}. Mg_{cat}-free β PGM_{WT} and Mg_{cat}-free β PGM_{D170N} were prepared by buffer-exchanging into standard buffer without MgCl₂. The final protein samples were concentrated using a Vivaspin (10 kDa molecular weight cut off; Sartorius) to a 1 mM concentration, as measured by Nanodrop One^C (Thermo Scientific) (β PGM molecular weight = 24.2 kDa, ϵ_{280} = 19,940 M⁻¹ cm⁻¹), and were stored at –20 °C.

4.6.4 NMR Spectroscopy:

All NMR spectra were acquired at 298 K, unless stated otherwise. ³¹P NMR time-course experiments were acquired using a Bruker 500 MHz Avance II spectrometer (operating at 202.456 MHz for ³¹P) equipped with a 5-mm room-temperature broadband probe and running TopSpin version 3.5. One-dimensional experiments consisting of 256 transients were recorded with a recycle delay of 1 s with proton-phosphorus decoupling and took 479.4 s to acquire. Where stated, experiments were acquired without phosphorus decoupling and took 370.4 s to record. For the AcP hydrolysis experiments, no proton-phosphorus decoupling was used and samples contained 50 mM AcP in 200 mM K⁺ HEPES buffer (pH 7.2), 10% ²H₂O (v/v) and 1 mM trimethylsilyl propionate (TSP) without MgCl₂, together with either 300 μ M β PGM_{WT} or 300 μ M β PGM_{D170N}. For the reactions involving the β PGM-catalysed conversion of β G1P to G6P, samples contained: 300 μ M β PGM_{WT}, 10 mM β G1P and 50 mM AcP in 200 mM K⁺ HEPES buffer (pH 7.2), 10% ²H₂O (v/v) and 1 mM TSP without MgCl₂ and with no proton-phosphorus decoupling used; 20 μ M β PGM_{D170N}, 10 mM β G1P and 20 mM AcP in 200 mM

K^+ HEPES buffer (pH 7.2), 10% 2H_2O (v/v) and 1 mM TSP with 100 mM $MgCl_2$ and with no proton-phosphorus decoupling used; 400 μM $\beta PGMD_{170N}$, 10 mM $\beta G1P$ and 20 mM AcP in 200 mM K^+ HEPES buffer (pH 7.2), 10% 2H_2O (v/v) and 1 mM TSP with 5 mM $MgCl_2$; 400 μM $\beta PGMD_{170N}$, 10 mM $\beta G1P$ and 20 mM AcP in 200 mM K^+ HEPES buffer (pH 7.2), 10% 2H_2O (v/v) and 1 mM TSP with 100 mM $MgCl_2$; 400 μM $\beta PGMD_{170N}$, 10 mM $\beta G1P$ and 20 mM AcP in 200 mM K^+ HEPES buffer (pH 7.2), 10% 2H_2O (v/v) and 1 mM TSP with 5 mM magnesium acetate and 200 mM NaCl. For the $\beta PGMD_{170N}$ stability measurements, samples contained 200 μM $\beta PGMD_{170N}$ (preincubated at 25 °C either for 0 h, 24 h or 48 h), 10 mM $\beta G1P$ and 20 mM AcP in 200 mM K^+ HEPES buffer (pH 7.2), 10% 2H_2O (v/v) and 1 mM TSP with 100 mM $MgCl_2$. For the experiment representative of 0.1% reversion of $\beta PGMD_{170N}$ to βPGM_{WT} through deamidation, the sample contained 200 μM $\beta PGMD_{170N}$ and 200 nM βPGM_{WT} , 10 mM $\beta G1P$ and 20 mM AcP in 200 mM K^+ HEPES buffer (pH 7.2), 10% 2H_2O (v/v) and 1 mM TSP with 100 mM $MgCl_2$. To measure apparent K_m (Mg^{2+}) values for the Step 1 production of $\beta G16BP$ and the Step 2 production of G6P, samples contained 5 μM $\beta PGMD_{170N}$, 10 mM $\beta G1P$ and 20 mM AcP in 200 mM K^+ HEPES buffer (pH 7.2), 10% 2H_2O (v/v) and 1 mM TSP with increasing concentrations of $MgCl_2$ (5, 10, 20, 30, 50, 100 mM). ^{19}F experiments were recorded at 278 K using a Bruker 500 MHz Avance III spectrometer (operating at 470.59 MHz for ^{19}F) equipped with a 5-mm QCI-F cryoprobe and z-axis gradients running TopSpin version 3.5. Samples of 0.5 mM $\beta PGMD_{170N}$ were prepared in 200 mM K^+ HEPES buffer (pH 7.2) containing 5 mM or 100 mM $MgCl_2$, 10 mM NaF, 0.2 mM deferoxamine, 10% 2H_2O (v/v) and 1 mM TSP. $^1H^{15}N$ TROSY NMR spectra were recorded for βPGM_{WT} using a Bruker 500 MHz Avance III spectrometer equipped with a 5-mm QCI-F cryoprobe and z-axis gradients running TopSpin version 3.5. The sample contained 1 mM ^{15}N - βPGM_{WT} in 50 mM K^+ HEPES buffer (pH 7.2) with 5 mM $MgCl_2$, 2 mM NaN_3 , 10% (v/v) 2H_2O and 1 mM TSP. $^1H^{15}N$ TROSY NMR spectra were recorded for $\beta PGMD_{170N}$ using a Bruker 800 MHz Neo spectrometer equipped with a 5-mm TCI cryoprobe and z-axis gradients running TopSpin version 4.0. The sample contained 0.5 mM ^{15}N - $\beta PGMD_{170N}$ (preincubated at 25 °C either for 0 h, 24 h or 48 h) in 50 mM K^+ HEPES buffer (pH 7.2) with 5 mM $MgCl_2$, 2 mM NaN_3 , 10% (v/v) 2H_2O and 1 mM TSP. $^1H^{15}N$ TROSY experiments were acquired with 16 transients with 256 increments and spectral widths of 32 or 36 ppm centred at 120 ppm or 118 ppm in the indirect ^{15}N dimension. For the final $\beta G16BP$ product prepared in 100% 2H_2O containing 1 mM TSP, 1H and natural abundance $^1H^{13}C$ -HSQC experiments were recorded

using standard Bruker pulse sequences on an 800 MHz Bruker Neo spectrometer with a 5-mm TCI cryoprobe equipped with z-axis gradients and running TopSpin version 4.0. ^{31}P experiments were also recorded for this sample, as described above. ^1H and ^{13}C chemical shifts were referenced to TSP resonating at 0.0 ppm. ^{31}P experiments were either referenced to 1 M HPO_3 resonating at 0.0 ppm, sealed inside a glass capillary and inserted into the sample NMR tube or were referenced indirectly to TSP using the gyromagnetic ratios of the ^1H and ^{31}P nuclei. ^{19}F experiments were referenced indirectly to TSP using the gyromagnetic ratios of the ^1H and ^{19}F nuclei. NMR data were processed with baseline correction and Lorentzian apodisation using either FELIX (Felix NMR, Inc.) or TopSpin version 4.0 (Bruker). Quantitative NMR experiments were performed using a recycle delay of 60 s. To measure apparent $K_m(\text{Mg}^{2+})$ values from ^{31}P NMR time-course experiments, the initial rate for the Step 1 production of βG16BP and the Step 2 production of G6P was obtained using an in-house Python linear least-squares fitting program. The initial rates were subsequently fitted to Equation 4.1 using an in-house Python non-linear least-squares fitting program, which uses bootstrap error estimation.

$$v_0 = \frac{V_{\max}[A]}{K_{m(\text{app})} + [A]} \quad (4.1)$$

Where v_0 represents the initial rate of reaction, A represents the activator being tested, V_{\max} represents the apparent maximal rate, $K_{m(\text{app})}$ represents the apparent Michaelis constant for activation of the enzyme by A .

4.6.5 Kinetic Assays:

Kinetic assays for $\beta\text{PGM}_{\text{WT}}$ and $\beta\text{PGM}_{\text{D170N}}$ were conducted using a G6PDH coupled assay. Here, the G6P product of $\beta\text{PGM}_{\text{WT}}$ activity is oxidised to 6-phosphogluconolactone by G6PDH, while the concomitant reduction of NAD^+ to NADH is monitored by measuring changes in absorbance at 340 nm ($\epsilon_{340} = 6220 \text{ M}^{-1}\text{cm}^{-1}$). Reactions were run at 25 °C using a FLUOstar OMEGA microplate reader (BMG Labtech). To measure the MgCl_2 dependence of the $\beta\text{PGM}_{\text{WT}}$ - and $\beta\text{PGM}_{\text{D170N}}$ -catalysed conversion of βG1P to G6P, reactions (160 μL) were conducted in 200 mM K^+ HEPES buffer (pH 7.2) containing different concentrations of MgCl_2 (0, 0.1, 0.3, 0.6, 1.0, 1.5, 2.5, 5, 10, 20, 50 and 100 mM), 1 mM NAD^+ , 5 U/mL G6PDH, 1 mM βG1P and either 1 nM $\beta\text{PGM}_{\text{WT}}$ with 100 μM βG16BP , or 10 μM $\beta\text{PGM}_{\text{D170N}}$ with 1250 μM βG16BP . Initial rates of the reactions were obtained using an in-house Python linear least-

squares fitting program. Initial rates were subsequently fitted to Equation 4.2 using an in-house Python non-linear least-squares fitting program, which uses bootstrap error estimation.

$$v_0 = \frac{V_{\max}[A]}{K_{m(\text{app})} + [A] \left(\frac{1 + [A]}{K_i} \right)} \quad (4.2)$$

Where v_0 represents the initial rate of reaction, A represents the activator being tested, V_{\max} represents the apparent maximal rate, $K_{m(\text{app})}$ represents the apparent Michaelis constant for activation of the enzyme by A and K_i represents the apparent inhibition constant of the enzyme for A . To measure the apparent K_m (β G16BP) of β PGM_{D170N}, reactions (160 μ L) were conducted in 200 mM K⁺ HEPES buffer (pH 7.2) with 5 mM MgCl₂, 1 mM NAD⁺, 5 U/mL G6PDH, 10 μ M β PGM_{D170N} and 1 mM β G1P, and were initiated using increasing concentrations of β G16BP (10, 25, 50, 100, 150, 250, 350, 750, 1000, 1500, 2500 μ M). Initial rates of G6P production were obtained using a linear least-squares fitting routine and these rates were subsequently fitted to Equation 4.1 using an in-house Python non-linear least squares fitting program. To measure the dependence of initial reaction velocity for β PGM_{D170N} on β G1P concentration, reactions (160 μ L) were conducted in 200 mM K⁺ HEPES buffer (pH 7.2) with 5 mM MgCl₂, 1 mM NAD⁺, 5 U/mL G6PDH, 10 μ M β PGM_{D170N} and increasing concentrations of β G1P (50, 100, 200, 300, 500, 700, 1000, 1500, 2000, 3000, 5000 μ M) and were initiated using 250 μ M β G16BP. Initial rates of G6P production were obtained using a linear least-squares fitting routine and these rates were subsequently fitted to Equation 4.2 to derive values for K_m (β G1P) and K_i (β G1P). To measure the effect of different phosphorylating agents on the β PGM_{WT}-catalysed conversion of β G1P to G6P, reactions (160 μ L) were conducted in 200 mM K⁺ HEPES buffer (pH 7.2) with 5 mM MgCl₂, 1 mM NAD⁺, 5 U/mL G6PDH, 5 nM β PGM_{WT}, 50 μ M β G1P with either 1 μ M of the final β G16BP product or 8 mM AcP as the phosphorylating agent. Blank absorbance measurements were obtained using solutions identical to the reaction mixtures, but without the addition of β PGM.

4.6.6 β G1P preparation:

β G1P was prepared enzymatically from maltose using maltose phosphorylase (EC 2.4.1.8). A solution of 611 mM maltose was incubated overnight with 1.2 U/mL maltose phosphorylase in 0.5 M sodium phosphate buffer (pH 7.0) at 30 °C. The production of β G1P was confirmed using ³¹P NMR spectroscopy. Maltose phosphorylase (molecular weight = 90 kDa) was removed from the solution by centrifugation using a Vivaspin (5 kDa molecular weight cut off;

Sartorius). The concentration of β G1P in the flow-through was measured to be 149 mM using quantitative ^{31}P NMR experiments in which a known amount of G6P had been added to a sample of the β G1P product, along with 10% $^2\text{H}_2\text{O}$ (v/v) and 1 mM TSP. This concentration represents a yield of 24%. The β G1P product was contaminated with glucose, maltose and P_i (estimated concentrations were 150 mM, 850 mM and 350 mM, respectively), and was not purified further since these compounds are bystanders in the reaction catalysed by β PGM.

4.6.7 β G16BP production and purification:

A 15 mL reaction was prepared containing 20 μM β PGM_{D170N} in 200 mM K⁺ HEPES buffer together with 100 mM MgCl₂, 2 mM NaN₃, 20 mM β G1P and was initiated with 40 mM AcP. The concentration of β G16BP reached a maximum after 265 min, whereupon the reaction was quenched by heat-denaturation of β PGM_{D170N} at 90 °C for 10 min. Precipitated enzyme was pelleted using centrifugation (Sigma Model 3-15) and the β G16BP-rich supernatant was collected and filtered with a Vivaspin (5 kDa molecular weight cut off; Sartorius) using a benchtop centrifuge (Thermo Scientific Heraeus Labofuge 400 R). The resulting enzyme-free solution was passed through a 20 × 10 mm column packed with IR120 (H⁺) ion-exchange resin, which had been washed with 15 mL of milliQ water. This step acidified the solution, which was then neutralised using 0.2 M barium hydroxide solution, resulting in significant precipitation. The solution was kept on ice during neutralisation to increase the solubility of the mono-phosphorylated glucosaccharide barium salts.¹⁸⁵ Fractions obtained along the course of the barium salt formation were analysed using ^{31}P NMR experiments, which indicated that the β G16BP barium salt was contained mainly in the precipitate, and that the β G1P and G6P barium salts remained in solution. The precipitate was pelleted using centrifugation at 4 °C (4,500 rpm, Thermo Scientific Heraeus Labofuge 400 R) and the supernatant was discarded. To convert the β G16BP barium salt to the more soluble sodium salt the pellet was resolubilised in a large volume (~1 L) of cold milliQ water and passed through a 20 × 10 mm column packed with IR120 (Na⁺) ion-exchange resin. The flow-through was then frozen at -80 °C and lyophilised to leave a fine powder as the final β G16BP product.

4.7 Figures

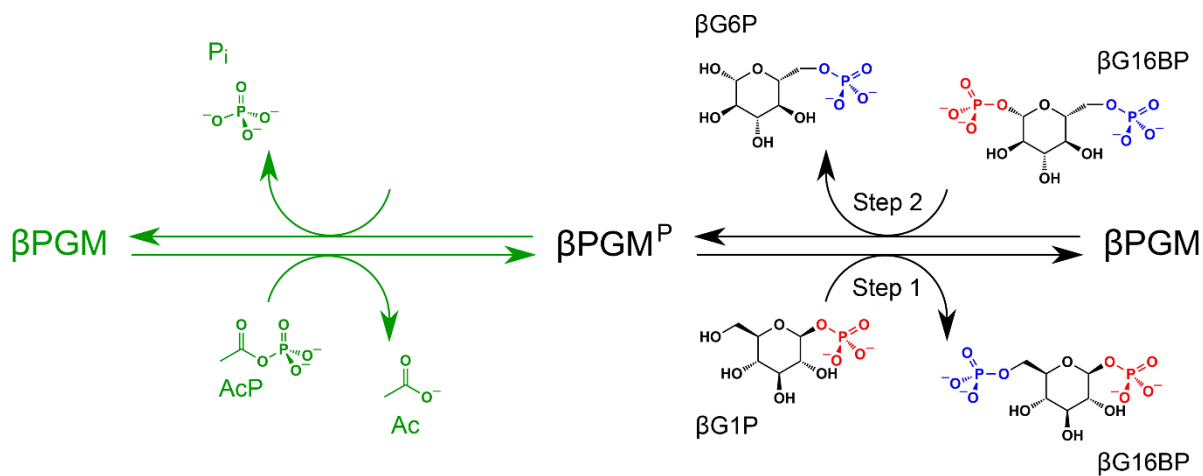


Figure 4.1. *In vitro* phosphorylation and catalytic cycle of βPGM . AcP phosphorylates βPGM generating βPGM^P (phosphorylated on residue D8) in a Mg^{2+} -independent reaction (green ink). In the Mg^{2+} -dependent catalytic cycle (black ink), Step 1 involves phosphoryl transfer from βPGM^P to the βG1P substrate forming the βG16BP intermediate, whereas Step 2 comprises phosphoryl transfer from βG16BP (bound in the alternate orientation) to βPGM forming the G6P product and regeneration of βPGM^P . In the phosphorylated glucosaccharide structures, 1-phosphate groups are coloured red and 6-phosphate groups are coloured blue. The black arrows denote the dominant direction of the corresponding reversible reactions. In the absence of the βG1P substrate, βPGM^P has a half-life of 30 s and hydrolyses readily to βPGM liberating inorganic phosphate (P_i).⁸⁴

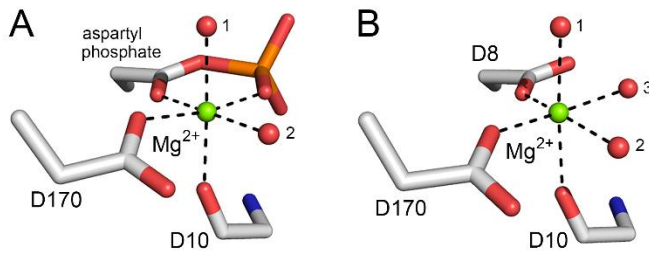


Figure 4.2. Comparison of octahedral Mg_{cat} coordination in $\beta\text{PGMwt}^{\text{P}}$ (Step 1) and βPGMwt (Step 2). (a) A model of $\beta\text{PGMwt}^{\text{P}}$ derived from the crystal structure of the $\beta\text{PGMwt:BeF}_3$ complex (PDB: 2WFA³¹) showing Mg_{cat} coordination. The ligands comprise a carboxylate oxygen atom of residue D170, the carbonyl oxygen atom of residue D10 and two water molecules (indicated by numbers), together with the carboxylate oxygen atom and a phosphate oxygen atom of the D8 aspartyl phosphate moiety, creating bidentate coordination of Mg_{cat} in a six-membered ring of atoms. (b) The crystal structure of substrate-free βPGMwt (PDB: 6YDL¹⁷⁹) showing Mg_{cat} coordination. The ligands involve a carboxylate oxygen atom of residue D8, a carboxylate oxygen atom of residue D170, the carbonyl oxygen atom of residue D10 and three water molecules (indicated by numbers). Mg_{cat} is depicted as a green sphere, water molecules are illustrated as red spheres and metal ion coordination is shown as black dashes.

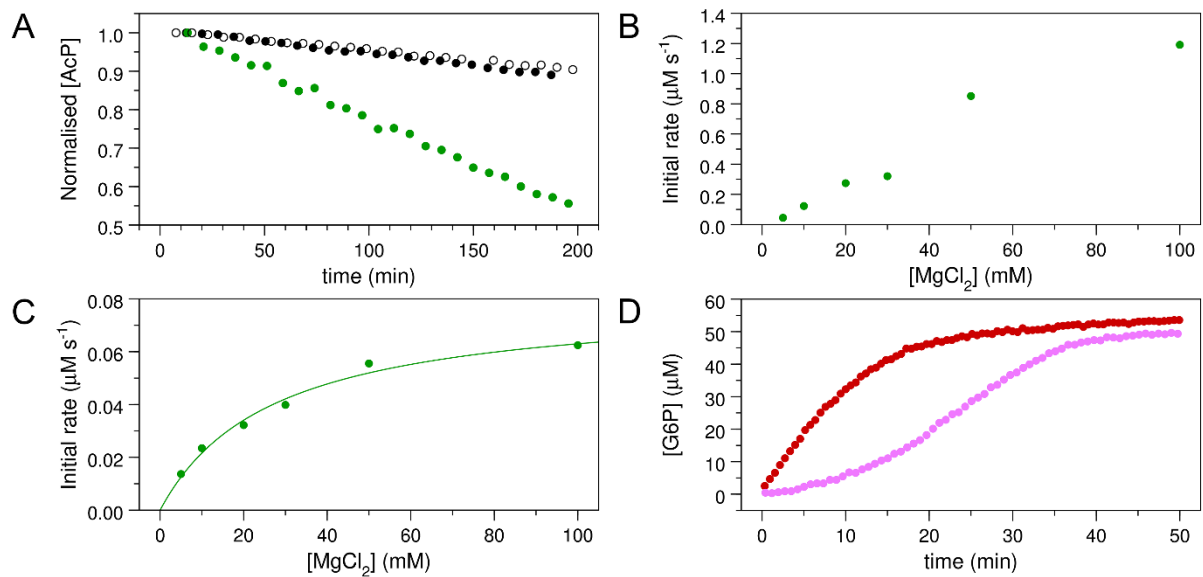


Figure 4.3. Kinetic experiments involving $\beta\text{PGM}_{\text{WT}}$ and $\beta\text{PGM}_{\text{D170N}}$. (a) Effect of $\beta\text{PGM}_{\text{WT}}$ and $\beta\text{PGM}_{\text{D170N}}$ on the hydrolysis of AcP monitored using ³¹P NMR time-course experiments. AcP hydrolysis profiles were derived from normalised peak intensities obtained from reactions containing 50 mM AcP in 200 mM K⁺ HEPES buffer (pH 7.2) without MgCl₂ (white circles) and separately in the presence of 300 μM $\beta\text{PGM}_{\text{WT}}$ (black circles) or presence of 300 μM $\beta\text{PGM}_{\text{D170N}}$ (green circles). (b–c) Activity of $\beta\text{PGM}_{\text{D170N}}$ with increasing MgCl₂ concentration monitored using ³¹P NMR time-course experiments. Samples contained 5 μM $\beta\text{PGM}_{\text{D170N}}$ and 10 mM βG1P in 200 mM K⁺ HEPES buffer (pH 7.2), 10% ²H₂O (v/v) and 1 mM TSP with increasing concentrations of MgCl₂ (5, 10, 20, 30, 50, 100 mM). The reactions were initiated by and timed from the addition of 20 mM AcP. Initial rate measurements for (b) the Step 1 production of βG16BP and (c) the Step 2 production of G6P were obtained from linear least-squares fitting of normalised integral values of the ³¹P resonances of βG16BP and G6P present in the spectra. Subsequent fitting of the Step 2 initial rate values to Equation 4.1 using an in-house Python non-linear least squares fitting program yielded an apparent $K_m(\text{Mg}^{2+}) = 27 \pm 4$ mM. (d) Kinetic profiles for the conversion of βG1P to G6P by $\beta\text{PGM}_{\text{WT}}$ monitored using a G6PDH coupled assay. Reactions were conducted in 200 mM K⁺ HEPES buffer (pH 7.2) containing 5 mM MgCl₂, 1 mM NAD⁺, 5 U/mL G6PDH, 50 μM βG1P and 5 nM $\beta\text{PGM}_{\text{WT}}$ with either 1 μM of the final βG16BP product (red circles) or 8 mM AcP (pink circles) as the phosphorylating agent. For clarity, only half of the acquired data points have been included.

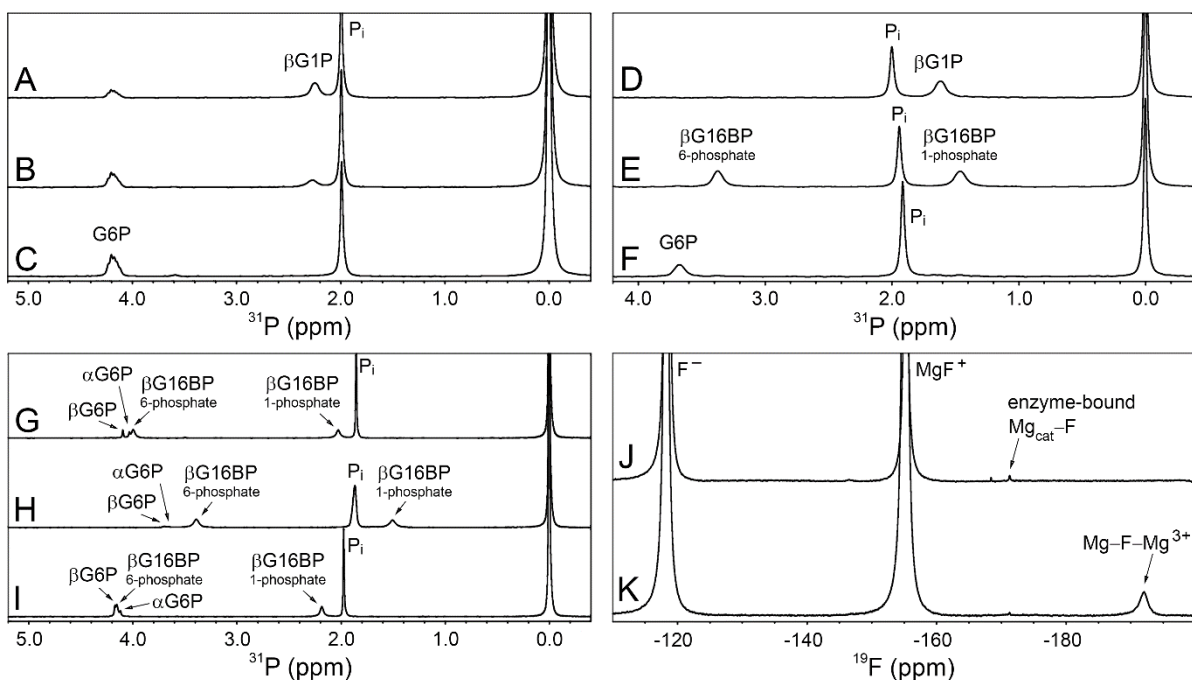


Figure 4.4. ^{31}P and ^{19}F NMR experiments involving $\beta\text{PGM}_{\text{WT}}$ and $\beta\text{PGM}_{\text{D170N}}$. (a–c) The $\beta\text{PGM}_{\text{WT}}$ -catalysed conversion of βG1P to G6P via βG16BP in the absence of Mg^{2+} ions. (a) Reaction containing 300 μM $\beta\text{PGM}_{\text{WT}}$ and 10 mM βG1P in 200 mM K^+ HEPES buffer (pH 7.2) without MgCl_2 , acquired 23 min after the addition of 50 mM AcP. (b) Reaction after 42 min showing the presence of βG1P and G6P . (c) Reaction after 72 min showing complete conversion of βG1P to G6P . (d–f) The $\beta\text{PGM}_{\text{D170N}}$ -catalysed conversion of βG1P to G6P , together with the accumulation of βG16BP . (d) Reaction containing 20 μM $\beta\text{PGM}_{\text{D170N}}$ and 10 mM βG1P in 200 mM K^+ HEPES buffer (pH 7.2) with 100 mM MgCl_2 , prior to the addition of 20 mM AcP. (e) Reaction after 87 min showing the generation of βG16BP . (f) Reaction after 1179 min showing complete conversion of βG1P to G6P . (g–i) The $\beta\text{PGM}_{\text{D170N}}$ -catalysed conversion of βG1P to G6P together with the accumulation of βG16BP under variable ion concentrations. (g) Reaction containing 400 μM $\beta\text{PGM}_{\text{D170N}}$ and 10 mM βG1P in 200 mM K^+ HEPES buffer (pH 7.2) with 5 mM MgCl_2 , 35 min after the addition of 20 mM AcP. (h) Reaction containing 400 μM $\beta\text{PGM}_{\text{D170N}}$ and 10 mM βG1P in 200 mM K^+ HEPES buffer (pH 7.2) with 100 mM MgCl_2 , 19 min after the addition of 20 mM AcP. (i) Reaction containing 400 μM $\beta\text{PGM}_{\text{D170N}}$ and 10 mM βG1P in 200 mM K^+ HEPES buffer (pH 7.2) with 5 mM magnesium acetate and 200 mM NaCl, 36 min after the addition of 20 mM AcP. The peak at 1.9–2.0 ppm in panels A–I corresponds to inorganic phosphate (P_i), which is present in the stocks of both βG1P and AcP. ^{31}P chemical shifts were referenced to external 1 M $\text{HPO}_3 = 0.0$ ppm, which was sealed inside a glass capillary and inserted into the sample NMR tubes. The samples in g–i were recorded using experiments with proton-phosphorus decoupling in order to simplify the identification of the relevant species. (j–k) ^{19}F NMR experiments involving $\beta\text{PGM}_{\text{D170N}}$ acquired in 200 mM K^+ HEPES buffer (pH 7.2) at 5 °C. (j) A sample containing 0.5 mM $\beta\text{PGM}_{\text{D170N}}$ with 5 mM MgCl_2 , 10 mM NaF and 0.2 mM deferoxamine shows an enzyme-bound ^{19}F resonance (~−171 ppm) that corresponds to a $\text{Mg}_{\text{cat}}\text{-F}$ moiety. (k) A sample containing 0.5 mM $\beta\text{PGM}_{\text{D170N}}$ with 100 mM MgCl_2 , 10 mM NaF and 0.2 mM deferoxamine reveals that an increase in Cl^- ion concentration results in a decrease in the peak intensity of the $\text{Mg}_{\text{cat}}\text{-F}$ moiety. Three free ^{19}F species are present in solution: Free F^- (~−118 ppm), free MgF^+ (~−155 ppm) and a free Mg-F-Mg^{3+} species (~−192 ppm), which have been assigned based on the partitioning behaviour between discrete species as the MgCl_2 concentration is increased.

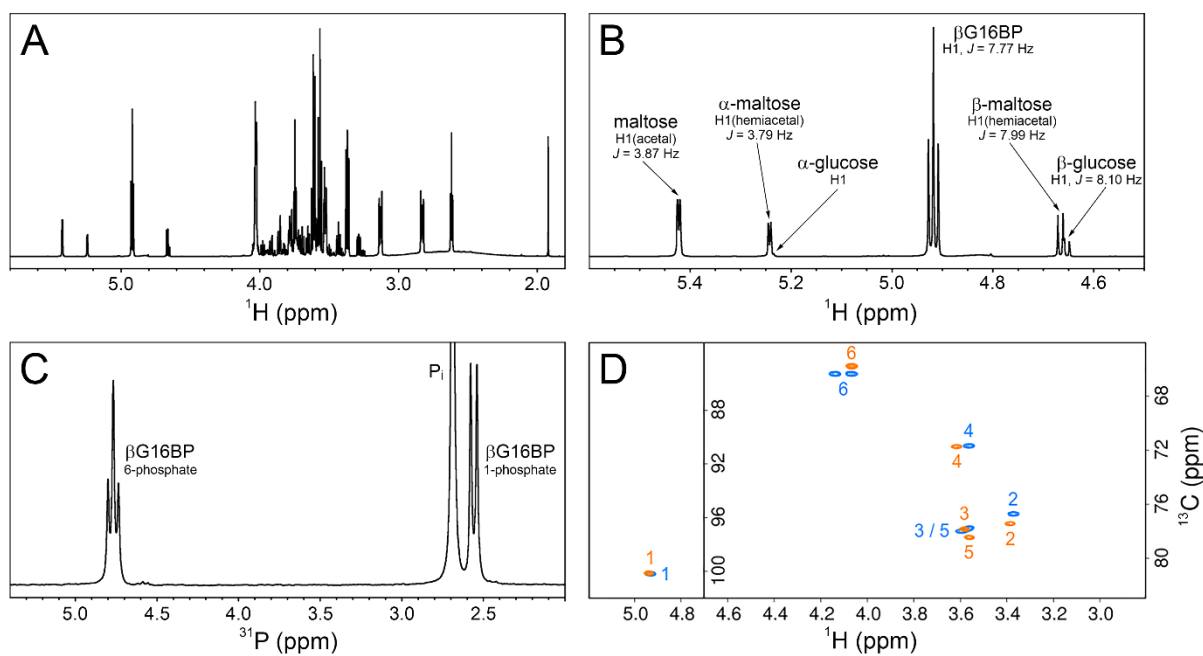
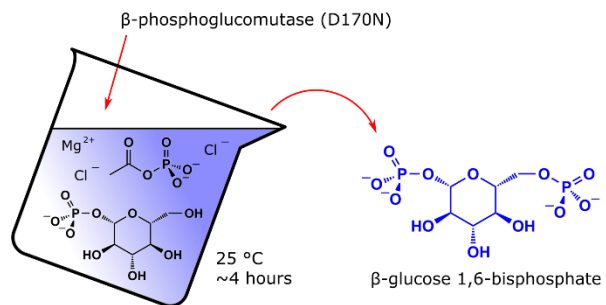


Figure 4.5. NMR experiments recorded on a sample of the final β G16BP product, purified following its production by β PGM_{D170N} and prepared in 100% $^2\text{H}_2\text{O}$. (a) ^1H spectrum showing β G16BP and other glucosaccharide species present in the sample. (b) A region of the ^1H spectrum showing the anomeric proton glucosaccharide signals, together with their assignments. (c) ^{31}P spectrum showing the two phosphorus signals of β G16BP (6-phosphate, 4.76 ppm (triplet) and 1-phosphate, 2.55 ppm (doublet)) and the signal corresponding to inorganic phosphate (P_i , 2.70 ppm (singlet), truncated for clarity). (d) Natural abundance $^1\text{H}^{13}\text{C}$ -HSQC spectra comparing the final β G16BP product (orange) with chemically synthesised β G16BP (blue).⁸⁴ Peaks are labelled with carbon ring atom assignments.

TOC Figure



20 Word Sentence

Green synthesis strategy generating a valuable metabolite through manipulation of the catalytic magnesium coordination of an enzyme.

**5. Novel alginic conformation facilitates dual specificity of
alginic lyase, dp0100.**

Novel alginate conformation facilitates dual specificity of alginate lyase, dp0100.

Henry P. Wood^{a,1}, Shiqi Ji^{b,1}, Samuel R. Dix^a, Andrea M. Hounslow^a, Svetlana E. Sedelnikova^a, Patrick J. Baker^a, Jon Agirre^c, Jonathan P. Walther^{a,d}, David W. Rice^{a,*}.

^aKrebs Institute for Biomolecular Research, Department of Molecular Biology and Biotechnology, The University of Sheffield, Sheffield, S10 2TN, United Kingdom; ^bState Key Laboratory of Microbial Technology, Shandong University, 72 Binhai Road, Qingdao 266237, P. R. China; ^cDepartment of Chemistry, University of York, Heslington, York, YO10 5DD, United Kingdom; ^dManchester Institute of Biotechnology and School of Chemistry, The University of Manchester, Manchester, M1 7DN, United Kingdom.

¹H.P.W. and S.J. contributed equally to this work

*To whom correspondence may be addressed: Prof. David Rice, Krebs Institute for Biomolecular Research, Department of Molecular Biology and Biotechnology, University of Sheffield, Sheffield, S10 2TN, United Kingdom, +44 114 222 4242, d.rice@sheffield.ac.uk.

Keywords: alginate | alginate lyase | enzyme mechanism | chair conformation | NMR spectroscopy | X-ray crystallography

5.1 Abstract

Alginate is a linear, copolysaccharide formed from the uronic acids, α -L-guluronic acid (G) and β -D-mannuronic (M). The use of alginate is widespread in the food and biotechnology industries owing to its propensity to form gels when mixed with Ca^{2+} ions. Alginate is found in brown algae and some species of bacteria, where it plays a structural role. Many bacteria have evolved alginate lyase enzymes to metabolise alginate and, given the commercial utility of alginate, these enzymes are of considerable interest. Typically, alginate lyases exhibit the ability to cleave either polyG or polyM, with the proposed conformations of the two polysaccharides being considerably different. However, some alginate lyases possess the ability to cleave both polyG and polyM. The mechanism underpinning this dual specificity is not known. Herein, we describe a non-typical conformation of polyG that is stabilised in the active site of one such dual-specific alginate lyase, Dp0100. The alternative conformation leads to a chain structure that is much closer to the structure of polyM and the enzyme is therefore able to use a similar catalytic mechanism for both substrates.

5.2 Introduction

Alginate is a linear, co-polysaccharide of α -L-guluronic acid (G) and its C5 epimer, β -D-mannuronic acid (M).^{85,86} The polysaccharide is found in various species of brown algae and bacteria, where its function is primarily structural. In algae, alginate is a major cell-wall constituent alongside fucoidans and cellulose.^{87,88} In bacteria of the genera *Azotobacter* and *Pseudomonas*, alginate functions as an extracellular polysaccharide and has many suggested purposes including a role during encystment, where the bacterium is enclosed in a polysaccharide capsule.^{96,186–190} The structural utility of alginate derives from its ability to form gels in the presence of Ca^{2+} ions. This structural property, along with the fact that alginate is nontoxic and nonimmunogenic, have led to its adoption in many biotechnologies and foodstuffs, including drug delivery technologies, wound dressings and cell culture.^{97,98} The commercial value of alginate has spawned multiple research efforts attempting to obtain a deeper understanding of its structural and chemical properties.^{92,101,104}

Structurally, a considerable amount is known about alginate. The G and M units comprising alginate are arranged either as homopolymeric blocks (polyG and polyM) or as blocks in which the G and M residues alternate.¹⁹³ The length and distribution of the blocks in the alginate chain

depends on the species from which the alginate originates, and this is known to vary considerably.^{90,91} This heterogeneity is generated by epimerases post-polymerisation, and alginate is initially synthesised as polyM.⁸⁹ The gelation process of alginate is understood to occur in the presence of Ca²⁺ ions between the polyG blocks of adjacent alginate chains.^{194,195} At the resultant junction zones between chains, the stoichiometry of Ca²⁺ ions to G residues is proposed to be 4:1.⁹² On the residue level, fibre diffraction, X-ray crystallography and NMR data have shown that G and M residues adopt the chair conformation, with G existing in the ¹C₄ chair conformation and M in the ⁴C₁ chair conformation.^{90,91,100–105} Informed by these structural data, various models have been suggested for the atomic arrangement of polyG and polyM, although a consensus has not yet been reached.^{93–95,106,196} PolyM is proposed to adopt a ribbon-like structure. In contrast, the adoption of the ¹C₄ chair conformation by residues comprising polyG leads to a kinked chain structure.¹⁰⁸

In vivo, alginate chains are manipulated by two types of enzyme: epimerases, which catalyse the C5 epimerisation reaction between G and M, and lyases, which depolymerise alginate chains. Alginate lyases are a class of enzyme that fall within the larger taxonomic bracket of polysaccharide lyases (PL), and constitute 9 of the 38 known PL families. Alginate lyases operate in both endo- and exo-specific manners and are known to have different substrate specificities, with their activities divided between cleaving polyG, polyM and heteropolymeric GM regions.¹⁰⁸ It is of considerable interest to be able to manipulate the structure of alginate chains either through depolymerisation or epimerisation, in order to control the properties of alginate. Alginate depolymerisation is of particular interest in light of research suggesting that guluronate oligosaccharides boost the antibacterial activities of macrophages.¹⁹² Additionally, the fact that mammals do not possess alginate lyases means that there are therapeutic concerns about being able to purge high molecular weight (>48,000 Da) alginate fragments from the body.¹⁹⁷ The catalytic mechanism of alginate lyases has been proposed to consist of three steps: neutralisation of the negative charge of the carboxylate group, abstraction of the proton at C5, and β-elimination of the glycosidic bond to form an unsaturated monosaccharide.¹¹⁰ This proposed mechanism was recently corroborated by the observation of a truncation variant of the alginate lyase Dp0100 (TM5) in complexes with a five-residue polyM oligosaccharide and with a trisaccharide cleavage product (ΔMM)¹⁰⁸. Details of the cleavage site revealed a histidine residue (H405) that is well-positioned to act as a general base, alongside another histidine (H187) and an asparagine residue (Asn186) that could stabilise the hypothetical *aci*-

carboxylate during the reaction, with a tyrosine (Y239) to act as a general acid (Figure 5.1). Interestingly, Dp0100 operates with dual specificity, and can cleave both polyG and polyM alginate. Given the strikingly different chain structures proposed for polyG and polyM, it is curious how this arrangement of amino acid residues in the active site of Dp0100 is able to accommodate and catalyse reactions of the two types of chain. This study reports the observation of a Dp0100 variant in complex with polyG and shows, through the use of X-ray crystallography and NMR, how the oligosaccharide deviates from its solution structure when in the active site of the enzyme to facilitate catalysis.

5.3 Results

5.3.1 Atypical conformation of polyG exists in TM5 biding site.

The ability of alginate lyase to hydrolyse both polyG and polyM, despite considerable differences in the proposed structures of these molecules, is surprising. To understand how Dp0100 is capable of accommodating the two different alginate chains in its active site, the TM5 truncation mutant of Dp0100 was crystallised in the presence of polyG alginate and the structure was solved using molecular replacement at a resolution of 2.11 Å (Table 5.1). This variant has been shown to contain the minimal structure required for catalytic activity of both polyG and polyM, and has been previously crystallised bound to uronic acid oligomers.¹⁰⁸ The resultant structure contains four monomers of TM5 in the asymmetric unit, three of which have a trisaccharide bound in their active site cleft (Figure 5.1A,B). The reducing end residue of the trisaccharide is unsaturated with a double bond between C4 and C5, creating trigonal planar geometry at C5. The presence of a partly unsaturated trisaccharide indicates that this is a truncation product of the polyG alginate, with the nonreducing end residue occupying the +1 subsite (sugar-binding subsites are numbered according to the nomenclature proposed by Davies et al.¹⁹⁸). Given that the degree of polymerisation (d.p.) of the polyG alginate included in the crystal motherliquor is not exact, this unsaturated trisaccharide was named differently to the polyM cleavage product (Δ MM), and was instead termed triG_u to distinguish it from triG, which is not unsaturated. In one triG_u-bound monomer, the triG_u is accompanied by two molecules of acetate, which is present in the crystallisation mother liquor. In another triG_u-bound monomer, one molecule of acetate and one molecule of ethylene glycol, which was used as a cryoprotectant, are also present in the active site. In addition to these two molecules, the active site also contains a Ca²⁺ ion, which is not present in the other triG_u-bound monomer.

The density for the active site of the third monomer was much poorer and no additional bound molecules or ions were modelled.

The carboxylate group of the non-reducing terminal residue is bicoordinated by residue N186. The positions of proposed catalytic residues N186, Y239 and H405 (PDB 6JPH)¹⁰⁸ are almost identical to their positions in the ΔMM-bound TM5 structure, with an overall R.M.S.D. between the two structures of 0.169 Å. Interestingly, the residues in triG_u are not uniform in their conformation. Residues in the +1 and +3 subsite are observed in the ¹C₄ chair conformation (although the unsaturated residue at the nonreducing end is not a true chair), whereas the G residue in the +2 subsite adopts a ⁴C₁ chair conformation. In this position the bulky carboxylate side chain forms a 3.1 Å hydrogen bond to residue S127. The ring hydroxyls occupy approximately the same positions as the analogous hydroxyl groups in the ΔMM-bound TM5 structure, forming hydrogen bonds to residues R183 and N404. Because the sugar is a cleavage product, there is no hydrogen atom attached to C5. However, the configuration of G means that prior to cleavage, H5 would be situated on the opposite face of the sugar to the proposed general base, H405. This is not the case with M residues; for example, in a structure of TM5 bound to a M pentasaccharide, the analogous H5 atom is positioned 2.9 Å from the imidazole group of residue H405 (PDB 6JPN). This interaction would be impossible in a polyG bound active site.

5.3.2 Atypical coordination of polyG repeats in active site of TM5

The observation of a trisaccharide in the active site of TM5 is analogous to the observation of co-crystals containing TM5 complexed with a three-residue truncation product of a M pentasaccharide.¹⁰⁸ Following the previous observation of this trisaccharide bound to TM5, an inactive H187A variant of TM5 was crystallised by the researchers and was observed to bind an intact five-residue polyM oligomer. For this reason, a similar approach was adopted here. The H187A variant of TM5 was crystallised in the presence of hexaG and the structure was solved using molecular replacement to a resolution of 2.71 Å (Table 5.1). The crystal structure again contains four monomers in the asymmetric unit, with three of the monomers bound to hexaG. No additional small-molecules are present in the active site and two of the three hexaG-bound monomers contain a Ca²⁺ ion in their active site. The hexaG residues in the +1, +2 and +3 subsites of TM5 overlay well with the TM5-bound triG_u (Supplementary Figure 5.1A). Remarkably, in both triG and hexaG, the chair conformation of the residues is non-uniform,

contrary to the uniform ${}^1\text{C}_4$ conformation that has been proposed in models of polyG structure to date, with hexaG residues in the -2 , $+1$, $+3$ and $+4$ subsites adopting the ${}^1\text{C}_4$ chair conformation and residues in the -1 and $+2$ subsites adopting the ${}^4\text{C}_1$ chair conformation. The hexaG residue in the $+2$ subsite, although close to a true ${}^4\text{C}_1$ chair conformation, has a slightly skewed conformation in all three of its instances in the asymmetric unit. In this conformation, the bond between atom C5 and the ring oxygen, and the bond between atoms C2 and C3 are not parallel and the reference plane, from which the type of chair conformation can be deduced, is not formed. The orientation of the ring hydroxyl groups however, reflect a ${}^4\text{C}_1$ chair conformation. Likewise, in one of the three instances of hexaG in the asymmetric unit, the residue at the reducing end of the oligomer adopts a boat conformation rather than the ${}^1\text{C}_4$ chair conformation adopted by the two reducing-end residues in the other two TM5 monomers.

In this arrangement of mixed chair conformations, the oligomers in the crystal possess a ribbon-like structure (Figure 5.2, Supplementary Figure 5.1B), similar to that observed for polyM, and in stark contrast to the kinked-chain structure hypothesised for polyG.¹⁰⁸ The observation of L-guluronic acid in a mixed chair conformation is new and goes against a considerable body of crystallographic, NMR and computational data, which have so far supported the hypothesis that L-guluronic acid adopts the ${}^1\text{C}_4$ chair conformation, in both monomeric and polymeric arrangements.

5.3.3 PolyG residue environment is not uniform.

To investigate whether the conformation of polyG observed *in crystallo* is also present in solution, 1-D ${}^1\text{H}$ NMR experiments were conducted using a selection of polyG oligomers of increasing length. Samples of L-guluronic acid in di-, tri-, tetra-, penta- and hexa-saccharide form (diG, triG, tetraG, pentaG and hexaG, respectively) at concentrations between 3–11 mM were prepared in 100% ${}^2\text{H}_2\text{O}$ containing 2 mM NaN_3 and 50 mM HEPES at pD 8–8.05, and a 1-D ${}^1\text{H}$ NMR experiment was recorded for each sample (Figure 5.3A–J). The assignment of peaks in the ${}^1\text{H}$ spectra was performed using COSY and TOCSY experiments (Table 5.2, Supplementary Figure 5.2–5.11), using previously published chemical shifts for the anomeric protons of the reducing end residue as a starting point.¹⁰⁴ A full peak assignment was precluded by peak overlap for some of the oligomers. The assignment corroborated that made previously^{91,104} although the greater resolution of experiments used in this study (800 MHz vs. 100–500 MHz) revealed a heterogeneity in chemical shifts that has hitherto gone unreported.

Such heterogeneity is particularly clear in the portion of the spectrum containing the anomeric proton peaks (Figure 5.3F–J).

In order to assign the anomeric proton peaks to the different residues in each oligomer, quantitative ^1H spectra were recorded for each polyG oligomer and peak integrals were calibrated so that a proton from a single residue corresponded to 1 unit (Table 5.3). Individual residues are referred to by their number, with G1 being the residue at the reducing end, and, for the reducing end residue, the configuration at the anomeric carbon (α/β). There are four anomeric peaks that exhibit roughly constant peak integrals and chemical shifts across the spectra of all five polyG oligomers. Three of the peaks correspond to the reducing end residue in its α -pyranose, β -pyranose and β -furanose configurations. The remaining peak ($\delta = 5.1$ ppm, integral value ≈ 1) is likely to correspond to the nonreducing end residue, and its $J_{1,2}$ value of 4.1 Hz is in accordance with it being linked by an $\alpha(1\rightarrow 4)$ glycosidic bond to the adjacent residue. In the simplest case, that of the spectrum for diG, therefore, the anomeric portion of the spectrum contains peaks corresponding to the reducing end and the nonreducing end (Figure 5.3J). Other low intensity peaks are present in the spectrum and may correspond to contaminating M residues, as observed previously in preparations of polyG⁹¹, or low populations of Na^+ -bound polyG. Increasing the d.p. of the oligomer by one results in the appearance of an additional peak in the spectrum of triG ($\delta = 5.057$), which has an integral value close to 1 (Figure 5.3I). This peak therefore likely corresponds to the anomeric proton for residue triG₂, the residue which, *in crystallo*, is observed in the $^4\text{C}_1$ chair conformation. In the spectrum for tetraG, the peak assigned as the anomeric proton of triG₂ grows to an integral value of ~ 2 , suggesting that the conformations of triG₂, tetraG₂ and tetraG₃ are very similar (Figure 5.3H). In the spectrum of pentaG, all of the peaks observed in the spectrum of tetraG remain, but an additional peak is present as well ($\delta = 5.064$ ppm) (Figure 5.3G). This new peak forms a shoulder to the peak that was assigned in the tetraG spectrum as tetraG₂ and tetraG₃ anomeric protons, and the overlap precludes direct quantification. However, because the intensity of the shoulder peak is approximately half that of the dominant peak and the integral value for the two peaks together is 3, the shoulder peak likely represents the anomeric proton of one of the interposing residues in pentaG (pentaG₂, pentaG₃ or pentaG₄).

Given that the three residues that interpose the terminal residues of pentaG all experience very similar environments, the observation that one of the residues has a different chemical shift is surprising. This difference can possibly be explained by one of the interposing residues

adopting a different ring conformation to the other two. The anomeric region of the spectrum for hexaG, is very similar to that of pentaG (Figure 5.3F). The two peaks that represent the interposing residues in pentaG grow from 3 integral units to ~4 integral units, suggesting that the peaks now represent the four residues that interpose the terminal residues of hexaG. There are two ways to interpret the new peak shape: the first option is that the peak hypothesised to represent a different residue environment in pentaG ($\delta = 5.064$ ppm) grows by a single integral unit, giving a peak shape comprising two doublets of the same size. This interpretation leads to the conclusion that the additional residue present in hexaG occupies the same alternative environment. The second interpretation is more complex, and is that the additional residue occupies a second alternative environment, and produces a shoulder peak that is upfield of the other peaks. This second interpretation however is not supported by the TOCSY experiment, which suggests that there are only two peaks. Through comparison of the anomeric regions of the spectra for incrementally longer polyG oligomers, it is therefore possible to conclude that the residues do not exist in identical environments along the whole chain, and at least two distinct environments exist for the interposing residues in pentaG and hexaG.

5.3.4 Dominant solution conformation of triG is not 4C_1 chair conformation

One hypothesis to explain the non-uniform environment experienced by residues in polyG in solution is that the oligomers contain a mixture of residues in both the 1C_4 and the 4C_1 chair conformations. To explore this hypothesis, there are certain parameters that can be measured to distinguish between the two chair conformations. In the 4C_1 chair conformation of α -L-guluronic acid, H1 and H3 bear the same axial orientation below the reference plane of the ring. This puts them in close proximity to one another, as can be seen from the crystal structure of triG-bound Dp0100 where the intra-residue H1–H3 distance is 2.4 Å. This inter-nuclear spacing is sufficiently small for substantial through-space transfer of magnetisation by the nuclear Overhauser effect (NOE) to occur and should be detectable using NOESY experiments. Previously, a 2D NOESY spectrum of polyG revealed a H1–H3 NOE correlation, but it was considered an artefact caused by spin diffusion.¹⁰⁴ This possibility is made easier to discern through the use of ROESY experiments in which spin diffusion over two steps produces crosspeaks bearing the opposite sign to single step NOEs. To test for the intra-residue NOE between H1 and H3 therefore, ROESY experiments were recorded using the five polyG oligomer samples (Figure 5.4, Supplementary Figure 5.12–5.15) and NOEs for the anomeric protons were measured (Table 5.4). Owing to the dispersion of the resonances in the anomeric

proton region in the ^1H spectrum, the experiments using triG proved the simplest to interpret (Figure 5.4). Each of the identifiable L-guluronic acid residues in the spectrum (that is triG₁ in both the α (triG_{1 α}) and β (triG_{1 β}) configurations, triG₂ and triG₃) exhibited a H1–H2 intra-residue NOE and a H1–H5 intra-residue NOE. H1–H4 NOEs and H1–H3 NOEs, both to the preceding residue (triG_{1 β} in the case of triG₂), were observed for residues triG₂ and triG₃, which is a consequence of the $\alpha(1\text{--}4)$ glycosidic linkage that connects them. No evidence for an intra-residue H1–H3 was observed for any of the triG residues. Similarly, the ROESY spectra of diG, tetraG, pentaG and hexaG did not contain any H1–H3 NOE correlations of strong intensity. Residue diG₂ exhibited intra-residue H1–H2, H1–H3 and H1–H5 NOE correlations, with the intensity of the H1–H3 and H1–H5 NOEs being six-fold lower than the H1–H2 NOE based on a 1D-slice of the spectrum. Low intensity H1–H3 NOE correlations were also observed in the ROESY spectra of pentaG and hexaG for the interposing residues in each oligomer and for residue hexaG₆. Due to peak overlap it was not possible to distinguish between the possibilities that the H1–H3 NOEs of the interposing residues were intra- or inter-residue correlations using chemical shifts, but the low intensity of the peaks suggests that the contributing H1 and H3 protons are not in close proximity. In the case of hexaG₆, the H1–H3 NOE correlation was 7-fold less intense than the intra-residue H1–H2 NOE correlation suggesting magnetisation transfer between H1 and H3 occurs over a greater distance through space than the transfer between H1 and H2. Together these results lead to the conclusion that the $^4\text{C}_1$ chair conformation is not a dominant conformation in polyG oligomers.

5.3.5 Dominant solution structure of polyG contains no residues in the $^4\text{C}_1$ chair conformation

To further examine the solution structure of polyG, the orientation of the H1 proton with respect to the reference plane for each residue was investigated. As well as the proximity of H1 and H3, the orientation of the anomeric proton provides an additional touchstone for saccharide conformation. In α -L-guluronic acid, the anomeric proton occupies an axial position when the ring adopts the $^4\text{C}_1$ chair conformation. In contrast, the same proton exists in an equatorial orientation when the ring takes the $^1\text{C}_4$ chair conformation. This orientation can be discerned from the size of the geminal coupling constant between H1 and C1, $^1\text{J}_{\text{C}1,\text{H}1}$,¹⁹⁹ with $^1\text{J}_{\text{C}1,\text{H}1}$ values of \sim 160 Hz for anomeric protons in the axial orientation and \sim 170 Hz for anomeric protons in the equatorial orientation. To explore the solution conformations for residues of polyG oligomers therefore, $^1\text{H}^{13}\text{C}$ -HSQC experiments were acquired without ^{13}C -decoupling using

the same five polyG oligomers and the geminal coupling constants for the anomeric protons were measured (Figure 5.5, Supplementary Figure 5.16–5.19). In each of the five oligomers, the G_{1α} residue, the nonreducing end residue and the interposing residues had ¹J_{C1,H1} values of 170–174 Hz. The interposing residues of pentaG and hexaG bearing different ¹H chemical shifts were overlapped and appeared as one peak in the ¹H¹³C-HSQC spectra. Conversely, the G_{1β} residue presented ¹J_{C1,H1} values of 163–165 Hz across all five spectra. Given that the interposing residues and the nonreducing end residue adopt the α configuration at C1, as evidenced by ³J_{1,2} values, these geminal coupling constants are consistent with all of the residues existing in the ¹C₄ chair conformation. Two low intensity unassigned peaks were also present however, that did not match the chemical shifts of contaminating M.¹⁰⁴ These peaks were present in all spectra at 4.69 and 4.64–4.67 ppm (Figure 5.3A–E) and were termed Peak 1 and Peak 2, respectively. The peaks presented ¹J_{C1,H1} values of 157–165 Hz with ³J_{1,2} values <4 Hz and the carbon and proton shifts for these peaks are consistent with them being anomeric nuclei. If these peaks belonged to L-guluronic acid, therefore, the data are consistent with the ⁴C₁ chair conformation. Confident identification of the species was not possible however. Peak 1 presented a crosspeak in the TOCSY spectrum corresponding to the H2 proton in G_{1α}. Peak 2 was overlapped with the H5 for G_{1α} and did not exhibit any separate connectivity. The dominant population of polyG in solution, therefore, is composed of residues that adopt a ¹C₄ chair conformation.

5.4 Discussion

The TM5 variant of Dp0100 binds to its substrate, polyG, in the same active site cleft that the enzyme uses to bind and cleave polyM. In the crystal structure of the TM5-bound complex, the conformation of individual G residues in polyG is not uniform, with the residues at the -1 and +1 sub-site adopting the ⁴C₁ chair conformation and the other residues bound in the ¹C₄ chair conformation. In this arrangement, the polyG chain takes on a ribbon-like structure that is very similar to the conformation of polyM chains observed bound to TM5.¹⁰⁸ Despite the approximate structural overlap between the positions of the TM5-bound polyG and polyM chains, the precise arrangement of amino acid residues at the proposed cleavage site is not conducive to polyG cleavage occurring by the same mechanism proposed for polyM cleavage. In the polyM-bound TM5 crystal structure, the imidazole group of H405 is positioned 2.9 Å away from the C5 proton, where it likely acts as a general base, facilitating the abstraction of this proton during the catalytic cycle. The observation of triG_u bound to TM5 in an analogous

way to the binding of the Δ MM trisaccharide, with the unsaturated nonreducing end residue in site +1, is strongly suggestive that the site of cleavage is the same for the Dp0100-catalysed depolymerisation of both polyG and polyM. Hence, given that there are no large conformational changes between the polyG- and polyM-bound structures, the position of H405 is no longer appropriate for it to function as a general base, and the C5 proton of the G residue lies on the opposite face of the sugar. In this position, the C5 proton is instead 2.6 Å away from the imidazole group of a different histidine residue, H187. H187 may therefore play the role of general base that H405 performs in polyM depolymerisation. Mutation of this residue to alanine has been shown to completely deactivate TM5¹⁰⁸, providing support for the alternative role of H187. Interestingly, the carboxylate group of the unsaturated nonreducing end residue occupies a near-identical position to the carboxylate that mirrors it in the polyM-bound TM5 complex, where it forms a hydrogen bond to residue N186. This interaction is thought to facilitate stabilisation of the *aci*-carboxylate that forms temporarily during the catalytic cycle, hence the identical positioning of the uronic acid carboxylate means that the stabilising action of residue N186 is not specific to either polyG or polyM. Remarkably, therefore, the only catalytic residues with epimer-dependent roles are H405 and H187, with the roles of N186 and Y239 being the same in both polyG and polyM depolymerisation.

The mixed chair conformation observed in TM5-bound polyG contradicts the consensus solution structure of G-rich alginate, in which G residues are uniformly in the ¹C₄ chair conformation. In NMR experiments using polyG oligomers 2–6 residues in length, the ¹C₄ chair conformation of G residues is shown to predominate. The ¹C₄ chair conformation is to be expected for L-guluronic acid because in this conformation, the bulky COO[−] group at C5 is in an equatorial orientation. Generally, the more stable conformation of a saccharide is that which has the highest number of hydroxyls or bulky substituents in equatorial configurations. Although, the ¹C₄ chair conformation has only one equatorial hydroxyl (at C2) as oppose to three in the ⁴C₁ chair conformation (at C1, C3 and C4), the COO[−] group has a greater steric presence than a hydroxyl and therefore contributes more to the stability of the molecule. Despite the uniform ¹C₄ chair conformation of polyG oligomers, the residues interposing the termini are not identical to each other, and bear subtly different chemical shifts. This may be explained by a scenario where it is not only the terminal residues which have distinct chemical shifts, but also the residues directly adjacent to the terminal residues, namely polyG₂ and polyG_{non-1}, where polyG_{non} is the nonreducing end residue. This has been observed for other

oligosaccharides²⁰⁰, but has not been reported for L-guluronic acid. This is partly because of the low resolution of previously acquired spectra, but could also be due to the higher d.p. of polyG fragments used in other studies, which lowers the relative intensity of residues with unique chemical shifts.

The observation of H1–H3 NOEs that cannot be unambiguously assigned as intra- or inter-molecular means that the possibility of a minor population of polyG alginate existing in the ⁴C₁ chair conformation cannot be completely ruled out. It is also possible that a small population of residues in the ⁴C₁ chair conformation are in fast exchange with the dominant ¹C₄ chair conformation, although this is unlikely given that different pyranose conformations are usually in slow exchange with each other¹⁹⁹. The dominance of the evidence in favour of polyG alginate adopting a ¹C₄ chair conformation in solution suggests that the mixed chair conformation observed bound to TM5 is a consequence of stabilising interactions between the polyG and active site residues. The active site of TM5 is lined with polar and charged amino acids that provide opportunities for electrostatic interactions to occur. Of the two G residues that adopt the ⁴C₁ chair conformation in the hexaG-bound TM5 crystal structure, the carboxylate of one forms a strong (2.4 Å) hydrogen bond with Y135. The carboxylate of the other residue forms only a weak hydrogen bond (3.1 Å) with S127, which alone seems unlikely to provide a large stabilising influence. The close proximity of a bound Mg²⁺ ion suggests that, although not resolved in the crystal structure, there is likely to be a conserved water molecule capable of providing another hydrogen bond donor to the carboxylate of the uronic acid. Having water molecules perform this important binding role may confer the flexibility required to accommodate both polyG and polyM in the active site. One question that cannot be answered on the basis of the crystal structure is how far the mixed chair conformation of the chain continues beyond the edge of the TM5 active site. Given the absence of ⁴C₁ chair conformations in the solution structure of polyG, it is unlikely that G-rich alginate is able to adopt the mixed chair conformation without additional stabilisation. Seeing as TM5 is a truncation mutant of Dp0100, there may be other domains in the full length protein that enable the mixed chair conformation to extend beyond the active site cleft where depolymerisation occurs. There is evidence from native affinity page experiments that the CBM35 domain of Dp0100 has a high affinity for alginate, and may well stabilise propagation of the mixed chain conformation of polyG. In summary, the dual specificity of Dp0100 is possible through the stabilisation of a mixed chair conformation of polyG that is not dominant in solution. Two active site histidine

residues switch roles to accommodate the two orientations of the C5 proton in G and M residues, and other active site residues are capable of fulfilling their roles regardless of which epimer is involved in the reaction.

5.5 Materials and Methods

5.5.1 Preparation of polyG

Alginic acid from brown algae (species unknown) was purchased from Qingdao BZ Oligo Biotech Co., Ltd, China and then processed by heterogeneously reacting the alginic acid with 1 M oxalic acid at 100 °C for several hours. Depolymerisation to the desired d.p. was achieved by controlling the duration of this hydrolysis step. G-rich alginate was isolated by bringing the solution to pH 2.85 and harvesting the precipitate. This precipitate contained G-rich alginate.

5.5.2 X-ray crystallography, data collection, structure determination and refinement

Samples of both the TM5 and TM5 H187A inactive mutant were prepared and crystallised as previously described¹⁰⁸, with the only modification being the addition of either polyG or hexaG, respectively, to a final concentration of 5 mM prior to crystallisation. Protein crystals were subsequently cryo-protected by the addition of 25 % ethylene glycol before being flash cooled in liquid nitrogen to 100 K. Data on crystals containing TM5 + polyG were collected on the I03 MX beamline at Diamond Light Source, Oxford and were processed using xia2-DIALS^{203,204} to 2.11 Å in the spacegroup C222₁. Alternatively, data on crystals containing TM5 H187A + hexaG were collected at the Shanghai Institute of Applied Physics, Chinese Academy of Science and were processed using XDS autoPROC^{206,207} to 2.71 Å in the spacegroup C222₁.

The structures of both co-crystallised species were determined through molecular replacement by Phaser²⁰² using the TM5 substrate-free structure (PDB ID: 6JP4) as the initial search model. Iterative model building and refinement was carried out using COOT and Refmac5, respectively.^{163,164} A new chemical dictionary was generated for the polyG and hexaG polysaccharide ligands identified in the two structures, however, at this point, they were not energetically minimised. The ligands were therefore modelled into their respective electron density without activating torsion restraints, allowing the sugars to adopt the two different carbohydrate ring pockers (¹C₄ and ⁴C₁) observed. Once the polysaccharides had been optimally aligned in the electron density and close to their low-energy chair conformation, torsion restraints were activated. Subsequently, further harmonic restraints were applied prior

to the final polyG and hexaG dictionaries being created in the CCP4 program, acedrg.²⁰⁸ Carbohydrate validation was performed using a developer build of privateer MKIV.²⁰⁵ The final models of both TM5 + polyG and TM5 H187A + hexaG contain four protein molecules (Chains A-D) consisting of residues 1-770, and 1-772, respectively, from the expected 789 residue (772 from the protein and 17 from the poly-His tag) mature protein. In both models, three molecules of their respective polysaccharide ligands can be observed in chains A, B, and C. However, ligands were not modelled bound to chain D due to the poor density associated with this chain in both systems. The final refinement statistics for both structures are shown in Table 1. Figures were produced using PyMOL (Schrödinger) version 2.4.1. R.M.S.D. values were calculated using the align function of PyMOL.

5.5.3 NMR spectroscopy

Samples of polyG for NMR were prepared in 100% $^2\text{H}_2\text{O}$ containing 1 mM trimethylsilyl propionate (TSP), 2 mM NaN₃ and 50 mM HEPES. The sample of diG was 10.6 mM and pD 8.05. The sample of triG was 7.3 mM and pD 8.05. The sample of tetraG was 6.2 mM and pD 8.05. The sample of pentaG was 10.0 mM and pD 8.0. The sample of hexaG was 3.3 mM and pD 8.0. All NMR spectra were recorded at 298 K using an 800 MHz Bruker Neo spectrometer with a 5 mm TCI cryoprobe equipped with z-axis gradients and running TopSpin version 4.0 (Bruker). One-dimensional ^1H experiments consisting of 64 transients were recorded using a recycle delay of 2 s. Quantitative ^1H experiments were recorded using a recycle delay of 60 s. COSY experiments were acquired with 8 transients consisting of 256 increments with a spectral width of 14.2 ppm and a recycle delay of 3 s. TOCSY experiments using a mixing time of 90 ms consisted of 16 transients with 512 increments with a spectral width of 14.2 ppm and a recycle delay of 3 s. ROESY experiments with a mixing time of 200 ms were acquired using 16 or 32 transients consisting of 512 increments with a spectral width of 10.2 ppm and a recycle delay of 1.5 or 3 s. NMR data were processed using baseline correction and, unless otherwise stated, with Lorentzian apodization using Topspin 4.0. Peak integrals were calculated using Topspin version 4.0 and calibrated so that the integral of the peak corresponding to the reducing end residue in its β configuration equated to 0.75 units, in accordance with the distribution of α and β configurations in monomeric L-guluronic acid in $^2\text{H}_2\text{O}$ (77% at 297 K and pD 7¹⁰³ and 75% at 313 K and pD 7¹⁰⁴). Where this calibration was precluded by the H_2O signal, the peaks corresponding to the reducing end residue in its α configuration and its furanose form were together calibrated to 0.25 units. ^1H chemical shifts were referenced to the TSP signal, which

resonates at 0.0 ppm. ^{13}C chemical shifts were referenced indirectly to the TSP signal resonating at 0.0 ppm using the gyromagnetic ratios of ^1H and ^{13}C nuclei.

5.5.4 Data availability

Images used in X-ray data processing are available upon request. The atomic co-ordinates and structure factors for TM5 bound to triG_u and TM5 H187A bound to hexaG are available at the PDB under the accession codes XXXX and XXXX, respectively.

5.6 Tables and Figures

Data collection –	TriG _u bound structure	HexaG bound structure
Wavelength (Å)	0.9718	0.97914
Resolution range (Å)	60.96-2.11 (2.15-2.11)	108.86-2.71 (2.85-2.71)
Space group	C 2 2 2 ₁	C 2 2 2 ₁
Unit cell (a,b,c) (Å)	261.4, 394.9, 112.0	261.0, 394.6, 111.8
(α,β,γ) (°)	90.0, 90.0, 90.0	90.0, 90.0, 90.0
Total reflections	4502456 (225413)	2027614 (325016)
Unique reflections	329687 (16311)	151341 (22709)
Multiplicity	13.7 (13.8)	13.4 (14.3)
Completeness (%)	99.9 (99.8)	96.5 (100.0)
Mean I/σ	12.3 (1.2)	14.6 (2.5)
Wilson B factor (Å ²)	40.5	49.5
R _{merge}	0.145 (2.550)	0.186 (1.614)
R _{pim}	0.041 (0.705)	0.052 (0.438)
CC _{1/2}	0.999 (0.644)	0.998 (0.817)

Refinement		
R _{factor}	0.221	0.202
R _{free}	0.248	0.25
Atoms		
Protein	24960	24988
Ligands	160	219
Ions	11	14
Water	862	54
Protein residues	3072	3080
RMSD (bonds) (Å)	0.014	0.014
RMSD (angles) (°)	1.89	1.96
Ramachandran favoured (%)	93.6	91.6
Ramachandran outliers (%)	0.4	0.9
Favoured rotamers (%)	92.1	87.9
Poor rotamers (%)	2.0	3.4
Average B factors		
Main chain (Å ²)	65	72
Side chains (Å ²)	67	75
Ligands (Å ²)	69	71
Ions (Å ²)	48	61
Water (Å ²)	48	40
PDB ID	XXXX	XXXX

Table 5.1. X-ray crystallographic data.

	Proton	$G_{1\alpha}$	$G_{1\beta}$	$G_{\text{interposing}}$	G_{non}
diG	H1	5.228	4.903	n/a	5.022
	H2	3.960	3.631	n/a	3.935
	H3	u	4.162	n/a	3.968
	H4	u	4.039	n/a	4.161
	H5	u	u	n/a	4.426
triG	H1	5.236	4.895	5.056	5.019
	H2	3.938	3.632	3.924	3.927
	H3	4.093	4.129	4.053	3.927
	H4	4.168	4.058	4.144	4.150
	H5	4.646	4.424	4.490	4.411
tetraG	H1	5.234	4.892	5.059	5.015
	H2	3.933	3.627	3.918	3.941
	H3	u	4.118	4.026	3.936
	H4	u	4.051	4.132	4.134
	H5	4.646	u	4.479	4.409
pentaG	H1	5.234	4.892	5.056	5.064
	H2	3.932	3.623	3.916	3.922
	H3	4.092	4.120	4.010	4.035
	H4	4.163	4.052	4.133	4.142
	H5	4.646	4.422	4.477	4.407
hexaG	H1	5.232	4.889	5.050	5.061
	H2	3.938	3.623	3.912	3.920
	H3	4.090	4.119	4.003	4.036
	H4	4.161	4.051	4.131	4.140
	H5	4.644	4.421	4.470	4.405

Table 5.2. Chemical shifts in ppm for polyG oligomers. $G_{1\alpha}$ and $G_{1\beta}$ represent the reducing end residue in its α and β configuration, respectively. $G_{\text{interposing}}$ represents the residues between the reducing and the nonreducing end residues. G_{non} represents the residue at the nonreducing end. The letter ‘u’ indicates that a chemical shift was unmeasurable.

	diG	triG	tetraG	pentaG	hexaG
G _{1α} & G _{1β}	0.25	0.25	0.25	0.25	0.17
G _{1β}	0.99	u	u	0.57	0.75
G _{interposing}	n/a	0.86	1.98	2.99	3.80
G _{non}	0.85	1.07	1.12	1.05	0.90

Table 5.3. Peak integrals for anomeric proton resonances in quantitative 1-D ¹H spectra of polyG oligomers. G_{1α}, G_{1β} and G_{1β} represent the reducing end residue in its α configuration, its β configuration and its β furanose configuration, respectively. G_{interposing} represents the residues between the reducing and the nonreducing end residues. G_{non} represents the residue at the nonreducing end. The letter ‘u’ indicates that an integral was unmeasurable.

	Residue	NOE correlations					
diG	G _{1α}	H2, intra	4.002				
	G _{1β}	H2, intra	H5, inter, G _{non}				
	G _{interposing}	n/a					
	G _{non}	H2, intra	H3, intra	H4, inter, G _{1β}	H5, intra		
triG	G _{1α}	H2, intra	H5, intra				
	G _{1β}	H2, intra	H5, intra				
	G _{interposing}	H2, intra	H3, inter, G _{1β}	H4, inter, G _{1β}	H5, intra		
	G _{non}	H2, intra	H3, inter, G _{interposing}	H4, inter, G _{interposing}	H5, intra		
tetraG	G _{1α}	H2, intra	H5, intra				
	G _{1β}	H2, intra	H5, intra				
	G _{interposing}	H2, intra	H4, inter, G _{1β}	4.149			
	G _{non}	H2, inter, G _{interposing}	H4, inter, G _{interposing}	4.042			
pentaG	G _{1α}	H2, intra	H5, intra				
	G _{1β}	H2, intra	H5, intra				
	G _{interposing}	H2, intra	H3, inter/intra, G _{interposing}	H4, inter, G _{1β}	H4, inter/intra, G _{interposing}	H5, intra	4.146
	G _{non}	H2, intra	H3, inter, G _{interposing}	H4, inter, G _{interposing}	H5, intra		1.488
hexaG	G _{1α}	H2, intra	H5, intra				
	G _{1β}	H2, intra	H5, intra				
	G _{interposing}	H2, intra	H3, inter/intra, G _{interposing}	H4, inter, G _{1α}	H4, inter, G _{1β}	H4, inter/intra, G _{interposing}	H5, intra
	G _{non}	H2, intra	H3, intra	H3, inter, G _{interposing}	H4, inter, G _{interposing}	H5, intra	

Table 5.4. Correlations in ROESY spectrum involving anomeric protons of polyG oligomers. Where no assignment was possible, the correlation is indicated by the chemical shift of the partner proton in ppm. A label of ‘inter/intra’ indicates that the inter- or intra-residue nature of the correlation was ambiguous. G_{1α} and G_{1β} represent the reducing end residue in its α and β configuration, respectively. G_{interposing} represents the residues between the reducing and the nonreducing end residues. G_{non} represents the residue at the nonreducing end.

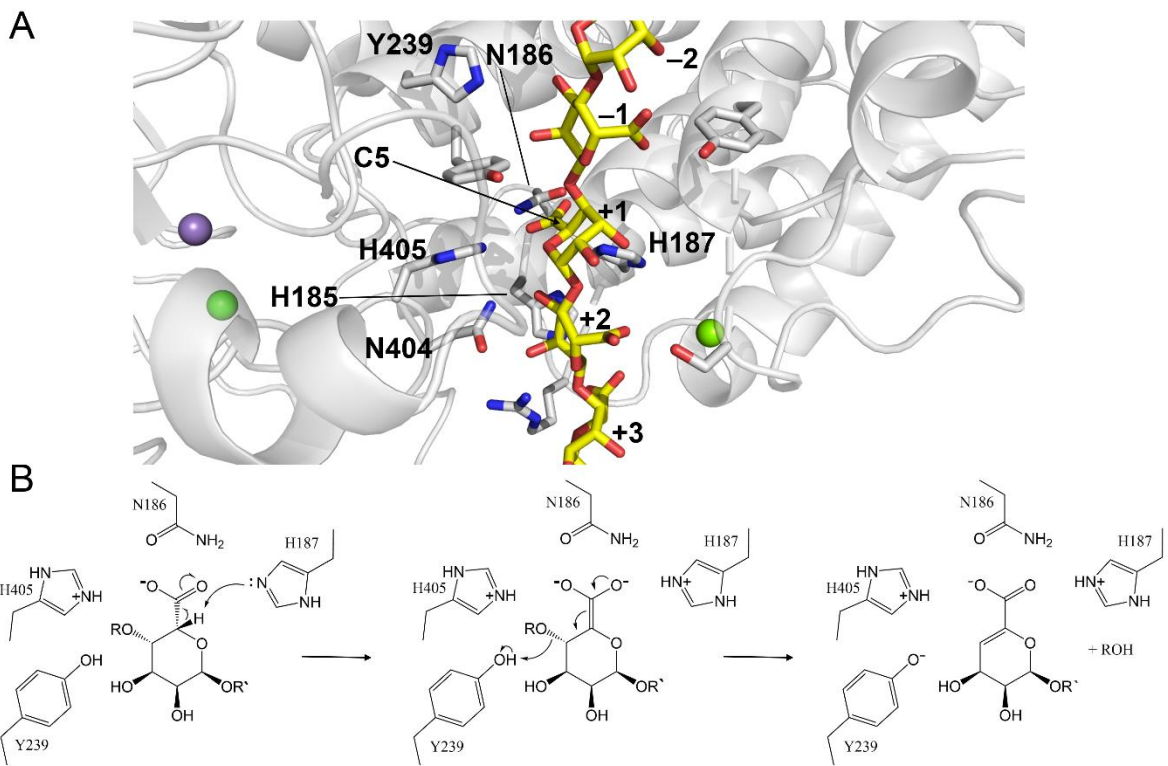


Figure 5.1. Proposed mechanism of Dp0100-catalysed depolymerisation of polyG alginate. (a) X-ray crystal structure of hexaG overlaid on the active site of a TM5 structure with H187 present. Protein coordinates are taken from triG_u-bound TM5 and hexaG ligand is overlaid, using the ligand position from hexaG-bound TM5 H187A variant. The enzyme is shown in cartoon representation with the central domain coloured yellow and the N-terminal domain coloured pink. Key residues are shown in stick representation. The Ca²⁺ ion is shown as a green sphere. The black arrow indicates the location of C5 of the α-L-guluronic acid residue in the +1 position. (b) Diagram of the proposed scheme for Dp0100-catalysed depolymerisation of polyG alginate. Abstraction of the H5 proton generates an aci-carboxylate, which collapses to leave an unsaturated sugar.

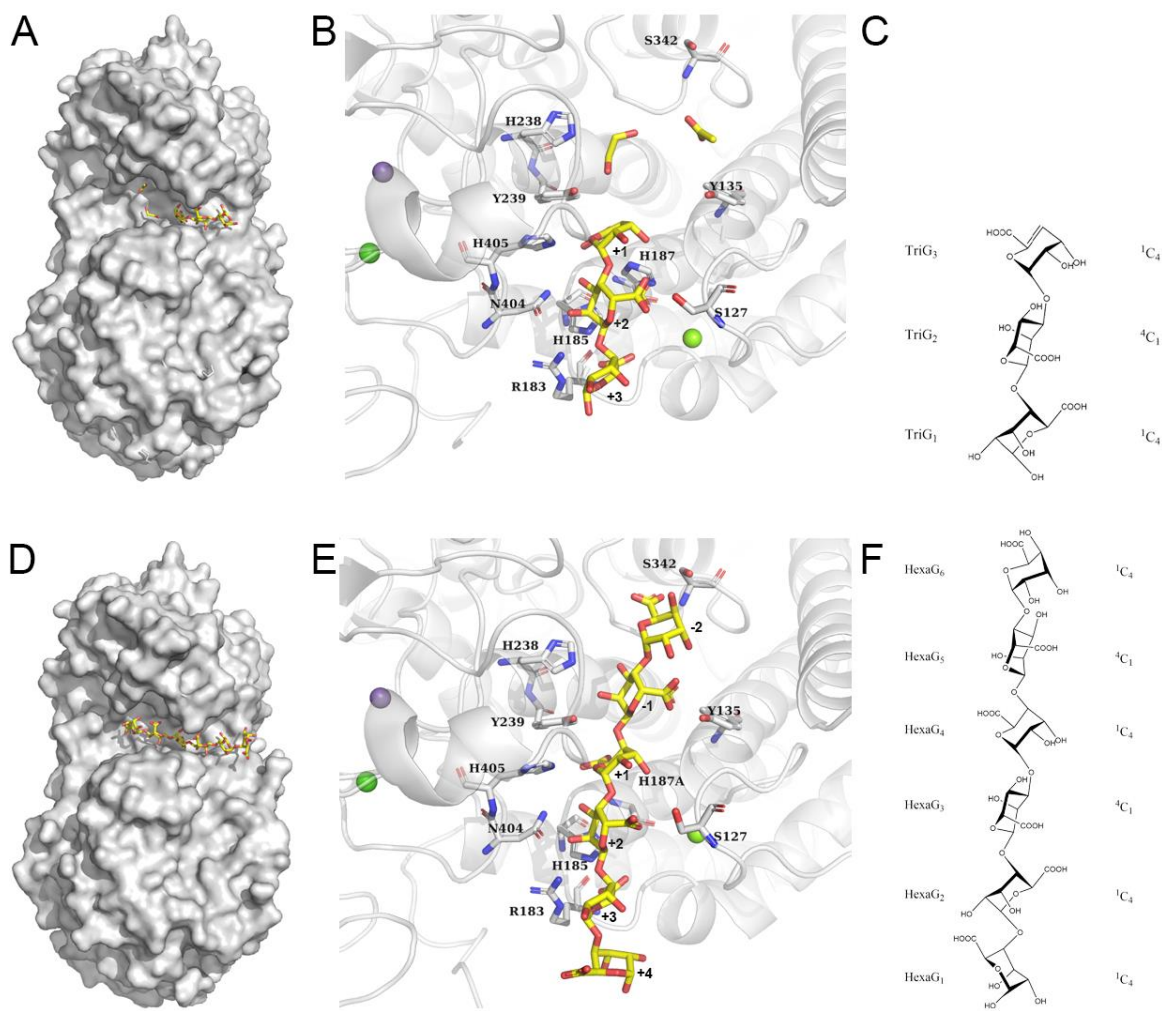


Figure 5.2. X-ray crystal structure of TM5 in complex with polyG oligomers. **a, b, c** X-ray crystal structure and scheme of TM5 complexed with triG oligomer. **(a)** Surface representation of TM5 (grey) complexed with triG, which is shown as sticks (yellow carbon atoms). **(b)** Binding site of TM5 complexed with triG, which is shown as sticks (yellow carbon atoms). Key residues are shown as sticks (grey carbon atoms) and the rest of the structure is shown in transparent cartoon representation (grey). **(c)** Scheme depicting structure and conformation of triG in the active site of TM5. **d, e, f** X-ray crystal structure of TM5 H187A variant complexed with hexaG oligomer. **(d)** Surface representation of TM5 H187A variant (grey) complexed with hexaG, which is shown as sticks (yellow carbon atoms). **(e)** Binding site of TM5 H187A variant complexed with hexaG, which is shown as sticks (yellow carbon atoms). Key residues are shown as sticks (grey carbon atoms) and the rest of the structure is shown in transparent cartoon representation (grey). Starting from the top hexaG residue, the subsites are numbered -2 , -1 , $+1$, $+2$, $+3$ and $+4$. Ca^{2+} and Mn^{2+} ions are shown as green and purple spheres, respectively. **(f)** Scheme depicting structure and conformation of hexaG in the active site of TM5 H187A variant.

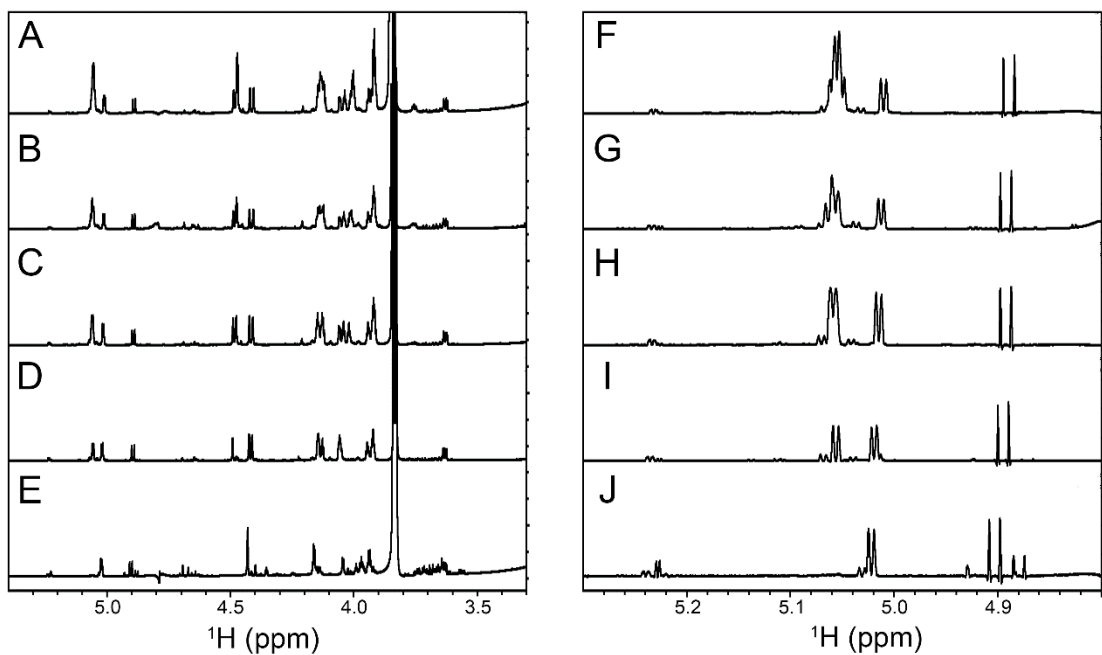


Figure 5.3. 1-D ^1H NMR spectra of L-guluronic acid oligomers.. **a–e**, Comparative overlay of 1-D ^1H NMR spectra of diG, triG, tetraG, pentaG and hexaG. **(a)** hexaG **(b)** pentaG **(c)** tetraG **(d)** triG **(e)** diG. In panels **a–e**, spectra were processed using 0.5 Hz Lorentzian line-broadening. **f–j**, Comparative overlay of 1-D ^1H NMR spectra of diG, triG, tetraG, pentaG and hexaG, focusing on the anomeric proton signals. **(f)** hexaG **(g)** pentaG **(h)** tetraG **(i)** triG **(j)** diG. In panels **f–j**, spectra were processed using a Gaussian function with a max position of 0.9 and Lorentzian line-broadening set to -1.0 Hz, and the spectra were scaled so that the intensity of the peak for the reducing residue in its β configuration was the same in each spectrum. Samples of all five oligomers were prepared at concentrations of 3–11 mM in 100% $^2\text{H}_2\text{O}$ containing 1 mM TSP, 2 mM NaN_3 and 50 mM HEPES at pH 8–8.05.

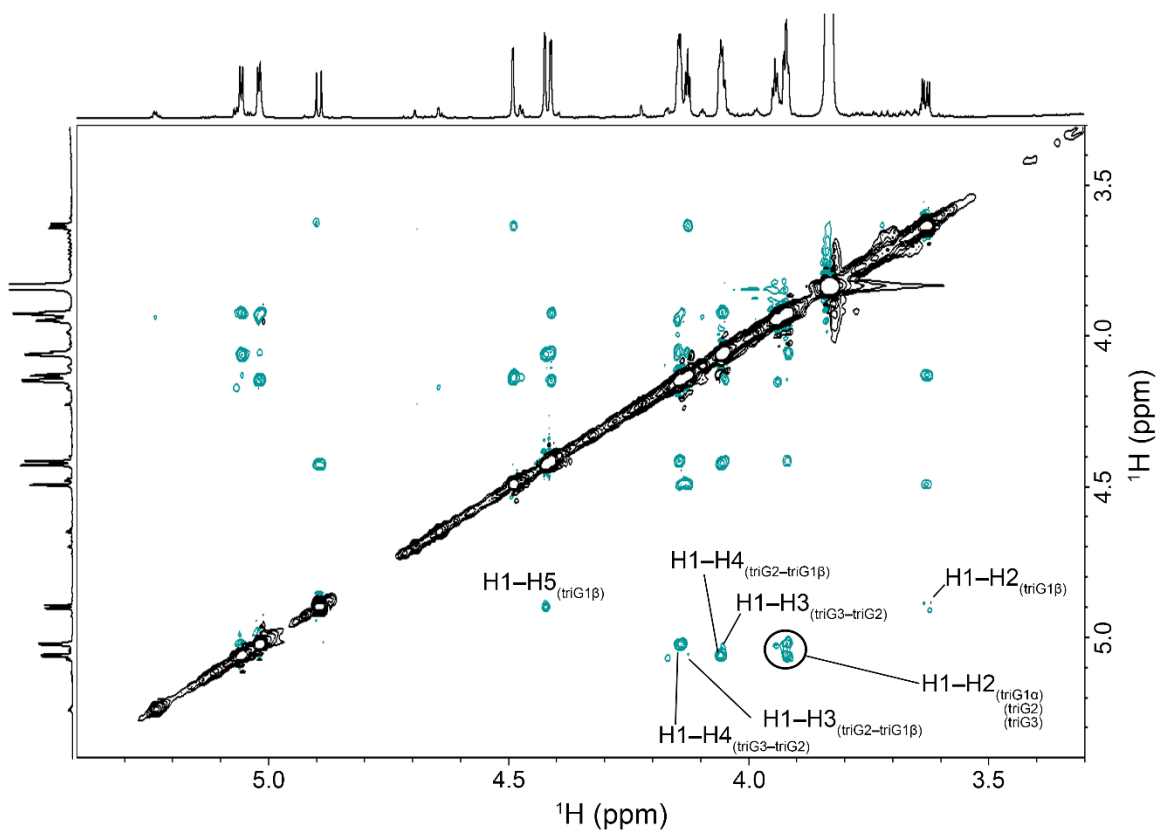


Figure 5.4. ROESY spectrum of triG. A ROESY spectrum recorded using a sample of 7.3 mM triG prepared in 100% $^2\text{H}_2\text{O}$ with 1 mM TSP, 2 mM NaN_3 , 50 mM HEPES at pD 8.05 and a mixing time of 200 ms. An external ^1H spectrum of the sample was used to produce the horizontal and vertical axes traces. Positive peaks along the diagonal are coloured black and negative crosspeaks are coloured green.

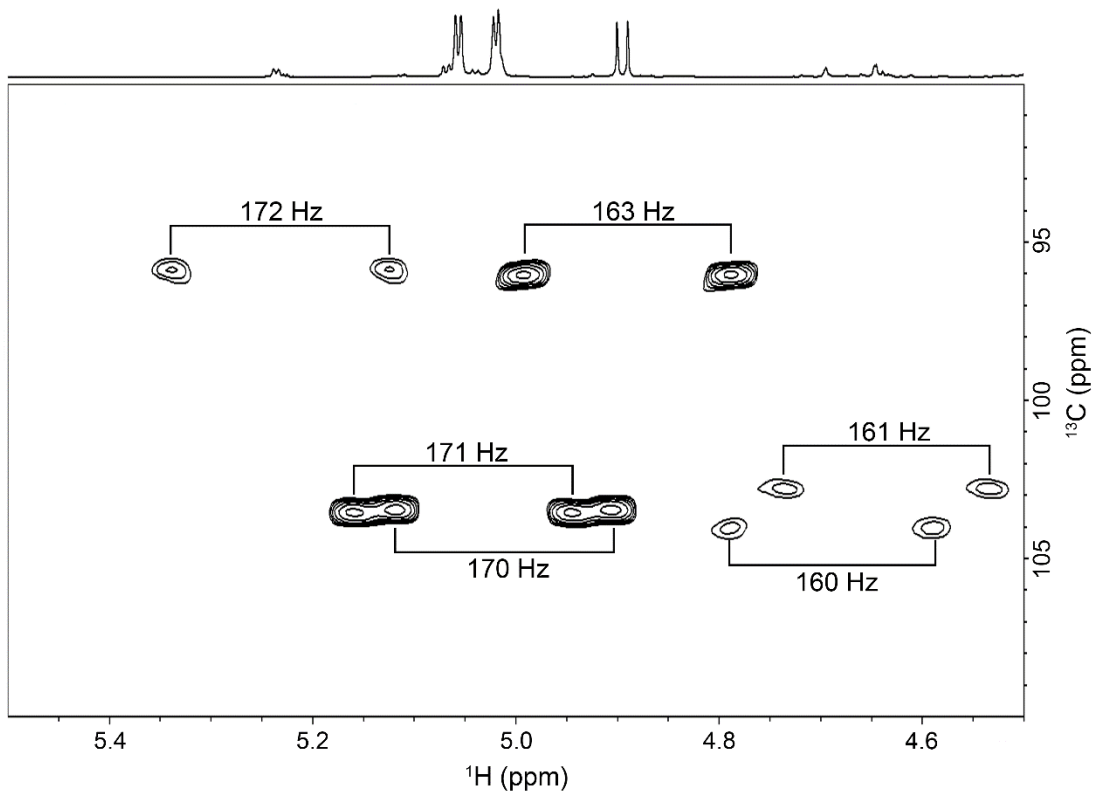


Figure 5.5. $^1\text{H}^{13}\text{C}$ -HSQC spectrum of triG. A $^1\text{H}^{13}\text{C}$ -HSQC spectrum recorded without ^{13}C -decoupling using a sample of 7.3 mM triG prepared in 100% $^2\text{H}_2\text{O}$ with 1 mM TSP, 2 mM NaN_3 and 50 mM HEPES at pD 8.05. An external ^1H spectrum of the sample was used to produce the horizontal axis trace. Each pair of peaks is labelled with its $^1\text{J}_{\text{C}_1,\text{H}_1}$ value. For clarity only positive peaks are shown.

6. Conclusions and Future Directions

This work has investigated the roles of conformational changes in two biomolecules. In the first part of the thesis, β PGM was shown to exist in two conformations in the substrate-free state, which each constitute around 50% of the population. This multi-second dynamic was shown to arise from a *cis-trans* proline isomerism on the periphery of the active site. Owing to the coupling of this isomerism to the position of a vital catalytic lysine residue, the exchange process results in the two populations having considerably different activities. In the presence of the activator, which acts as a substrate, the population becomes biased towards full activity. In the absence of the activator, activity is reduced, which prevents the non-desirable dephosphorylation of key glycolytic intermediates. This elegant regulatory mechanism, termed allomorphy, could have evolved to enable organisms to rapidly switch between nutrient sources, giving them a competitive advantage over organisms that relied on coarse control mechanisms at the level of transcription and translation to adapt to changes in the environment.

Allomorphy manifests similarly to two other known post-translational regulatory mechanisms that act on enzymes: allosterity and the less well-known allokairy. All of these mechanisms involve two or more distinct conformations of the enzyme, emphasising the importance of understanding protein dynamics. Allostery has been exploited in drug development and many drugs are known to act allosterically. For example, benzodiazepines, which are a globally important class of drugs, bind to the γ -aminobutyric acid (GABA) receptor and allosterically enhance the activity of the GABA neurotransmitter.²¹⁰ Allokairy, having been discovered more recently than allosterity, is yet to be exploited to create therapeutic drugs, however it is already implicated in certain types of diabetes and hyperinsulinemic hypoglycemia. The prevalence and therefore the therapeutic usefulness of allomorphy is yet to be seen. Although β PGM of *L. lactis* does not represent an important target of modern drug development, the observation of a novel regulatory mechanism could present new opportunities for drug discovery in other enzymes. Several other enzymes are known to exhibit similar kinetic behaviour in response to different activating molecules. If allomorphy was found to be present in other systems, it may inspire the design of new classes of activators and inhibitors, which work to bias the two-species exchange in favour of either the active or less active enzyme form. This possibility presents an opportunity for future research, particularly given the impact that the concept of allosterity has had on drug development. The discovery of allomorphy also highlights the

importance of understanding fundamental dynamic phenomena in proteins. NMR is an excellent technique for furthering this understanding and the development of powerful computational techniques is likely to generate increasingly accurate insight into protein dynamics.

In the second part of this thesis, an enzyme with a more direct commercial relevance was investigated. Here, the mechanism that enables the alginate lyase, Dp0100, to depolymerise both polyG and polyM forms of its alginate substrate was uncovered. Because of the considerable differences between the chain conformations of polyG and polyM, most of the alginate lyase enzymes discovered to date are capable of depolymerising only one of them. Dp0100 is unusual in that it has dual specificity towards these substrates. Crystallographic evidence was presented indicating that an alternative conformation of polyG alginate is stabilised in the active site of Dp0100. In this alternative conformation, the chain structure of polyG mirrors that of its C5 epimer, polyM. The few structural differences that remain between the two substrates are then managed by the existence in the active site of two separate residues that can act as a general base.

The alternative polyG conformation present in the active site of Dp0100 goes against the literature consensus for the structure of polyG. Efforts were therefore made to observe this alternative polyG conformation in solution. In corroboration of previous results, little evidence was found to suggest that the alternative conformation exists in any substantial population in solution. It is therefore concluded that the active site of Dp0100 is able to stabilise the alternative conformation. It is possible that Dp0100 is capable of catalysing the conformational change required for the reaction with polyG and this is an area in which more research is required. What is also unclear is whether this alternative conformation is important in the poorly understood process of alginate gelation. Ca^{2+} ions are required for alginate gelation to occur and the presence of a Ca^{2+} ion in the alginate-bound Dp0100 active site hints that stabilisation of this alternative polyG conformation may be involved in gelation. The structure of the inter-chain junction zones in Ca-alginate gels is still disputed and this new conformation of polyG identified here shows that alternative conformations of alginate must be considered in hypotheses concerning the structure of alginate gels. X-ray crystal structures give excellent insight into the workings of enzymes like Dp0100 and β PGM, but with the support of techniques that are capable of measuring dynamic properties of these molecules, a far richer

structural description can be achieved. As with allomorphy in β PGM, without an understanding of the conformational changes that occur during catalysis, the behaviour of Dp0100 would be difficult to explain.

These investigations into β PGM and Dp0100 give specific evidence of the ways in which conformational changes contribute to enzyme catalysis. In both instances, a conformational change alters the way the enzyme interacts with substrate. In the case of β PGM, the two different conformers of the substrate-free enzyme interact differently with substrates, with alternative phosphorylating agents such as F16BP unable to immediately generate a fully active β PGM population. In Dp0100, it is the substrate itself that changes conformation, enabling a single active site to catalyse the cleavage of two distinct polymers. The intricacy of the mechanisms described in this thesis for just two enzymes raises the staggering possibility that there exists just as much complexity in the mechanisms of a vast number of enzymes across the kingdom of life.

In conclusion, it is clear that conformational changes are important in the function of biomolecules such as enzymes. A deeper understanding of the conformational changes that take place during enzyme catalysis could provide a platform for new classes of drugs or different ways to control the gelling properties of alginate.

7. References

1. Urquhart, L. Top Companies and Drugs by Sales in 2019. *Nat. Revs. Drug Discovery.* **19**, 228 (2020).
2. Kries, H., Blomberg, R., Hilvert, D. *De Novo* Enzymes by Computational Design. *Curr. Op. Chem. Biol.* **17**, 221–228 (2013).
3. Eyring, H. The Activated Complex in Chemical Reactions. *J. Chem. Phys.* **3**, 107 (1935).
4. Pauling, L. Nature of Forces between Large Molecules of Biological Interest. *Nature.* **161**, 707–709 (1948).
5. Schramm, V. L. Enzymatic Transition States and Transition State Analogues. *Curr. Op. Struct. Biol.* **15**, 604–613 (2005).
6. Tramontano, A., Janda, K. D., Lerner, R. A. Catalytic Antibodies. *Science.* **234** (4783), 1566–1570 (1986).
7. Hilvert, D. Critical Analysis of Antibody Catalysis. *Annu. Rev. Biochem.* **69**, 751–793 (2000).
8. Štrajbl, M., Shurki, A., Kato, M., Warshel, A. Apparent NAC Effect in Chorismate Mutase Reflects Electrostatic Transition State Stabilization. *J. Am. Chem. Soc.* **125**, 10228–10237 (2003).
9. Warshel, A., Sharma, P. K., Kato, M., Xiang, Y., Liu, H., Olsson, M. H. M. Electrostatic Basis for Enzyme Catalysis. *Chem. Rev.* **106**, 3210–3235 (2006).
10. Burschowsky, D., van Eerde, A., Ökvist, M., Kienhöfer, A., Kast, P., Hilvert, D., Krengel, U. Electrostatic Transition State Stabilization Rather than Reactant Destabilization Provides the Chemical Basis for Efficient Chorismate Mutase Catalysis. *Proc. Natl. Acad. Sci. U.S.A.* **111**, 17516–17521 (2014).
11. Warshel, A. & Bora, R. P. Perspective: Defining and Quantifying the Role of Dynamics in Enzyme Catalysis. *J. Chem. Phys.* **144**, 1–17 (2016).
12. Stroud, R. M. & Finer-Moore, J. S. Conformational Dynamics Along an Enzymatic Reaction Pathway: Thymidylate Synthase, “the Movie”. *Biochemistry* **42** (2), 239–247 (2003).

13. Amyes, T. L. & Richard, J. P. Specificity in Transition State Binding: The Pauling Model Revisited. *Biochemistry* **52**, (12), 2021–2035 (2013).
14. Lahiri, S. D., Zhang, G., Dai, J., Dunaway-Mariano, D., Allen, K. N. Analysis of the Substrate Specificity Loop of the HAD Superfamily Cap Domain. *Biochemistry* **43**, 2812–2920 (2004).
15. Sigala, P. A., Fafarman, A. T., Bogard, P. E., Boxer, S. G., Herschlag, D. Do Ligand Binding and Solvent Exclusion Alter the Electrostatic Character Within the Oxyanion Hole of an Enzymatic Active Site? *J. Am. Chem. Soc.* **129**, 12104–12105 (2007).
16. Archer, D. G. & Wang, P. The Dielectric Constant of Water and Debye-Hückel Limiting Law Slopes. *J. Phys. Chem. Ref. Data.* **19**, 371–411 (1990).
17. Song, X., Wang, Y., Zhang, S., Yan, S., Li, T., Yao, L. Characterization of the Dielectric Constant in the *Trichoderma reesei* Cel7B Active Site. *J. Chem. Inf. Model.* **55**, 1369–1376 (2015).
18. Hernández, G., Jenney, F. E. Jr., Adams, M. W. W., LeMaster, D. M. Millisecond Time Scale Conformational Flexibility in a Hyperthermophile Protein at Ambient Temperature. *Proc. Natl. Acad. Sci. U.S.A.* **97**, 3166–3170 (2000).
19. Codreanu, S. G., Ladner, J. E., Xiao, G., Stourman, N. V., Hachey, D. L., Gilliland, G. L., Armstrong, R. N. Local Protein Dynamics and Catalysis: Detection of Segmental Motion Associated with Rate-Limiting Product Release by a Glutathione Transferase. *Biochemistry* **41**, 15161–15172 (2002).
20. Wolf-Watz, M., Thai, V., Henzler-Wildman, K., Hadjipavlou, G., Eisenmesser, E. Z., Kern, D. Linkage Between Dynamics and Catalysis in a Thermophilic-Mesophile Enzyme Pair. *Nat. Struct. Mol. Biol.* **11**, 945–949 (2004).
21. Jarymowycz, V. A. & Stone, M. J. Fast Time Scale Dynamics of Protein Backbones: NMR Relaxation Methods, Applications, and Functional Consequences. *Chem. Rev.* **106**, 1624–1671 (2006).
22. Watt, E. D., Shimada, H., Kovrigin, E. L., Loria, J. P. The Mechanism of Rate-Limiting Motions in Enzyme Function. *Proc. Natl. Acad. Sci. U.S.A.* **104**, 11981–11986 (2007).

23. Benkovic, S. J. & Hammes-Schiffer, S. A Perspective on Enzyme Catalysis. *Science*. **301**, 1196–1202 (2003).
24. Agarwal, P. K. A Biophysical Perspective on Enzyme Catalysis. *Biochemistry* **58**, 438–449 (2019).
25. Kerns, S. J., Agafonov, R. V., Cho, Y. –J., Pontiggia, F., Otten, R., Pachov, D. V., Kutter, S., Phung, L. A., Murphy, P. N., Thai, V., Alber, T., Hagan, M. F., Kern, D. The Energy Landscape of Adenylate Kinase During Catalysis. *Nat. Struct. Mol. Biol.* **22**, 124–131 (2015).
26. Jencks, W. P. Binding Energy, Specificity, and Enzymic Catalysis: The Circe Effect. *Adv. Enzymol. Relat. Areas. Mol. Biol.* **43**, 219–410 (1975).
27. Warshel, A. Electrostatic Origin of the Catalytic Power of Enzymes and the Role of Preorganized Active Sites. *J. Biol. Chem.* **273**, 27035–27038 (1998).
28. Bruice, T. C. Some Pertinent Aspects of Mechanism as Determined with Small Molecules. *Annu. Rev. Biochem.* **45**, 331–373 (1976).
29. Hur, S. & Bruice, T. C. The Mechanism of Catalysis of the Chorismate to Prephenate Reaction by the *Escherichia coli* Mutase Enzyme. *Proc. Natl. Acad. Sci. U.S.A.* **99**, 1176–1181 (2002).
30. Hur, S. & Bruice, T. C. Just a Near Attack Conformer for Catalysis (Chorismate to Prephenate Rearrangements in Water, Antibody, Enzymes, and Their Mutants. *J. Am. Chem. Soc.* **125**, 10540–10542 (2003).
31. Griffin, J. L., Bowler, M. W., Baxter, N. J., Leigh, K. N., Dannatt, H. R. W., Hounslow, A. M., Blackburn, G. M., Webster, C. E., Cliff, M. J., Waltho, J. P. Near Attack Conformers Dominate β -Phosphoglucomutase Complexes Where Geometry and Charge Distribution Reflect Those of Substrate. *Proc. Natl. Acad. Sci. U.S.A.* **109**, 6910–6915 (2012).
32. Johnson, L. A., Robertson, A. J., Baxter, N. J., Trevitt, C. R., Bisson, C., Jin, Y., Wood, H. P., Hounslow, A. M., Cliff, M. J., Blackburn, G. M., Bowler, M. W., Waltho, J. P. van der Waals Contact Between Nucleophile and Transferring Phosphorus is Insufficient to Achieve Enzyme Transition-State Architecture. *ACS Catal.* **8**, 8140–8153 (2018).
33. Kraut, D. A., Carroll, K. S., Herschlag, D. Challenges in Enzyme Mechanism and Energetics. *Annu. Rev. Biochem.* **72**, 517–571 (2003).

34. Kamerlin, S. C. L. & Warshel, A. At the Dawn of the 21st Century: Is Dynamics the Missing Link for Understanding Enzyme Catalysis? *Proteins*. **78**, 1339–1375 (2010).
35. Herschlag, D. & Natarajan, A. Fundamental Challenges in Mechanistic Enzymology: Progress Toward Understanding the Rate Enhancement of Enzymes. *Biochemistry* **52**, 2050–2067 (2013).
36. Jacob, F. & Monod, J. Genetic Regulatory Mechanisms in the Synthesis of Proteins. *J. Mol. Biol.* **3**, 318–356 (1961).
37. Lewis, M. The *lac* Repressor. *Comptes Rendus Biologies*. **328**, 521–548 (2005).
38. Schimke, R. T. & Doyle, D. Control of Enzyme Levels in Animal Tissues. *Annu. Rev. Biochem.* **39**, 929–976 (2017).
39. Ciechanover, A. Proteolysis: From the Lysosome to Ubiquitin and the Proteasome. *Nat. Revs. Mol. Cell Biol.* **6**, 79–87 (2005).
40. de Graffenreid, C. L. & Bertozzi, C. R. The Roles of Enzyme Localization and Complex Formation in Glycan Assembly within the Golgi Apparatus. *Curr. Opin. Cell. Biol.* **16**, 356–363 (2004).
41. Castellana, M., Wilson, M. Z., Xu, Y., Joshi, P., Cristea, I. M., Rabinowitz, J. D., Gitai, Z., Wingreen, N. S. Enzyme Clustering Accelerates Processing of Intermediates Through Metabolic Channeling. *Nat. Biotechnol.* **32**, 1011–1018 (2014).
42. Krebs, E. G. & Beavo, J. A. Phosphorylation-Dephosphorylation of Enzymes. *Ann. Rev. Biochem.* **48**, 923–959 (1979).
43. Zhao, S., Xu, W., Jiang, W., Yu, W., Lin, Y., Zhang, T., Yao, J., Zhou, L., Zeng, Y., Li, H., Li, Y., Shi, J., An, W., Hancock, S. M., He, F., Qin, L., Chin, J., Yang, P., Chen, X., Lei, Q., Xiong, Y., Guan, K. -L. Regulation of Cellular Metabolism by Protein Lysine Acetylation. *Science*. **327**, 1000–1004 (2010).
44. Monod, J., Changeux, J. -P., Jacob, F. Allosteric Proteins and Cellular Control Systems. *J. Mol. Biol.* **6**, 306–329 (1963).
45. Changeux, J. -P. 50 Years of Allosteric Interactions: the Twists and Turns of the Models. *Nat. Revs. Mol. Cell Biol.* **14**, 819–829 (2013).

46. Motlagh, H. N., Wrabl, J. O., Li, J., Hilser, V. J. The Ensemble Nature of Allostery. *Nature*. **508**, 331–339 (2014).
47. Liu, X., Lu, S., Song, K., Shen, Q., Ni, D., Li, Q., He, X., Zhang, H., Wang, Q., Chen, Y., Li, X., Wu, J., Sheng, C., Chen, G., Liu, Y., Lu, X., Zhang, J. Unraveling Allosteric Landscapes of Allosterome with ASD. *Nucleic Acids Res.*. **48**, D394–D401 (2020).
48. Whittington, A. C., Larion, M., Bowler, J. M., Ramsey, K. M., Brüschweiler, R., Miller, B. G. Dual Allosteric Activation Mechanism in Monomeric Human Glucokinase. *Proc. Natl. Acad. Sci. U.S.A.* **112**, 11553–11558 (2015).
49. Hilser, V. J., Anderson, J. A., Motlagh, H. N. Allostery vs. “Allokairy”. *Proc. Natl. Acad. Sci. U.S.A.* **112** (37), 11430–11431 (2015).
50. Westheimer, F. L. Why Nature Chose Phosphates. *Science*. **235**, 1173–1178 (1987).
51. Lad, C., Williams, N. H., Wolfenden, R. The Rate of Hydrolysis of Phosphomonoester Dianions and the Exceptional Catalytic Proficiencies of Protein and Inositol Phosphatases. *Proc. Natl. Acad. Sci. U.S.A.* **100**, 5607–5610 (2003).
52. Radzicka, A. & Wolfenden, R. A Proficient Enzyme. *Science*. **267**, 90–93 (1995).
53. Manning, G., Whyte, D. B., Martinez, R., Hunter, T., Sudarsanam, S. The Protein Kinase Complement of the Human Genome. *Science*. **298**, 1912–1934 (2002).
54. Wolfenden, R. & Snider, M. J. The Depth of Chemical Time and the Power of Enzymes as Catalysts. *Acc. Chem. Res.* **34**, 938–945 (2001).
55. Jin, Y., Molt, R. W. Jr. , Blackburn, G. M. Metal Fluorides: Tools for Structural and Computational Analysis of Phosphoryl Transfer Enzymes. *Top. Curr. Chem. (Cham.)* **375**, 36 (2017).
56. Rall, T. W. & Sutherland, E. W. Formation of a Cyclic Adenine Ribonucleotide by Tissue Particles. *J. Biol. Chem.* **232**, 1065–1076 (1958).
57. Sternweis, P. C. & Gilman, A. G. Aluminium: A Requirement for Activation of the Regulatory Component of Adenylate Cyclase by Fluoride. *Proc. Natl. Acad. Sci. U.S.A.* **79**, 4888–4891 (1982).

58. Bigay, J., Deterre, P. Pfister, C. & Chabre, M. Fluoroaluminates Activate Transducin-GDP by Mimicking the Gamma-Phosphate of GTP in its Binding Site. *FEBS Lett.* **191**, 181–185 (1985).
59. Higashijima, T., Graziano, M. P., Suga, H., Kainosh, M., Gilman, A. G. ^{19}F and ^{31}P NMR Spectroscopy of G Protein Alpha Subunits. Mechanism of Activation by Al_3^+ and F^- . *J. Biol. Chem.* **266**, 3396–3401 (1991).
60. Coleman, D. E., Berghuis, A. M., Lee, E., Linder, M. E., Gilman, A. G., Sprang, S. R. Structures of Active Conformations of $\text{G}_{\alpha 1}$ and the Mechanism of GTP Hydrolysis. *Science*. **265**, 1405–1412 (1994).
61. Sondek, J., Lambright, D. G., Noel, J. P., Hamm, H. E., Sigler, P. B. GTPase Mechanism of G Proteins from the 1.7-Å Crystal Structure of Transducin α -GDP AlF_4^- . *Nature*. **372**, 276–279 (1994).
62. Prive, G. G., Milburn, M. V., Tong, L., de Vos, A. M., Yamaizumi, Z., Nishimura, S., Kim, S. H. X-ray Crystal Structures of Transforming P21 Ras Mutants Suggest a Transition-State Stabilization Mechanism for GTP Hydrolysis. *Proc. Natl. Acad. Sci. U.S.A.* **89**, 3649–3653 (1992).
63. Graham, D. L., Eccleston, J. F., Lowe, P. N. The Conserved Arginine in Rho-GTPase-Activating Protein is Essential for Efficient Catalysis but Not for Complex Formation with Rho-GDP and Aluminium Fluoride. *Biochemistry* **38**, 985–991 (1999).
64. Graham D. L., Lowe, P. N., Grime, G. W., Marsh, M., Rittinger, K., Smerdon, S. J., Gamblin, S. J., Eccleston, J. F. MgF_3^- as a Transition State Analogue of Phosphoryl Transfer. *Chem. Biol.* **9**, 375–381 (2002).
65. Baxter, N. J., Blackburn, G. M., Marston, J. P., Hounslow, A. M., Cliff, M. J., Bermel, W., Williams, N. H., Hollfelder, F., Wemmer, D. E., Walther, J. P. Anionic Charge Is Prioritized over Geometry in Aluminum and Magnesium Fluoride Transition State Analogs of Phosphoryl Transfer Enzymes. *J. Am. Chem. Soc.* **130**, 3952–3958 (2008).
66. Cliff, M. J., Bowler, M. W., Varga, A., Marston, J. P., Szabó, J., Hounslow, A. M., Baxter, N. J., Blackburn, G. M., Vas, M., Walther, J. P. Transition State Analogue Structures of Human Phosphoglycerate Kinase Establish the Importance of Charge Balance in Catalysis. *J. Am. Chem. Soc.* **132**, 6507–6516 (2010).

67. Xiaoxia, L., Marston, J. P., Baxter, N. J., Hounslow, A. M., Yufen, Z., Blackburn, G. M., Cliff, M. J., Waltho, J. P. Prioritization of Charge over Geometry in Transition State Analogues of a Dual Specificity Protein Kinase. *J. Am. Chem. Soc.* **133**, 3989–3994 (2011).
68. Jin, Y., Cliff, M. J., Baxter, N. J., Dannatt, H. R. W., Hounslow, A. M., Bowler, M. W., Blackburn, G. M., Waltho, J. P. Charge-Balanced Metal Fluoride Complexes for Protein Kinase A with Adenosine Diphosphate and Substrate Peptide SP20. *Angew. Chem. Int. Ed.* **51**, 12242–12245 (2012).
69. Danko, S. J. & Suzuki, H. The Use of Metal Fluoride Compounds as Phosphate Analogs for Understanding the Structural Mechanism in P-type ATPases. *Methods in Molecular Biology.* **1377**, 195–209 (2016).
70. Jin, Y., Molt, R. W. Jr., Waltho, J. P., Richards, N. G. J., Blackburn, G. M. ^{19}F NMR and DFT Analysis Reveal Structural and Electronic Transition State Features for RhoA-Catalyzed GTP Hydrolysis. *Angew. Chem. Int. Ed.* **55**, 3318–3322 (2016)
71. Zeymer, C., Werbeck, N. D., Zimmerman, S., Reinstein, J., Hansen, D. F. Characterizing Active Site Conformational Heterogeneity Along the Trajectory of an Enzymatic Phosphoryl Transfer Reaction. *Angew. Chem.* **128**, 11705–11709 (2016).
72. Ampaw, A., Carroll, M., von Velsen, J., Bhattachari, D., Cohen, A., Bowler, M. W., Jakeman, D. L. Observing Enzyme Ternary Transition State Analogue Complexes by ^{19}F NMR Spectroscopy. *Chem. Sci.* **8**, 8427–8434 (2017).
73. Jin, Y. Molt, R. W. Jr., Pellegrini, E., Cliff, M. J., Bowler, M. W., Richards, N. G. J., Blackburn, G. M., Waltho, J. P. Assessing the Influence of Mutation on GTPase Transition States by Using X-ray Crystallography, ^{19}F NMR, and DFT Approaches. *Angew. Chem. Int. Ed.* **56**, 9732–9735 (2017).
74. McCormick, N. E., Forget, S. M., Syvitski, R. T., Jakeman, D. L. MgF₃– and AlF₄– Transition State Analogue Complexes of Yeast Phosphoglycerate Kinase. *Biochem. Cell Biol.* **95**, 295–303 (2017).
75. Mengyu, G., Molt, R. W. Jr., Jenkins, H. T., Blackburn, G. M., Jin, Y., Antson, A. A. An Unprecedented Octahedral Trifluoromagnesate MgF₃(Wat)– Transition State Analog Reveals The Molecular Mechanism of ATP Hydrolysis by Zika Virus Helicase. Preprint at <https://doi.org/10.26434/chemrxiv.11908401.v1> (2020).

76. Lahiri, S. D., Zhang, G., Dunaway-Mariano, D., Allen, K. N. The Pentacovalent Phosphorus Intermediate of a Phosphoryl Transfer Reaction. *Science*. **299**, 2067–2017 (2003).
77. Baxter, N. J., Olguin, L. F., Goličnik, M., Feng, G., Hounslow, A. M., Bermel, W., Blackburn, G. M., Hollfelder, F., Waltho, J. P., Williams, N. H. A Trojan Horse Transition State Analogue Generated by MgF₃⁻ Formation in an Enzyme Active Site. *Proc. Natl. Acad. Sci. U.S.A.* **103**, 14732–14737 (2006).
78. Lahiri, S. D., Zhang, G., Radstrom, P., Dunaway-Mariano, D., Allen, K. N. Crystallization and Preliminary X-Ray Diffraction Studies of Beta-Phosphoglucomutase from *Lactococcus lactus*. *Acta Crystallogr. D. Biol. Crystallogr.* **58**, 324–326 (2002).
79. Zhang, G. Dai, J., Wang, L., Dunaway-Mariano, D., Tremblay, L. W., Allen, K. N. Catalytic Cycling in Beta-Phosphoglucomutase: A Kinetic and Structural Analysis. *Biochemistry* **44**, 9404–9416 (2005).
80. Dai, J., Wang, L., Allen, K. N., Radstrom, P., Dunaway-Mariano, D. Conformational Cycling in β-Phosphoglucomutase Catalysis: Reorientation of the β-D-Glucose 1,6-(Bis)phosphate Intermediate. *Biochemistry* **45**, 7818–7824 (2006).
81. Lahiri, S. D., Zhang, G., Dunaway-Mariano, D., Allen, K. N. Caught in the Act: Structure of Phosphorylated β-Phosphoglucomutase from *Lactococcus lactis*. *Biochemistry* **41**, 8351–8359 (2002).
82. Baxter, N. J., Bowler, M. W., Alizadeh, T., Cliff, M. J., Hounslow, A. M., Wu, B., Berkowitz, D. B., Williams, N. H., Blackburn, G. M., Waltho, J. P. Atomic Details of Near-Transition State Conformers for Enzyme Phosphoryl Transfer Revealed by MgF₃⁻ Rather than by Phosphoranes. *Proc. Natl. Acad. Sci. U.S.A.* **107**, 4555–4560 (2010).
83. Jin, Y., Bhattachari, D., Pellegrini, E., Forget, S. M., Baxter, N. J., Cliff, M. J., Bowler, M. B., Jakeman, D. L., Blackburn, G. M., Waltho, J. P. α-Fluorophosphonates Reveal How a Phosphomutase Conserves Transition State Conformation Over Hexose Recognition in its Two-Step Reaction. *Proc. Natl. Acad. Sci. U.S.A.* **111**, 12384–12389 (2014).
84. Goličnik, M., Olguin, L. F., Feng, G., Baxter, N. J., Waltho, J. P., Williams, N. H., Hollfelder, F. Kinetic Analysis of β-Phosphoglucomutase and its Inhibition by Magnesium Fluoride. *J. Am. Chem. Soc.* **131**, 1575–1588 (2009).

85. Hirst, E. & Rees, D. A. The Structure of Alginic Acid. Part V. Isolation and Unambiguous Characterization of Some Hydrolysis Products of the Methylated Polysaccharide. *J. Chem. Soc.* 1182–1187 (1965).
86. Rees, D. A. & Samuel, J. W. B. The Structure of Alginic Acid. Part VI. Minor Features and Structural Variations. *J. Chem. Soc. C*. **0**, 2295–2298 (1967).
87. Michel, G., Tonon, T., Scornet, D., Cock, J. M., Kloareg, B. The Cell Wall Polysaccharide Metabolism of the Brown Alga *Ectocarpus siliculosus*. Insights into the Evolution of Extracellular Matrix Polysaccharides in Eukaryotes. *New Phytol.* **188**, 82–97 (2010).
88. Rabillé, H., Torode, T. A., Tesson, B., Le Bail, A., Billoud, B., Rolland, E., Le Panse, S., Jam, M. Charrier, B. Alginates Along the Filament of the Brown Alga *Ectocarpus* Help Cells Cope With Stress. *Sci. Rep.* **9**, 1–17 (2019).
89. Valla, S., Li, J.-P., Ertesvag, H., Barbeyron, T., Lindahl, U. Hexuronyl C5-Epimerases in Alginate and Glycosaminoglycan Biosynthesis. *Biochimie*. **83**, 819–830 (2001).
90. Penman, A. & Sanderson, G. R. A Method for the Determination of Uronic Acid Sequence in Alginates. *Carbohydr. Res.* **25**, 273–282 (1972).
91. Grasdalen, H., Larsen, B., Smidsrød, O. A P.M.R. Study of the Composition and Sequence of Uronate Residues in Alginates. *Carbohydr. Res.* **68**, 23–31 (1979).
92. Morris, E. R., Rees, D. A., Thom, D., Boyd, J. Chiroptical and Stoichiometric Evidence of a Specific Primary Dimerisation Process in Alginate Gelation. *Carbohydr. Res.* **66**, 145–154 (1978).
93. Grant, G. T., Morris, E. R., Rees, D. A., Smith, P. J. C. Thom, D. Biological Interactions Between Polysaccharides and Divalent Cations: The Egg-Box Model. *FEBS Lett.* **32**, 195–198 (1973).
94. Braccini, I. & Pérez, S. Molecular Basis of Ca^{2+} -Induced Gelation in Alginates and Pectins: The Egg-Box Model Revisited. *Biomacromolecules*. **2**, 1089–1096 (2001).
95. Li, L., Fang, Y., Vreeker, R., Appelqvist, I., Mendes, W. Reexamining the Egg-Box Model in Calcium-Alginate Gels with X-ray Diffraction. *Biomacromolecules*. **8**, 464–468 (2007).

96. Rehm, B. H. A. & Valla, S. Bacterial Alginates: Biosynthesis and Applications. *Appl. Microbiol. Biotechnol.* **48**, 281–288 (1997).
97. Szekalska, M., Puciłowska, A., Szymańska, E., Ciosek, P., Winnicka, K. Alginate: Current Use and Future Perspectives in Pharmaceutical and Biomedical Applications. *Int. J. Polym. Sci.* **2016**, 1–17 (2016).
98. Lee, K. Y. & Mooney, D. J. Alginate: Properties and Biomedical Applications. *Prog. Polym. Sci.* **37**, 106–126 (2012).
99. Ionescu, A. R., Bérçes A., Zgierski, M. Z., Whitfield, D. M., Nukada, T. Conformational Pathways of Saturated Six-Membered Rings. A Static and Dynamical Density Functional Study. *J. Phys. Chem. A.* **109**, 8096–8105 (2005).
100. Grasdalen, H., Larsen, B., Smidsrød, O. ^{13}C -N.M.R. Studies of Alginate. *Carbohydr. Res.* **56**, C11–C15 (1977).
101. Grasdalen, H., Larsen, B., Smidsrød, O. ^{13}C -N.M.R. Studies of Monomeric Composition and Sequence in Alginate. *Carbohydr. Res.* **89**, 179–191 (1981).
102. Mo, F., Brobak, T. J., Siddiqui, I. R. Crystal Structure at 87 K of Sodium α -L-Guluronate Dihydrate. *Carbohydr. Res.* **145**, 13–21 (1985).
103. Grasdalen, H., Mo, F., Bjørgum, J. O. Solution and Solid-State ^1H - and ^{13}C -N.M.R. Spectroscopy of Sodium α -L-Guluronate Dihydrate. *Carbohydr. Res.* **203**, 281–286 (1990).
104. Steginsky, C. A., Beale, J. M., Floss, H. G., Mayer, R. M. Structural Determination of Alginic Acid and the Effects of Calcium Binding as Determined by High-Field N.M.R. *Carbohydr. Res.* **225**, 11–26 (1992).
105. McIntyre, D. D., Ceri, H., Vogel, H. J. Nuclear Magnetic Resonance Studies of the Heteropolysaccharides Alginate, Gum Arabic and Gum Xanthan. *Starch/Stärke.* **48**, 285–291 (1996).
106. Mackie, W., Pérez, S., Rizzo, R., Taravel, F., Vignon, M. Aspects of the Conformation of Polyguluronate in the Solid State and in Solution. *Int. J. Biol. Macromol.* **5**, 329–341 (1983).

107. Lee, S. I., Choi, S. H., Lee, E. Y. Molecular Cloning, Purification, and Characterization of a Novel PolyMG-Specific Alginate Lyase Responsible for Alginate MG Block Degradation in *Strenotrophomas maltophilia* KJ-2. *Appl. Microbiol. Biotechnol.* **95**, 1643–1653 (2012).
108. Ji, S., Dix, S. R., Aziz, A. A., Sedelnikova, S. E., Baker, P. J., Rafferty, J. B., Bullough, P. A., Tzokov, S. B., Agirre, J., Li, F.-L., Rice, D. W. The Molecular Basis of Endolytic Activity of a Multidomain Alginate Lyase from *Defluviitalea phaphyphila*, a Representative of a New Lyase Family, PL39. *J. Biol. Chem.* **294**, 18077–18091 (2019).
109. Lombard, V., Golaconda Ramulu, H., Drula, E., Coutinho, P. M., Henrissat, B. The Carbohydrate-Active Enzymes Database (CAZy) in 2013. *Nucleic Acids Res.* **42**, D490–495 (2014).
110. Gacesa, P. A Proposed Unified Mechanism of Action for the Lyases and Epimerases. *FEBS Lett.* **212**, 199–202 (1987).
111. Yip, V. L. Y. & Withers, S. G. Nature's Many Mechanisms for the Degradation of Oligosaccharides. *Org. Biomol. Chem.* **2**, 2707–2713 (2004).
112. Garron, M. -L. & Cygler, M. Structural and Mechanistic Classification of Uronic Acid-Containing Polysaccharide Lyases. *Glycobiology* **20**, 1547–1573 (2010).
113. Zhu, B. & Yin, H. Alginate Lyase: Review of Major Sources and Classification, Properties, Structure-Function Analysis and Applications. *Bioengineered.* **6**, 125–131 (2015).
114. Ji, S., Wang, B., Lu, M., Li, F. -L. *Defluviitalea phaphyphila* sp. nov., A Novel Thermophilic Bacterium that Degrades Brown Algae. *Appl. and Environ. Microbiol.* **82**, 868–877 (2016).
115. Derome, A. E. *Modern NMR Techniques for Chemistry Research*. 6th Edition. Kidlington: Pergamon, 1987. ISBN: 0-08-032513-0.
116. Neuhaus, D. & Williamson, M. P. *The Nuclear Overhauser Effect in Structural and Conformational Analysis*. Chichester: John Wiley & Sons, 1989. ISBN: 9780471186847
117. Levitt, M. H. *Spin Dynamics. Basics of Nuclear Magnetic Resonance*. Chichester: John Wiley & Sons, 2001. ISBN: 978-0-470-51117-6.

118. Pascal, S. M. *NMR Primer: An HSQC-Based Approach*. Chichester: IM Publications LLP, 2008. ISBN: 978-1-901019-08-7.
119. Keeler, J. *Understanding NMR Spectroscopy*. 2nd Edition. New Jersey: John Wiley & Sons, 2011. ISBN: 978-0-470-74608-0.
120. Wegner A., Meiser, J., Weindl, D., Hiller, K. How metabolites modulate metabolic flux. *Cur.r Opin. Biotechnol.* **34**, 16–22 (2015).
121. Pardee, A. B. Regulatory molecular biology. *Cell Cycle* **5**, 846–852 (2006).
122. Iommarini, L., Ghelli, A., Gasparre, G., Porcelli, A. M. Mitochondrial metabolism and energy sensing in tumor progression. *Biochim. Biophys. Acta, Bioenergetics*. **1858**, 582–590 (2017).
123. Schimke, R.T., Doyle, D. Control of enzyme levels in animal tissues. *Annu. Rev. Bioch.* **39**, 929–976 (1970).
124. Welch, G. R. On the role of organized multienzyme systems in cellular metabolism: A general synthesis. *Prog. Biophys. Mol. Biol.* **32**, 103–191 (1978).
125. Monod, J., Wyman, J., Changeux, J. P. On the nature of allosteric transitions: A plausible model. *J. Mo.l Biol.* **12**, 88–118 (1965).
126. Koshland, D. E. Jr., Némethy, G., Filmer, D. Comparison of experimental binding data and theoretical models in proteins containing subunits. *Biochemistry* **5**, 365–385 (1966).
127. Changeux, J. P. 50 years of allosteric interactions: The twists and turns of the models. *Nat. Rev. Mol. Cell Biol.* **14**, 819–829 (2013).
128. Neves, A. R., Pool, W. A., Kok, J., Kuipers, O. P., Santos, H. Overview on sugar metabolism and its control in *Lactococcus lactis* – The input from in vivo NMR. *FEMS Microbiol. Rev.* **29**, 531–554 (2005).
129. Qian, N., Stanley, G. A., Hahn-Hägerdal, B., Rådström, P. Purification and characterization of two phosphoglucomutases from *Lactococcus lactis* subsp. *lactis* and their regulation in maltose- and glucose-utilizing cells. *J. Bacteriol.* **176**, 5304–5311 (1994).
130. Qian, N., Stanley, G. A., Bunte, A., Rådström, P. Product formation and phosphoglucomutase activities in *Lactococcus lactis*: Cloning and characterization of a novel

phosphoglucomutase gene. *Microbiology* **143**, 855–865 (1997).

131. Andersson, U., Molenaar, D., Rådström, P., de Vos, W. M. Unity in organization and regulation of catabolic operons in *Lactobacillus plantarum*, *Lactococcus lactis* and *Listeria monocytogenes*. *Syst. Appl. Microbiol.* **28**, 187–195 (2005).
132. Andersson, U., Levander, F., Rådström, P. Trehalose 6-phosphate phosphorylase is part of a novel metabolic pathway for trehalose utilization in *Lactococcus lactis*. *J. Biol. Chem.* **276**, 42707–42713 (2001).
133. Sjöberg, A., Hahn-Hägerdal, B. β -Glucose 1-phosphate, a possible mediator for polysaccharide formation in maltose-assimilating *Lactococcus lactis*. *Appl. Environ. Microbiol.* **55**, 1549–1554 (1989).
134. Levander, F., Andersson, U., Rådström, P. Physiological role of β -phosphoglucomutase in *Lactococcus lactis*. *Appl. Environ. Microbiol.* **67**, 4546–4553 (2001).
135. Dai, J., Finci, L., Zhang, C., Lahiri, S., Zhang, G., Peisach, E., Allen, K. N., Dunaway-Mariano, D. Analysis of the structural determinants underlying discrimination between substrate and solvent in β -phosphoglucomutase catalysis. *Biochemistry* **48**, 1984–1995 (2009).
136. Wong, M., Khirich, G., Loria, J. P. What's in your buffer? Solute altered millisecond motions detected by solution NMR. *Biochemistry* **52**, 6548–6558 (2013).
137. Gardner, K. H., Kay, L. E. The use of ^2H , ^{13}C , ^{15}N multidimensional NMR to study the structure and dynamics of proteins. *Annu. Rev. Biophys. Biomol. Struct.* **27**, 357–406 (1998).
138. Shen, Y. & Bax, A. Protein backbone and sidechain torsion angles predicted from NMR chemical shifts using artificial neural networks. *J. Biomol. NMR* **56**, 227–241 (2013).
139. Goel, A., Santos, F., de Vos, W. M., Teusink, B., Molenaar, D. Standardized assay medium to measure *Lactococcus lactis* enzyme activities while mimicking intracellular conditions. *Appl. Environ. Microbiol.* **78**, 134–143 (2012).
140. Zamberlin, Š., Antunac, N., Havranek, J., Samaržija, D. Mineral elements in milk and dairy products. *Mljekarstvo* **62**, 111–125 (2012).
141. Grathwohl, C., Wüthrich, K. NMR studies of the rates of proline *cis-trans* isomerisation in oligopeptides. *Biopolymers* **20**, 2623–2633 (1981).

142. Lu, K. P., Finn, G., Lee, T. H., Nicholson, L. K. Prolyl *cis-trans* isomerisation as a molecular timer. *Nat. Chem. Biol.* **3**, 619–629 (2007).
143. Shen, Y. & Bax, A. Prediction of Xaa-Pro peptide bond conformation from sequence and chemical shifts. *J. Biomol. NMR* **46**, 199–204 (2010).
144. Cruz-Navarrete, F. A., Baxter, N. J., Wood, H. P., Hounslow, A. M., Walther, J. P. ^1H , ^{15}N and ^{13}C backbone resonance assignment of the P146A variant of β -phosphoglucomutase from *Lactococcus lactis* in its substrate-free form. *Biomol. NMR Assign.* **13**, 349–356 (2019).
145. Klein, A. H., Shulla, A., Reimann, S. A., Keating, D. H., Wolfe, A. J. The intracellular concentration of acetyl phosphate in *Escherichia coli* is sufficient for direct phosphorylation of two-component response regulators. *J. Bacteriol.* **189**, 5574–5581 (2007).
146. Bennett, B. D., Kimball, E. H., Gao, M., Osterhout, R., Van Dien, S. J., Rabinowitz, J. D. Absolute metabolic concentrations and implied enzyme active site occupancy in *Escherichia coli*. *Nat. Chem. Biol.* **5**, 593–599 (2009).
147. Odefey, C., Mayr, L. M., Schmid, F. X. Non-prolyl *cis-trans* peptide bond isomerisation as a rate-determining step in protein unfolding and refolding. *J. Mol. Biol.* **245**, 69–78 (1995).
148. Frieden, C. Slow transitions and hysteretic behavior in enzymes. *Ann. Rev. Biochem.* **48**, 471–489 (1979).
149. Ricard, J., Meunier, J. C., Buc, J. Regulatory behavior of monomeric enzymes: The mnemonical enzyme concept. *Eur. J. Biochem.* **49**, 195–208 (1974).
150. Ainslie, G. R., Shill, J. P., Neet, K. E. Transients and cooperativity: A slow transition model for relating transients and cooperative kinetics of enzymes. *J. Biol. Chem.* **247**, 7088–7096 (1972).
151. Chae, Y. K., Markley, J. L. Functional recombinant rabbit muscle phosphoglucomutase from *Escherichia coli*. *Protein Expr. Purif.* **20**, 124–127 (2000).
152. Zhang, C., Allen, K. N., Dunaway-Mariano, D. Mechanism of substrate recognition and catalysis of the haloalkanoic acid dehalogenase family member α -phosphoglucomutase. *Biochemistry* **57**, 4504–4517 (2018).

153. Oesterhelt, C., Schnarrenberger, C., Gross, W. The reaction mechanism of phosphomannomutase in plants. *FEBS Lett.* **401**, 35–37 (1997).
154. Reed, M. A. C., Hounslow, A. M., Sze, K. H., Barsukov, I. G., Hosszu, L. L. P., Clarke, A. R., Craven, C. J., Walther, J. P. Effects of domain dissection on the folding and stability of the 43 kDa protein PGK probed by NMR. *J. Mol. Biol.* **330**, 1189–1201 (2003).
155. Wood, H. P., Baxter, N. J., Trevitt, C. R., Cruz-Navarrete, F. A., Hounslow, A. M., Walther, J. P. Enzymatic production of β-glucose 1,6-bisphosphate through manipulation of catalytic magnesium coordination. *Green Chem.* **23**, 752–762 (2021).
156. Hyberts, S. G., Robson, S. A., Wagner, G. Exploring signal-to-noise ratio and sensitivity in non-uniformly sampled multi-dimensional NMR spectra. *J. Biomol. NMR* **55**, 167–178 (2013).
157. Hyberts, S. G., Milbradt, A. G., Wagner, A. B., Arthanari, H., Wagner, G. Application of iterative soft thresholding for fast reconstruction of NMR data non-uniformly sampled with multidimensional Poisson Gap scheduling. *J. Biomol. NMR* **52**, 315–327 (2012).
158. Sun, Z. Y. J., Frueh, D. P., Selenko, P., Hoch, J. C., Wagner, G. Fast assignment of ¹⁵N-HSQC peaks using high-resolution 3D HNcocaNH experiments with non-uniform sampling. *J. Biomol. NMR* **33**, 43–50 (2005).
159. Midelfort, C. F., Gupta, R. K., Rose, I. A. Fructose 1,6-bisphosphate: Isomeric composition, kinetics, and substrate specificity for the aldolases. *Biochemistry* **15**, 2178–2185 (1976).
160. Winter, G. *xia2*: An expert system for macromolecular crystallography data reduction. *J. Appl. Cryst.* **43**, 186–190 (2010).
161. Evans, P. R., Murshudov, G. N. How good are my data and what is the resolution? *Acta Cryst. D* **69**, 1204–1214 (2013).
162. Vagin, A., Teplyakov, A. MOLREP: An automated program for molecular replacement. *J. Appl. Cryst.* **30**, 1022–1025 (1997).
163. Emsley, P., Lohkamp, B., Scott, W. G., Cowtan, K. Features and development of COOT. *Acta Cryst. D* **66**, 486–501 (2010).

164. Murshudov, G. N., Vagin, A. A., Dodson, E. J. Refinement of macromolecular structures by the maximum-likelihood method. *Acta. Cryst.* **D53**, 240–255 (1997).
165. Chen, V. B., Arendall, W. B., Headd, J. J., Keedy, D. A., Immormino, R. M., Kapral, G. J., Murray, L. W., Richardson, J. S., Richardson, D. C. MolProbity: All-atom structure validation for macromolecular crystallography. *Acta. Cryst.* **D66**, 12–21 (2010).
166. The PyMOL Molecular Graphics System, Version 1.8. (Schrödinger, LLC, 2015).
167. McNicholas, S., Potterton, E., Wilson, K. S., Noble, M. E. M. Presenting your structures: The CCP4mg molecular-graphics software. *Acta. Cryst.* **D67**, 386–394 (2011).
168. Huang, P.-S., Boyken, S. E., Baker, D. The coming of age of *de novo* protein design. *Nature* **357**, 320–327 (2016).
169. Chen, K. & Arnold, F. H. Engineering new catalytic activities in enzymes. *Nat. Catal.* **3**, 203–213 (2020).
170. Bolon, D. N. & Mayo, S. L., Enzyme-like proteins by computational design. *Proc. Natl. Acad. Sci. U.S.A.* **98**, 14274–14279 (2001).
171. Wen, F., Nair, N. U., Zhao, H. Protein engineering in designing tailored enzymes and microorganisms for biofuels production. *Curr. Opin. Biotechnol.* **20**, 412–419 (2009).
172. Zanghellini, A. *De novo* computational enzyme design. *Curr. Opin. Biotechnol.* **29**, 132–138 (2014).
173. Yoshida, S., Hiraga, K., Takehana, T., Taniguchi, I., Yamaji, H., Maeda, Y., Toyohara, K., Miyamoto, K., Kimura, Y., Oda, K. A bacterium that degrades and assimilates poly(ethylene terephthalate). *Science* **351**, 1196–1199 (2016).
174. Jones, S. & Selitsianos, D. A simple and effective method for phosphoryl transfer using TiCl₄ catalysis. *Org. Lett.* **4**, 3671–3673 (2002).
175. Jones, S., Selitsianos, D., Thompson, K. J., Toms, S. M. An improved method for Lewis acid catalyzed phosphoryl transfer with Ti(t-BuO)₄. *J. Org. Chem.* **68**, 5211–5216 (2003).

176. Elsässer, B., Dohmeier-Fischer, S., Fels, G. Theoretical investigation of the enzymatic phosphoryl transfer of β -phosphoglucomutase: Revisiting both steps of the catalytic cycle. *J. Mol. Model.* **18**, 3169–3179 (2012).
177. Chan, P. S., Black, C. T., Williams, B. J. Separation of cyclic 3',5'-AMP from ATP, ADP, and 5'-AMP by precipitation with inorganic compounds. *Anal. Biochem.* **55**, 16–25 (1973).
178. Carlson, M., Carter, J. D., Rohloff, J. Improved preparation of 2 M triethylammonium bicarbonate. *Green Chem. Lett. Rev.* **8**, 37–39 (2015).
179. Wood, H. P., Cruz-Navarrete, F. A., Baxter, N. J., Trevitt, C. R., Robertson, A. J., Dix, S. R., Hounslow, A. M., Cliff, M. J., Walther, J. P. Allomorphy as a mechanism of post-translational control of enzyme activity. *Nat. Commun.* **11**, 1–12 (2020).
180. Paradisi, F., Dean, J. L., Geoghegan, K. F., Engel, P. C. Spontaneous chemical reversion of an active site mutation: Deamidation of an asparagine residue replacing the catalytic aspartic acid of glutamate dehydrogenase. *Biochemistry* **44**, 3636–3643 (2005).
181. Holt, L. E., Pierce, J. A., Kajdi, C. N. The solubility of the phosphates of strontium, barium, and magnesium and their relation to the problem of calcification. *J. Colloid. Sci.* **9**, 409–426 (1954).
182. Seegmiller, J. E. & Horecker, B. L. The synthesis of glucose-6-phosphate and 6-phosphogluconate. *J. Biol. Chem.* **192**, 175–180 (1951).
183. Brown, D. M. & Usher, D. A. Hydrolysis of hydroxyalkyl phosphate esters: The epoxide route. *J. Chem. Soc.*, 6547–6558 (1965).
184. Brown, D. M. & Usher, D. A. Hydrolysis of hydroxyalkyl phosphate esters: Effect of changing ester group. *J. Chem. Soc.*, 6558–6564 (1965).
185. Posternak, T. Synthesis of α - and β -glucose-1,6-diphosphate. *J. Biol. Chem.* **180**, 1269–1278 (1949).
186. Linker, A. & Jones, R. S. A. Polysaccharide Resembling Alginic Acid from a *Pseudomonas* Micro-Organism. *Nature* **204**, 187–188 (1964).
187. Larsen, B. & Haug, A. Biosynthesis of Alginate. *Carbohydr. Res.* **17**, 287–296 (1971).

188. Sadoff, H. L. Encystment and Germination in *Azotobacter vinelandii*. *Bacteriol. Rev.* **39**, 516–539 (1975).
189. Cote, G. L. & Krull, L. H. Characterization of the Exocellular Polysaccharides from *Azotobacter chroococcum*. *Carbohydr. Res.* **181**, 143–152 (1988).
190. May, T. B. & Chakrabarty, A. M. *Pseudomonas aeruginosa*: genes and enzymes of alginate synthesis. *Trends in Microbiol.* **2**, 151–157 (1994).
191. Lee, K. Y. & Mooney, D. J. Alginate: Properties and Biomedical Applications. *Prog. Polym. Sci.* **37**, 106–126 (2012).
192. Xu, X., Bi, D., Wu, X., Wang, Q., Wei, G., Chi, L., Jiang, Z., Oda, T., Wan, M. Unsaturated Guluronate Oligosaccharide Enhances the Antibacterial Activities of Macrophages. *FASEB*. **28**, 2645–2654 (2014).
193. Haug, A., Larsen, B., Smidsrød, O. A Study on the Constitution of Alginic Acid by Partial Acid Hydrolysis. *Acta Chem. Scand.* **20**, 183–190 (1966).
194. Smidsrød, O. & Haug, A. Dependence Upon the Gel-Sol State of the Ion-Exchange Properties of Alginates. *Acta Chem. Scand.* **26**, 2063–2074 (1972).
195. Morris, E. R., Rees, D. A., Thom, D. Characterization of Polysaccharide Structure and Interactions by Circular Dichromism: Order-Disorder Transition in Calcium Alginate System. *J. Chem. Soc., Chem. Commun.* **7**, 245–246 (1973).
196. Braccini, I., Grasso, R. P., Pérez, S. Conformational and Configurational Features of Acidic Polysaccharides and Their Interactions with Calcium Ions: a Molecular Modeling Investigation. *Carbohydr. Res.* **317**, 119–130 (1999).
197. Al-Shamkhani, A. & Duncan, R. Radioiodination of Alginate via Covalently-Bound Tyrosinamide Allows Monitoring of its Fate In Vivo. *J. Bioact. Compat. Polym.* **10**, 4–13 (1995).
198. Davies, G. J., Wilson, K. S., Henrissat, B. Nomenclature for Sugar-Binding Subsites in Glycosyl Hydrolases. *Biochem. J.* **321**, 557–559 (1997).
199. Bubb, W. A. NMR Spectroscopy in the Study of Carbohydrates: Characterizing the Structural Complexity. *Concepts in Magnetic Resonance Part A*. **19**, 1–19 (2003).

200. Laignel, B., Bliard, C., Massiot, G., Nuzillard, J. M. Proton NMR Spectroscopy Assignment of D-Glucose Residues in Highly Acetylated Starch. *Carbohydr. Res.* **298**, 251–260 (1997).
201. Murshudov, G. N., Skubák, P., Lebedev, A. A., Pannu, N. S., Steiner, R. A., Nicholls, R. A., Winn, M. D., Long, F., Vagin, A. A. REFMAC5 for the refinement of macromolecular crystal structures. *Acta Crystallogr. Sect. D Biol. Crystallogr.* **67**, 355–367 (2011).
202. McCoy, A. J., Grosse-Kunstleve, R. W., Adams, P. D., Winn, M. D., Storoni, L. C., Read, R. J. Phaser crystallographic software. *J. Appl. Crystallogr.* **40**, 658–674 (2007).
203. Winter, G. Xia2: An expert system for macromolecular crystallography data reduction. *J. Appl. Crystallogr.* **43**, 186–190 (2010).
204. Winter, G. & McAuley, K. E. Automated data collection for macromolecular crystallography. *Methods* **55**, 81–93 (2011).
205. Agirre, J., Iglesias-Fernandez, J., Rovira, C., Davies, G. J., Wilson, K. S., and Cowtan, K. D. Privateer: software for the conformational validation of carbohydrate structures. *Nat. Struct. Mol. Biol.* **22**, 833–834 (2015).
206. Kabsch, W. Xds. *Acta Crystallogr. Sect. D Biol. Crystallogr.* **66**, 125–132 (2010).
207. Vonrhein, C., Flensburg, C., Keller, P., Sharff, A., Smart, O., Paciorek, W., Womack, T., Bricogne, G. Data processing and analysis with the autoPROC toolbox. *Acta Crystallogr. Sect. D Biol. Crystallogr.* **67**, 293–302 (2011).
208. Nonaka, T. The CCP4 Suite-Computer Programs for Protein Crystallography. *Nihon Kessho Gakkaishi.* **36**, 224–227 (1994).
209. Monticelli, M, Liguori, L., Allocca, M., Andreotti, G., Cubellis, M. V. β -Glucose-1,6-bisphosphate stabilizes pathological phophomannomutase2 mutants in vitro and represents a lead compound to develop pharmacological chaperones for the most common disorder of glycosylation, PMM2-CDG. *Int. J. Mol. Sci.* **20**, 4164 (2019).
210. Sigel, E. & Baur, R. Allosteric Modulation by Benzodiazepine Receptor Ligands of the GABA_A Receptor Channel Expressed in *Xenopus* Oocytes. *J. Neurosci.* **8**, 289–295 (1988).

8. Appendix A – Supplementary Information

SUPPLEMENTARY INFORMATION

Allomorphy as a mechanism of post-translational control of enzyme activity

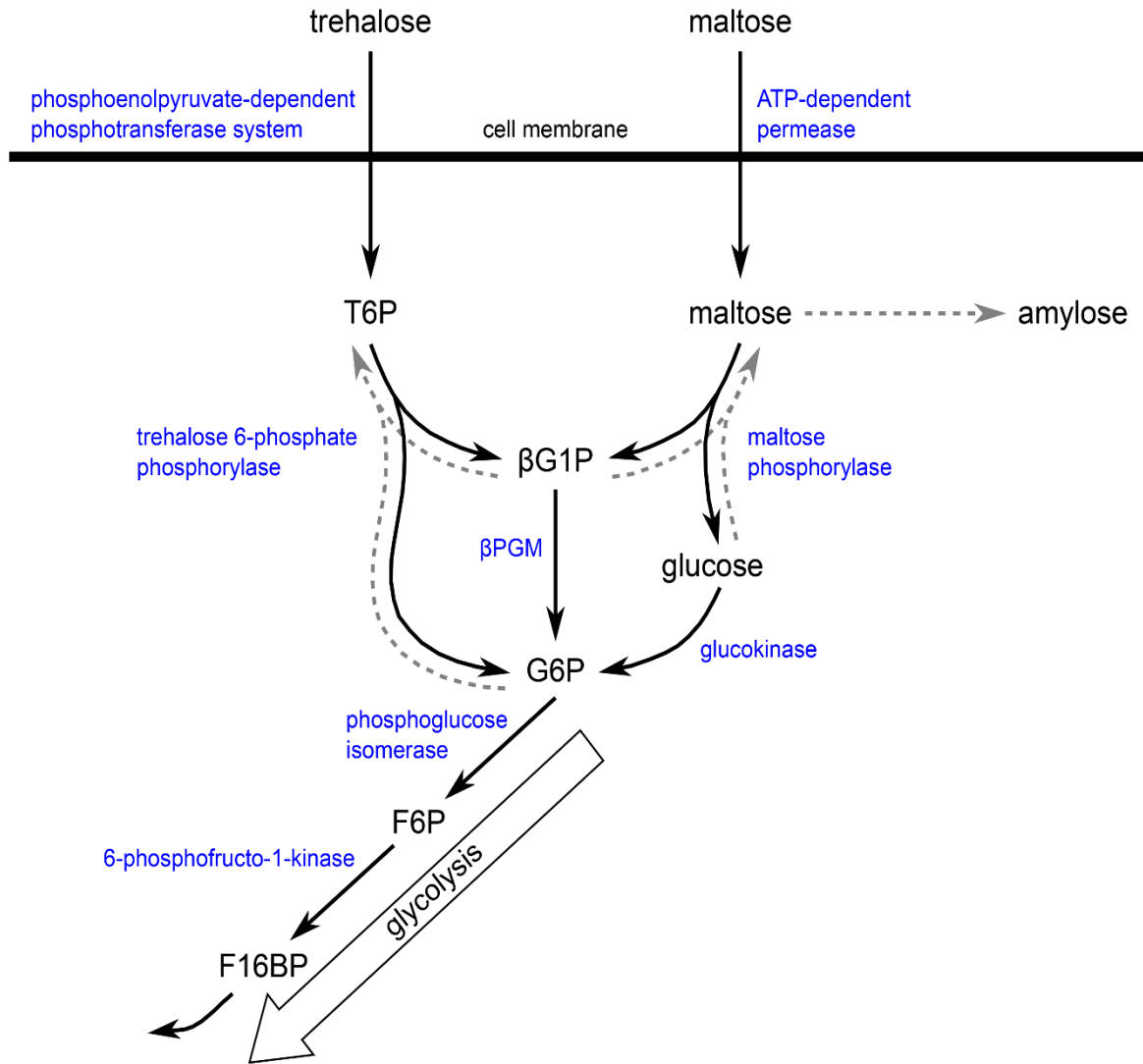
Henry P. Wood^{a,1}, F. Aaron Cruz-Navarrete^{a,1,*}, Nicola J. Baxter^{a,b,1}, Clare R. Trevitt^a, Angus J. Robertson^{a,c}, Samuel R. Dix^a, Andrea M. Hounslow^a, Matthew J. Cliff^b, and Jonathan P. Waltho^{a,b,*}

^aKrebs Institute for Biomolecular Research, Department of Molecular Biology and Biotechnology, The University of Sheffield, Sheffield, S10 2TN, United Kingdom;

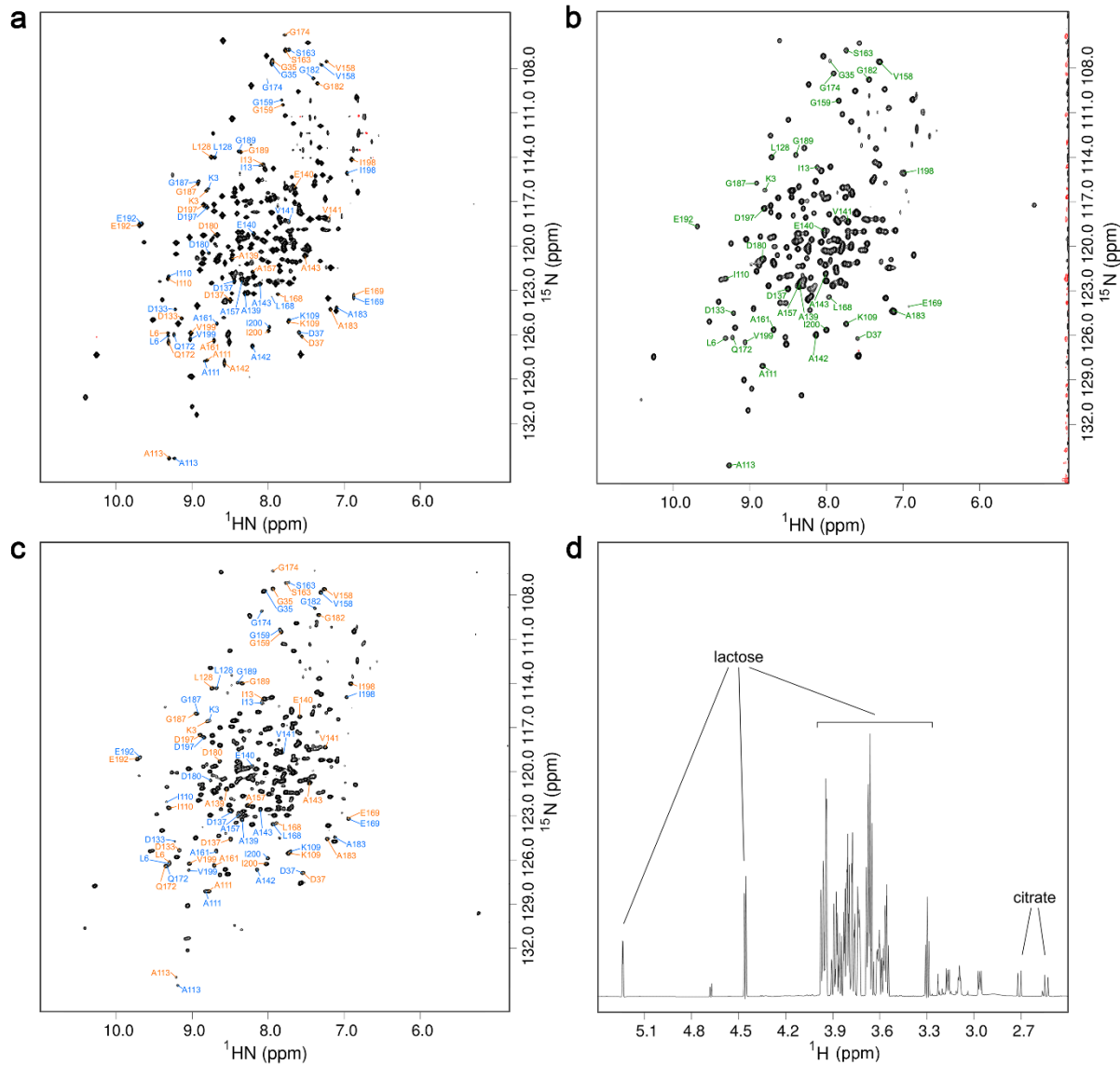
^bManchester Institute of Biotechnology and School of Chemistry, The University of Manchester, Manchester, M1 7DN, United Kingdom; ^cPresent address: Laboratory of Chemical Physics, National Institute of Diabetes and Digestive and Kidney Diseases, National Institutes of Health, Bethesda, Maryland 20892, United States

¹H.P.W., F.A.C.N. and N.J.B contributed equally to this work

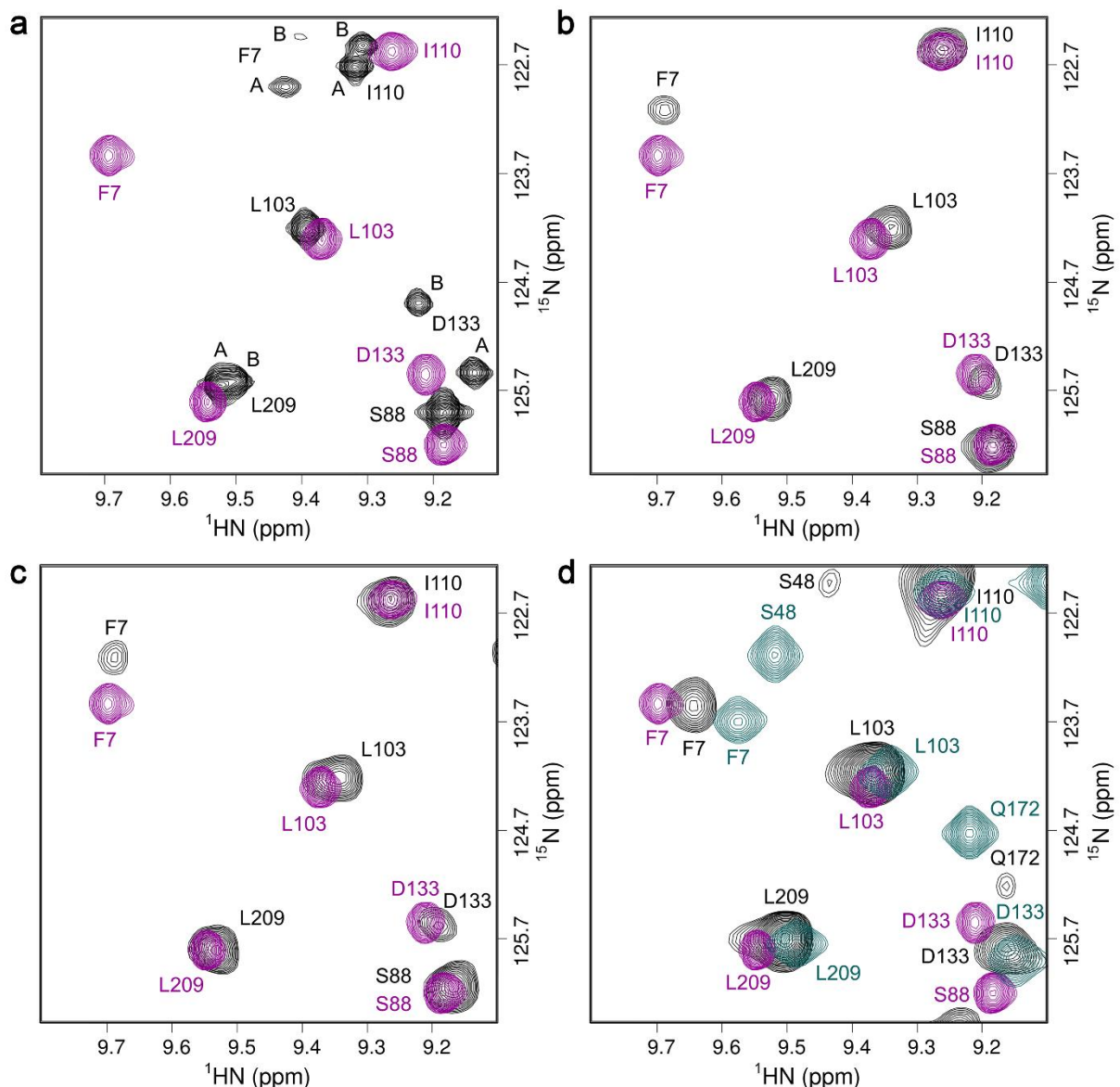
*To whom correspondence may be addressed: Prof. Jonathan Waltho and F. Aaron Cruz-Navarrete, Krebs Institute for Biomolecular Research, Department of Molecular Biology and Biotechnology, University of Sheffield, Sheffield, S10 2TN, United Kingdom, +44 114 22717, j.waltho@sheffield.ac.uk, ORCID 0000-0002-7402-5492, facruznavarrete1@sheffield.ac.uk, ORCID 0000-0002-5233-581X



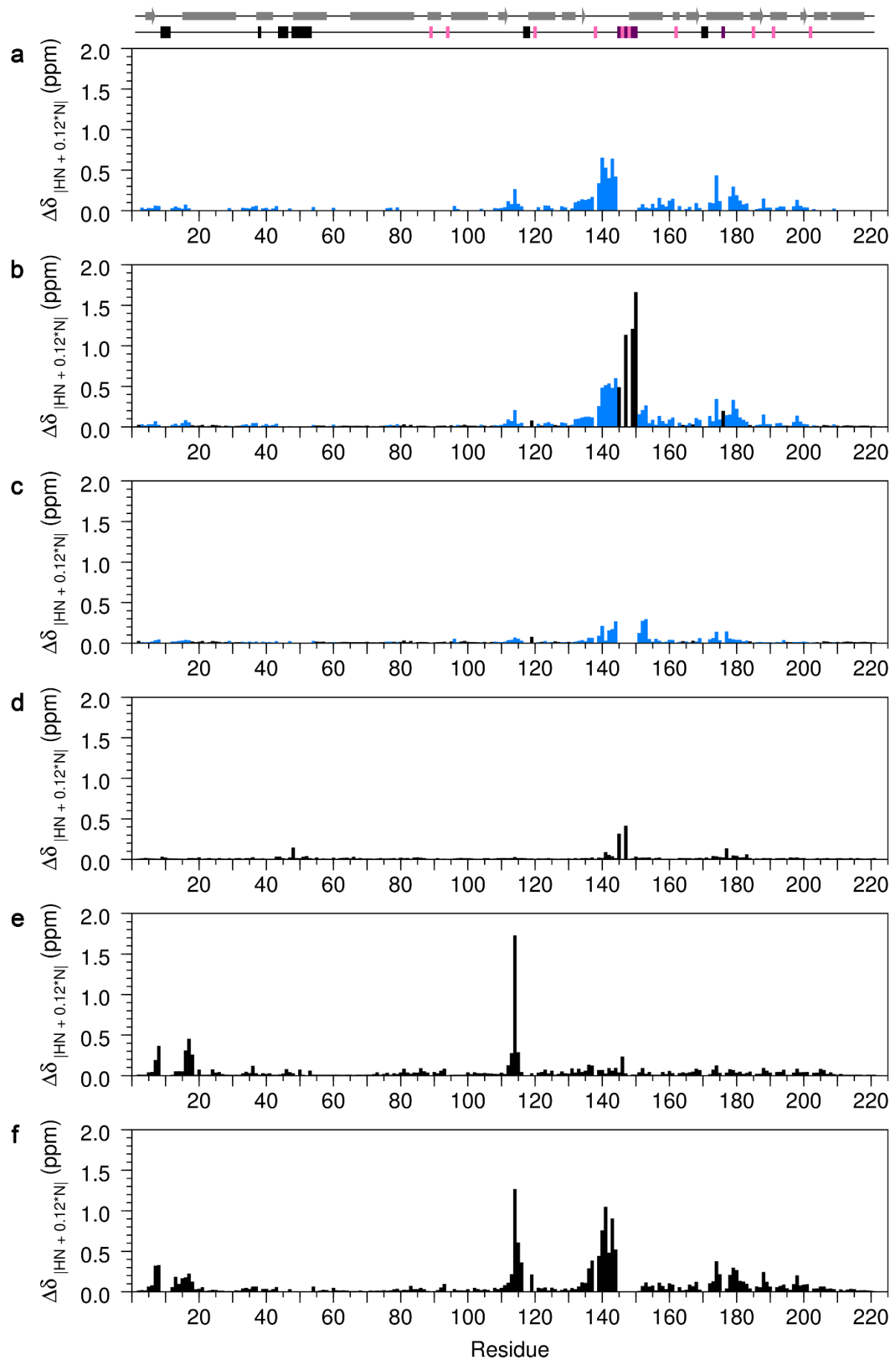
Supplementary Figure 3.1. Pathways for trehalose and maltose metabolism in *L. lactis*. Trehalose is transported into cells by the phosphoenolpyruvate-dependent phosphotransferase system yielding T6P, which is phosphorolysed by P_i -dependent trehalose 6-phosphate phosphorylase to β G1P and G6P. In contrast, maltose enters cells by the ATP-dependent permease system and is phosphorolysed by the action of P_i -dependent maltose phosphorylase to β G1P and glucose. Glucose is subsequently phosphorylated to G6P by glucokinase and enters glycolysis via fructose 6-phosphate (F6P) and F16BP. β PGM catalyses the isomerisation of β G1P to G6P, allowing complete catabolism of both trehalose and maltose. β PGM deficient *L. lactis* is unable to grow on trehalose and when cultured on maltose (disaccharide composed of $\alpha(1\rightarrow4)$ -linked glucose units) the cells excrete β G1P into the growth medium and accumulate intracellularly β G1P (~0.7 M), T6P (~2.7 M) and amylose (polysaccharides composed of $\alpha(1\rightarrow4)$ -linked glucose units). This observation is consistent with both P_i -dependent trehalose 6-phosphate phosphorylase and P_i -dependent maltose phosphorylase operating in the reverse sense (grey dotted arrows) to their physiological roles in wild-type *L. lactis*, resulting in excess β G1P being combined with G6P to form T6P or polymerised as $\alpha(1\rightarrow4)$ glucose units to form amylose.



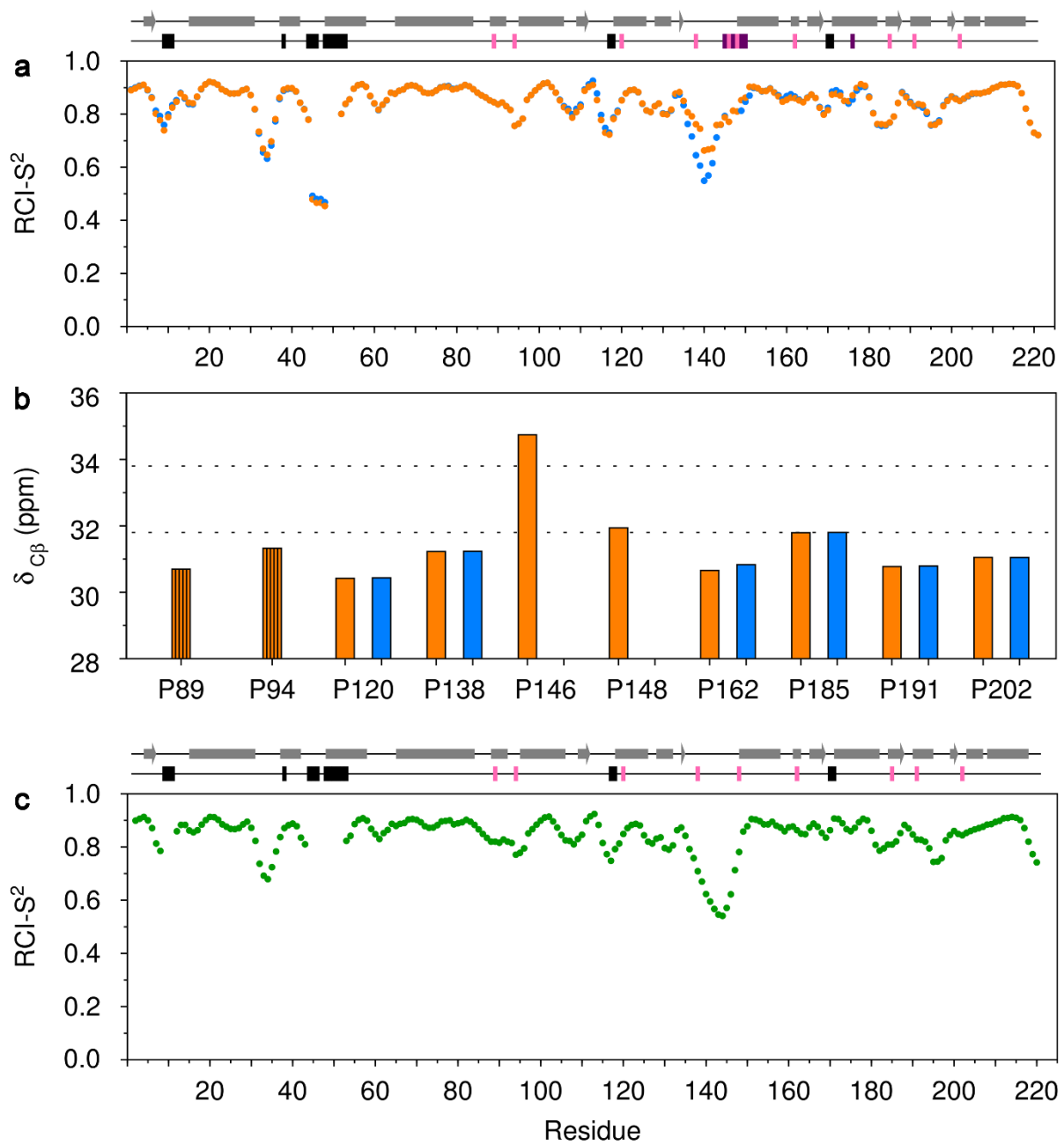
Supplementary Figure 3.2. Solution behaviour of β PGM. (a) $^1\text{H}^{15}\text{N}$ -TROSY spectrum of $^{2\text{H}}{^{15}\text{N}}^{13}\text{C}$ - β PGM_{WT} in standard NMR buffer containing 5 mM tris. A selection of well-resolved residues are labelled which populate conformer A (orange labels) and conformer B (blue labels) in slow exchange. (b) $^1\text{H}^{15}\text{N}$ -TROSY spectrum of $^{2\text{H}}{^{15}\text{N}}^{13}\text{C}$ - β PGM_{P146A} in standard NMR buffer. β PGM_{P146A} populates one conformer and the same selection of residues has been labelled in dark green for comparison. (c) $^1\text{H}^{15}\text{N}$ -TROSY spectrum of ^{15}N - β PGM_{WT} in filtered milk where both conformers are populated. (d) ^1H NMR spectrum of ^{15}N - β PGM_{WT} in filtered milk showing the major milk components. The concentrations of lactose and citrate are estimated as 17 mM and 5 mM, respectively.



Supplementary Figure 3.3. Effect of different phosphorylating agents on β PGM_{WT}. **a–d**, Comparative overlays of a section of $^1\text{H}^{15}\text{N}$ -TROSY spectra highlighting the behaviour of residues F7, S48, S88, L103, I110, D133, Q172 and L209. **(a)** β PGM_{WT} (black) populates conformer A and conformer B in slow exchange for a subset of these residues. The addition of 3 mM BeCl₂ and 10 mM NH₄F to the β PGM_{WT} sample induces the population of a single β PGM_{WT}:BeF₃ complex (magenta) (BMRB 17851), which is an analogue of phosphorylated conformer A (A^{P}). **(b)** β PGM_{WT} supplemented with AcP (black) populates A^{P} as the dominant species, which shows a good degree of correspondence with the A^{P} analogue (magenta). **(c)** β PGM_{WT} supplemented with F16BP (black) populates A^{P} as the dominant species, which again overlays well with the A^{P} analogue (magenta). **(d)** β PGM_{WT} supplemented with β G16BP (black) populates a β PGM_{WT}: β G16BP complex (A: β G16BP), which shares a better correspondence with the Mg²⁺-saturated β PGM_{D10N}: β G16BP complex (pale blue) (BMRB 27174) than with the A^{P} analogue (magenta).

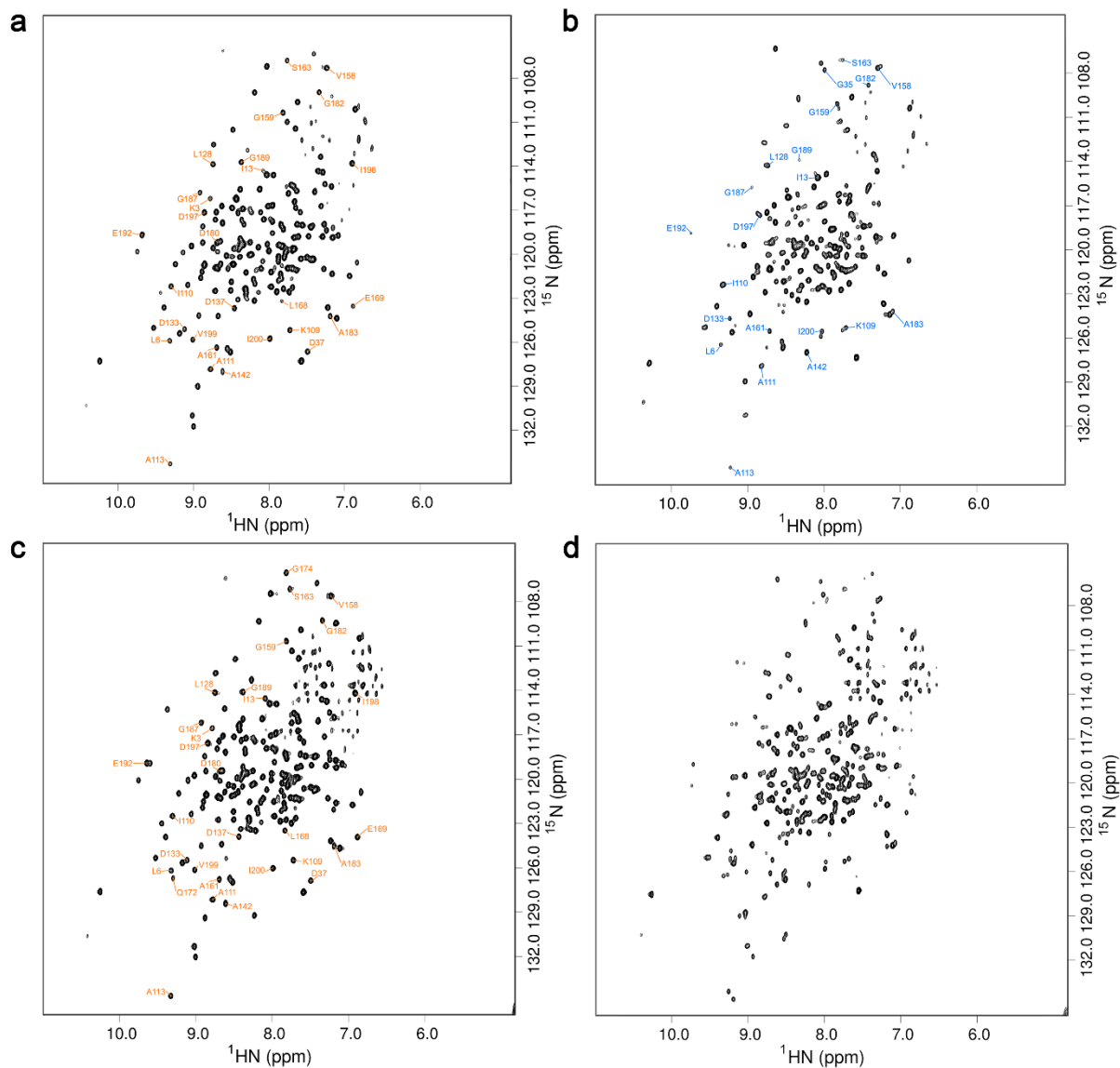


Supplementary Figure 3.4. Residue specific backbone amide group chemical shift differences ($\Delta\delta$) for β PGM_{WT} and β PGM_{P146A}. (a) Chemical shift differences between conformer A and conformer B. (b) Chemical shift differences between conformer A and β PGM_{P146A}. (c) Chemical shift differences between conformer B and β PGM_{P146A}. (d) Chemical shift differences between the β PGM_{WT}:MgF₃:G6P TSA and the β PGM_{P146A}:MgF₃:G6P TSA complexes. (e) Chemical shift differences between β PGM_{P146A} and phosphorylated β PGM_{P146A} (B^P). (f) Chemical shift differences between conformer B and the β PGM_{WT}:BeF₃ complex (A^P analogue). In panels (b) and (c), bars are coloured blue if residues in (a) showed a $\Delta\delta$ value greater than zero, otherwise bars are coloured black. Disregarding the dominant effect of the P146A substitution (large black bars), there are smaller and fewer chemical shift perturbations (blue bars) in (c) than in (b) suggesting that conformer B adopts a conformation closely similar to β PGM_{P146A}. At the top of the panel, secondary structure elements from β PGM_{WT} (PDB 2WHE) are indicated by grey bars (α -helices) and arrows (β -strands). Residues in conformer A and conformer B with missing backbone amide peaks in the ¹H¹⁵N-TROSY spectrum of β PGM_{WT} are shown by black rectangles, whereas missing backbone amide peaks in conformer B only are shown by purple rectangles. Proline residues in β PGM_{WT} are denoted by pink rectangles.

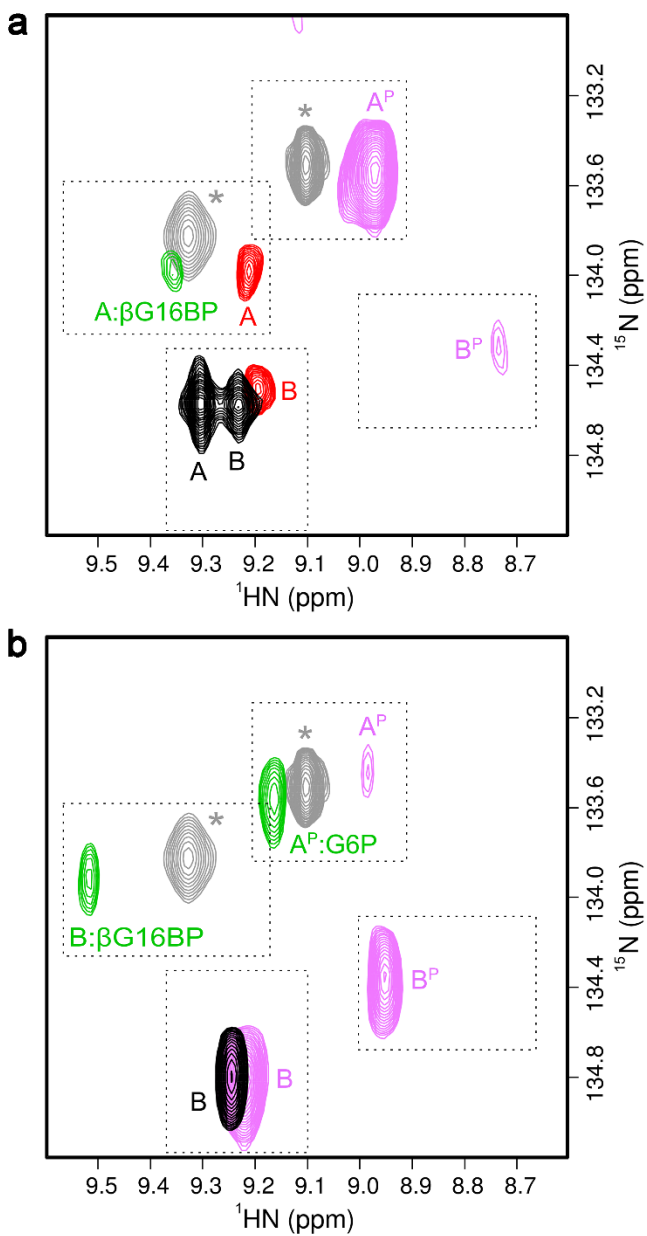


Supplementary Figure 3.5. Chemical shift analysis of β PGMwt and β PGMP146A. (a) Random coil index order parameter (RCI- S^2) prediction of conformer A (orange circles) and conformer B (blue circles) obtained using TALOS-N. Secondary structure elements, the extent of assignment and proline residue locations are presented at the top of the panel for β PGMwt as described previously. (b) Comparison of assignable proline $^{13}\text{C}\beta$ chemical shifts in β PGMwt for conformer A (orange bars) and conformer B (blue bars). Orange bars with vertical black shading indicate identical chemical shifts for conformer A and conformer B. The $^{13}\text{C}\beta$ resonances of P146 and P148 in conformer B are likely to be broadened beyond detection due to conformation exchange in the K145–I150 region occurring on the millisecond timescale. Dotted horizontal lines represent average proline $^{13}\text{C}\beta$ chemical shift values with *trans* (31.8 ± 1.0 ppm) and *cis* (33.8 ± 1.2 ppm) Xaa-Pro peptide bonds. (c) RCI- S^2 prediction of β PGMP146A (dark green circles) obtained using TALOS-N. Secondary structure elements, the extent of

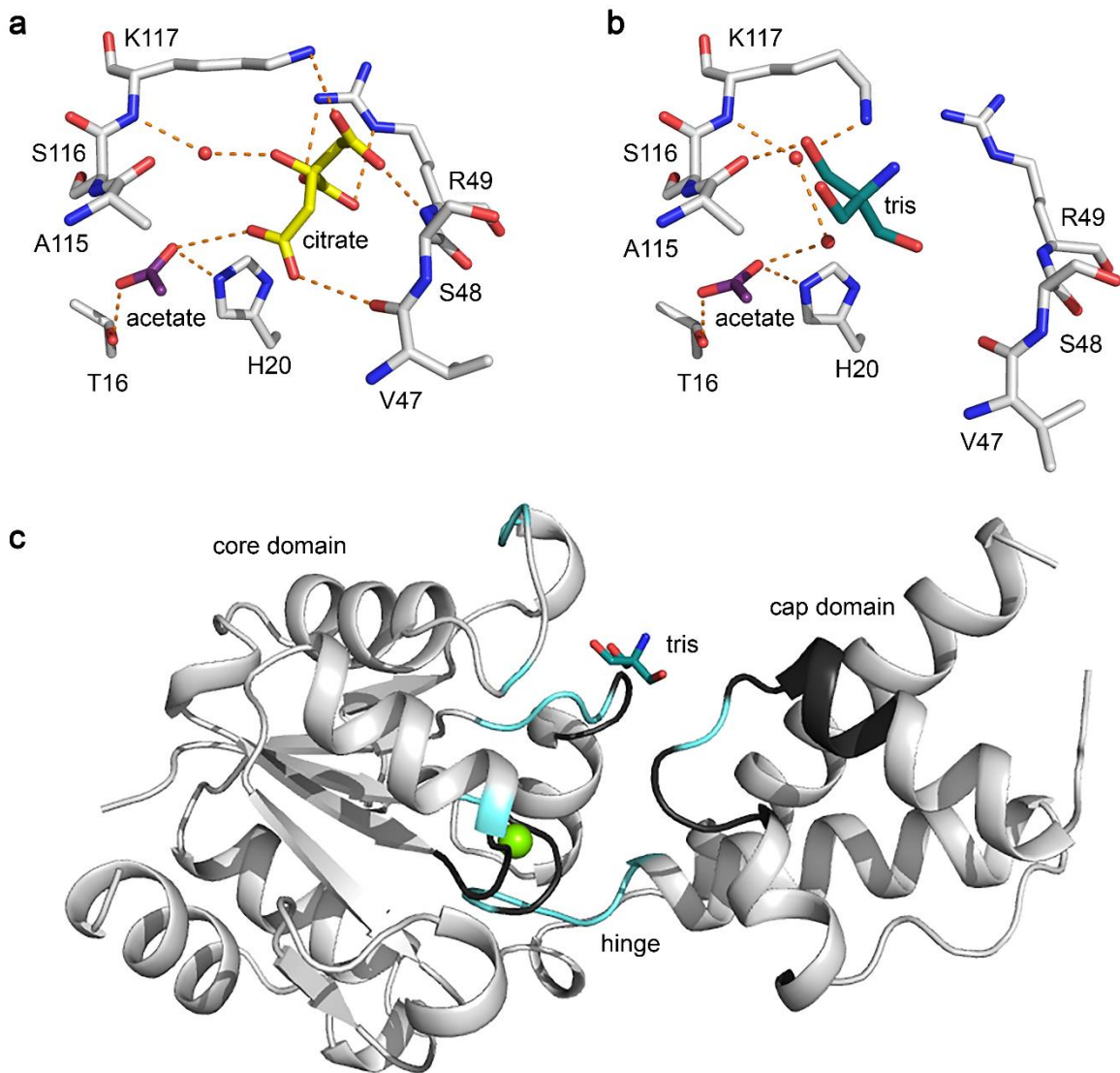
assignment and proline residue locations are presented at the top of the panel for β PGM_{P146A} as described previously.



Supplementary Figure 3.6. Solution behaviour of β PGM under variable ion concentrations. (a) $^1\text{H}^{15}\text{N}$ -TROSY spectrum of ^{15}N - β PGM_{WT} in standard NMR buffer containing 200 mM NaCl. The dominant population of β PGM_{WT} is conformer A. (b) $^1\text{H}^{15}\text{N}$ -TROSY spectrum of ^{15}N - β PGM_{WT} in deionised water. The dominant population of β PGM_{WT} is conformer B. (c) $^1\text{H}^{15}\text{N}$ -TROSY spectrum of ^{15}N - β PGM_{WT} in standard NMR buffer containing 100 mM MgCl₂. The dominant population of β PGM_{WT} is conformer A. (d) $^1\text{H}^{15}\text{N}$ -TROSY spectrum of ^{15}N - β PGM_{WT} in Mg²⁺-free standard NMR buffer. Both conformer A and conformer B are populated.

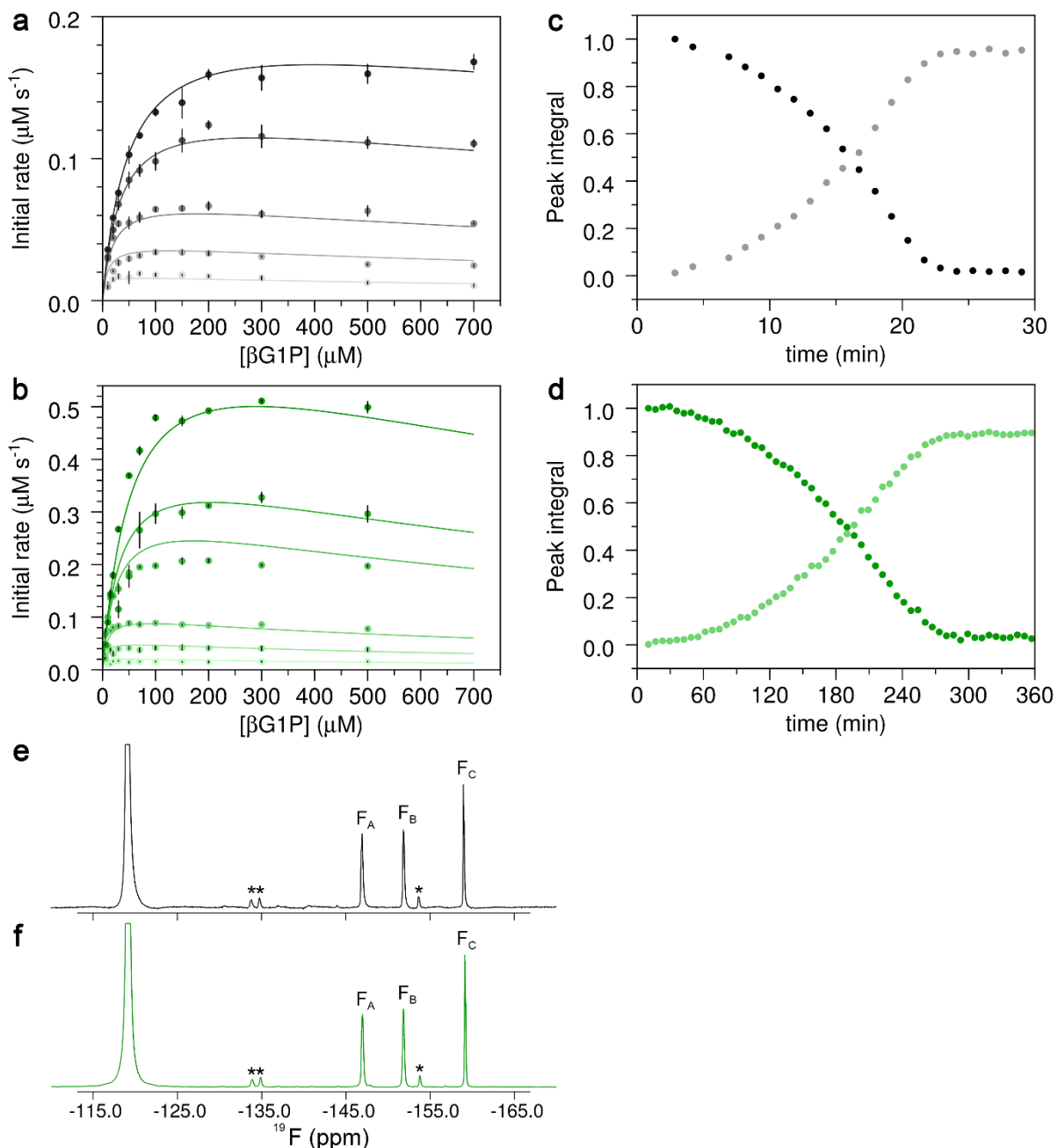


Supplementary Figure 3.7. Effect of different phosphorylating agents on βPGM. **a, b,** Overlays of a section of $^1\text{H}^{15}\text{N}$ -TROSY spectra for $\beta\text{PGM}_{\text{WT}}$ and $\beta\text{PGM}_{\text{P146A}}$ highlighting the behaviour of residue A113. **(a)** $\beta\text{PGM}_{\text{WT}}$ (black) populates conformer A and conformer B in slow exchange. $\beta\text{PGM}_{\text{WT}}$ recorded in filtered milk (red) populates conformer A and conformer B. $\beta\text{PGM}_{\text{WT}}$ supplemented with AcP (pink) populates A^{P} as the dominant species and B^{P} . $\beta\text{PGM}_{\text{WT}}$ supplemented with βG16BP (green) populates an $\text{A}:\beta\text{G16BP}$ complex. **(b)** $\beta\text{PGM}_{\text{P146A}}$ (black) populates conformer B. $\beta\text{PGM}_{\text{P146A}}$ supplemented with AcP (pink) populates conformer B, A^{P} and B^{P} . $\beta\text{PGM}_{\text{P146A}}$ supplemented with βG16BP (green) populates an $\text{A}^{\text{P}}:\text{G6P}$ complex and a $\text{B}:\beta\text{G16BP}$ complex. Peaks indicated by grey asterisks correspond to the $\beta\text{PGM}_{\text{WT}}:\text{BeF}_3$ complex (grey; $\delta_{\text{N}} = 133.5$ ppm; BMRB 17851), which is an analogue of A^{P} , and the Mg^{2+} -saturated $\beta\text{PGM}_{\text{D10N}}:\beta\text{G16BP}$ complex (grey; $\delta_{\text{N}} = 133.8$ ppm; BMRB 27174), which is a mimic of the $\text{A}:\beta\text{G16BP}$ complex, and are shown for comparison.



Supplementary Figure 3.8. Binding of small molecules to β PGMwt. **a, b**, Active site coordination for citrate, acetate and tris in the β PGMwt:citrate complex (PDB 6YDM). β PGMwt was crystallised in the presence of citrate in a crystallisation buffer containing acetate and tris. Selected active site residues and ligands are shown as sticks with β PGMwt (grey carbon atoms), citrate (gold carbon atoms), acetate (purple carbon atoms) and tris (teal carbon atoms) for both chains of the crystallographic asymmetric unit. Red spheres indicate structural water molecules and orange dashes show probable hydrogen bonds. **c**, Changes in intermediate exchange behaviour on tris binding. Cartoon representation of the β PGMwt:citrate complex highlighting the extent of active site residues undergoing intermediate exchange behaviour in the original β PGMwt assignment (without tris; cyan backbone, D8, L9, D10, G11, V12, I13, T14, D15, T16, R38, L44, K45, G46, V47, S48, R49, E50, D51, S52, L53, S114, A115, S116, K117, N118, V141, A142, K145, S171 and Q172; BMRB 7235) and in the assignment of conformer A (with tris; black backbone, L9, D10, G11, R38, L44, K45, G46, S48, R49, E50, D51, S52, L53, K117, N118, D170 and S171; BMRB 28095). The coordination of tris (teal carbon atoms) in the active site cleft perturbs the exchange behaviour for some loop residues,

with the result that the corresponding resonances are no longer broadened beyond detection and can therefore be assigned. The catalytic Mg²⁺ ion is shown as a green sphere.



Supplementary Figure 3.9. Activity of $\beta\text{PGM}_{\text{WT}}$ and $\beta\text{PGM}_{\text{P146A}}$. **a, b,** Initial rate measurements for $\beta\text{PGM}_{\text{WT}}$ and $\beta\text{PGM}_{\text{P146A}}$ using the coupled assay. The solid lines represent a global fit of the data to Equation 3.1 and vertical black lines indicate standard error of the mean of three replicate measurements. **(a)** $\beta\text{PGM}_{\text{WT}}$ initial rate measurements at a range of βG1P concentrations (10, 20, 30, 50, 70, 100, 150, 200, 300, 500, 700 μM) and βG16BP concentrations (0.4, 1, 2, 5, 10 μM , grey gradient increasing with concentration). **(b)** $\beta\text{PGM}_{\text{P146A}}$ initial rate measurements at a range of βG1P concentrations (5, 10, 15, 20, 30, 50, 70, 100, 200, 300, 500 μM) and βG16BP concentrations (2, 5, 10, 35, 50, 100 μM , green gradient increasing with concentration). **c, d,** Reaction kinetics monitored by ^{31}P NMR spectra for $\beta\text{PGM}_{\text{WT}}$ (grey tones) and $\beta\text{PGM}_{\text{P146A}}$ (green tones) for the equilibration of βG1P with G6P in standard kinetic buffer. The reactions were initiated by the addition of 20 mM AcP. Normalised integral values for the βG1P peak (black / dark green) and the G6P peak (grey / light green) are shown. **e, f,** ^{19}F NMR spectra showing the conversion of G6P to βG1P . Peaks are labeled F_A, F_B, and F_C. Asterisks and double asterisks indicate minor peaks.

light green) are plotted as a function of time. **e, f**, ^{19}F NMR spectra of the $\beta\text{PGM}:\text{MgF}_3:\text{G6P}$ TSA complexes formed using either $\beta\text{PGM}_{\text{WT}}$ (black) or $\beta\text{PGM}_{\text{P146A}}$ (green) in standard NMR buffer, supplemented with 15 mM NaF and 10 mM G6P. Chemical shifts are given in ppm for each ^{19}F resonance: $\beta\text{PGM}_{\text{WT}}:\text{MgF}_3:\text{G6P}$ TSA complex ($F_A = -146.9$, $F_B = -151.9$ and $F_C = -159.0$) and $\beta\text{PGM}_{\text{P146A}}:\text{MgF}_3:\text{G6P}$ TSA complex ($F_A = -147.0$, $F_B = -151.8$ and $F_C = -159.2$). Resonances indicated by black asterisks correspond to an alternative conformation of the $\beta\text{PGM}:\text{MgF}_3:\text{G6P}$ TSA complexes. Free F^- resonates at -119.1 ppm and the full peak intensity has been truncated for clarity.

Supplementary Table 3.1. Data collection, data processing and refinement statistics for the β PGM complexes

Complex	β PGM _{WT} :citrate	β PGM _{WT}	β PGM _{P146A}	β PGM _{P146A:MgF₃:G6P}
PDB Code	PDB 6YDM	PDB 6YDL	PDB 6YDK	PDB 6YDJ
Crystallisation conditions	0.6 mM β PGM _{WT} 50 mM citrate	0.6 mM β PGM _{WT}	0.5 mM β PGM _{P146A}	0.4 mM β PGM _{P146A} 10 mM G6P 15 mM NaF
Crystal morphology	Rod shaped crystals	Rod shaped crystals	Rod shaped crystals	Large plate crystals
Wavelength (Å)	0.97179	0.92819	0.97950	0.91587
Beamline, Facility	Beamline i03, DLS	Beamline i04-1, DLS	Beamline i04, DLS	Beamline i04-1, DLS
Resolution (Å) ¹	46.57 – 2.10 (2.16 – 2.10)	44.65 – 1.52 (1.56 – 1.52)	43.95 – 2.02 (2.05 – 2.02)	54.25 – 1.04 (1.06 – 1.04)
Space group	P2 ₁ 2 ₁ 2 ₁	P2 ₁ 2 ₁ 2 ₁	P2 ₁ 2 ₁ 2 ₁	P2 ₁ 2 ₁ 2 ₁
Cell dimensions: a, b, c (Å) α , β , γ (°)	53.1, 76.6, 117.3 90.0, 90.0, 90.0	53.3, 54.1, 81.9 90.0, 90.0, 90.0	53.3, 56.2, 77.7 90.0, 90.0, 90.0	37.1, 54.3, 104.3 90.0, 90.0, 90.0
Total reflections ¹	239876 (15971)	264843 (16619)	103063 (2568)	680305 (21980)
Unique reflections ¹	27995 (2095)	36815 (2658)	15683 (686)	101730 (5021)
Multiplicity ¹	8.6 (7.6)	7.2 (6.3)	6.6 (3.7)	6.7 (4.4)
Completeness (%) ¹	97.5 (90.1)	99.3 (99.3)	98.8 (88.9)	99.9 (99.3)
$\langle I/\sigma I \rangle$ ¹	13.7 (3.7)	18.8 (1.3)	14.4 (1.2)	12.4 (1.1)
Wilson B factor (Å ²)	24.2	21.2	32.2	7.4
R _{merge} ¹	0.093 (0.536)	0.044 (1.190)	0.075 (0.953)	0.067 (1.138)
R _{pim} ¹	0.033 (0.198)	0.019 (0.561)	0.031 (0.506)	0.028 (0.609)
CC-half ¹	0.999 (0.899)	1.000 (0.536)	0.999 (0.556)	0.999 (0.544)
Molecular replacement model	PDB 2WHE	PDB 2WHE	PDB 2WHE	PDB 2WF5
R _{factor}	0.230	0.183	0.214	0.149
R _{free}	0.290	0.216	0.253	0.169
Number of atoms:				
Protein	3379	1733	1708	1704
Ligands	38	0	0	29
Metal ions	2	1	1	2
Water	187	148	36	209
Protein residues	438	219	221	218
RMS deviations:				
Bonds (Å)	0.0089	0.0145	0.0125	0.0093
Angles (°)	1.482	1.497	1.522	1.473
Average B factors (Å ²)				
Main chain	32	25	15	11
Side chains	36	29	27	13
Ligands	50	N/A	N/A	10
Metal ions	27	27	44	10
Water	33	36	39	24
Ramachandran analysis				
Favoured/allowed (%)	97.7	98.6	97.7	97.7
Disallowed (%)	0.0	0.0	0.0	0.0
Favoured rotamers (%)	94.1	96.2	96.7	95.1
Poor rotamers (%)	1.10	0.54	1.11	0.55
MolProbity score	1.29 (99 th percentile, 2.10 ± 0.25 Å)	0.93 100 th percentile, 1.52 ± 0.25 Å)	0.98 (100 th percentile, 2.02 ± 0.25 Å))	0.66 (99 th percentile, 1.04 ± 0.25 Å)

¹ Values for the higher resolution shell are in parentheses

9. Appendix B – Supplementary Information

SUPPLEMENTARY INFORMATION

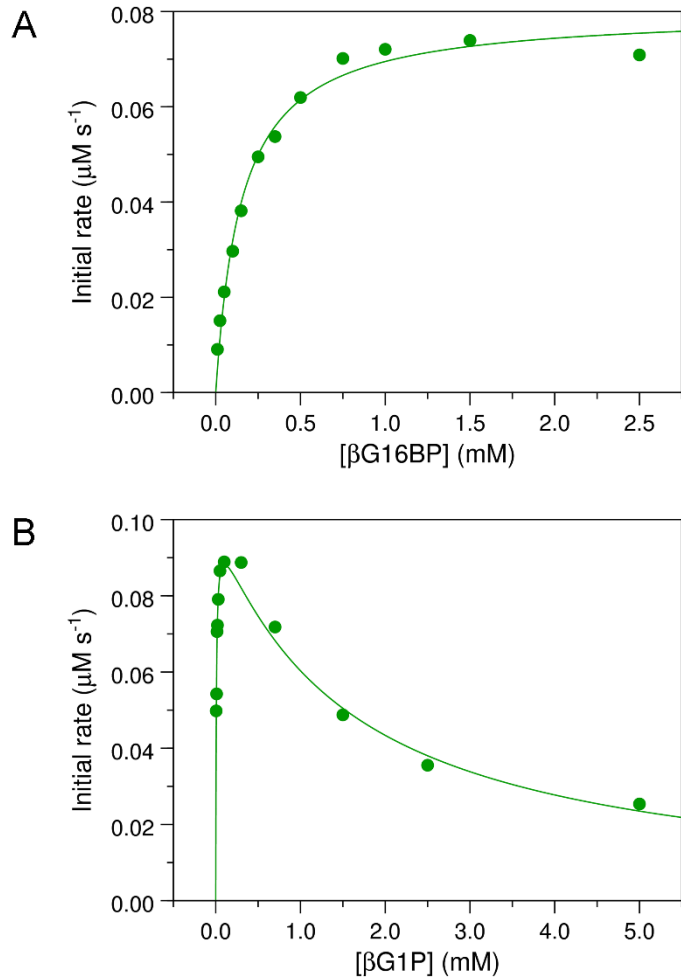
Enzymatic production of β -glucose 1,6-bisphosphate through manipulation of catalytic magnesium coordination

Henry P. Wood,^a Nicola J. Baxter,^{a,b} F. Aaron Cruz-Navarrete,^a Clare R. Trevitt,^a Andrea M. Hounslow^a and Jonathan P. Waltho^{a,b,*}

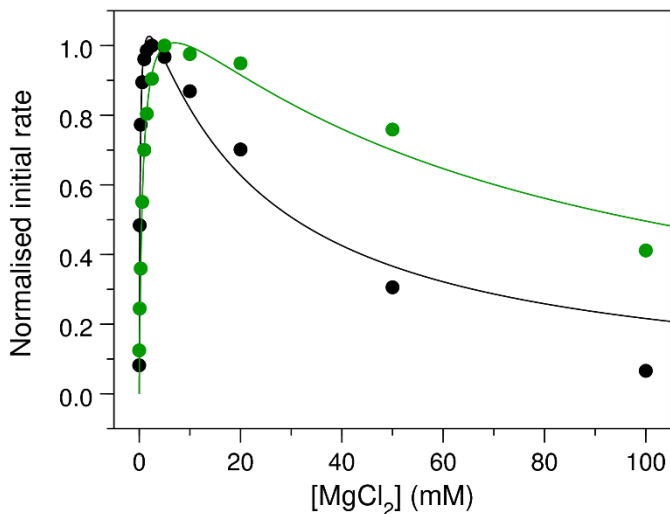
^aKrebs Institute for Biomolecular Research, Department of Molecular Biology and Biotechnology, The University of Sheffield, Sheffield, S10 2TN, United Kingdom; ^bManchester Institute of Biotechnology and School of Chemistry, The University of Manchester, Manchester, M1 7DN, United Kingdom

*To whom correspondence may be addressed: Prof. Jonathan Waltho, Krebs Institute for Biomolecular Research, Department of Molecular Biology and Biotechnology, The University of Sheffield, Sheffield, S10 2TN, +44 114 22717, j.waltho@sheffield.ac.uk, ORCID 0000-0002-7402-5492

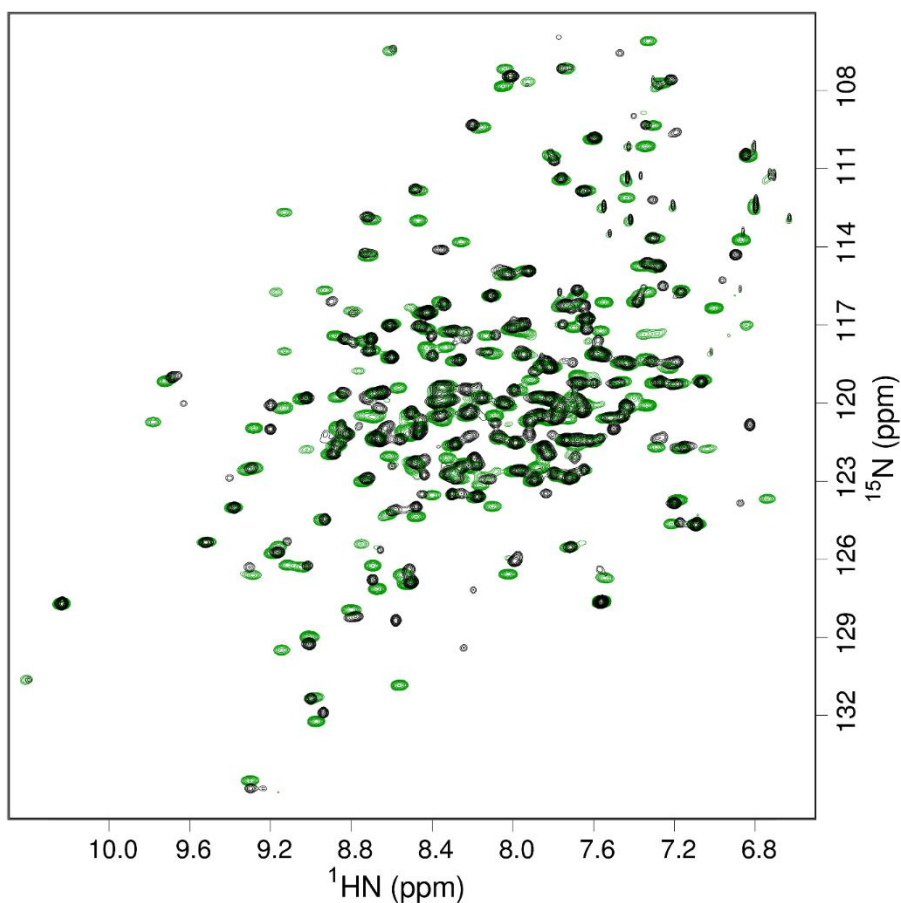
Keywords: glucose bisphosphate | enzymatic production | NMR spectroscopy



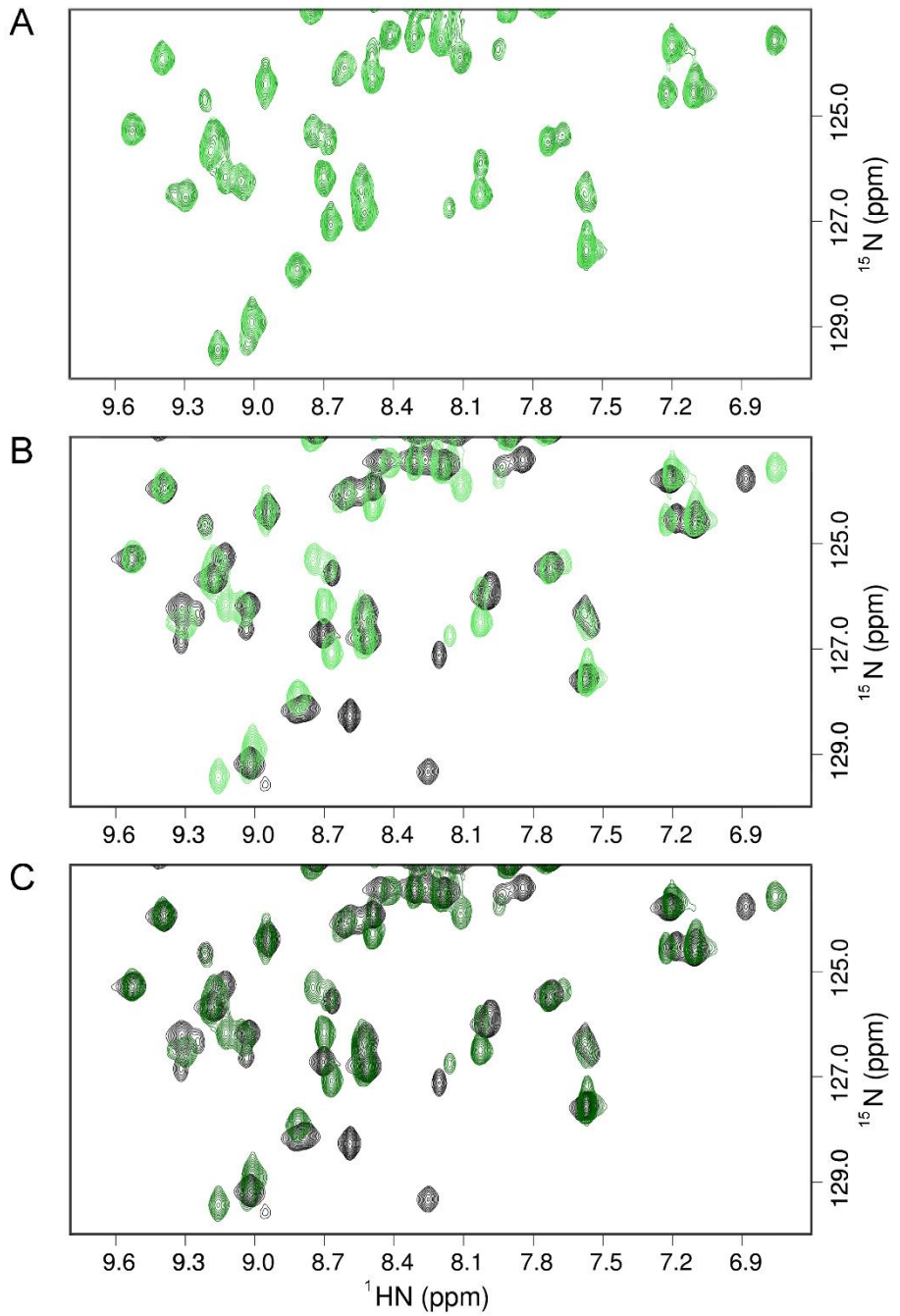
Supplementary Figure 4.1. Initial rate measurements for the conversion of β G1P to G6P catalysed by β PGM_{D170N} monitored using a glucose 6-phosphate dehydrogenase (G6PDH) coupled assay. (A) Reactions were conducted in 200 mM K⁺ HEPES buffer (pH 7.2), 5 mM MgCl₂, 1 mM NAD⁺ and 5 U/mL G6PDH containing 10 μ M β PGM_{D170N}, 1 mM β G1P and were initiated using increasing concentrations of β G16BP (10, 25, 50, 100, 150, 250, 350, 750, 1000, 1500, 2500 μ M). Initial rates of G6P production were obtained using a linear least-squares fitting routine. Subsequent fitting of these rates to Equation 4.1 using an in-house Python non-linear least squares fitting program yielded an apparent K_m (β G16BP) = 150 \pm 13 μ M. (B) Reactions were conducted in 200 mM K⁺ HEPES buffer (pH 7.2), 5 mM MgCl₂, 1 mM NAD⁺ and 5 U/mL G6PDH containing 10 μ M β PGM_{D170N} and increasing concentrations of β G1P (50, 100, 200, 300, 500, 700, 1000, 1500, 2000, 3000, 5000 μ M) and were initiated using 250 μ M β G16BP. Initial rates of G6P production were obtained using a linear least-squares fitting routine. Subsequent fitting of these rates to Equation 4.2 using an in-house Python non-linear least squares fitting program yielded an apparent K_m (β G1P) = 6.9 \pm 1.0 μ M and an apparent K_i (β G1P) = 1536 \pm 170 μ M.



Supplementary Figure 4.2. Activity of $\beta\text{PGM}_{\text{WT}}$ and $\beta\text{PGM}_{\text{D170N}}$ with increasing MgCl_2 concentration. Normalised initial rate measurements for the conversion of βG1P to G6P by either $\beta\text{PGM}_{\text{WT}}$ (black circles) or $\beta\text{PGM}_{\text{D170N}}$ (green circles) at different concentrations of MgCl_2 monitored using a G6PDH coupled assay. Reactions were conducted in 200 mM K^+ HEPES buffer (pH 7.2) containing different concentrations of MgCl_2 (0, 0.1, 0.3, 0.6, 1.0, 1.5, 2.5, 5, 10, 20, 50 and 100 mM), 1 mM NAD^+ , 5 U/mL G6PDH, 1 mM βG1P and either 1 nM $\beta\text{PGM}_{\text{WT}}$ with 100 μM βG16BP , or 10 μM $\beta\text{PGM}_{\text{D170N}}$ with 1250 μM βG16BP . Initial rates of G6P production were obtained using a linear least-squares fitting routine. Subsequent fitting of these rates to Equation 4.2 using an in-house Python non-linear least squares fitting program yielded an apparent $K_m(\text{Mg}^{2+}) = 180 \pm 40 \mu\text{M}$ for $\beta\text{PGM}_{\text{WT}}$ and an apparent $K_m(\text{Mg}^{2+}) = 690 \pm 110 \mu\text{M}$ for $\beta\text{PGM}_{\text{D170N}}$. The standard error of the mean of three technical replicates falls within the radii of the data points. The discrepancy between the $K_m(\text{Mg}^{2+})$ value obtained using the G6PDH coupled assay and ^{31}P NMR time-course experiments (Fig. 3B–C) is likely due to the different conditions employed, although similar maximal initial rates of reaction are observed using each technique (maximal initial rate using G6PDH coupled assay = 0.009 s^{-1} ; maximal initial rate using ^{31}P NMR time-course experiments = 0.012 s^{-1}). These observations indicate that a component of the reaction mixture used in the ^{31}P NMR experiments is competing with Mg^{2+} ions to bind to $\beta\text{PGM}_{\text{D170N}}$. One notable difference between the conditions of each technique is the 10-fold higher βG1P concentration used in the ^{31}P NMR experiments. Given that $\beta\text{PGM}_{\text{D170N}}$ experiences βG1P inhibition (Fig. S1B) at a comparable level to $\beta\text{PGM}_{\text{WT}}$, this behaviour provides a likely source for the competitive inhibition observed in the ^{31}P NMR experiments. Although the mechanism for βG1P inhibition has not been structurally characterised, it is plausible that βG1P binds to Mg_{cat} -free $\beta\text{PGM}_{\text{D170N}}$ to form a closed complex, thus preventing βG16BP production in Step 1 and G6P production in Step 2, until dissociation occurs.

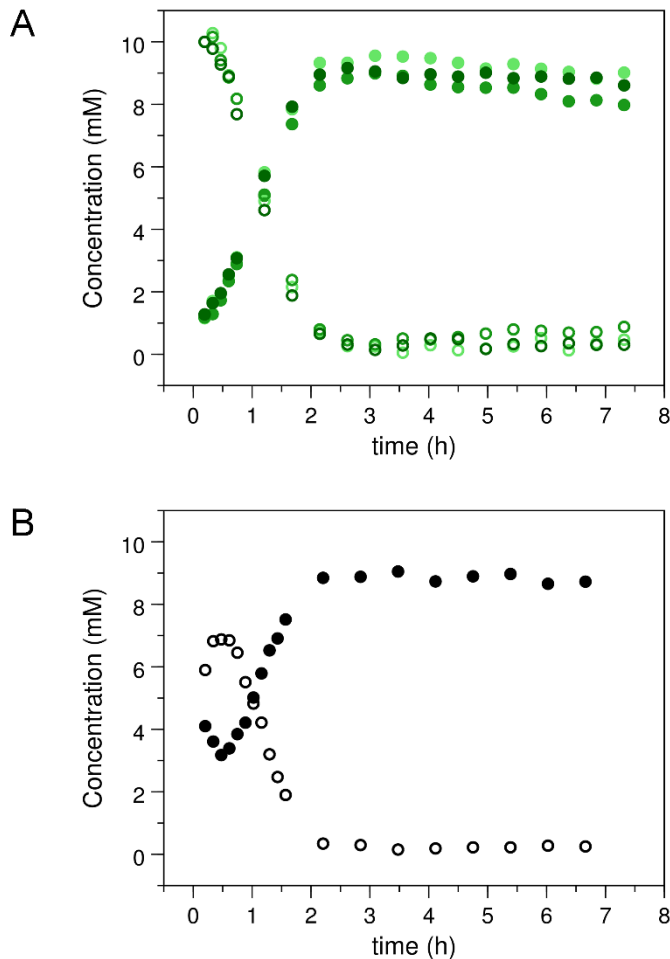


Supplementary Figure 4.3. Solution behaviour of substrate-free β PGM. Overlay of $^1\text{H}^{15}\text{N}$ -TROSY spectra for substrate-free β PGM_{WT} (black) and substrate-free β PGM_{D170N} (green), recorded in 50 mM K⁺ HEPES buffer (pH 7.2), 5 mM MgCl₂, 2 mM NaN₃, 10% $^2\text{H}_2\text{O}$ (v/v) and 1 mM TSP. There is a broad correspondence between peaks of β PGM_{WT} and β PGM_{D170N}, indicating a similar solution behaviour and overall protein fold. Two conformers are present in slow exchange (~70% conformer A and ~30% conformer B) for both β PGM_{WT} and β PGM_{D170N}, which arise from *cis-trans* isomerisation at the K145-P146 peptide bond.^{23,179} Additionally, ~15 peaks are present for β PGM_{D170N}, which are absent in β PGM_{WT} due to backbone conformational exchange on the millisecond timescale.^{23,179} This observation indicates that residue N170 in β PGM_{D170N} abolishes the intermediate exchange dynamic that residue D170 propagates in β PGM_{WT}.



Supplementary Figure 4.4. Comparative overlays of a section of $^1\text{H}^{15}\text{N}$ -TROSY spectra for substrate-free βPGM recorded in 50 mM K^+ HEPES buffer (pH 7.2), 5 mM MgCl_2 , 2 mM NaN_3 , 10% $^2\text{H}_2\text{O}$ (v/v) and 1 mM TSP. (A) Comparison of substrate-free $\beta\text{PGM}_{\text{D}170\text{N}}$ that had been preincubated at 25 °C for 0 h (light green) and 48 h (dark green). Near-identical spectra indicate that the incubation process has a negligible effect on the stability of substrate-free $\beta\text{PGM}_{\text{D}170\text{N}}$. (B) Comparison of substrate-free $\beta\text{PGM}_{\text{D}170\text{N}}$ preincubated at 25 °C for 0 h (light green) and substrate-free $\beta\text{PGM}_{\text{WT}}$ (black). (C) Comparison of substrate-free $\beta\text{PGM}_{\text{D}170\text{N}}$ preincubated at 25 °C for 48 h (dark green) and substrate-free $\beta\text{PGM}_{\text{WT}}$ (black). The absence of observable $\beta\text{PGM}_{\text{WT}}$ peaks in the $\beta\text{PGM}_{\text{D}170\text{N}}$ spectrum indicates that reversion of

β PGM_{D170N} to β PGM_{WT} through deamidation is not a process that occurs readily under these sample conditions.



Supplementary Figure 4.5. Activity of β PGM_{D170N} in 200 mM K⁺ HEPES buffer (pH 7.2) and 100 mM MgCl₂ monitored using ³¹P NMR time-course experiments. (A) Reaction kinetics for the equilibration of 10 mM β G1P with G6P catalysed by 200 μ M β PGM_{D170N} that had been preincubated at 25 °C for 0 h (light green symbols), 24 h (medium green symbols) and 48 h (dark green symbols). The reactions were initiated by and timed from the addition of 20 mM AcP. Normalised integral values of the ³¹P resonances of β G16BP and G6P have been converted to concentrations and are plotted as a function of time for β G16BP (open circles) and G6P (closed circles). (B) Reaction kinetics for the equilibration of 10 mM β G1P with G6P catalysed by 200 μ M β PGM_{D170N} containing 200 nM β PGM_{WT} (representative of 0.1% reversion of β PGM_{D170N} to β PGM_{WT} through deamidation). The reaction was initiated by and timed from the addition of 20 mM AcP. Normalised integral values of the ³¹P resonances of β G16BP and G6P have been converted to concentrations and are plotted as a function of time for β G16BP (open circles) and G6P (closed circles).

10. Appendix C – Supplementary Information

SUPPLEMENTARY INFORMATION

Novel alginate conformation facilitates dual specificity of alginate lyase, dp0100.

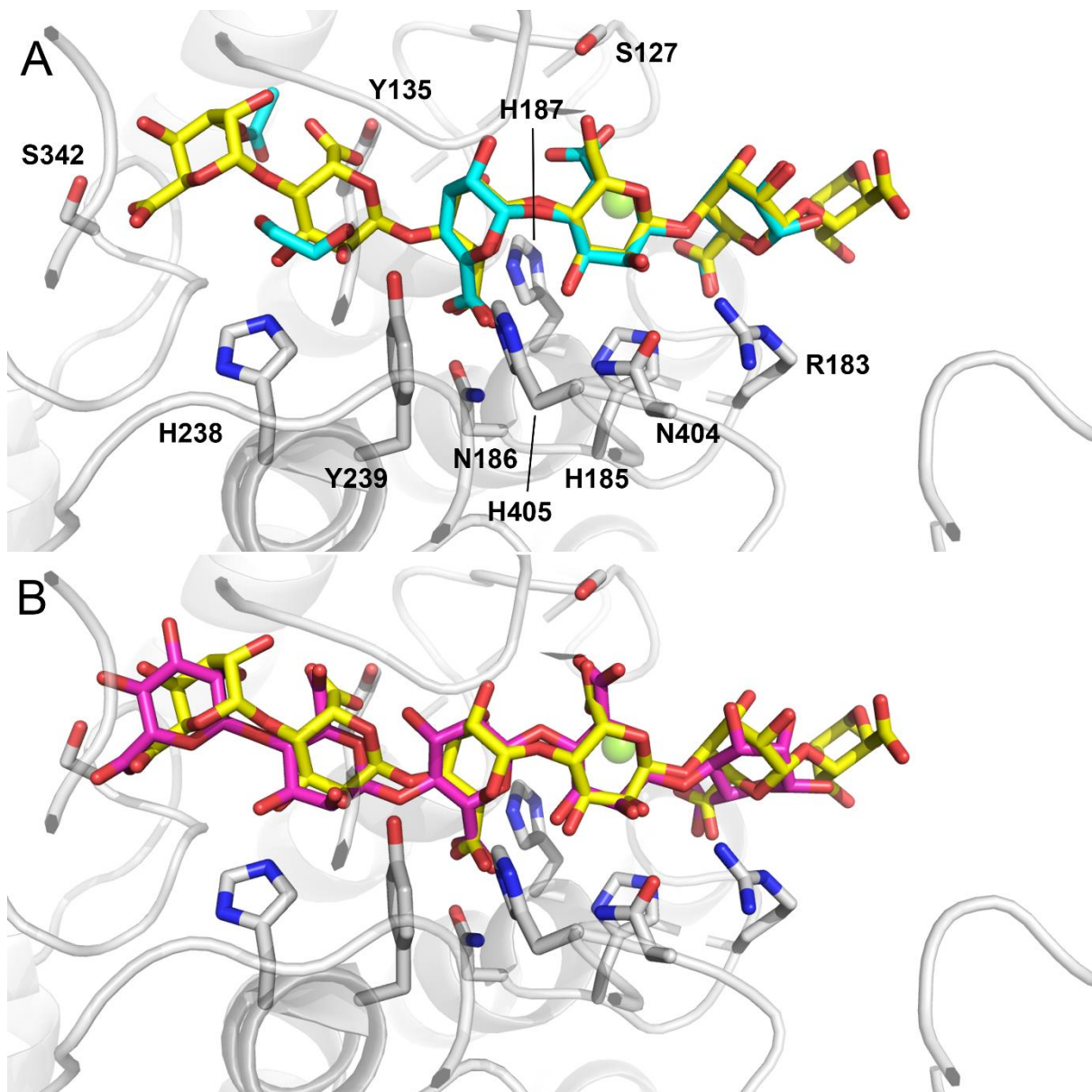
Henry P. Wood^{a,1}, Shiqi Ji^{b,1}, Samuel R. Dix^a, Andrea M. Hounslow^a, Svetlana E. Sedelnikova^a, Patrick J. Baker^a, Jon Agirre^c, Jonathan P. Walther^{a,d}, David W. Rice^{a,*}.

^aKrebs Institute for Biomolecular Research, Department of Molecular Biology and Biotechnology, The University of Sheffield, Sheffield, S10 2TN, United Kingdom; ^bState Key Laboratory of Microbial Technology, Shandong University, 72 Binhai Road, Qingdao 266237, P. R. China; ^cDepartment of Chemistry, University of York, Heslington, York, YO10 5DD, United Kingdom; ^dManchester Institute of Biotechnology and School of Chemistry, The University of Manchester, Manchester, M1 7DN, United Kingdom.

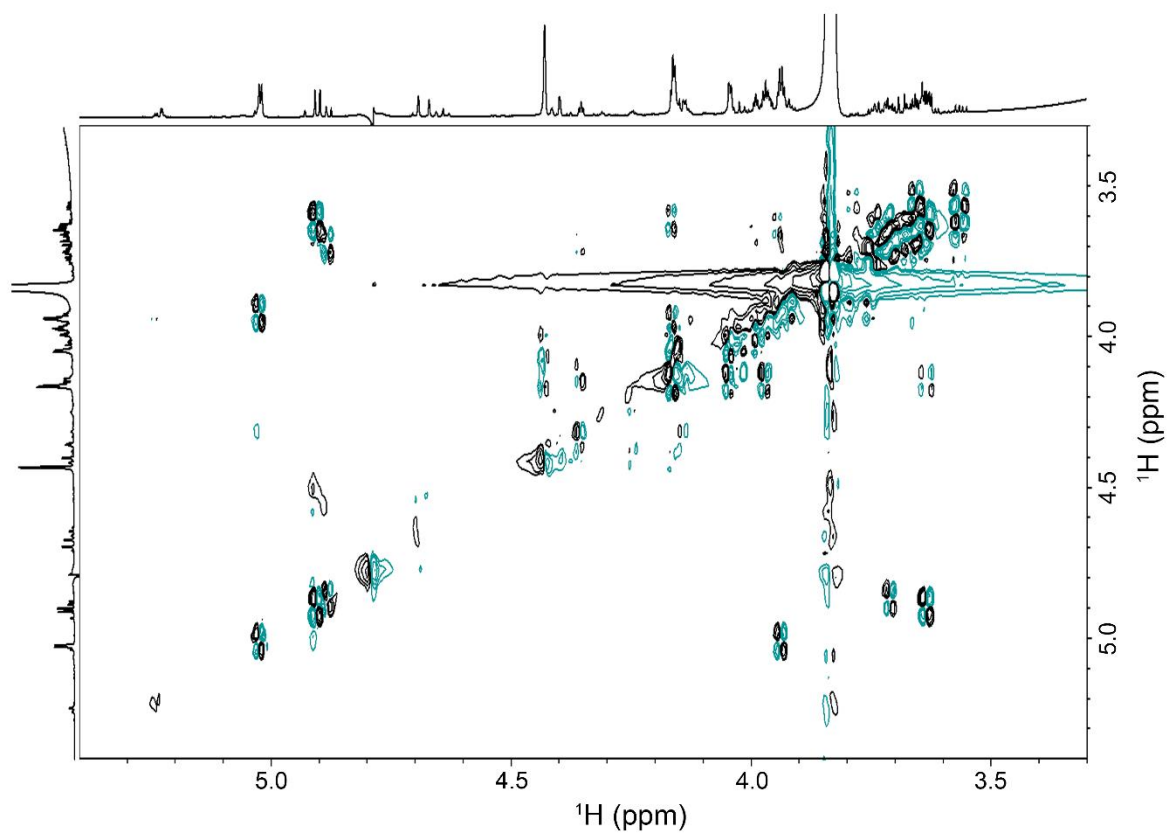
¹H.P.W. and S.J. contributed equally to this work

*To whom correspondence may be addressed: Prof. David Rice, Krebs Institute for Biomolecular Research, Department of Molecular Biology and Biotechnology, University of Sheffield, Sheffield, S10 2TN, United Kingdom, +44 114 222 4242, d.rice@sheffield.ac.uk.

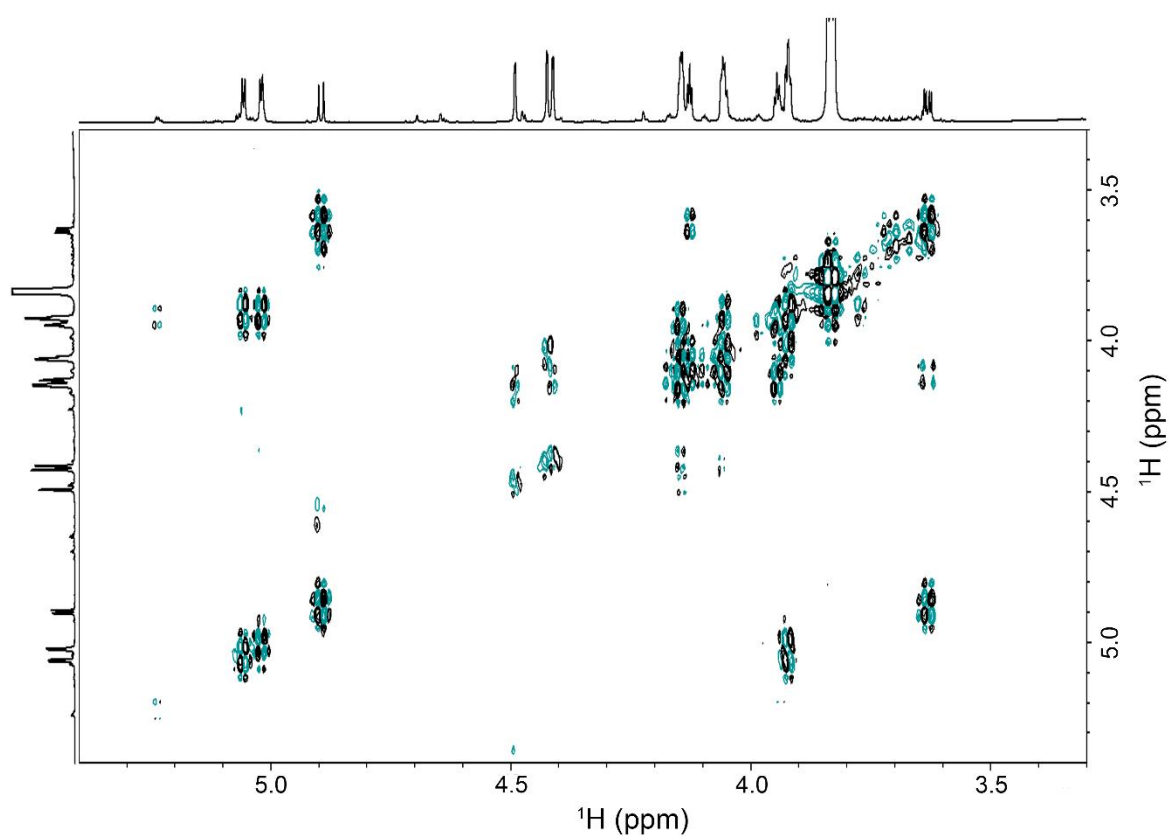
Keywords: alginate | alginate lyase | enzyme mechanism | chair conformation | NMR spectroscopy | X-ray crystallography



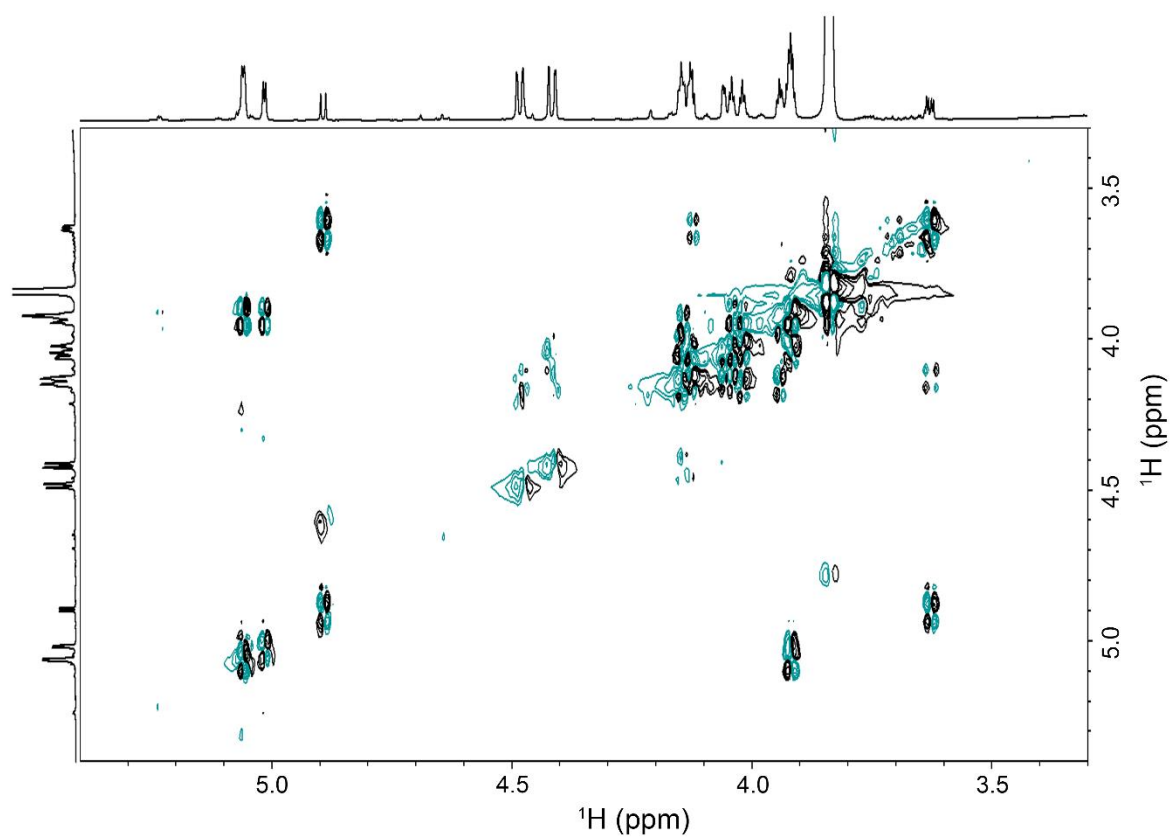
Supplementary Figure 5.1. Comparison of TM5 substrate positions. (a) Overlay of triG_u (sticks, cyan carbon atoms) and hexaG (sticks, yellow carbon atoms) in the active site of TM5 using the coordinates of the triG_u-bound enzyme to highlight key residues (sticks, grey carbon atoms). The rest of the TM5 active site is shown in grey cartoon representation, with the Ca^{2+} ion as a green sphere. (b) Overlay of hexaG and a polyM pentasaccharide (sticks, pink carbon atoms) in the active site of TM5. Colours are the same as in (a) except for polyM. Again, the coordinates of the triG_u-bound enzyme are used to highlight the positions of key residues.



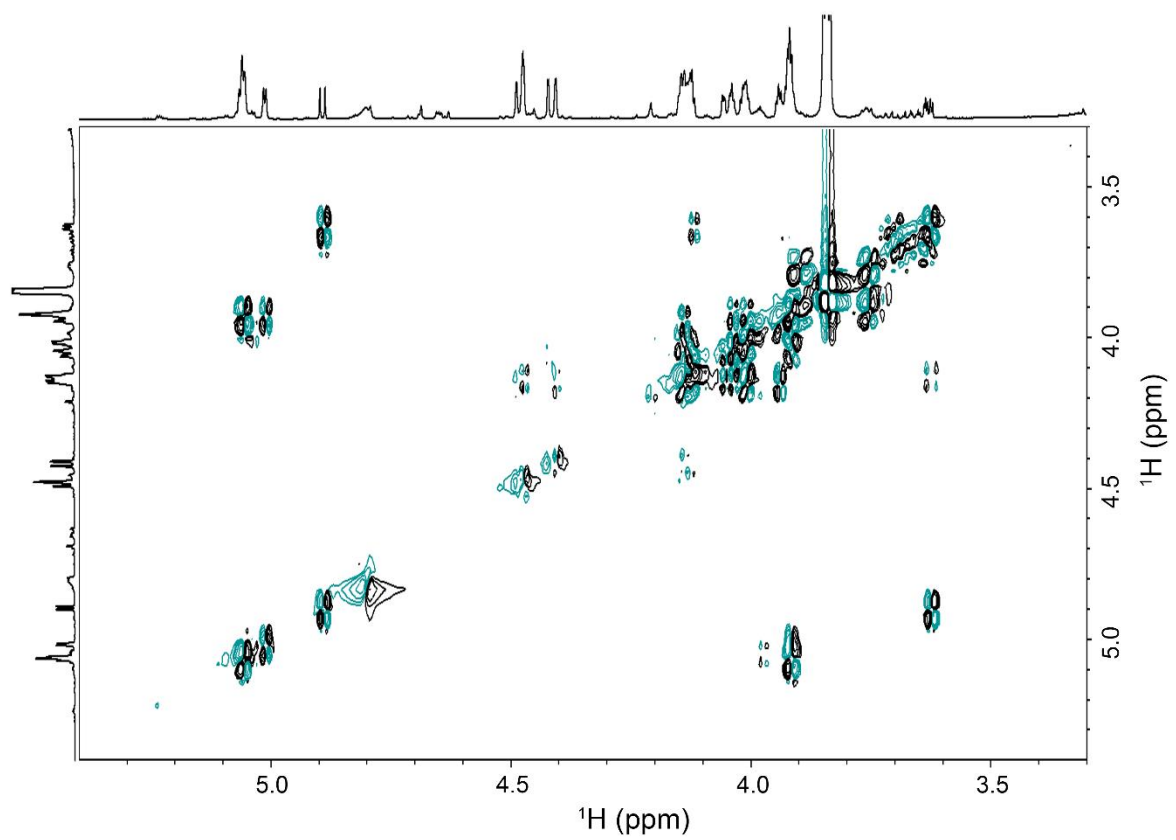
Supplementary Figure 5.2. COSY spectrum of diG. A COSY spectrum recorded using a sample of 10.6 mM diG prepared in 100% $^2\text{H}_2\text{O}$ with 1 mM TSP, 2 mM NaN_3 , 50 mM HEPES at pD 8.05. An external ^1H spectrum of the sample was used to produce the horizontal and vertical axes traces. Positive peaks are coloured black and negative crosspeaks are coloured green.



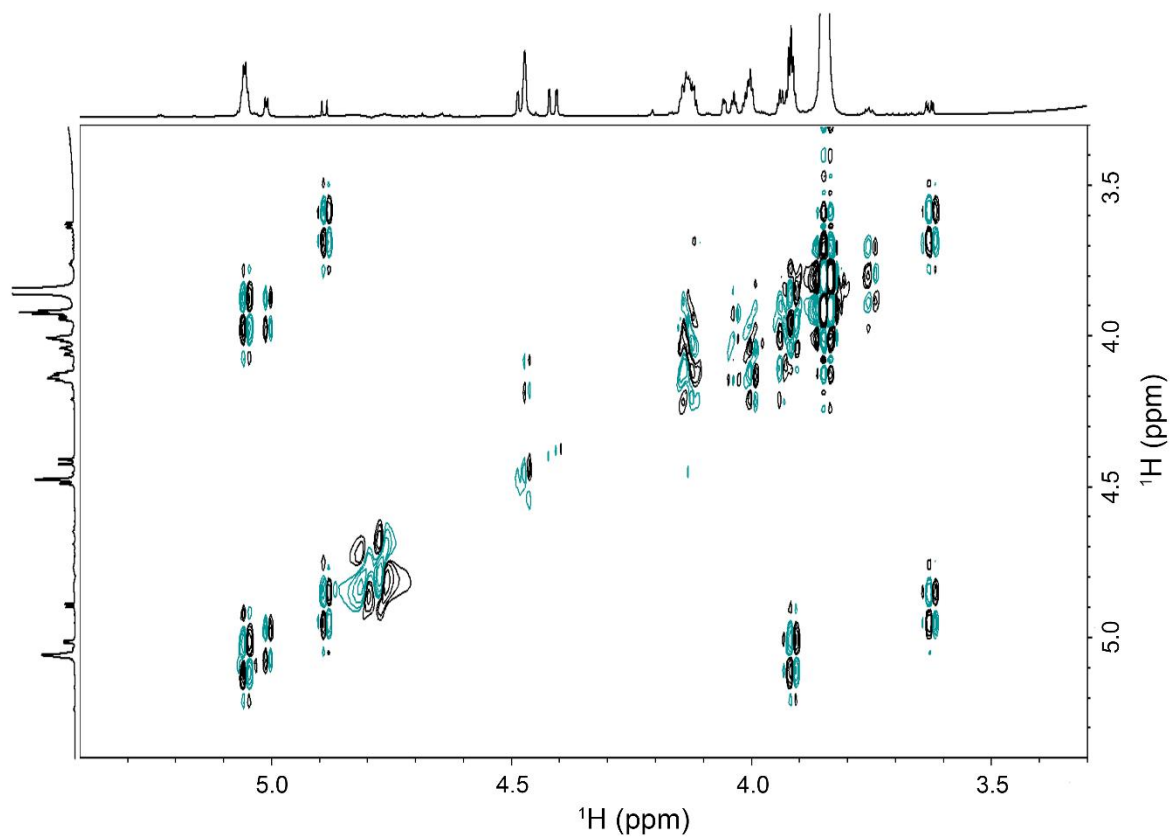
Supplementary Figure 5.3. COSY spectrum of triG. A COSY spectrum recorded using a sample of 7.3 mM triG prepared in 100% $^2\text{H}_2\text{O}$ with 1 mM TSP, 2 mM NaN_3 , 50 mM HEPES at pD 8.05. An external ^1H spectrum of the sample was used to produce the horizontal and vertical axes traces. Positive peaks are coloured black and negative crosspeaks are coloured green.



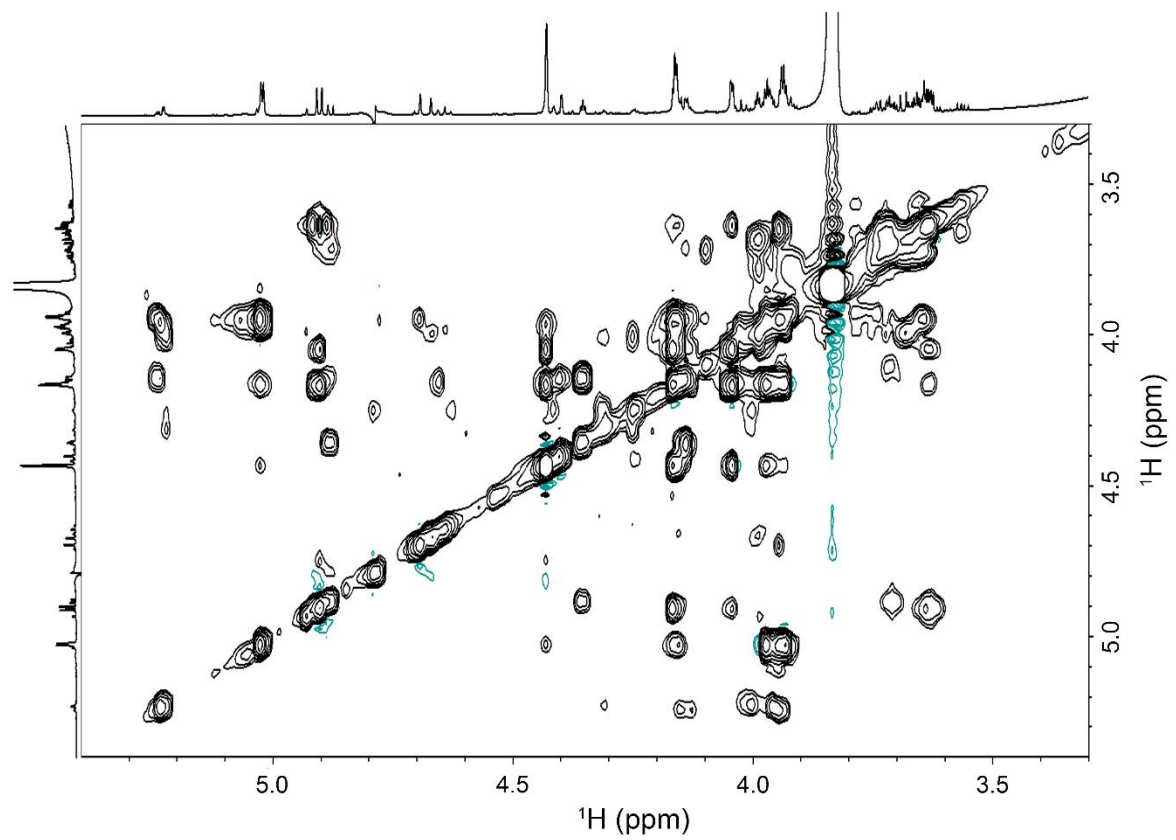
Supplementary Figure 5.4. COSY spectrum of tetraG. A COSY spectrum recorded using a sample of 6.2 mM tetraG prepared in 100% $^2\text{H}_2\text{O}$ with 1 mM TSP, 2 mM NaN_3 , 50 mM HEPES at pD 8.05. An external ^1H spectrum of the sample was used to produce the horizontal and vertical axes traces. Positive peaks are coloured black and negative crosspeaks are coloured green.



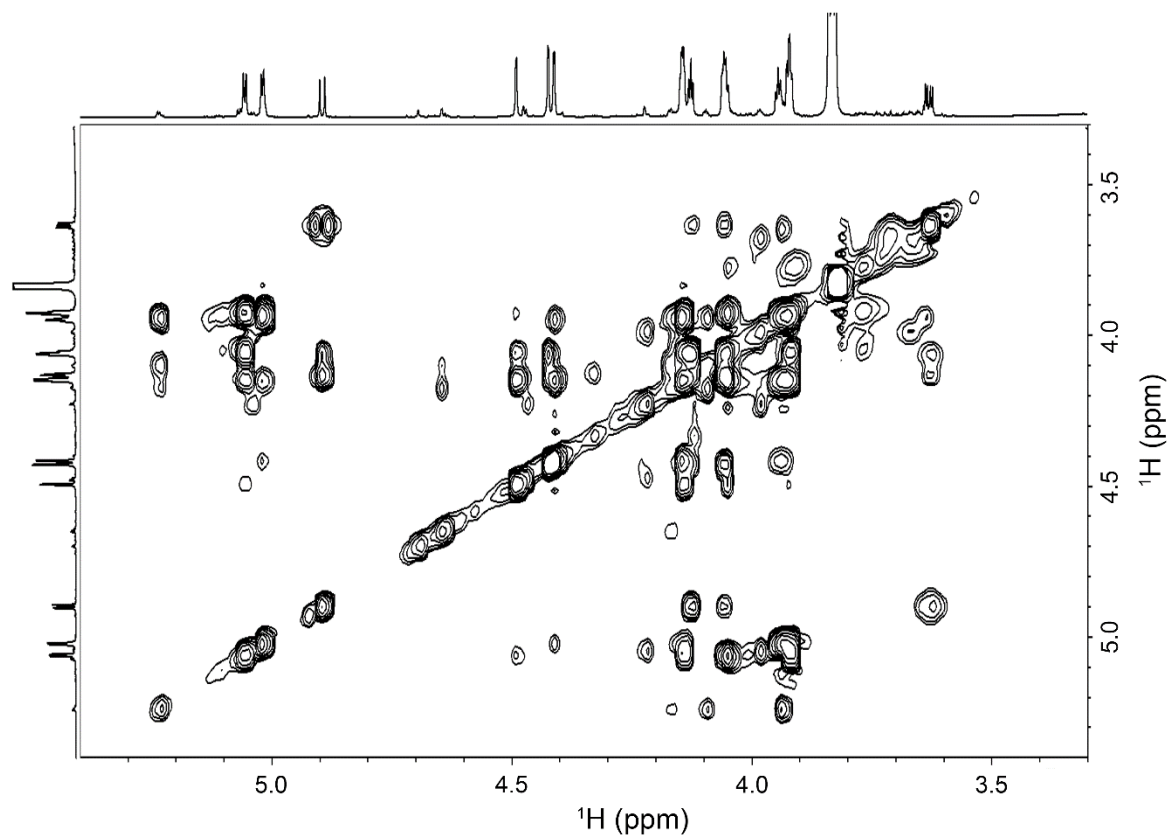
Supplementary Figure 5.5. COSY spectrum of pentaG. A COSY spectrum recorded using a sample of 10.0 mM pentaG prepared in 100% ${}^2\text{H}_2\text{O}$ with 1 mM TSP, 2 mM NaN_3 , 50 mM HEPES at pD 8.0. An external ${}^1\text{H}$ spectrum of the sample was used to produce the horizontal and vertical axes traces. Positive peaks are coloured black and negative crosspeaks are coloured green.



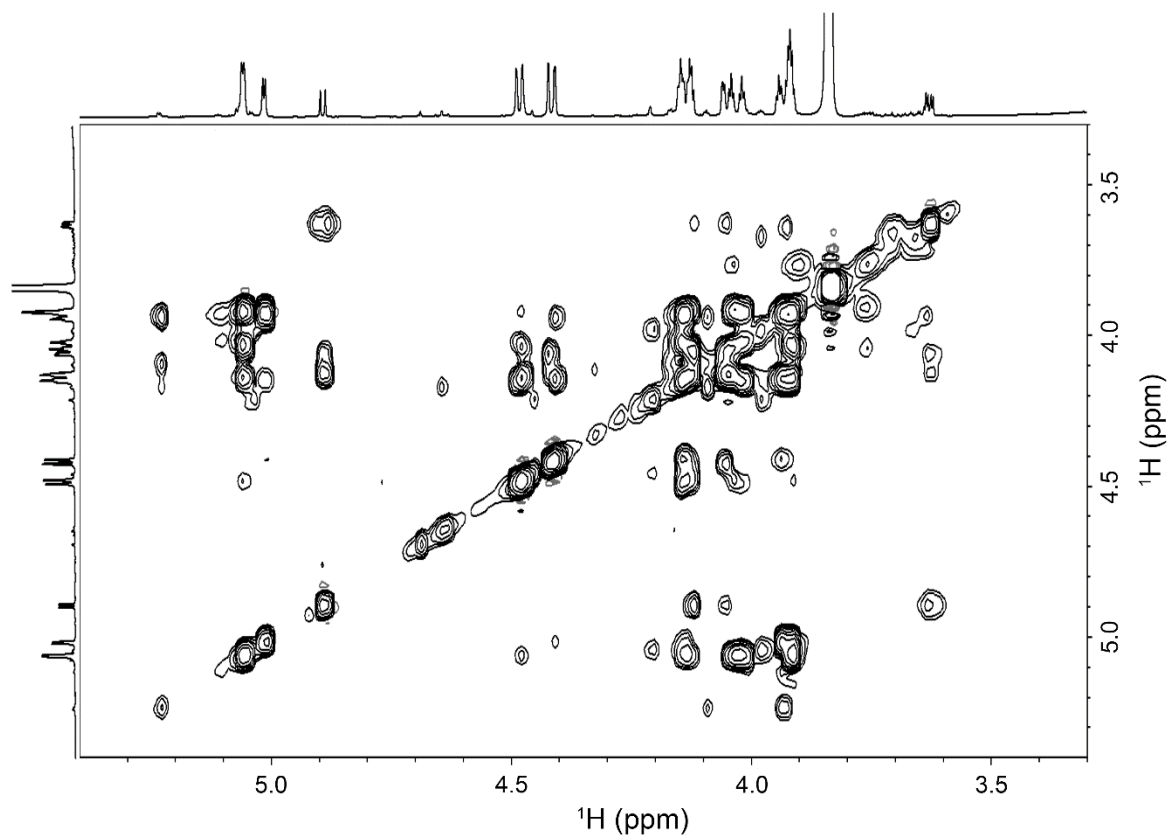
Supplementary Figure 5.6. COSY spectrum of hexaG. A COSY spectrum recorded using a sample of 3.3 mM hexaG prepared in 100% $^2\text{H}_2\text{O}$ with 1 mM TSP, 2 mM NaN_3 , 50 mM HEPES at pD 8.0. An external ^1H spectrum of the sample was used to produce the horizontal and vertical axes traces. Positive peaks are coloured black and negative crosspeaks are coloured green.



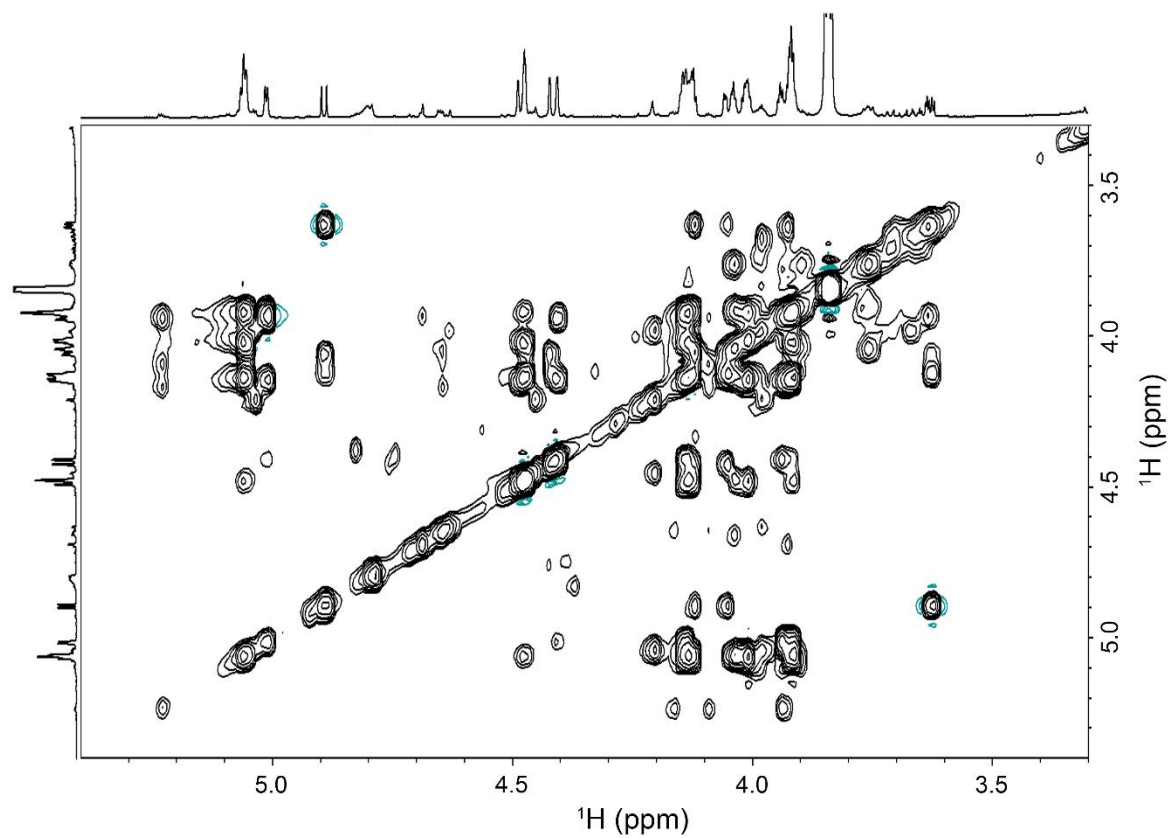
Supplementary Figure 5.7. TOCSY spectrum of diG. A TOCSY spectrum recorded using a sample of 10.6 mM diG prepared in 100% ²H₂O with 1 mM TSP, 2 mM NaN₃, 50 mM HEPES at pD 8.05. An external ¹H spectrum of the sample was used to produce the horizontal and vertical axes traces. Positive peaks are coloured black and negative crosspeaks are coloured green.



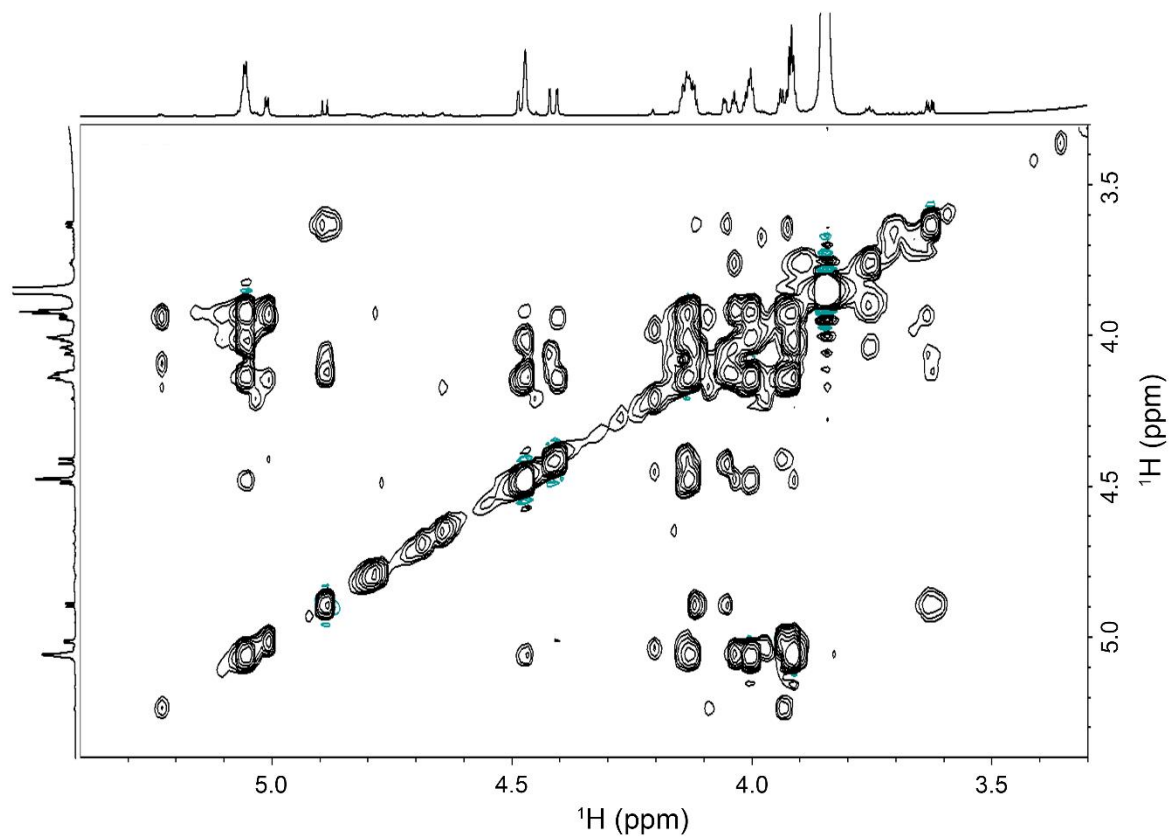
Supplementary Figure 5.8. TOCSY spectrum of triG. A TOCSY spectrum recorded using a sample of 7.3 mM triG prepared in 100% ²H₂O with 1 mM TSP, 2 mM NaN₃, 50 mM HEPES at pD 8.05. An external ¹H spectrum of the sample was used to produce the horizontal and vertical axes traces. Positive peaks are coloured black and negative crosspeaks are coloured green.



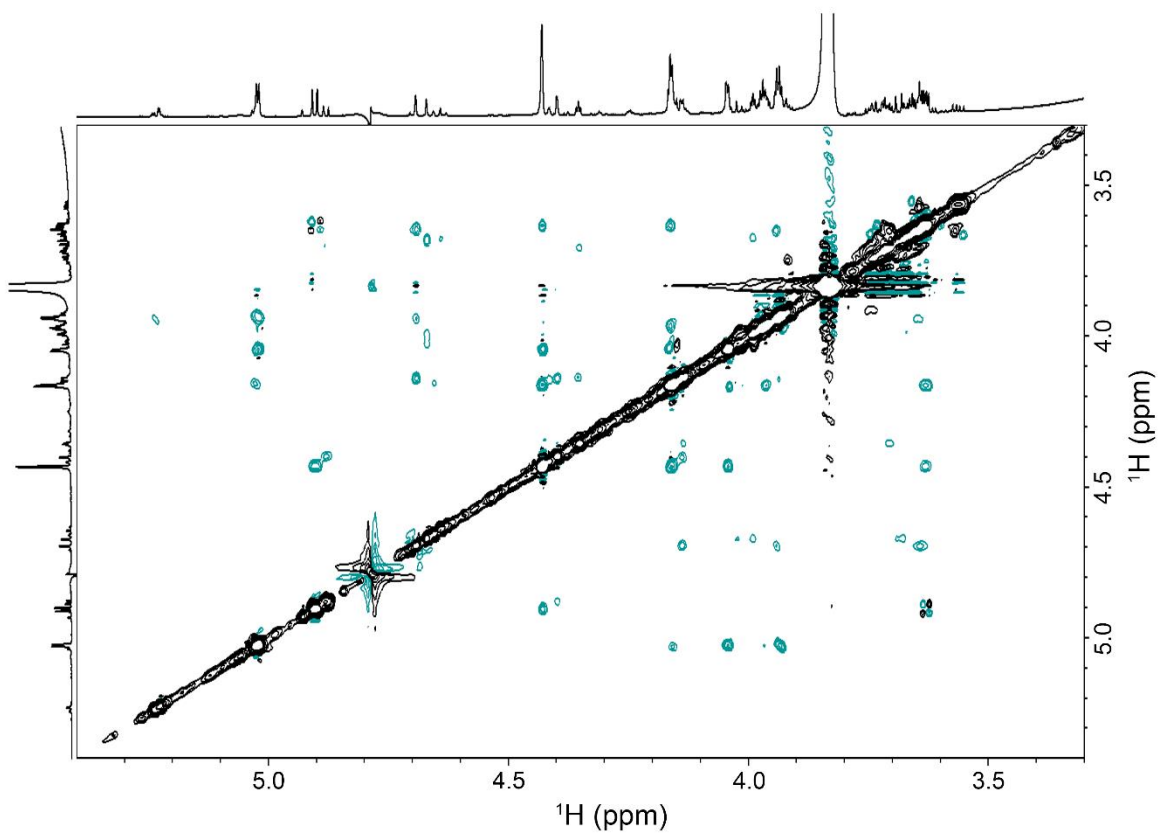
Supplementary Figure 5.9. TOCSY spectrum of tetraG. A TOCSY spectrum recorded using a sample of 6.2 mM tetraG prepared in 100% $^2\text{H}_2\text{O}$ with 1 mM TSP, 2 mM NaN_3 , 50 mM HEPES at pD 8.05. An external ^1H spectrum of the sample was used to produce the horizontal and vertical axes traces. Positive peaks are coloured black and negative crosspeaks are coloured green.



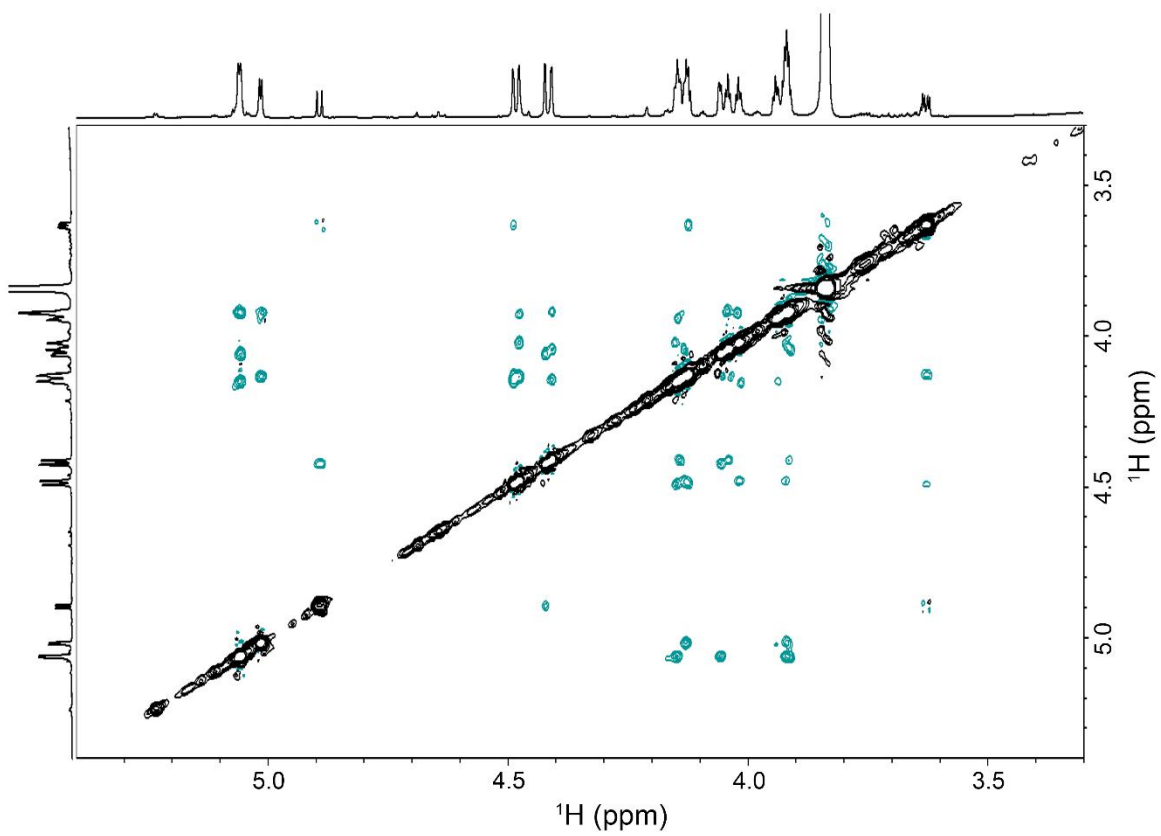
Supplementary Figure 5.10. TOCSY spectrum of pentaG. A TOCSY spectrum recorded using a sample of 10.0 mM pentaG prepared in 100% ²H₂O with 1 mM TSP, 2 mM NaN₃, 50 mM HEPES at pD 8.0. An external ¹H spectrum of the sample was used to produce the horizontal and vertical axes traces. Positive peaks are coloured black and negative crosspeaks are coloured green.



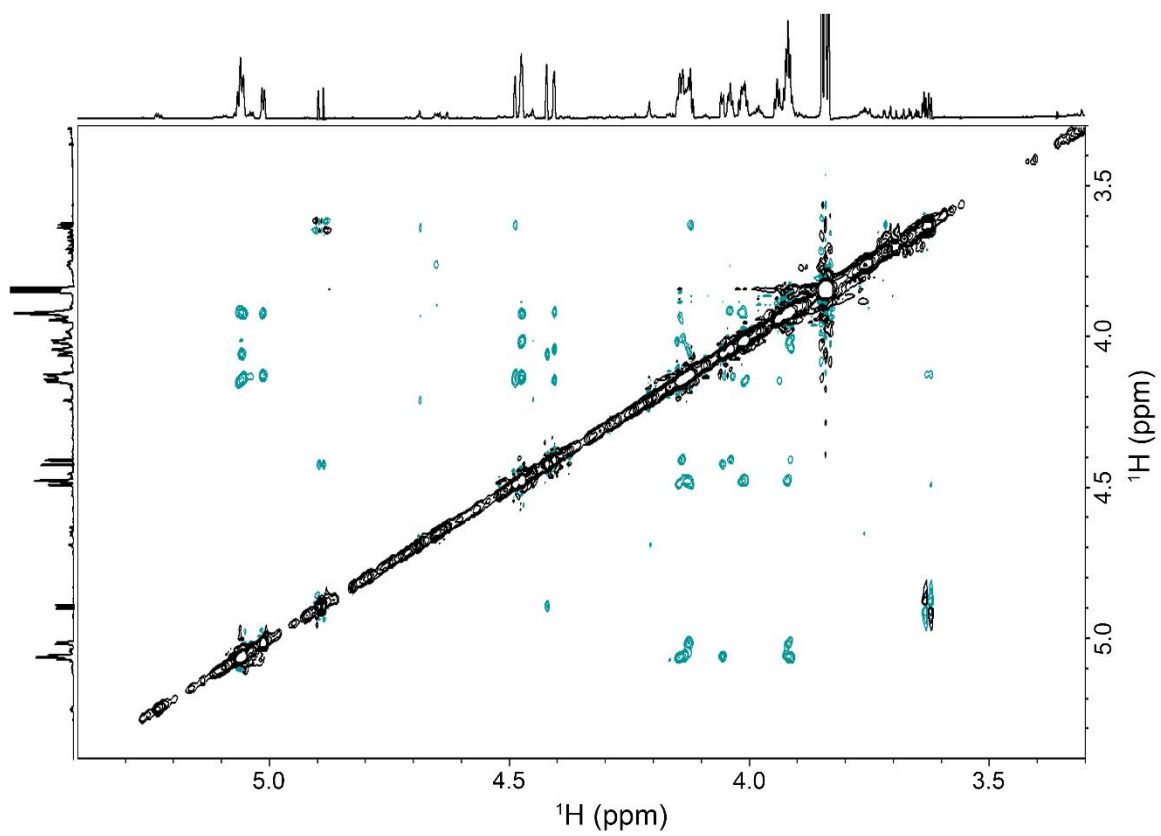
Supplementary Figure 5.11. TOCSY spectrum of hexaG. A TOCSY spectrum recorded using a sample of 3.3 mM hexaG prepared in 100% $^2\text{H}_2\text{O}$ with 1 mM TSP, 2 mM NaN_3 , 50 mM HEPES at pD 8.0. An external ^1H spectrum of the sample was used to produce the horizontal and vertical axes traces. Positive peaks are coloured black and negative crosspeaks are coloured green.



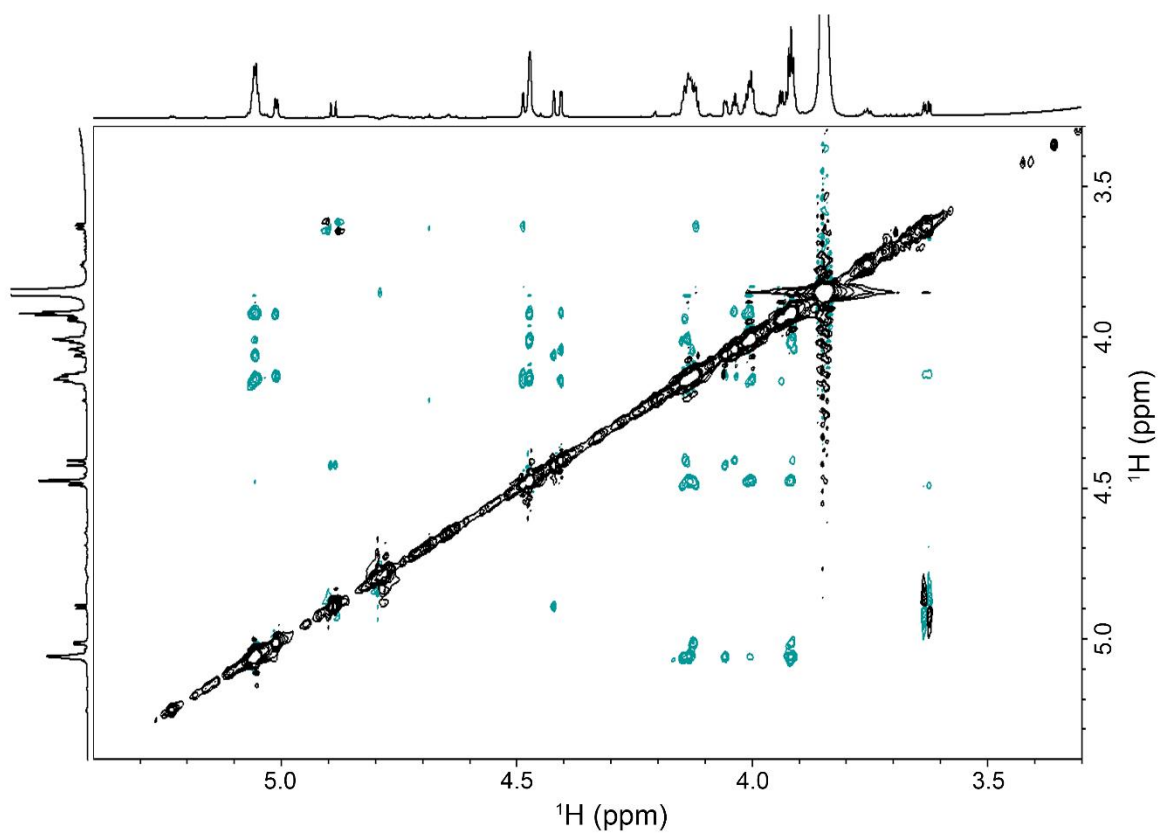
Supplementary Figure 5.12. ROESY spectrum of diG. A ROESY spectrum recorded using a sample of 10.6 mM diG prepared in 100% $^2\text{H}_2\text{O}$ with 1 mM TSP, 2 mM NaN_3 , 50 mM HEPES at pD 8.05. An external ^1H spectrum of the sample was used to produce the horizontal and vertical axes traces. Positive peaks are coloured black and negative crosspeaks are coloured green.



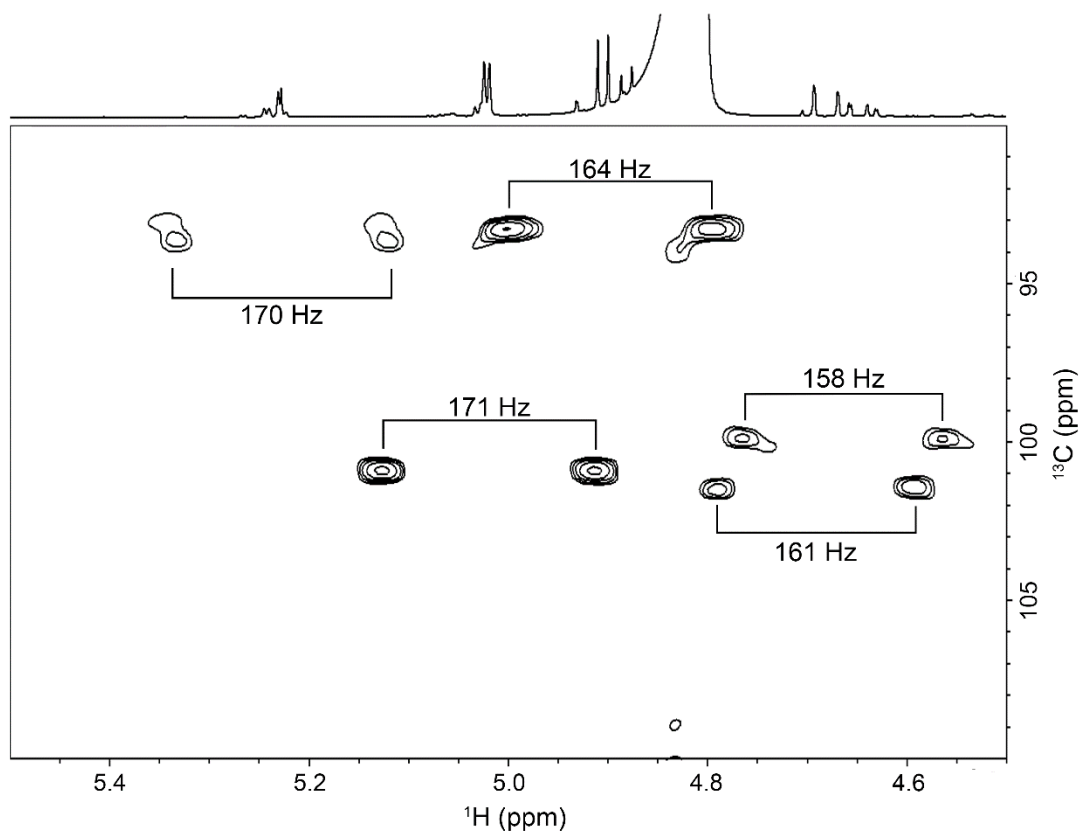
Supplementary Figure 5.13. ROESY spectrum of tetraG. A ROESY spectrum recorded using a sample of 6.2 mM tetraG prepared in 100% $^2\text{H}_2\text{O}$ with 1 mM TSP, 2 mM NaN_3 , 50 mM HEPES at pH 8.05. An external ^1H spectrum of the sample was used to produce the horizontal and vertical axes traces. Positive peaks are coloured black and negative crosspeaks are coloured green.



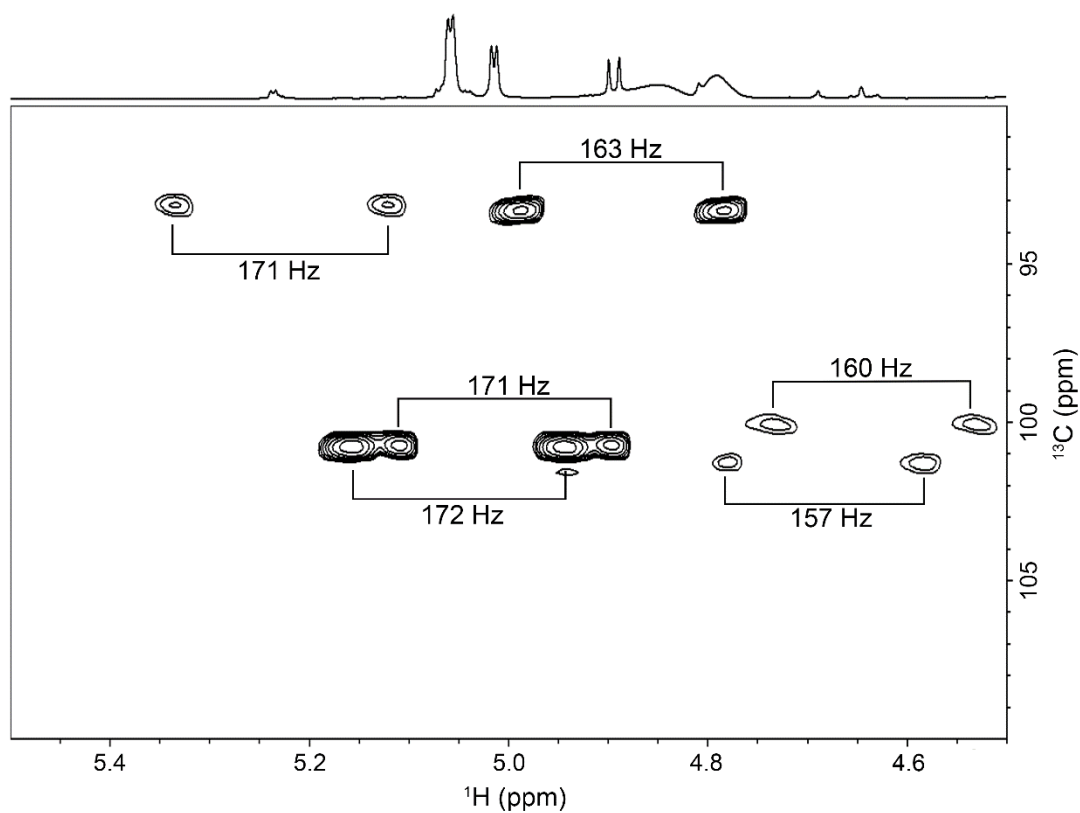
Supplementary Figure 5.14. ROESY spectrum of pentaG. A ROESY spectrum recorded using a sample of 10.0 mM pentaG prepared in 100% $^2\text{H}_2\text{O}$ with 1 mM TSP, 2 mM NaN_3 , 50 mM HEPES at $\text{pD}\ 8.0$. An external ^1H spectrum of the sample was used to produce the horizontal and vertical axes traces. Positive peaks are coloured black and negative crosspeaks are coloured green.



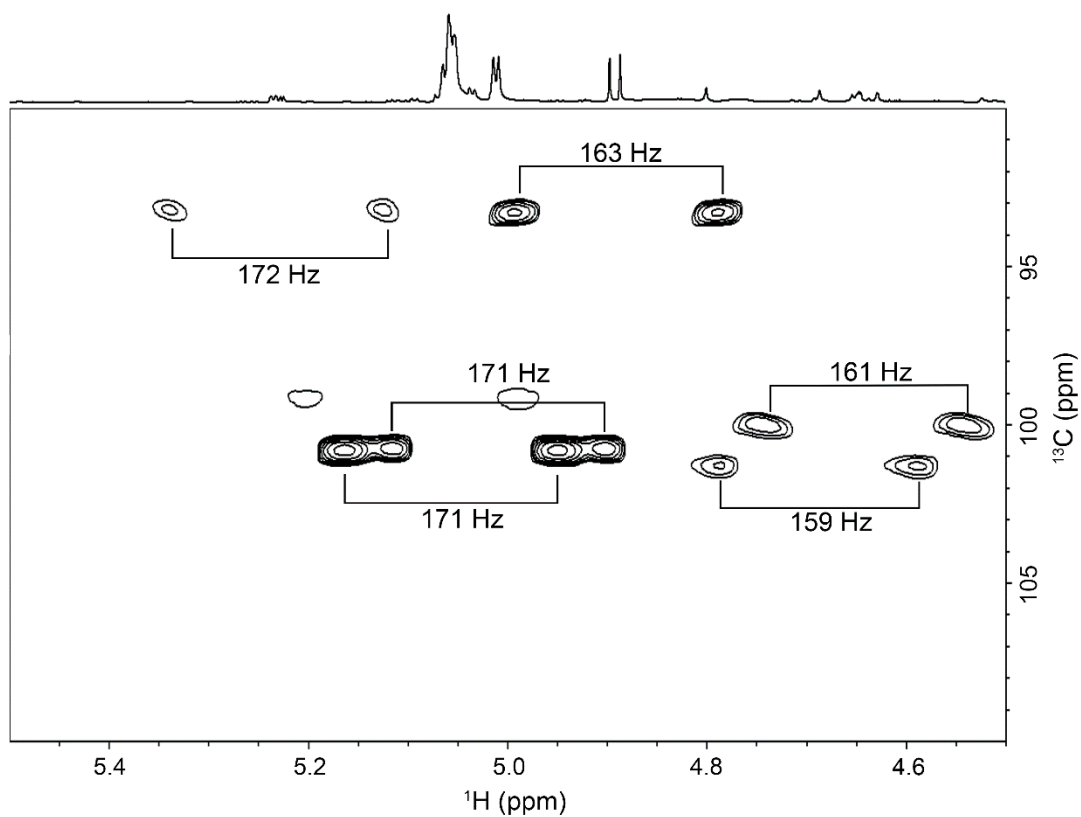
Supplementary Figure 5.15. ROESY spectrum of hexaG. A ROESY spectrum recorded using a sample of 3.3 mM hexaG prepared in 100% $^2\text{H}_2\text{O}$ with 1 mM TSP, 2 mM NaN_3 , 50 mM HEPES at pD 8.0. An external ^1H spectrum of the sample was used to produce the horizontal and vertical axes traces. Positive peaks are coloured black and negative crosspeaks are coloured green.



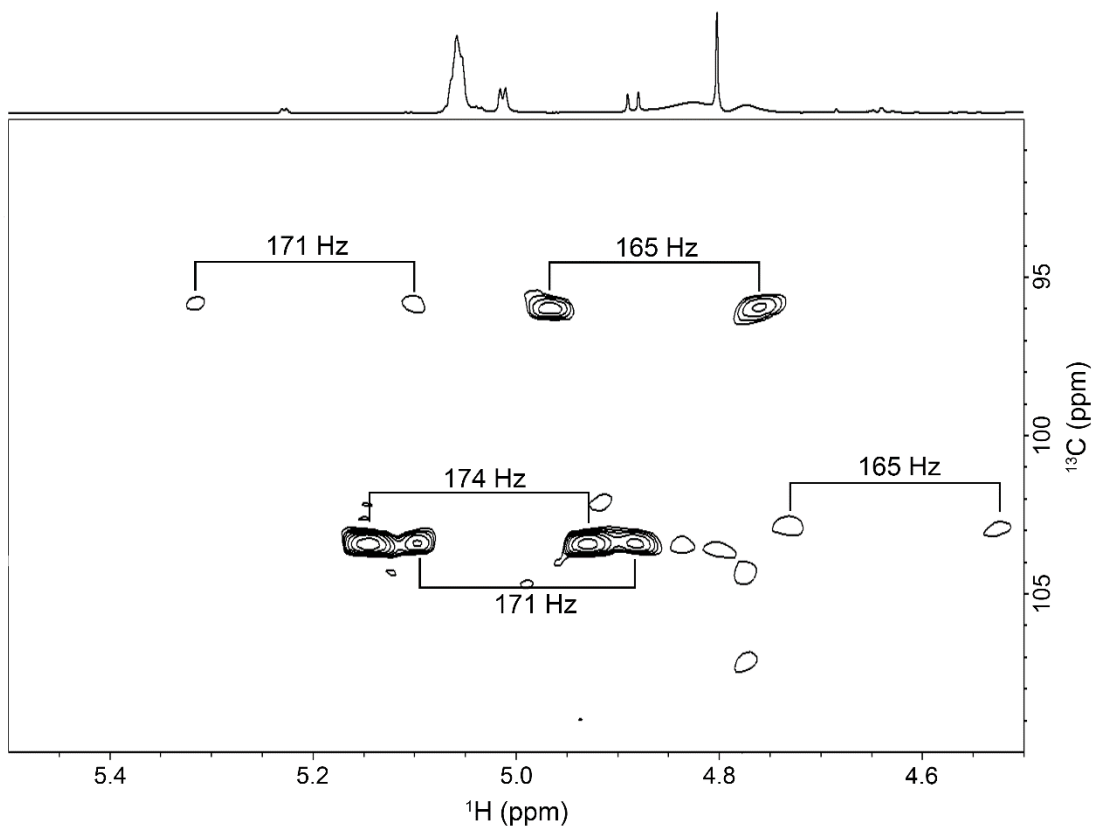
Supplementary Figure 5.16. $^1\text{H}^{13}\text{C}$ -HSQC spectrum of diG. A $^1\text{H}^{13}\text{C}$ -HSQC spectrum recorded without proton decoupling using a sample of 10.6 mM diG prepared in 100% $^2\text{H}_2\text{O}$ with 1 mM TSP, 2 mM NaN_3 and 50 mM HEPES at pD 8.05. An external ^1H spectrum of the sample was used to produce the horizontal axis trace. Each pair of peaks is labelled with its $^1\text{J}_{\text{C}1,\text{H}1}$ value. For clarity only positive peaks are shown.



Supplementary Figure 5.17. $^1\text{H}^{13}\text{C}$ -HSQC spectrum of tetraG. A $^1\text{H}^{13}\text{C}$ -HSQC spectrum recorded without proton decoupling using a sample of 6.2 mM tetraG prepared in 100% $^2\text{H}_2\text{O}$ with 1 mM TSP, 2 mM NaN_3 and 50 mM HEPES at pD 8.05. An external ^1H spectrum of the sample was used to produce the horizontal axis trace. Each pair of peaks is labelled with its $^1\text{J}_{\text{C}1,\text{H}1}$ value. For clarity only positive peaks are shown.



Supplementary Figure 5.18. $^1\text{H}^{13}\text{C}$ -HSQC spectrum of pentaG. A $^1\text{H}^{13}\text{C}$ -HSQC spectrum recorded without proton decoupling using a sample of 10.0 mM pentaG prepared in 100% $^2\text{H}_2\text{O}$ with 1 mM TSP, 2 mM NaN_3 and 50 mM HEPES at pH 8.0. An external ^1H spectrum of the sample was used to produce the horizontal axis trace. Each pair of peaks is labelled with its J_{CH} value. For clarity only positive peaks are shown.



Supplementary Figure 5.19. $^1\text{H}^{13}\text{C}$ -HSQC spectrum of hexaG. A $^1\text{H}^{13}\text{C}$ -HSQC spectrum recorded without proton decoupling using a sample of 3.3 mM hexaG prepared in 100% $^2\text{H}_2\text{O}$ with 1 mM TSP, 2 mM NaN_3 and 50 mM HEPES at pD 8.0. An external ^1H spectrum of the sample was used to produce the horizontal axis trace. Each pair of peaks is labelled with its $^1J_{\text{CH},\text{HI}}$ value. For clarity only positive peaks are shown.